# ABSTRACT


| | |
|---|---|
| Title of Dissertation: | NANOCOMPOSITE AND SOLUBLE ENERGETIC ADDITIVES FOR BURNING ENHANCEMENT OF HYDROCARBON FUELS |
| | Philip Michael Guerieri, Doctor of Philosophy, 2017 |
| Dissertation directed by: | Professor Michael R. Zachariah, Department of Chemistry & Biochemistry and Department of Chemical and Biomolecular Engineering |

Metallizing liquid fuels and propellants to improve performance of energy conversion and propulsion systems has been of interest for decades but past attempts to do so using micron-sized metal powders demonstrated inefficient combustion and low burning rates of modified hydrocarbons. “Nanofuels” composed of energetic nanoparticles like nanoaluminum suspended in liquid fuels have slowly emerged in scientific research over the last two decades with promising results. Increased burning rates, lower ignition delays, and high suspension stabilities compared to slurry fuels of micron-sized particles have been demonstrated; however, the effects of various energetic nanoparticles on the combustion of hydrocarbons remain poorly understood while particle agglomeration remains a performance-limiting problem.

The research in this dissertation identifies strategies for inclusion of aluminum into hydrocarbons which promote combustion performance in a free-droplet burning experiment developed herein. Considering the low burning rates which plagued micron particle-based slurry fuels, specific attention is paid to characterizing and understanding effects on droplet burning rate constants. Classical characterization of this metric based on the $D^2$-law for isolated droplet combustion is found to be unsuitable with heterogeneous energetic additives and thusly an original scheme for experimental approximation of burning rate constant is set forth. Several beneficial strategies for aluminum inclusion and burning rate enhancement are studied including co-addition of nanoaluminum with the gas generator nitrocellulose (NC), dissolution of Al-containing molecules including organometallic clusters into hydrocarbons, and burning rate enhancements realized with oxygen-carrying nanoparticle co-additives. Arguably the most impactful strategy identified however is the preassembly of active nanoparticles into NC-bound clusters or controlled agglomerates, termed "mesoparticles" (MPs), by electrospray which drastically improves droplet burning rate increases and nanofuel suspension stabilities observed compared to nanofuels of unassembled nanoparticles. Mechanisms of the various additives studied are probed with a variety of diagnostic techniques and burning rate enhancements are linked to physical effects of droplet disruptions on the diffusion-limited burning droplet system. The MP architecture causes a feedback loop between physical disruptions by gas liberation from droplets, transport of active additives into the flame where they react, and promotion of further gas evolution repeating and accelerating this process.

# NANOCOMPOSITE AND SOLUBLE ENERGETIC ADDITIVES FOR BURNING ENHANCEMENT OF HYDROCARBON FUELS

by

Philip Michael Guerieri

Dissertation submitted to the Faculty of the Graduate School of the
University of Maryland, College Park, in partial fulfillment
of the requirements for the degree of
Doctor of Philosophy
2017

Advisory Committee:
Professor Bryan Eichhorn, Dean's Representative
Professor Kenneth Kiger
Professor Johan Larsson
Professor Peter B. Sunderland
Professor Michael R. Zachariah, Chair

# Dedication

To my partner, my best friend, my inspiration, my alarm clock, and my better half Shannon, for her unwavering love, cheer, distractions, and care. To my parents Pamela and Dennis who have made everything I am and ever will be possible. To my siblings, Lauren, Kyle, and Jessop for their constant presence and inspiration. To the reasons our family works so hard, Henry, Anna, Owen, and those to come. To my grandparents, Eleanore, Robert, Alfred, Gladys, Arold, Alva, and Mac for teaching me who I can become and providing the means to get there. To Calvin for going anywhere with me, “things are never quite as scary when you’ve got a best friend”. To Andrew, Ashley, Charlotte, and Steven, for sharing a passion for living life. To the members of 814, for grounding me when it’s all too easy to lose perspective. And to all other friends and family, Guerieri, Hunt, O’Brien, Prag, Milano, Hunter, Sander, Bramble, Reilly, Campbell, and otherwise, I am only where I am for the support you all provide.

# Acknowledgements

This work would not have been possible without the abundance of support provided by advisors, colleagues, collaborators, and sponsors. I would foremost like to my advisor, Dr. Michael Zachariah, for his irreplaceable mentorship, patience, and support throughout my five years in his research group. This dissertation would not exist without Dr. Zachariah's leadership. Additional thanks to my current and former colleagues in the Zachariah lab for their invaluable scientific discourse, cooperative spirit, and collaborative efforts including Dr. Haiyang Wang, Dr. Jeffery DeLisio, Dr. Garth Egan, Rohit Jacob, Dylan Kline, Miles Rehwoldt, Xizheng Wang, Scott Holdren, Tao Wu, Kevin Yang, and Carlos Rodriguez. Thanks to my various research collaborators for their patience, inspiration, knowledge, and hard work including in particular Dr. Samantha DeCarlo, Dr. Dennis Mayo, Dr. Bryan Eichhorn Dr. Andrew Kerr, Dr. Edward Foos, Dr. Gregory Young, Xin Tang, Zachary Hicks, Dr. Kit Bowen, Lauren Stevens and Dr. Will Gibbons. Thank you to my advisory committee for generously sharing their time and expertise, Professor Bryan Eichhorn, Professor Kenneth Kiger, Professor Johan Larsson, and Professor Peter Sunderland. Special thanks are given to Terry Connell and Professor Richard Yetter of Penn State University for providing the original droplet combustion experiment equipment. This work was made possible from the support of an Air Force Office of Scientific Research MURI grant and the Defense Threat Reduction Agency. Thanks to these sponsors for their ongoing investment in academic research.

# Table of Contents

# List of Tables

# List of Figures

# List of Abbreviations

| | |
|---|---|
| AP | Ammonium Perchlorate |
| CEA | NASA Chemical Equilibrium with Applications |
| DSC | Differential Scanning Calorimetry |
| EDS | Energy Dispersive X-Ray Spectroscopy |
| ES | Electrospray |
| EM | Energetic Material |
| HTPB | Hydroxyl-terminated polybutadiene |
| IUPAC | International Union of Pure and Applied Chemistry |
| LOX | Liquid Oxygen |
| LPG | Liquified Petroleum Gas |
| MP | Mesoparticle |
| nAl | Nanoaluminum |
| NC | Nitrocellulose |
| NP | Nanoparticle |
| PMT | Photomultiplier Tube |
| PTFE | Polytetrafluoroethylene |
| PVDF | Polyvinylidene Fluoride |
| RDX | Cyclotrimethylenetrinitramine |
| SDT | Simultaneous DSC/TGA |
| SEM | Scanning Electron Microscopy |

| | |
|---|---|
| SOP | Standard Operating Procedure |
| TGA | Thermal Gravimetric Analysis |
| TiBAl | Triisobutylaluminum |
| TiBam | Triisobutylamine |
| T-Jump | Temperature Jump |
| TNT | 2,4,6-trinitrotoluene |
| TOFMS | Time-of-Flight Mass Spectroscopy |
| TOPO | Trioctylphosphine Oxide |
| XRD | X-Ray Diffraction |

# Chapter 1: Introduction

## *1.1 Reactive Metals and Nanoenergetics*

A primary mode of energy storage and transfer utilized in numerous technologies and systems is chemical energy, which is predicated upon differences in bond energies in various chemical substances that arise from electrons in different energy levels depending on chemical bond characteristics. The definition of bond energy according to IUPAC is "the energy required to break a given type of bond between atoms in certain valence states…commonly derived by dissecting the heat of atomization of a molecule into contributions of individual bonds" [1]. Namely, energy is added to a compound to break its chemical bonds and if they reform into compounds with lower total bond energy, then conservation of energy indicates that energy must be released in the process. An example of this is given by simple hydrogen combustion.

$$2\,H_2 + O_2 \rightarrow 2H_2O \tag{1}$$

The bond energies in this reaction at 298 K are: 436.0 kJ/mol for H-H, 498.5 kJ/mol for O=O, and 463.5 kJ/mol for O-H [2]. The total bond energy of the reactants is 1370.5 kJ and the products 1854.0 kJ, and recalling energy is required to break chemical bonds and released when bonds are formed reveals this combustion reaction releases 483.5 kJ.

Energetic materials (EM) are those like the hydrogen/oxygen mixture considered above: which contain a large amount of potential chemical energy that upon reaction can be released. Such materials are usually composed of a fuel and oxidizer

(e.g. the $H_2$ and $O_2$ respectively) and depending on their purpose can be classified as fuels (e.g. gasoline/air), rocket propellants (e.g. RP-1/LOX), gun propellants (e.g. smokeless powder), pyrotechnics (e.g. sulfur/potassium nitrate), or high explosives (e.g. TNT). The energy potential does not change as long as the chemical composition of the EM remains the same which lends particular usefulness to EM for energy storage. Many of these EM types/purposes have specific desired characteristics including minimum energy density or energy release rate. For example, high explosives are meant to detonate and use the shockwave and heat to destroy objects and thusly must have an exceedingly high energy release rate compared to other EMs. Because the fuel and oxidizer in these formulations must interact to react and release chemical energy, their proximity to each other (among other characteristics) dictates the rate of the reaction. High explosives are usually monomolecular EMs meaning the fuel and oxidizer are contained within a single molecule like RDX so that their proximity is incredibly close and thusly their energy release rates tremendously high [3]. On the basis of oxidation and fluorination energetics, Figure 1 shows the relative combustion energy available from different atoms up to Argon along with bulk densities of those species, illustrating how EM characteristics are highly dependent on composition. Notably, several metals including Li, Be, B, Mg, Al and Si have high potential for efficient application in EMs owing to their high combustion energies and bulk densities and for these reasons are commonly employed in solid rocket engines (although Be is highly toxic and rarely used) [4]. Alternatively while monomolecular explosives

feature high energy release rates, they are mostly composed of CHNO compounds which have relatively low energy densities [5].

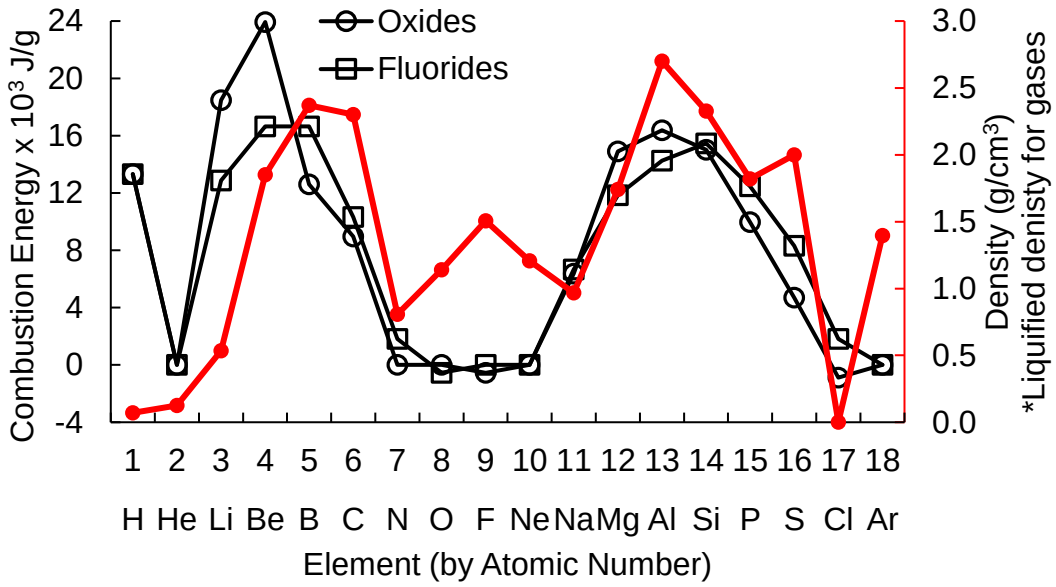


*Figure 1: Combustion Energy of Elements [6] with density of elements (liquified densities at b.p. shown for gases at s.t.p.).*

Metal fuels pose unique challenges when used in EMs, one of which is the control of their solid form at room temperature. Energetic liquids and gases can be flowed, compressed, and dispersed for intimate mixing with oxidizers. However, these tasks are non-trivial with a solid EM and conventionally metals have been ground into powders for easier storage, manipulation, and most of all mixing with an oxidizing component to facilitate combustion reactions. Returning to the discussion of reaction rates and the proximity of the fuel and oxidizer in composite EMs, the length scale of metal powder particles plays a key role in the resultant energy release rate. Conventionally, metal powders are ground to micron sizes which suffer from high ignition temperatures (as high as 2350 K for aluminum [7]), long ignition delays, and

low energy release rates due to slow heterogeneous reactions limited by diffusion of oxidizer and/or fuel to reach the other component through passivating metal oxide layers [5]. Following the logic of the shorter length scales between fuel and oxidizer in monomolecular explosives, metal-based EMs benefit from smaller particle sizes and greater interfacial mixing of fuel and oxidizer, the ideal system hypothetically being composed of metal and oxidizer homogenously mixed at the finest possible scale without chemical bonding wherein reaction rates are no longer limited by slow heterogeneous mass transport [5]. For these reasons, research on metal combustion reemerged heavily in the 2000s and onward as the ability to control and characterize nanoscale materials grew more routine [4].

Physiochemical properties of nanoparticles can vary significantly from the bulk material due to the increasing fraction of surface atoms with decreasing particle size and the excess energy attributed to these surface atoms [4, 7]. Nanometals compared to micron-sized metal powders have been observed experimentally to feature lower ignition temperature, lower ignition delays, and significantly higher energy release rates due to more intimate mixing made possible as particle size decreases [4]. However, metals also feature a passivating outer metal oxide layer on the order of a few nanometers in thickness and as the particle size decreases this non-energetic layer comprises an increasing and eventually overwhelming fraction of the material drastically decreasing the energy content of a nanometal [4]. Development of novel methods for passivating energetic nanomaterials is therefore an ongoing subject of

scientific research since prevention of the metal oxide layer formation could permit smaller useful nanometal particle sizes and thusly higher reaction rates [7].

### 1.1.1 Nanothermites and Reactive Sintering

When the metal fuel in an EM and an oxidizer composed of metal oxide are both synthesized and mixed as nanoparticles, they formulate a "nanothermite". In such materials, the metal (A) and metal oxide ($BO_x$) compositions must be suitable to undergo a thermodynamically favorable and usually highly exothermic intermetallic chemical reaction of the form below [8].

$$A + \frac{y}{x}BO_x \rightarrow \frac{y}{x}B + AO_y \quad (2)$$

Aluminum is commonly used as the reactive metal with metal oxides such as copper oxide, iron oxide, or bismuth oxide used as the oxidizer. Materials such as these are readily available as nanoparticles for mixing into nanothermites with significantly higher reaction rates than micron-sized thermite powders [7].

A detrimental phenomenon in practical nanothermite combustion seen earlier in reactive Al/Ni systems [9] was highlighted in nAl-based systems in 2012 when this "reactive sintering" was observed in nAl nanothermites on a timescale relevant to ignition and combustion of the material [10]. As-received energetic nanoparticles like nanoaluminum (nAl) are frequently claimed to be e.g. "80 nm particle size", however TEM of the material reveals that primary particles of this approximate size are aggregated into fractal shapes approximately an order of magnitude larger, as exemplified by Figure 2(a) showing TEM of "80 nm primary particle size" nAl from Novacentrix. Demonstrated in Figure 2, as such particles are heated their increased

mobility causes coalescence of their nanostructured, highly connected primary particles into larger cohesive bodies, a process called “reactive sintering” when it occurs in an EM as it heats towards ignition [10, 11]. Using in-situ microscopy with high heating rates meant to emulate nanothermite reaction conditions, Egan et al. have shown that this process occurs for both nAl alone and nAl/CuO nanothermites, the latter of which can occur in 0.5-5.0 μs depending on the particle size and result in “phase-separated adjoining spheroids” while pressure cell experiments with nanothermites demonstrate those reactions can reach peak pressure on the order of 10 μs from the start of heating [11, 12]. Recalling that shorter composite EM length scales decreases diffusion distances between fuel and oxidizer thereby speeding up the rate limiting heterogeneous reaction steps, it follows that reactive sintering detrimentally limits the improvements realized as particle sizes approach the nanoscale since their intimate mixing and short length scale is lost by reactive sintering in times relevant to nanothermite ignition. If nanothermites are designed with architectures which can either prevent reactive sintering or maintain the fuel/oxidizer interfacial contact and small length scales of nanoenergetics despite reactive sintering, then significant reactivity improvements could be realized [10].

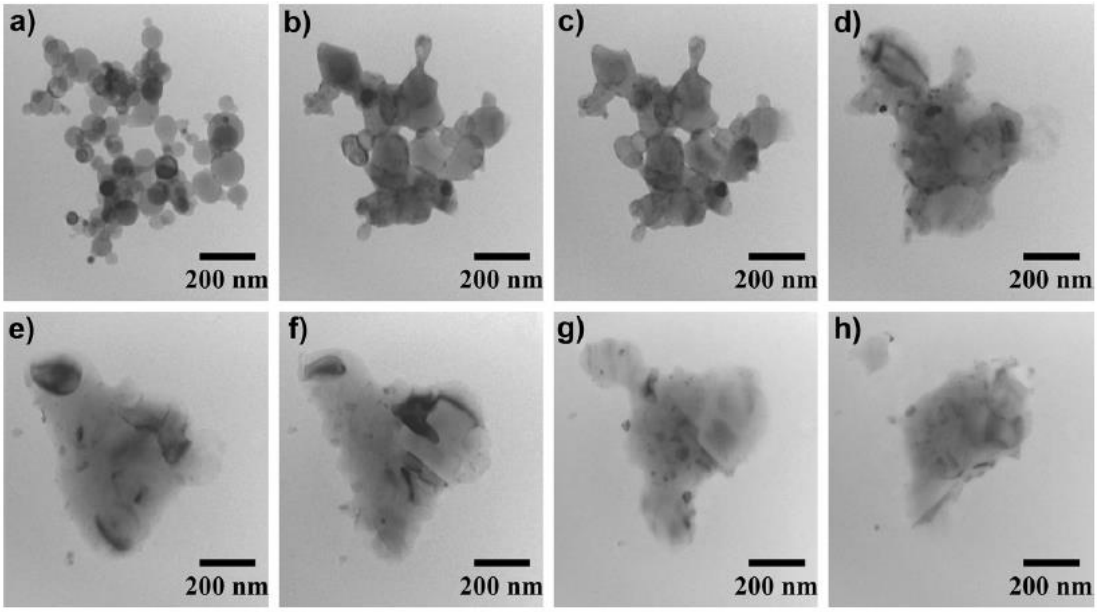


*Figure 2: 80 nm primary particle size nAl as-received from Novacentrix (a) heated with 12 ns laser pulses at 1.23 kJ/m$^2$ (b-h) by Egan et al. depicting sintering due to heating times relevant to nanothermite reaction times [11]. Reprinted with permission from AIP Publishing LLC.*

### 1.1.2 Mesoparticle Composites

Research seeking to identify such an architecture for nanothermites which could overcome reactive sintering yielded positive findings soon after the sintering was shown experimentally in nAl nanothermites. Wang et al. used electrospray particle assembly to formulate gelled nAl microspheres with high porosity held together with a nitrocellulose (NC) binder, one which would decompose rapidly to generate gas at relatively low temperature (~170 ºC) compared to nanothermite ignition temperatures [13]. Testing this material with wire ignition experiments, this work showed that such "mesoparticles" (MPs) significantly reduced the ignition delay and lengthened the burning time of the nanoaluminum compared to simple mixtures of nAl and NC without the electrospray preassembly [13]. In a follow-up study, this methodology was

extended to nAl/CuO nanothermites in NC-bound MPs and both wire ignition and constant-volume pressure cell combustion experiments demonstrated enhanced reactivity attributed to the MP architecture evidenced by higher maximum pressures and pressurization rates and longer burning times when electrospray preparation was utilized [14]. By electrospraying nanothermites with at least 5 wt% NC binder, the authors suggested that the NC decomposition step prior to thermite ignition expands the structure with heated gas promoting reaction of a locally dispersed hot cloud of nanothermite with low agglomerate interconnectivity thereby mitigating reactive sintering.

This principle has been reinforced by further research published since to probe the mechanisms of the MP architecture and demonstrate various applications. Incorporation of iodine into electrospray precursors resulted in iodine-impregnated nAl/CuO MPs which, at the cost of some performance, released iodine for biocidal applications upon reaction thereby demonstrating the flexible nature of the electrospray assembly method for tailoring specific nanothermite ingredients without unacceptable detriment to combustion performance [15]. Application of nAl MPs in experimental solid rocket propellants yielded higher burning rates than conventional micron-sized aluminum particles in [16]. While nanoparticles pose specific processing challenges precluding their widespread use in solid rockets owing to their high specific surface area, MPs are generally larger particles with the surface area and reactivity of nanoscale aluminum and therefore could mitigate such challenges [16]. More recently Jacob et al. sought to experimentally demonstrate and investigate the modes suggested by which

the MP strategy improves combustion [17]. That study electrosprayed nAl/NC MPs in a custom apparatus which entrained the resultant MPs in an aerosol flow for characterization and combustion testing by injection into the methane/oxygen flame of a Henken burner. Results showed short burning times of the nAl/NC MPs similar to those of the smallest agglomerates in as-received nAl, attributed to high combustion rates of these materials and suggesting the MP structure promoted combustion of small nAl agglomerates rather than large fractal aggregates. By quenching and examining combustion products by SEM, the investigators also collected evidence of smaller product particle sizes from the MP nAl/NC compared to commercial nAl and proposed a two-step mechanism of MP combustion wherein NC decomposes at relatively low temperature to disperse nAl particles which then oxidize classically as separate small groups [17]. This constitutes experimental evidence that electrospray assembly of nanoenergetic materials is an effective method to mitigate detrimental performance effects of reactive sintering.

### *1.2 Metallizing Liquid Propellants*

The application of various propulsion methods is limited by the operating envelope of the flight vehicle and energy source utilized [5]. Air-breathing propulsion, for instance, can deliver a higher specific impulse than rockets by utilizing atmospheric oxygen instead of an on-board oxidizer, but cannot operate outside specific flight envelopes without ample oxygen delivery to the engine [5, 7]. Such technological limitations on propulsion can be mitigated by modifying the combustion properties of fuels and propellants available to vehicle engineers. With their high density-specific

enthalpy of combustion, energetic metals can be added to propellants and explosives to drastically increase the volumetric energy density as evidenced in Figure 3. Historically, micron-sized metal particles have been studied and used in rocket propellant formulations as either the primary fuel (e.g. solid composite rocket propellants) or as an additive to increase the energy content of solid and gelled propellants. As mentioned previously, nanoparticles (with diameters between 1-100 nm) have demonstrated shorter ignition delays and higher burning rates than larger particles due to their increasing surface to volume ratio as particle size decreases [4]. Nano-scale metal additives are also better suited to liquid propellant incorporation since they can replace traditionally non-energetic gelling agents and boast lower settling velocities than larger particles. However, colloidal stability also remains a significant challenge as nanoparticles are highly prone to aggregate and settle out of suspension before the reactive benefits of the additive can be utilized [4].

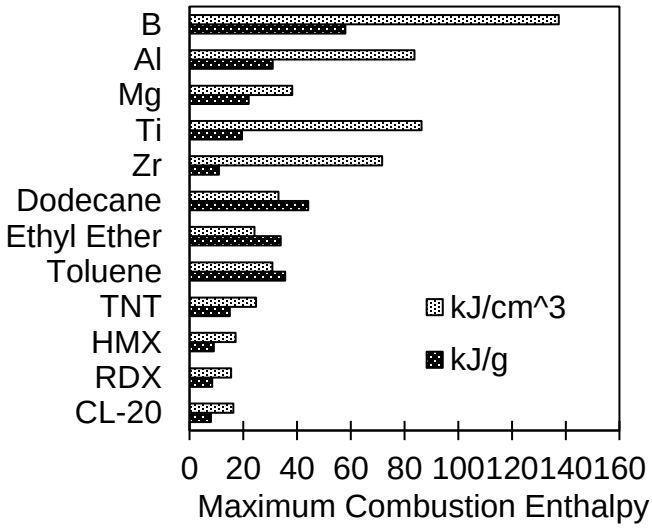


*Figure 3: Volume and mass specific maximum combustion enthalpies for select energetic metals, liquid fuels, and explosives based on data in [5].*

Thermodynamically, the benefit of metallizing a hydrocarbon to increase energy density for higher volume-limited payload capability is described by an increase in density-specific impulse upon metal addition [6, 18]. At ample loadings, metal particulate additives can replace conventionally inert gelling agents to form a higher viscosity propellant which is generally less prone to leaks, electrostatic discharge, impact, and friction without a solid propellant's propensity to crack [4]. The rocket equation relates the vehicle velocity change ($\Delta v$ in m/s), specific impulse ($I_{sp}$ in s), gravitation acceleration ($g$), initial mass ($m_i$ in kg), and final mass ($m_f$ in kg):

$$\Delta v = I_{sp} g \ln \frac{m_i}{m_f} \tag{3}$$

Vehicle performance is therefore characterized by several metrics including the velocity change, specific impulse, deliverable payload mass, and vehicle size. Considering a mission constraining velocity change and vehicle size, e.g. for an upper stage rocket, specific impulse and payload mass generally characterizes performance. Specific impulse is related to the enthalpy change of the propellant, or the heat release per unit weight. Assuming initial mass is the propellant ($\rho_{\text{prop}} V_{\text{prop}}$), payload ($m_{\text{Payload}}$), and dry vehicle masses ($m_{\text{Dry}}$), payload mass is proportional to propellant density neglecting aerodynamic forces for a volume-constrained mission [6].

$$I_{sp} \propto \sqrt{T_c / MW_p} \tag{4}$$

$$m_{\text{Payload}} = \frac{\rho_{\text{prop}} V_{\text{prop}}}{e^{(\Delta v / I_{sp} g)} - 1} - m_{\text{Dry}} \tag{5}$$

where $T_c$ is chamber temperature and $MW_p$ is the molecular weight of the combustion products. Therefore, elements beneficial for $I_{sp}$ and payload mass with high

combustion energy and low molecular weight, along with high density (evident in Figure 1) include Be and B followed by Al and Si. Be is unsuitable for its high toxicity and B, while a topic of ongoing research, so far exhibits poor combustion performance. Therefore, Al and Si are attractive metallizing agents despite their higher molecular weights owing to their high combustion energy and density.

Precise theoretical analysis of propellant performance is highly mission specific, but noting the importance of $I_{sp}$ and payload mass, Zurawski et al. expands the exponential term in Equation 5 to show that payload mass can serve as a preliminary propellant metric proportional to $\rho_{\text{prop}} {I_{sp}}^{n}$ where $n$ is a mission-specific constant which generally correlates with $\Delta v$ (e.g. n≈2 for an upper stage rocket) [6]. Hence the importance of so-called "density-specific impulse". To evaluate Al and Si, rocket calculations were performed in Cheetah 5.0 for an ideal nozzle expanding from 68 atm chamber pressure to 1 atm ambient with varying metal loadings in the propellant. The O/F ratio of each propellant formulation was optimized to maximize $I_{sp}$ and the resulting density-specific impulse (n=1) is shown in Figure 4. Benefits of metallizing RP-1 and Hydrazine with Al and Si are very similar at less than 50 wt% metal and both would theoretically continue to provide payload mass benefits at higher loadings. Consistent with similar analyses for rocket performance increases from Al addition reviewed in [7], this analysis illustrates the benefit of metallizing liquid propellants with Al or Si for increased payload mass capabilities of low-n missions.

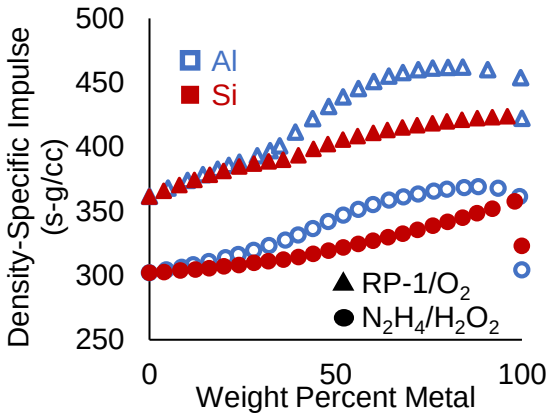


*Figure 4: Theoretical Density-Specific Impulse at optimized O/F ratios calculated with Cheetah 5.0.*

In light of this, increasing the volumetric energy density of liquid fuels/propellants with the addition of solid metal particles received attention since proposed in 1962 [19]. However, subsequent investigations examining "slurry fuels" of micron-sized metal powders in combustible liquids demonstrated deleterious agglomeration effects which caused low burning rates and poor combustion efficiencies [20]. Generally, droplets of slurry fuels were observed to combust in two stages: carrier liquid combustion and burn-off which precedes ignition and combustion of the micron-particle additives [20]. Significant evidence has been collected showing that agglomerates are formed within evaporating and/or combusting droplets from the micron-sized particles and these frequently created shells with hollow centers and created barriers to mass and heat transfer which caused slower and more inefficient combustion performance [21]. Research on slurry fuels also identified disruptive burning characterized by stochastic physical deformation of droplets and flames which resulted in deviations from the classical $D^2$-law linear relationship between the square of droplet diameter the burning time [20]. Any added energy density from micron-sized

metal powders used to formulate these slurry fuels fails to motivate the unacceptably low burning rates and poor combustion efficiencies observed compared to the carrier liquids. Even if the combustion efficiency could be improved, low burning rates would necessitate larger combustion chambers drastically increasing the dry weight of a vehicle and precluding any benefits to propulsion technology via increased propellant density for improved payload mass capabilities. As such, burning rates must be increased to at least that of the carrier liquid for solid metal loadings in liquid propellants to be viable. Recall that when nanoparticle technology reached the combustion research community, smaller particle sizes were quickly seen as a means to increase reaction rates relative to conventional micron-sized metal particles.

## *1.3 Nanofuels Literature Review*

### 1.3.1 Summary of Literature Review

In 1995, Choi and Eastman were the first to demonstrate that smaller particle sizes in the nanoscale range also enables the formulation of "nanofluids" in which repulsive electrostatic forces and Brownian motion counteract gravitational settling to suspend the NPs in the liquid [19]. Research in this area has grown rapidly since with the incorporation of nanoparticles into liquids impacting almost every field from medicine to basic physics. When such a strategy is employed specifically with energetic nanoparticles and carrier liquids, the resultant suspensions can be referred to as a “nanofuel”. According to Web of Science, publications whose stated topic includes “nanofluid” or “nanofuel” have become much more prevalent since the early 2000s

(shown in Figure 5), the same period in which nanoscale materials influenced combustion research with the advent of improved nanoparticle generation, control, and characterization technologies [4].

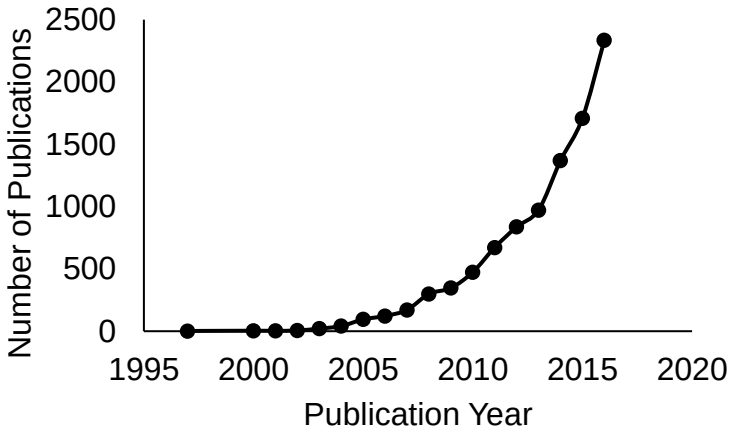


*Figure 5: Number of publications with topics including at least one of: "nanofuel", "nanofuels", "nanofluid", or "nanofluids" between 1997 and 2016 according to Clarivate Web of Science.*

The last decade of emerging research in nanofuel evaporation and combustion heavily supports the early promise of metal and metal oxide additives in liquid fuels for increased energy densities, shortened ignition delay times, higher heats of combustion, and promotion of evaporation and combustion rates. A variety of interacting processes and mechanisms have been proposed and supported by empirical observation including most notably temperature increase by radiative absorption of the additives, physical mixing and eruption of material by microexplosions, and the relatively rare instance of simultaneous particle/solvent burning. However, particle aggregation within the droplet has also been shown to occur at a similar timescale of

droplet evaporation and combustion, thereby limiting most of the additive's participation in combustion to the final stages of the droplet lifetime.

### 1.3.2 Early studies on nanoparticles in diesel, jet fuels, and monopropellants

Much of the early nanofuel research examined direct use of nanoparticles as diesel fuel additives for compression ignition engines. Various nanoparticle additives were shown to decrease NOx, hydrocarbon, and/or CO emissions including those of Al [22], $CeO_2$ [23], $Fe_3O_4$ [24], and Carbon Nanotubes (CNT) [25]. Mehta et al. showed that addition of nAl and nano-iron increased exhaust temperature, a negative result in their case since this increased NOx emissions [26]. However, this result reinforces that nanometal addition can affect the energetics realized from liquid fuels. Ignition is commonly promoted with the addition of nanoparticle metals or metal oxides to diesel exemplified by nAl or nanoscale $Al_2O_3$ increasing droplet ignition probability on a constant temperature hotplate [27], and nAl, nFe, nB decreasing ignition delay in a single cylinder diesel engine [26]. Brake thermal efficiencies and cylinder combustion heat have also been seen to increase in engine tests due to the presence of nAl [22] and CNTs [25] in water-diesel emulsions. While similar additives in diesel (nAl, nFe, nB) have shown potential to decrease fuel consumption with a lower ignition delay and higher calorific value, they do so only marginally at high engine loads. No effect and even a marginal decrease of thermal efficiency was observed with $CeO_2$ [23] and $Fe_3O_2$ [24] nanoparticle additives in diesel. A range of potential mechanisms have been set forth to account for these effects including catalytic activity of metal oxides [22] and enhanced radiative heat transfer of absorbing additives [27]. A recent comprehensive

review of research concerning nanoscale additives in diesel fuels for compression ignition engines was published by Shaafi et al. [28].

Jet fuels and monopropellants as the base liquid fuel also received early research attention concurrently with diesel. Metal oxide particles have been shown to participate directly or catalytically in the oxidation of JP-10 in an atomized flow reactor [29] and nAl reduced the apparent ignition delay of JP-8 in a rapid compression machine [30]. Efforts with nitromethane in pressure vessels have shown increased burning rates with the addition of functionalized graphene sheets [31], silica [32, 33], AlOOH [31], $Al_2O_3$ [33], or nAl [32, 34]. More recently as the research effort devoted to nanoscale additives for combusting liquids has accelerated, several sub-topics have garnered specific attention including: nanoscale carbon-based additives including carbon nanotubes, nanoparticles, graphene, and nanoplatelets in jet fuel or kerosene increasing burning rates and causing droplet disruptions [35, 36]; effects of different chemical dispersants and stabilizing methods including sorbitan oleate, oleic acid Tween 85, and surface modification by silane capping on the stability of boron and aluminum nanofuels [37-39]; and effects of nanoscale additives (usually $Al_2O_3$) on the spray characteristics of base fuels [40-42].

### 1.3.3 Nanometals in hydrocarbon droplet experiments

A relevant series of droplet evaporation and autoignition studies has been published by coworkers in the research group of Professor Seung Wook Baek at the Korea Advanced Institute of Science and Technology. In their earlier studies on this topic, an isothermal furnace is lowered over droplets suspended on a SiC filament to

observe evaporation and combustion upon autoignition [43-48]. Results of kerosene and heptane-based nanofuels with surfactant-coated nAl suggest a relationship between physical droplet disruption from gas formations/microexplosions and the degree of evaporation or burning rate increase [43-46]. In kerosene, no change in evaporation rate was observed at 400-600ºC while disruptive burning emerged at 700-800ºC with overall evaporation rate increases up to 57% for 0.5 wt% Al at 800ºC [44]. The degree of disruption (frequency and intensity of microexplosions) increased with temperature and nAl concentration [45]. A similar study with heptane droplet evaporation showed little to no droplet disruption with a marginal evaporation rate decrease at $T < 300$ºC and increase at $T > 400$ºC [43]. When heptane/nAl droplets were autoignited, microexplosions were observed whose intensity increased with temperature causing shorter burning times than pure droplets at $T > 700$ºC [46]. The authors attributed decreases in the evaporation rate of heptane droplets at low temperatures to compact agglomerate/surfactant shells forming in the droplets which were much more porous at high temperatures where the surfactant decomposes [43]. More recent work by the group demonstrated increased radiative heat flux to a droplet of LPG when nanoparticles of $Al_2O_3$ are incorporated [49].

The research group of Professor Li Qiao at Purdue University has also published several relevant studies of nanofuels in droplet combustion experiments. Nanoaluminum in ethanol and n-decane has been most extensively studied by the group who began by investigating the evaporation of surfactant-treated micron- and nano-aluminum in ethanol and n-decane in different convective environments [50]. This

work showed that nAl can increase the evaporation rate of both solvents but that this was likely qualified by the evaporation taking place with a shorter timescale than that of large particle aggregate formation [50]. In cases with higher convective environments, a lower boiling point solvent, and/or lower particle concentration, (cases in which the baseline evaporation takes place at shorter timescales and aggregation at longer timescales), the droplet diameter evolutions depart from the $D^2$-law predictions and evaporation times decrease compared to the pure solvent [50]. Contrary conditions with nAl in ethanol or n-decane showed either no change in the $D^2$-law evolution and evaporation rate of the solvent, or even a decrease in evaporation rate with decane-based nanofuels [50]. Particle aggregation modeling suggested that longer droplet lifetimes allows formation of a greater number of larger agglomerates that inhibit liquid transport and diffusion and can slow overall droplet evaporation [50]. In a subsequent study, the authors ignited the same formulations to observe the combustion characteristics which supported the presence of particle aggregation during droplet evaporation/combustion [51]. Most notably, nAl formulations formed a large agglomerate as the droplets burned and once the liquid droplet had been consumed this large agglomerate ignited in most cases [51]. Such as observation proves that significant particle aggregation occurs on the same timescale as the droplet evaporation and combustion. Both micron and nanoscale aluminum additives induced disruptive droplet combustion by causing local “microexplosions”, flares from presumed energy or material release under or within the flame; however, microexplosions observed in the micron-Al formulations occurred later and with greater intensity than those of nAl

formulations [51]. By drying unignited droplets and performing microscopy on the products, the authors propose that the nature of the aggregates formed, based on particle size, accounted for the difference in microexplosion observations [51]. A similar study of boron and iron nanoparticle additives supported this proposed role of particle aggregation: dense suspensions showed particles predominantly burning as large aggregates in the late stages of droplet combustion and most ethanol-based boron nanofuels failed to ignite late-stage boron aggregates [52]. Green color emission characteristic of $BO_2$ provided evidence of some simultaneous burning of the carrier liquid and particles while dilute suspensions without surfactant displayed ejection of particles by physical droplet disruptions which also facilitated simultaneous burning [52]. The authors propose that the source of microexplosions could be a combination of particle aggregation (iron caused earlier microexplosions from suspected faster aggregation) and water absorption by the solvent [52]. Radiative absorption by particle additives was also shown to be a significant mechanism of droplet heating with nAl, $nAl_2O_3$, CNTs, and carbon particles [53, 54]. In the wavelength range of 350-900 nm, the addition of nAl to ethanol decreases the transmission of the formulation from approximated 90% to 2%. To further investigate the notion that longer droplet lifetimes facilitate more formation of particle aggregates, inhibiting evaporation rate promotion, a subsequent study reduced the droplet lifetimes by generating a stream of smaller, 150-400 micron microdroplets and observing their combustion [55]. Similar to prior studies, microexplosions disrupted the burning behavior mostly in late stages of droplet burning but overall the ethanol-based nanofuels showed the greatest increase in burning rate

with the addition of nAl among the studies discussed with a 140% increase with 5 wt% of 80-nm nAl particles. The authors theoretically considered the role of radiative heat absorption by the particles to show that resulting temperature increases are a likely significant mechanism, it cannot account for the entirety of the burn rate increases observed. The Qiao group has also published work using molecular dynamics simulations to suggest that latent heat of vaporization of water and ethanol nanofluids is decreased by Ag or Fe nanoparticle addition while nAl inclusion slightly increases the heat of vaporization [56]. Recent publications from the group have focused on graphite nanoparticle additives to ethanol droplets, specifically to better understand the role of radiation effects. Results indicate that enhanced radiative absorption likely plays a role in increasing burning rates of the droplets and the radiative increase is experienced most near the surface of the droplets [57] and that radiative absorption and particle agglomeration compete to affect evaporation rates in droplets of graphite/ethanol nanofuels [58].

### 1.3.4 Mechanisms of nanoparticles in hydrocarbon droplets

Droplet evaporation and combustion studies have identified important interacting processes and mechanisms active upon NP addition [43-46, 50-55]. Radiative absorption of the additive from the flame, increased heat of combustion upon additive ignition, and droplet disruptions causing physical mixing and secondary atomization all promote evaporation and burning rates of nanofuel droplets [44-46, 53-55]. Combusting slurries composed of micron-sized particles studied prior to 1990 suffered problematic effects due to particle agglomeration including low burning rates

and combustion efficiencies [20]. While transitioning from micron- to nano-particles significantly decreases the burning time and ignition delay of the solids, NPs are still particularly prone to agglomeration that frequently necessitates chemical stabilization which can inhibit particle combustion [4]. Even when a stable nanofuel is attained, the NP mass fraction increases near the surface of the droplet as liquid gasifies during combustion, thereby forming agglomerated shells and inhibiting transport [59]. NP agglomeration has been shown to occur at a timescale similar to that of droplet evaporation and burning, in many cases delaying the additive's participation in combustion (by induced gas generation or agglomerate ignition) to the late stages of the droplet lifetime and mitigating evaporation or burning rate increases [45, 52, 54] or even decreasing droplet evaporation rates [43, 50].

Of these mechanisms, droplet disruption seems particularly capable of affecting burning rates by counteracting the formation of particle agglomerates, increasing physical mixing within the droplet (promoting species and thermal transport), deforming the droplet thereby changing the gas-liquid interfacial area, and causing secondary atomization of smaller droplets [59]. Disruptions are caused when the rate at which liquid is gasified within the droplet is higher than the rate at which the gas produced can escape, i.e. when internal gasification increases or multiphase transport decreases appreciably. Gasification rates can increase by several mechanisms including heterogeneous nucleation or localized heating around absorbing or reacting particles. When a droplet includes multiple liquid components with differing boiling points, one component can become superheated by the other and gasifies rapidly causing

disruptions [60-63]. Particle agglomeration, especially when a shell is formed, will also induce disruptions by inhibiting transport of gasified products through the agglomerates until the gas pressure exceeds the inter-particle forces and the gas is rapidly released from the droplet [59]. Work of Miglani and Basu has highlighted the apparent feedback loop between agglomerate shell formations and disruptions dismantling agglomerates or inhibiting shell growth [59]. The study found that dense particle loadings caused strong shell formation dominating over gas ejections which were largely suppressed, while dilute loadings showed high ejection frequencies that inhibited shell formation [59]. Since dominant agglomeration depresses the burning rate while disruptions enhance it, this interplay of mechanisms is a possible reason for the variety of burning rate effects observed in literature with NP addition.

### *1.5 Molecular Aluminum Additives*

Molecular cluster materials consisting of low valency metals soluble in hydrocarbons and other potential fuels provide an opportunity to further improve upon nanoscale metal additives. Such cluster materials used within their solubility limit would be significantly less prone to forming solid phase agglomerates, which can cause system clogs, extend particle burning times, and delay particle ignition to late stages of droplet combustion. Metal cluster additives would maintain a highly tunable nature with properties controllable by composition and size [7]. Even in compounds with higher Al oxidation states, organoaluminum molecules miscible in hydrocarbons are promising for propulsion and energetics applications. Alkylaluminums for example have been identified for use as hypergols since they react readily with air [64-66].

Utilization of materials with lower oxidation states of the aluminum however are more attractive for increasing energy density of carrier liquids with more chemical potential energy available from the lower oxidation aluminum atoms. Metal clusters of aluminum atoms in a low valency state can be synthesized from aluminum halides, but are highly reactive with water and air and can be thermally unstable and therefore are usually stabilized by organic ligands, e.g. Al(I) tetrameric cluster $[AlBrNEt_3]_4$ (Et = $C_2H_5$) stabilized by triethylamine which is soluble in a hydrocarbon co-solvent of toluene and ether [67-69]. The instability of such materials adds a significant practical complication to their investigation and use as agents to metallize hydrocarbons, necessitating novel experimental methods; however, their promise of high reactivity in a combustion system is attractive for increased energy densities along with high reaction rates and therefore motivates their consideration.

### *1.6 Droplet Combustion Theory*

An analytical framework is required to provide a basis of analysis for the combustion of liquid fuels with metallizing additives. Reducing complicated liquid propellant propulsion systems down to their basic combustion process reveals spray combustion in a chamber predicated upon the burning of numerous atomized droplets. Consideration of a single combusting droplet to improve understanding of a spray combustion system is a classical simplification step first considered in scientific research in the 1950s and provides a manageable scope to begin investigating effects of nanoscale or soluble metallizing agents on liquid hydrocarbon combustion.

Consideration of a phenomenological description of single droplet combustion theory dates back to the earliest descriptions of a quasi-steady state symmetrical case for a combusting droplet which, using numerous simplifying assumptions for idealized physical and thermal characteristics, suggested that a single-component isolated droplet would burn with a constant flame stand-off ratio, flame temperature, and burning rate (represented by the square of the droplet diameter versus time) [70-72]. Other early studies expanded the problem constraints considered to cover multicomponent droplets and combustion in a flowing gas [73-75] and much of this pioneering work was summarized in several reviews published since [61, 76-79]. Precise experimental validation of the early idealized theory of [70, 71], in which the droplet is isolated and motionless with a concentric flame has not been perfectly attained but microgravity experimentation in drop-towers beginning with Kumagai et al. [80, 81] have demonstrated general validity of the $D^2$-law with some quantitative and few qualitative variances which were described more accurately in later analytical studies including consideration of time-dependent droplet heat-up [82], finite-rate chemical kinetics effects [83-85], transport variations based on non-unity Lewis numbers [86], and fuel vapor accumulation [87]. Overall, the $D^2$-law, which results from the idealized analysis linearly relating the square of the droplet diameter and time, provides a quality approximation of single component droplet burning under both normal and microgravity conditions wherein experimental observations readily show the predicted linear regression of the square of the droplet diameter versus time for free-falling and suspended droplets after an initial heat-up period not exceeding 15-20% of the total

burning time [75]. An interested reader is directed to numerous available reviews and book chapters on the subject for a detailed description of the $D^2$-law and its more accurate analytical extensions including [72, 75, 88], but a brief description of the assumptions, physiochemical processes, and important results of an analytical representation of idealized droplet combustion leading to the $D^2$-law is covered here based on summaries in [75, 88].

### 1.6.1 Classical $D^2$-law for droplet combustion

Spherical idealized droplet combustion, as illustrated in Figure 6, is the situation which arises as fuel evaporates and its vapor is transported away from the droplet by Fickian diffusion and Stefan flow resulting from expansion upon its gasification, while oxidizer from the atmosphere diffuses towards the droplet where the two components mix to form a reactive layer in the flame zone. This reaction zone is assumed to be a thin sheet wherein chemical kinetics occur infinitely fast and the process is diffusion-controlled. Temperature increases radially from the boiling point of the liquid at the droplet surface, to the flame temperature at the reaction sheet and down to the ambient temperature beyond. Heat energy is transferred from the flame zone to the droplet primarily by conduction and leads to gasification of fuel at the droplet surface. Products of combustion diffuse in both directions away from the flame zone. The three most important physical processes governing this problem are gas-phase mass transport, gas-phase heat conduction, and phase change at the liquid-gas interface.

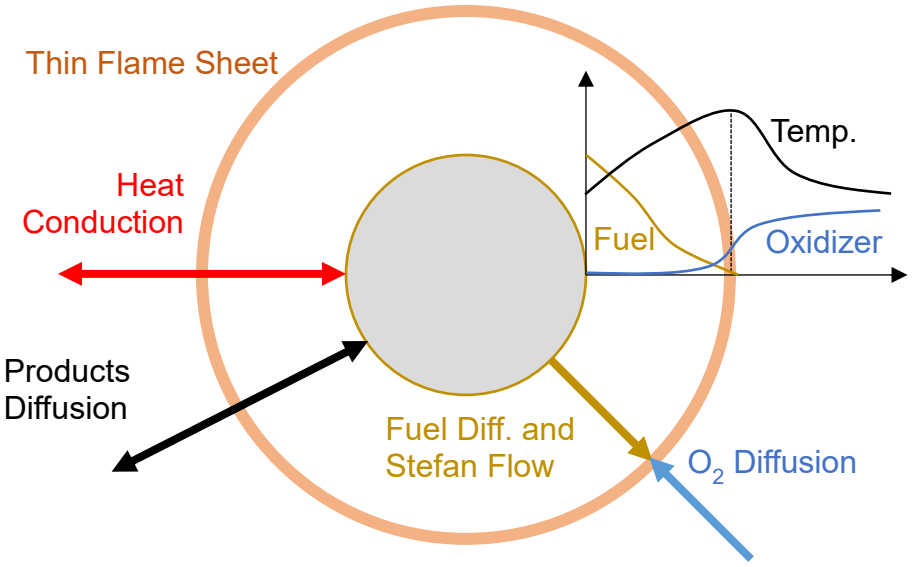


*Figure 6: Cartoon depiction of idealized symmetrical droplet combustion identifying important physiochemical processes.*

To describe the coupled physical processes analytically, several assumptions are made including: steady-state combustion, spherical symmetry, single-component stationary liquid fuel, constant temperature of the droplet equal to the liquid boiling point, infinite chemical reaction rates, negligible buoyancy effects, no radiative heat transfer, constant physical properties of the liquid and gases with unity Lewis numbers, stoichiometric fuel/oxidizer concentrations at the flame, and negligible Soret and Dufour effects. Governing equations for mass and energy conservation and appropriate boundary conditions are therefore:

$$\nabla \cdot (\rho \vec{v}) = 0 \tag{6}$$

$$\nabla \cdot (\rho \vec{v} \beta_i - \rho D \nabla \beta_i) = 0 \tag{7}$$

$$r \to \infty: C_O \to C_{O,\infty}, C_f \to 0, T \to T_\infty \tag{8}$$

$$r = r_s: \rho v_s C_O - \rho D \frac{dC_O}{dr} = 0, \rho v_s C_F - \rho D \frac{dC_F}{dr} = \rho v_s, T = T_s, \lambda \frac{dT}{dr} = \rho v_s q_e \tag{9}$$

where $\rho$ is the gas density, $\vec{v}$ is velocity, the coupling function $\beta_i = \frac{C_i}{\varphi_i} + \frac{c_p T}{q}$ ($\varphi_i$ is the stoichiometric O/F ratio equal to 1 for the fuel and $q$ is the heat of combustion), $C_O$ and $C_F$ are oxidizer and fuel concentrations, T is temperature, $v_s$ is the gas velocity at the droplet surface, $\lambda$ is thermal conductivity, $q_e$ is latent heat of vaporization, and the $s$ and $\infty$ subscripts refer to the droplet surface and ambient environment respectively. Integrating Equation 6 yields:

$$\rho v r^2 = \rho v_s r_s^{\,2} = \text{Constant} \equiv M \tag{10}$$

showing that the radial mass flux in the system outside the droplet is a constant, $m = 4\pi\rho v r^2$. Integrating Equation 7, substituting with Equation 10, and applying boundary conditions leads to expressions for the temperature distributions on either side of the flame which can be used to find the flame front position, $r_f$, by defining the temperature at the flame $T = T_f$ at $r = r_f$ and to derive the burning rate, $m_s$, by defining the surface temperature (equal to the liquid boiling point) $T = T_s$ at $r = r_s$:

$$r_F = \frac{M}{\rho D \ln\left(1 + {}^{C_{O,\infty}}/_{\varphi_O}\right)} \tag{11}$$

$$m_s = 4\pi\rho D r_s \ln(1 + B) \tag{12}$$

$$B = \frac{1}{q_e}\left[C_p(T_\infty - T_s) + {}^{C_{O,\infty} q}/_{\varphi_O}\right] \tag{13}$$

where B is the Spalding transfer number. Flame temperature and standoff ratio are also readily derived given by:

$$T_f = \frac{(q - q_e) + c_p T_\infty\left({}^{C_{O,\infty}}/_{\varphi_O} + {}^{T_s}/_{T_\infty}\right)}{c_p\left(1 + {}^{C_{O,\infty}}/_{\varphi_O}\right)} \tag{14}$$

$$\frac{r_f}{r_s} = \frac{\ln(1+B)}{\ln\left(1+{}^{C_{O,\infty}}/_{\varphi_O}\right)} \tag{15}$$

Since the droplet loses mass by vaporization only, conservation of mass for the liquid phase droplet dictates:

$$-\frac{d}{dt}\left(\frac{4}{3}\pi {r_s}^3 \rho_l\right) = m_s = 4\pi\rho D r_s \ln(1+B) \tag{16}$$

where $\rho_l$ is the liquid density and the integral of this equation now leads to the $D^2$-law in which $d_{s,0}$ is the initial droplet diameter and K is the burning rate constant:

$${d_s}^2 = {d_{s,0}}^2 - Kt \tag{17}$$

$$K = -\frac{d({d_s}^2)}{dt} = 8\frac{\rho D}{\rho_l}\ln(1+B) \tag{18}$$

If a droplet is assumed to burn completely, this burning rate constant can also be approximated using the initial droplet diameter and total burning time, $t_B$:

$$K = \frac{1-{}^{{d_s}^2}/_{{d_{s,0}}^2}}{{}^{t}/_{{d_{s,0}}^2}} \cong \overline{K} = \frac{{d_{s,0}}^2}{t_B} \tag{19}$$

### 1.6.2 Important practical deviations from the $D^2$-law

Generally, the $D^2$-law is a good approximation for droplet combustion even under normal gravity conditions. A few specific invalidities of this analytical prediction are particularly relevant to experimentation for propellant additive investigations. The idealized analytical model above assumes uniform, time invariant droplet temperature equal to the liquid boiling point. While this assumption is reasonable once the droplet has reached its boiling point, it is invalid during the earliest stage of droplet combustion during which it ignites at room temperature and a finite amount of energy is required

to heat the droplet, namely $\rho_l C_p(T_b - T_0)$ where $T_b$ is the boiling point and $T_0$ is the initial droplet temperature. In practical experiments, this heat-up time is evident as an initial deviation from linearity of droplet diameter squared versus time, an example of which is depicted in Figure 7. This shows data discussed in Chapter 4: the droplet diameter versus time, both normalized by initial droplet diameter, measured as a droplet of kerosene with surfactant burns on a horizontal SiC filament in air ignited as a pilot methane diffusion flame momentarily passes underneath (which deflects the droplet and filament slightly causing the underlying oscillation visible in the diameter signal). The first stage annotated "Heat-Up" shows the non-linearity as the droplet expands slightly as it heats from room temperature before settling into a linear regression consistent with the $D^2$-law.

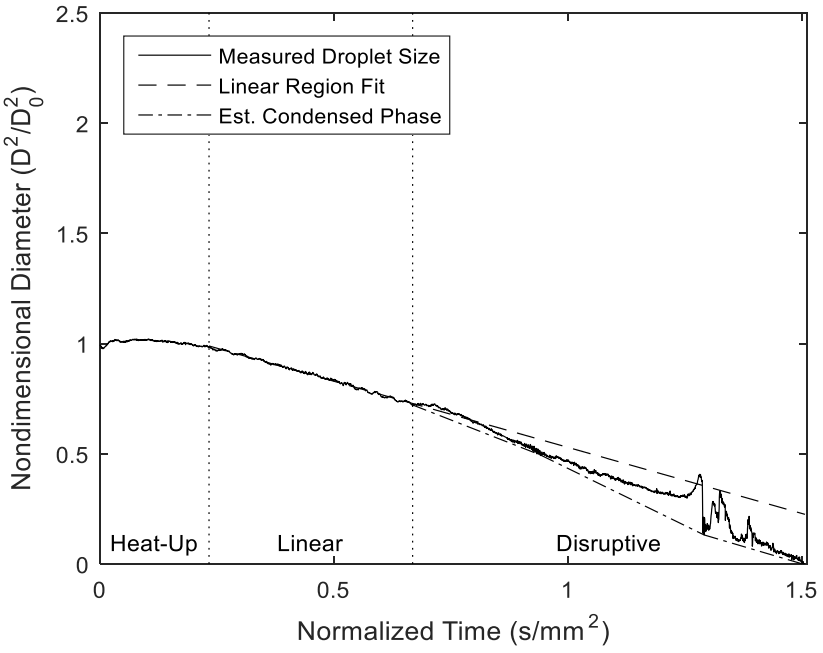


*Figure 7: Measured diameter evolution in time of a droplet of kerosene with 40 mg/mL of TOPO surfactant suspended on a horizontal SiC filament combusting in air when ignited by a passing methane pilot (as part of experimentation described in Chapter 4).*

Figure 7 also illustrates another important practical deviation from the idealized model: effects of multicomponent fuels as studied primarily by Law and coworkers [60-63]. Even though the surfactant in this kerosene droplet is also in the liquid phase, it has different physical properties than the primary kerosene component including boiling point. Qualitatively, when a combusting droplet is composed of multiple components of differing enough volatilities, burning begins consistent with the $D^2$-law for the more volatile component such that the concentration of the component of lower volatility increases near the droplet surface. As the mixture of less volatile component at the droplet surface increases, the droplet heats up closer to the boiling point of that component which will superheat the higher volatility component remaining within the mixture at the droplet core held by diffusion resistance. In the event this superheat reaches a high enough level, homogenous nucleation of the high volatility component in the core generates a gas disruption sometimes referred to as a "microexplosion". An example of such disruptive droplet burning is shown in the "Disruptive" region of Figure 7 since the boiling point of the surfactant is higher than that of the kerosene carrier fuel.

Spherical symmetry assumed in the idealized model is seldom replicated experimentally except loosely in microgravity experiments. More commonly, natural and/or forced convection in and around the droplet deforms the system geometry to more closely resemble the illustration in Figure 8 wherein forced convection is considered for a droplet hypothetically in free fall through a quiescent or vertically flowing gas. Analytical considerations have been updated for low relative velocities of

a droplet and surrounding gas [89], however flow characteristics at high Reynolds numbers are complicated enough to motivate the use of empirical relations for deviations from the classical idealized burning rate constant instead of using highly specific and computationally expensive analytical models [90]. Correction factors determined experimentally are of the following form [75].

$$K = K_0(1 + f_n)(1 + f_f) \tag{20}$$

$$f_n = 0.533Gr^{0.52} \tag{21}$$

$$f_n = 0.276Re_\infty^{\frac{1}{2}}Sc_\infty^{\frac{1}{3}} \tag{22}$$

$K_0$ is the burning rate constant in a quiescent environment, $Re_\infty$ and $Sc_\infty$ are the ambient conditions Reynolds and Schmidt numbers, and $Gr$ is the Grashof number at the mean temperature of the flame and ambient.

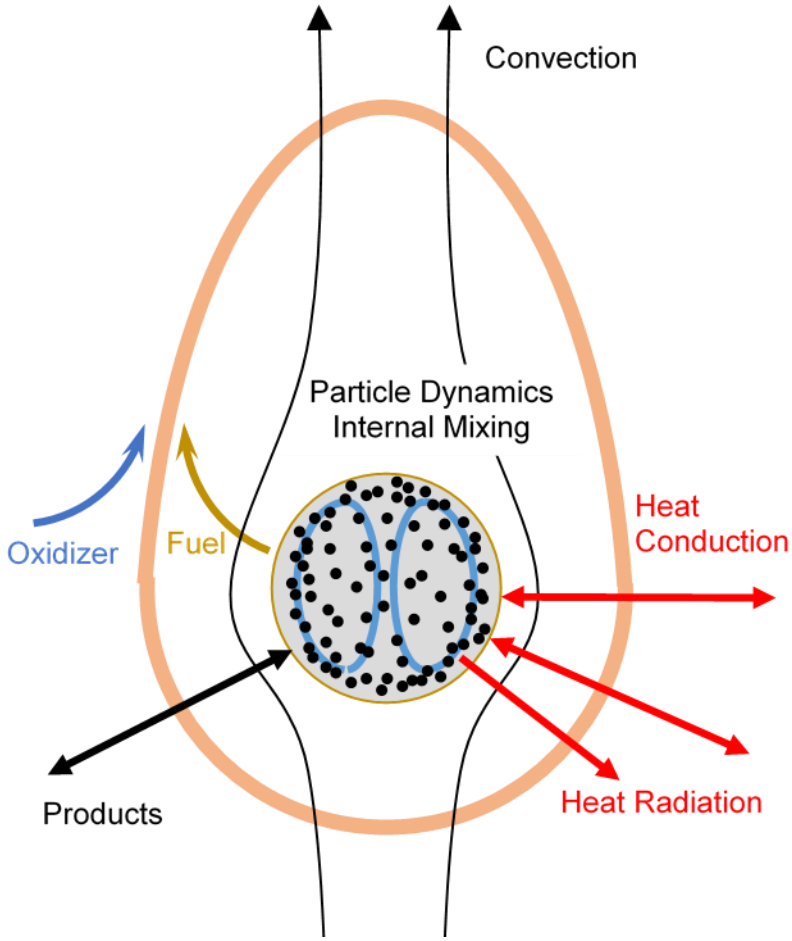


*Figure 8: Cartoon depiction of free-falling droplet combustion under normal gravity with particle additives.*

Despite the practical deviations from the idealized model for classical droplet combustion which leads to the $D^2$-law discussed up to this point, experimental droplet combustion observations subject to these practicalities are still approximated well by this classical model. Such experiments observe the droplet diameter evolving in time which represents the volume of unreacted fuel remaining at any moment, which can be fit to Equation 19 to measure a burning rate constant, K. However, upon incorporation of additives for metallizing propellants, particularly solid particles, this basis of analysis severely breaks down. The number of important physical processes expands

to include particle dynamics in the liquid and gas mediums, particle reaction, solid-liquid interface phases changes, and radiative absorption and emission of the particles. Possible complicating effects of energetic particle additives include changes in the fuel mean and localized heats of combustion, gas generation by particle decomposition or gasification at solid-liquid interfaces causing physical disruption, increased local heating around particles with high radiative absorption efficiency, or chemical reaction or catalytic effects of the particles with liquid or gaseous species or other particle constituents. When some particle additives such as aluminum oxidize, they can form solid products and if this occurs without such products leaving the droplet system (e.g. reaction of particle agglomerates near or after liquid burn-off), then the droplet diameter is no longer a direct measure of the remaining unburnt fuel. If gas is generated within the droplet, this will also decouple droplet diameter from unreacted fuel mass, especially when deformation of the droplet results. Therefore, diameter evolution in time becomes a poor measure of burning rate when solid particle additives are included in the reactive liquid. This is demonstrated in Figure 9 which shows diameter evolution of a kerosene/surfactant droplet on a horizontal filament with 2.5 wt% nAl/(10%)NC MPs added. During the disruptive stage the droplet swells and erupts as gas is generated within the droplet and any resemblance of the $D^2$-law that remained in Figure 7 before the particles were added is obscured. The question of how to analyze the burning rate of liquid fuels or propellant impregnated with energetic solid particles is vital to consider if effects of such additives are to be evaluated.

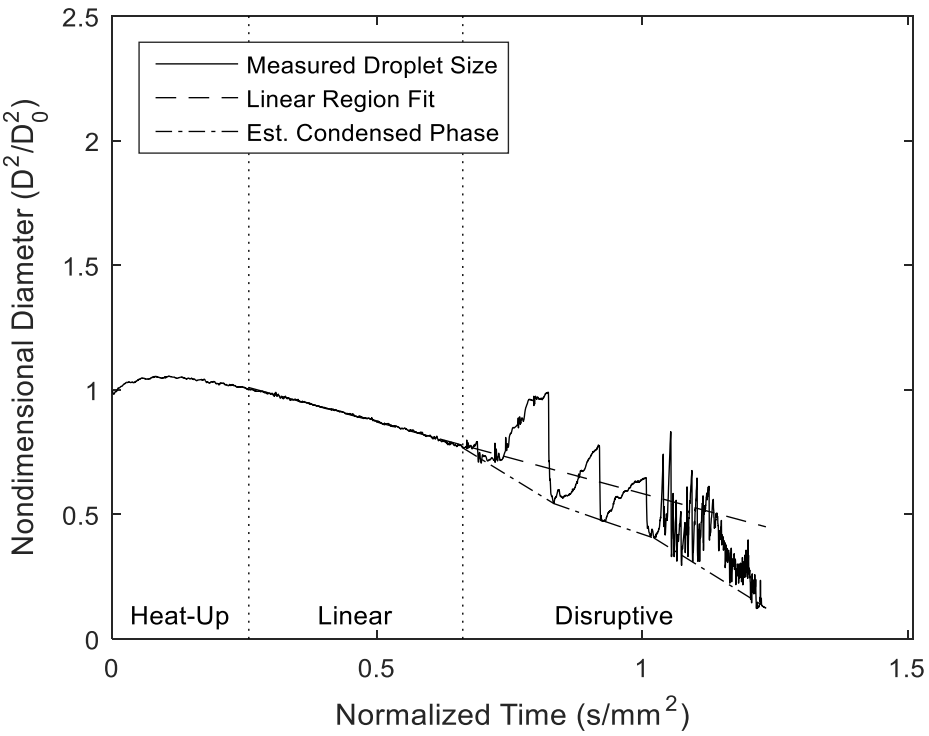


*Figure 9: Measured diameter evolution in time of a droplet of kerosene with 40 mg/mL of TOPO surfactant and 2.5 wt% nAl/NC MPs suspended on a horizontal SiC filament combusting in air when ignited by a passing methane pilot (as part of experimentation described in Chapter 4).*

## *1.7 Research Objectives, Scope, and Approach*

Considering the promise recent nanoenergetic materials have shown in dry combustion experiments, their documented ability to improve combustion performance relative to micron-sized energetic particles, and renewed interest by the scientific community in overcoming the problems which halted development of micron-sized particle additives for liquid propellants, the research presented in this dissertation has focused on the augmentation of liquid hydrocarbon droplet combustion using novel energetic additives composed of soluble aluminum containing compounds or

nanoaluminum and/or nanoscale oxides incorporated as nitrocellulose-bound mesoparticle composites. The objectives of this research are four-fold:

- Identify promising additive candidate materials or methods of inclusion which promote burning rates of the carrier hydrocarbon as a prerequisite for their application to increase propellant volumetric energy densities.
- Develop an experimental apparatus and methodology suitable for characterization of liquid droplet combustion performance in the presence of highly air, moisture, and temperature sensitive metal cluster additives or energetic nanoparticulate additives which induce disruptive droplet combustion obscuring classical burning rate measurement.
- Demonstrate the use of various peripheral diagnostics available with the potential to elucidate important active mechanisms by which promising additives improve liquid droplet combustion performance.
- Generate an initial basis of experience and apparatus for the research group to continue investigating combustion of liquid-based energetic materials in the future.

Chapter 2 presents development of the experimental apparatus, its operation principles, and analysis methodologies through multiple design iterations executed to meet the unique constraints of this mission, along with an overview of other experimental methods used. In Chapters 3-8, six related research projects are detailed which were undertaken to achieve the objectives of this dissertation. A soluble aluminum cluster additive is demonstrated as a proof of concept in Chapter 3 along

with the initial testing and validation of the developed droplet combustion apparatus. In Chapter 4, effects of nAl addition to kerosene with a surfactant are characterized with and without nitrocellulose, a gas generating co-additive. Electrospray of nAl and NC together is shown to provide significant benefits for combustion performance and suspension stability. Chapter 5 details work studying the same idea employed for oxygen-containing particles and the effect of their addition on kerosene when assembled in electrosprayed NC-bound mesoparticles. In Chapter 6, the emerging promise of the MP architecture for improving particle additive performance motivates study of the tunability afforded by this preassembly step. Effects of electrospray precursor loading on MP morphology, settling, and combustion performance are considered and improved colloidal stability of MPs compared to nanoparticles is quantitatively proven. In Chapter 7, the MP strategy is used to formulate composite thermite additives for kerosene inclusion and their mechanisms of activity are probed relative to different oxidizers employed with nAl in the MPs. In Chapter 8, another aluminum compound soluble in a carrier hydrocarbon is tested to provide more detail on modes by which soluble aluminum additives affect droplet disruptions and burning rates.

In addition to more detailed summaries preceding each chapter, the primary findings presented in this dissertation are summarized in Chapter 9 along with recommendations for future work regarding possible improvements to the experimental apparatus and methodology, further candidate materials and additive incorporation strategies worth investigating, and alternative combustion assessment techniques worth

considering to improve understanding of promising additive materials and assess their application challenges in propulsion systems. Appendices A-C provide supplemental information for Chapters 4, 5 and 7 and Appendix D presents detailed instructions for maintenance, operation, and data analysis of the free droplet combustion experiment.

# Chapter 2: Experimental Methods

## *2.1 Free Droplet Combustion Apparatus and Experimentation*

Classical droplet experiments are most often undertaken using one of three general configurations: a tube pumps liquid fuel to a porous sphere from which the liquid is fed and burned and the pumping rate is controlled to maintain the droplet size; a solid filament of quartz or SiC is used to tether a droplet which burns consuming the liquid; a "free" droplet is released into normal or microgravity to burn untethered, either as it falls, the experiment falls in a drop tower, or microgravity keeps the droplet relatively stationary [91]. Interferences of suspension filaments/tubes versus the magnitude of forced convection primarily drive a choice to employ one of these methods over the others. The idealized droplet model assumes that heat is only transferred by gas-phase conduction. Even in more sophisticated models, convection and radiation are considered but the droplet remains isolated by gas. Introducing a tube or filament which extends through the flame and into the droplet adds an avenue for heat conduction, heterogeneous nucleation on the solid surface, and in cases with suspended particles a surface with which particles can interact and deposit. Forced (and natural) convection on the other hand is known to affect the geometry and flow profile of the system thereby affecting burning rate. Ultimately, the reasoning leading to the development of a free droplet experiment for this work was based on: (1) influences of forced convection are more realistic and present in spray combustion than the existence of an interfering filament, and (2) a filament or tube would (and is shown to in Chapter

4) unacceptably interfere with particle dynamics and deposition inside the droplet which is of fundamental importance in studying particle additives in this work.

In designing a free-droplet experiment with possibly non-trivial natural and forced convection effects on the droplet combustion, it is vital to assess these contributions to ensure they remain acceptably consistent during operation of the experiment over many trials, or that the methodology is tailored in a way to account for existing variations. Effects of natural and forced convection on the droplet burning rate constant are described in Equations 20-22 and depend on non-dimensional numbers Re, Sc, and Gr which are described in Table 1.

*Table 1: Relevant non-dimensional numbers in droplet combustion experiment design*

| | | | |
|---|---|---|---|
| Reynolds Number | $Re_\infty = \frac{\rho U d}{\mu}$ | Ratio of inertial to viscous forces in a flow. | Forced Convection |
| Schmidt Number | $Sc_\infty = \frac{\mu}{D}$ | Ratio of momentum to mass diffusivity in a flow. | |
| Grashof Number | $Gr = \frac{g\beta\rho^2(T_f - T_\infty)d^3}{\mu^2}$ | Ratio of buoyancy to viscous forces | Natural Convection |

($U$ is the relative flow velocity, $d$ is characteristic droplet diameter, $\mu$ is the gas viscosity, $D$ is mass diffusivity, and $\beta$ is the thermal expansion coefficient.)

### 2.1.1 Apparatus Design Iteration One and Operating Principle

The droplet combustion experiment apparatus initially adapted from equipment made available by Dr. Richard Yetter of Penn State University is depicted in Figure 10 and was used to carry out work presented in Chapter 3 and initially prove the operating principle and burning rate approximation method before improving the apparatus design. A fuel droplet is generated at the top of a 0.5 m tall tower and released to free-fall into an oxygen-rich environment and ignition is initiated as the droplet passes two

small methane pilots. High speed videography is used to measure the initial droplet diameter generated. A second camera can be situated to either measure droplet diameters at multiple discrete heights in the tower (to fit the diameter evolution in time to a classical $D^2$-law curve), or to record the full trajectory of the droplet flame over time from a far-field perspective to assess a mean effective burning rate constant.

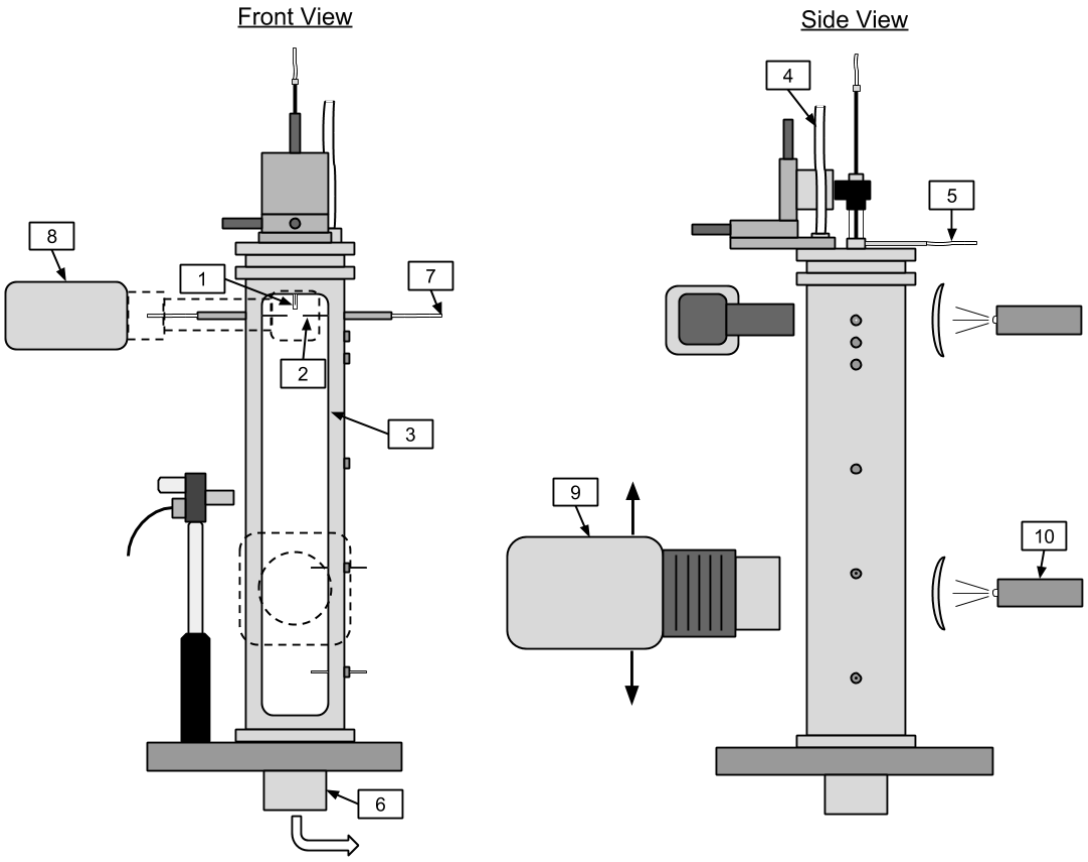


*Figure 10: Droplet combustion tower apparatus in design iteration 1. Point descriptions are listed in Table 2.*

*Table 2: Droplet combustion apparatus iteration 1 components descriptions for Figure 10.*

| Point | Description |
|---|---|
| 1 | Droplet generation source (capillary needle within a nozzle) |
| 2 | Methane delivery tubes for pilot flames |
| 3 | Glass viewing windows |
| 4 | Tower gas fed to a layer of expanded metal (Oxygen at 15 LPM) |
| 5 | Nozzle flow for droplet generation (Nitrogen at 0.25 LPM) |
| 6 | Exhaust Duct Outlet (active exhaust in Iteration 1, passive in 2) |
| 7 | Pilot gas delivery (methane at nominally 50 mL/min) |
| 8 | High-speed camera with magnifying periscope for initial droplet sizing |
| 9 | High-speed camera with discrete height settings for droplet sizing |
| 10 | Expanded LED backlighting |

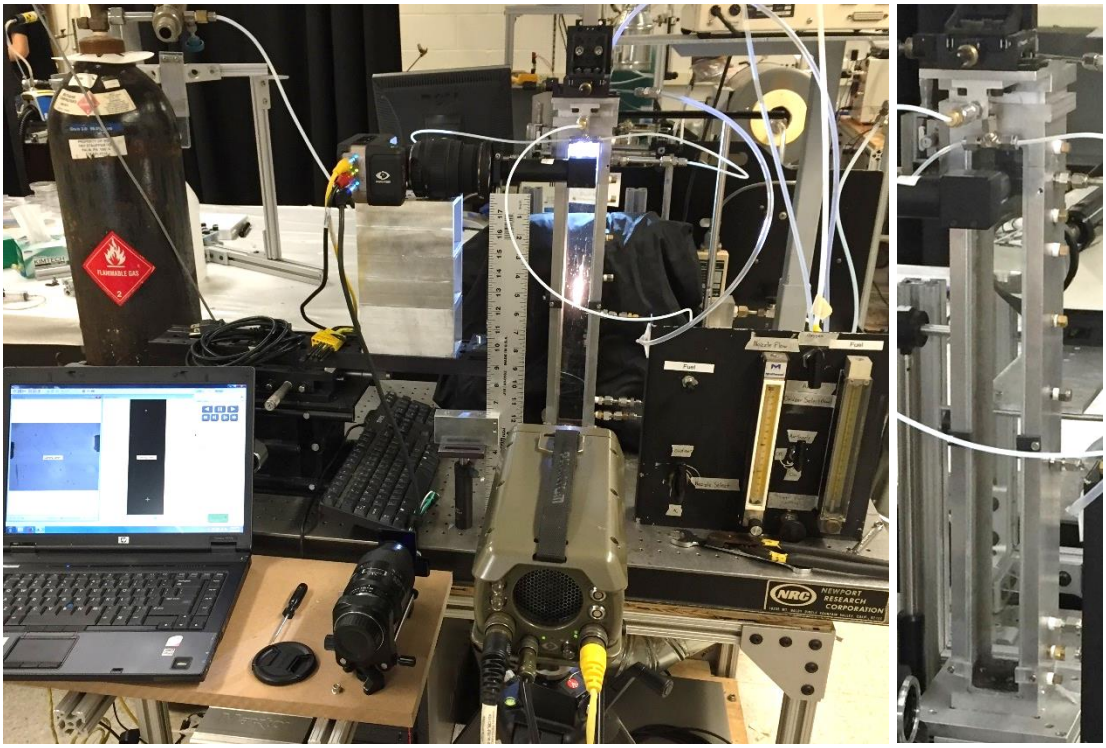


*Figure 11: Photographs of early design iteration of droplet combustion apparatus.*

The 0.5 m tall, 8 cm square tower is constructed of an aluminum frame with removable quartz windows on three sides. Primary sheath gas enters the tower via an oxygen flow at 12 LPM diffused through expanded metal delivered at the top of the

tower and the system is open to exhaust at the bottom where steel ducts direct exhaust gases to fume hoods. To ignite the droplets, methane is introduced via two 800 μm OD ceramic tubes from opposite sides of the tower at approximately 50 mL/min to create two stable diffusion flames ~1.7 cm below the droplet nozzle.

Droplet generation is achieved with a capillary needle assembly nested in a glass sheath tube supplied with nitrogen gas flow at approximately 0.25 LPM, as illustrated in Figure 12. The stainless-steel needles are assembled by clearance fitting 1.5-inch sections of 0.010" OD/0.005" ID SS capillary tubing (Microgroup, Inc.) inside of a 7-inch section of 1/16" OD/0.020" ID SS tube (IDEX Health & Science LLC.). The two sections are sealed together using steel-reinforced epoxy (updated assembly procedures for the latest apparatus design iteration are detailed in Appendix D). This design is chosen for disposability of the needles to minimize the risk of sample cross-contamination and to simplify experiment repair after common needle clogs caused by suspended particles in samples. During operation, liquid sample fed to the capillary enters the nozzle and is subject to a force balance between surface tension and aerodynamic drag (neglecting gravity). Droplet release will occur when the drag force dominates as shown below.

$$F_\gamma < F_D \rightarrow \pi d_d \gamma < \frac{\pi C_D \rho U^2}{8}\left({d_d}^2 - {d_n}^2\right) \tag{23}$$

$$U^2 = \frac{8 d_d \gamma}{C_D \rho \left({d_d}^2 - {d_n}^2\right)} \tag{24}$$

Where $U$ is the nozzle sheath gas velocity near the droplet, $d_d$ is the droplet diameter, $d_n$ is the nozzle inside diameter near the droplet, $\gamma$is the surface tension, $C_D$ is the drag coefficient of the droplet, and $\rho$ is the gas density. The nozzle gas flow should be

minimized to mitigate turbulence which can scatter the droplet trajectories and to limit the interference of the nitrogen flow with the ambient oxygen tower environment. Considering Equation 24, this is accomplished by practically minimizing the final diameter of the needle nested in the nozzle.

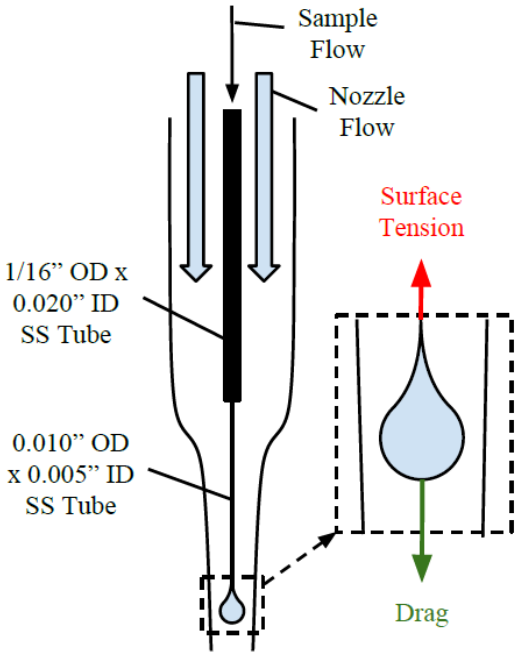


*Figure 12: Droplets generated by sheath gas drag overcoming surface tension of the droplet.*

*Figure 13: Photograph of droplet generation nozzle and capillary above unlit methane pilot tubes.*

The setup of the droplet generation and delivery system is where this apparatus is specifically well suited to analysis of highly reactive air-sensitive materials like those tested in Chapters 3 and 8. As described in more detail in Chapter 3, gas tight syringes with ball valves are used to contain the sample in an air-free vessel as it is loaded in a glove box and brought outside to the droplet experiment. Since the droplet generation system uses a nitrogen flow small enough to not interfere appreciably with the ambient oxidizing environment of the tower, the PTFE sample delivery lead from the syringe and the droplet generation nozzle can both be flushed with nitrogen before pumping air-sensitive sample. As droplets are generated and the experiment progresses, the sample remains in nitrogen until emerging from the nozzle as droplets immediately before ignition, protecting the sample supply from air and moisture. Temperature

sensitive samples can also be cooled with dry ice around the syringe in the syringe pump.

Recall that classical droplet combustion experiments use measurements of droplet diameter in time to fit data to the $D^2$-law given by the left-hand side of Equation 19. However, disruptive burning and/or particle additives usually invalidate this measurement method. The right-hand side of Equation 19 shows an approximation for the effective burning rate constant K assuming the fuel burns completely, repeated here:

$$K \cong \overline{K} = \frac{{d_{s,0}}^2}{t_B} \tag{25}$$

By eliminating $d_s(t)$ from the measurement expression, the complicating effects of droplet disruptions, gas generation, and suspended particles on the diameter of the droplet are avoided and instead the burning rate constant estimated is an "effective" one, which is sensitive to influences of $D^2$-law practical invalidities like the heat-up time (which can be removed from the measurement of K in classical experiments). This trade-off is acceptable as it facilitates the experiment with disruptive droplet burning by allowing influence of practical (but repeatable) nonidealities which will certainly exist in applied propulsion systems, albeit not in the same precise manner they manifest within this experiment (i.e. this experiment is for relative comparisons, not ubiquitous material property determinations). Heat-up time differences are a significant aspect affecting performance since a long heat-up time would lengthen ignition delay and therefore this influence is relevant and tolerable in experimental $\overline{K}$ estimates. Natural and forced convection effects do however skew results for $\overline{K}$ compared to K defined near ideal quiescent conditions. Therefore, while the $\overline{K}$ approximation renders this

constant specific to the experimental flow conditions used here and thusly it is not a ubiquitous material property of the sample fuel, it does provide a reliable basis of comparison since experimental flow conditions are maintained characterized by estimated non-dimensional numbers: $Re_\infty \approx 50$, $Sc_\infty \approx 0.7$, and $\mathrm{Gr} \approx 335$. Since $\left({}^{\mathrm{Gr}}/_{Re_\infty{}^2}\right) < 1$, buoyancy effects are negligible. Nominally, forced convection in this experiment would overestimate the quiescent burning rate constant according to Equations 20-22 by a factor of approximately 1.7.

In this first design iteration, the $\overline{K}$ approximation needed to be validated against a classical measurement of K and so two measurement configurations were implemented and compared in Chapter 3, validating the approximation with non-disruptive control samples. For the effective $\overline{K}$ approximation, only the initial droplet diameter and total burning times, $d_{\mathrm{s},0}$ and $t_B$, need to be measured for each specific droplet. To classically estimate K, the time evolution of the droplet diameter, $d_\mathrm{s}(t)$, needs to be measured. With a free-falling droplet and stationary cameras, this measurement of $d_\mathrm{s}(t)$ can only be fit to multiple diameter measurements at discrete heights, each for a separate droplet, which assumes the droplets burn consistently enough that they will converge to a statistically significant mean burning rate constant. The original equipment was designed based on this measurement procedure with only one high-speed camera thereby instilling the requirement and assumption that all droplets generated are the same size and their combustion highly repeatable (down to the droplet diameter versus time). This assumption was found to be unsound for multiple samples motivating the addition of a second camera to record and normalize

initial droplet sizes and ultimately reinforcing the decision to instead use the $\overline{K}$ approximation method.

For the $\overline{K}$ approximation method, two high-speed cameras are used in sync to observe the droplet combustion, the first "normalizing" camera being used in a static position to image the initial size of the droplets as they pass the methane igniters. An example frame image from this camera is shown in Figure 14. The second "main" camera is configured approximated 0.75 m from the tower with a 28-mm wide-angle lens (typically with f/11) and 2 μs exposure to observe the full trajectory of the droplets over their lifetime to facilitate burn time measurements. The burn time is based on the time from flame emission inception upon ignition to emission extinction when the camera no longer detects light at maximum gain, measured manually for each droplet in Vision Research PCC camera software used for playback. Ten to fifteen droplets are recorded combusting in the tower for each sample trial, and their burn times (normalized by each initial droplet size) averaged to estimate the effective $\overline{K}$ of each sample formulation.

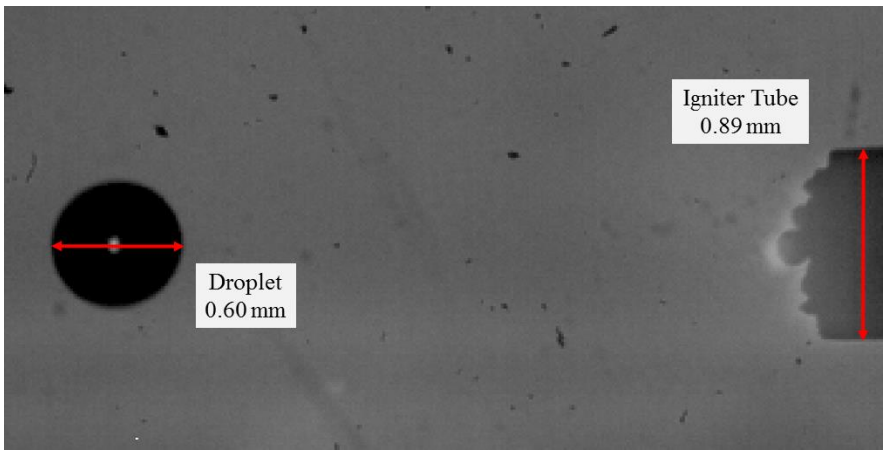


*Figure 14: Example of droplet imaged next to the igniter tube in design iteration 1 to measure initial droplet diameters.*

The alternative “magnified” configuration used to classically estimate K for validation of the $\overline{K}$ approximation method consists of the main camera configured instead approximately 0.2 m from the tower with a 105-mm lens (f/2), 1.7 μs exposure, and lens bellows for magnification. Using a quasi-collimated backlight and interference filters (0.64% transmittance from 315-445nm and 20% from 700-800nm) to attenuate the flame emission captured, the main camera in the magnified configuration can observe the diameter of the liquid droplets. By moving the main camera and backlight to various positions along the height of the tower, the droplet diameter evolution with time can be observed. The backlight is constructed of a small LED set at the focal point of a lens to project light through the tower to the normalizing camera. The camera magnifications and vertical positions are calibrated by incorporating bodies of known size into the fields of views of the cameras (i.e. stainless rods in tower side port feedthroughs).

In both configurations, the initial droplet size (when passing methane flames) is required to normalize the data and account for any fluctuations in generated droplet size. It is estimated by measuring and averaging the equivalent spherical diameter of the droplet in three image frames nearest the igniter tubes. The droplet is approximated by a plate-shaped ellipsoid whose minor axis is oriented vertically. Therefore, the equivalent spherical diameter is calculated as $(A^2B)^{(1/3)}$ where A is the diameter measured horizontally and B is the diameter measured vertically in the video. All video measurements were performed manually in this first apparatus design iteration with Vision Research Phantom Camera Control (PCC) Software.

### 2.1.2 Apparatus Update: Design Iteration Two and Diagnostics Integration

After the work presented in Chapter 3, the experimental apparatus and procedure was evaluated and several design and analysis changes were made. The key problems with the first design iteration were low precision of the initial droplet sizing and low rate of experimental data collection. Design and methodology changes were made to mitigate these problems. Precision was improved for the initial droplet sizing by increasing the image magnification using a lens train of two bi-convex lenses within the lens tubes of the camera periscope. By setting the focus of this camera to infinity, the magnification of the image on the camera sensor is achieved based on the object, image, and lens separation distances per the periscope and was increased beyond the maximum magnification of the stock camera lenses available. As magnification increased, more light was needed for acceptable contrast between the backlight and the droplets but the images were prone to blurring as fast-moving passed if exposure times were increases. More sizing frame images were also desired to more precisely measure initial droplet size which required higher framerate and shorter camera exposure time. Therefore, the LED backlight was replaced with a HeNe laser expanded to approximately 1-inch diameter beam size significantly improving the backlight intensity and approximating a shadowgraph setup (except for imperfect light collimation) to lengthen the depth of focus of the system to be more resilient to slight variations in droplet and nozzle positions. With the $\overline{K}$ approximation method validated in Chapter 3, only far-field imaging of the droplet flame emission over its full trajectory

was required and thusly the bottom backlight was removed. A schematic and photo of the updated apparatus and example droplet sizing frame are shown in Figures 15-17.

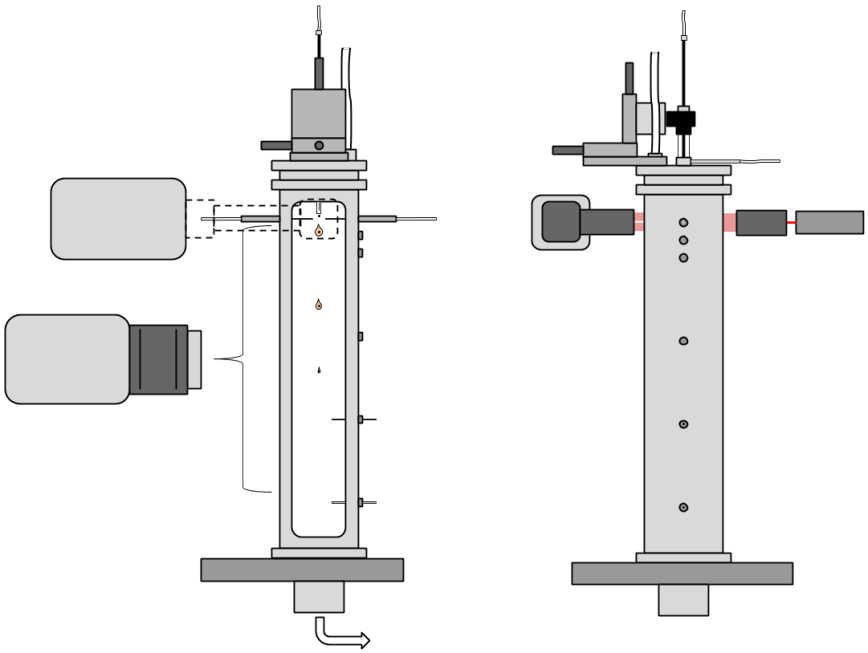

*Figure 15: Updated droplet experiment apparatus in burning rate measurement configuration.*

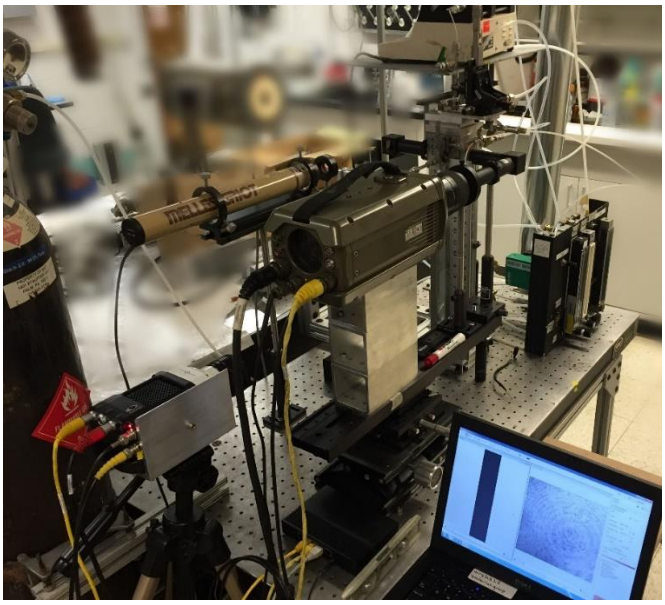

*Figure 16: Photograph of droplet experiment after design iteration 2 (camera on tripod was later static mounted to the optical platform).*

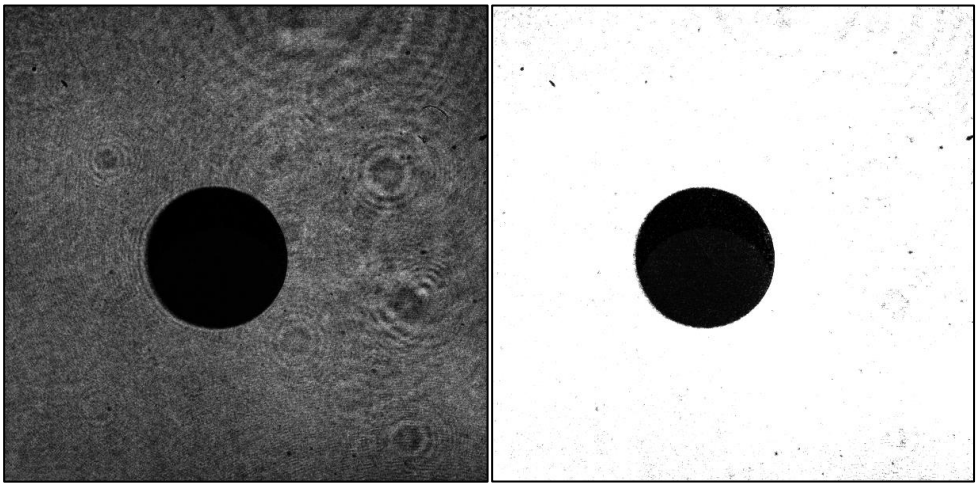

*Figure 17: Example initial droplet sizing images before and after artificial brightness increase (gain X5) images using the updated camera setup with an expanded HeNe laser. Droplet shown is 0.67 mm horizontally.*

Precision and rate of data collection and analysis could also be improved dramatically by automating the video-based measurements of burning time and initial droplet size and data analysis using MATLAB and a SDK provided by Vision Research used to interact with camera files (detailed in Appendix D). Sophistication of the automation algorithms designed and implemented for the research in this dissertation continued to evolve throughout the work presented in the subsequent chapters but the top-level method and algorithms remained the same.

1. Full camera memory capacities are saved as one video with on the order of 20-30 droplets imaged per video and a MATLAB script scans the normalization camera file for passing droplets, noting their time and saving only the relevant frames to save disk space.
2. MATLAB image processing is used to measure the cross-sectional pixel area of each droplet with nominally 8 frames of full droplet area in view,

thereby increasing precision with 8 individual measurements per droplet.

3. Equivalent circular diameter and eccentricity are calculated and magnification calibration using images of the known diameter igniter tubes is used to convert pixel diameters to mm with an estimated uncertainty of ±0.01mm. Eccentricity provides a metric to threshold for rare errors in image processing caused by image artifacts.
4. Videos from the second camera are opened by MATLAB frame-by-frame and intensity thresholded to find combusting droplets.
5. Droplets appearing high in the frames and disappearing low in the frame are marked as ignition and termination times respectively, measuring burning times ±3 ms.
6. MATLAB scripts consider the droplet size and time from the initial sizing and the ignition times in the flame trajectories to coordinate the data for respective droplets. Respective terminations are guessed based on the termination of the first droplet measured found by the user.
7. A table of ignition and termination times, initial droplet sizes, and calculated burning rate constants with estimated uncertainties of ±0.02 $mm^2/s$ is presented to the user who validates that each ignition and termination correspond to the same droplet.
8. Repetition for tens of droplets per sample to estimate an average $\overline{K}$.

A free-moving vertical translation stage was also designed and assembled to collect magnified color videos and spectroscopic data through a collection fiber optic as illustrated in Figure 18. Doing so with a stationary fiber and camera was also carried out before this translation stage was implemented for the work in Chapters 7 and 8, but those experiments suffered from short times of the droplet in view as it passed. By dropping the camera and fiber on a stage to fall onto foam pads, a droplet in view during the fall is visible for significantly longer time. If no droplet is captured on the fall, at the least data is collected as the stage is manually returned to the top position as its motion counters that of droplets continuing to pass falling downward (~3 drops of the stage actuated by hand can be executed during one camera recording).

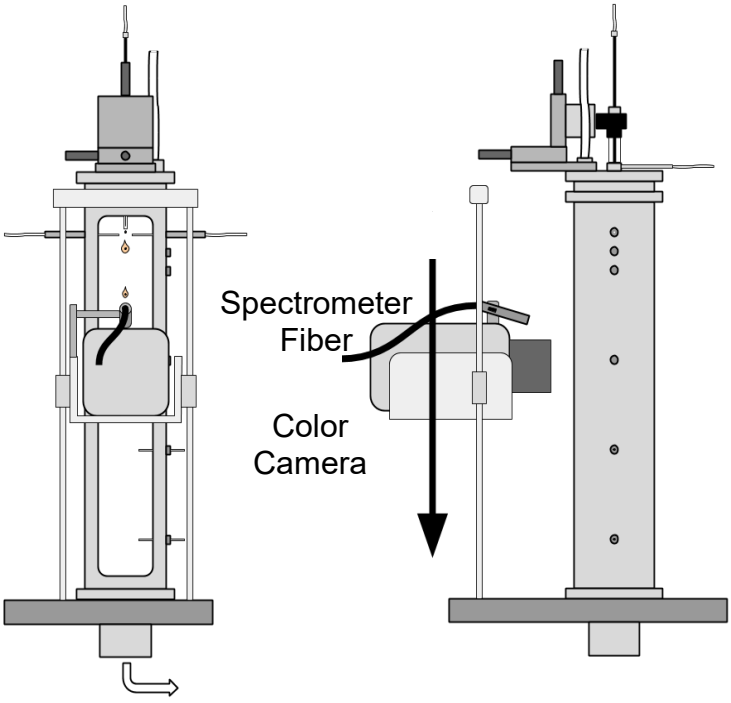


*Figure 18: Droplet combustion apparatus with alternate configuration for falling magnified camera and spectrometer fiber*

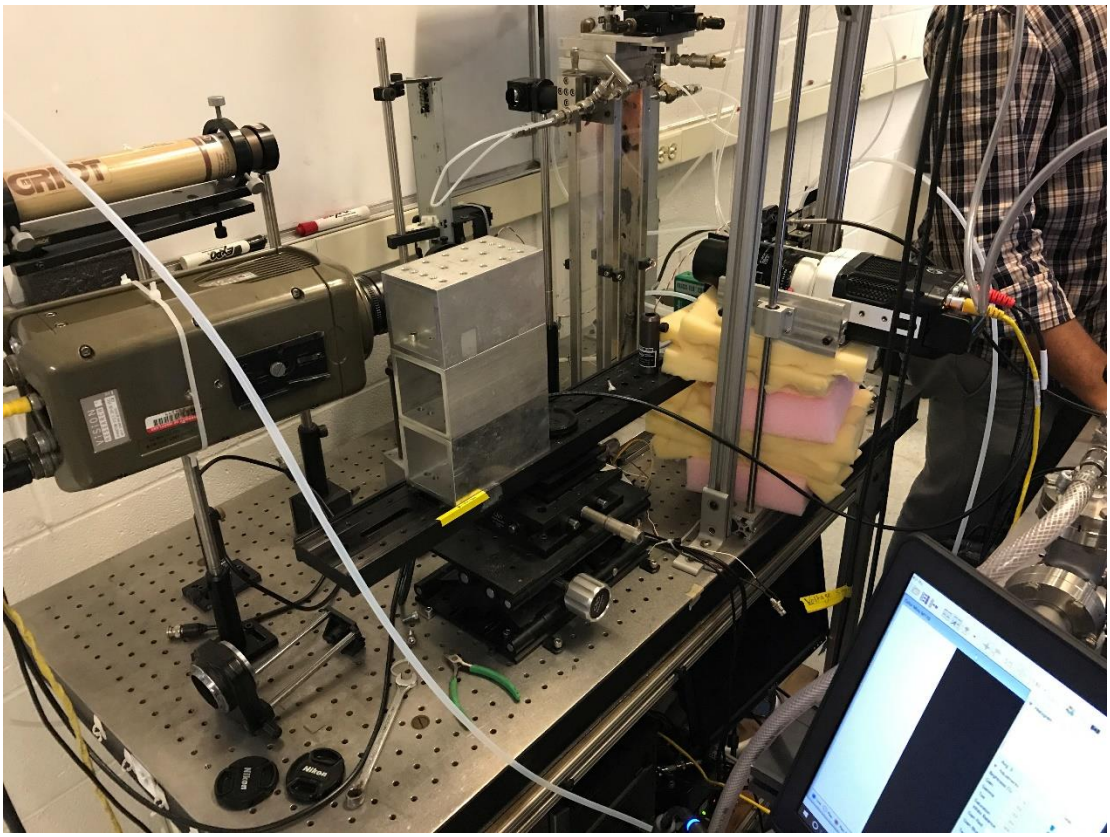

*Figure 19: Photograph of droplet experiment apparatus with camera and collection fiber vertical translation stage.*

## *2.2 Nanofuel Sample Preparation*

Preparation of various nanofuel samples is described in detail within each Chapter, specific to the methods used in each. However, the nominal process is common to most of the work presented and overviewed here. Particulate additives in these studies were primarily considered in kerosene fuel, as a reasonable surrogate hydrocarbon for RP-1. Reagent grade kerosene purchased from Sigma-Aldrich (SKU 329460) was used throughout the studies with kerosene. Reasonably stable suspensions of nAl could only be achieved using a surfactant and, based on a published demonstration with boron nanoparticles in a hydrocarbon [92], trioctylphosphine oxide

was chosen which readily dissolves in the kerosene carrier fuel. In general, nanofuels were mixed with constant batch volumes across samples and particles were suspended using a sonication bath (5 min to 1 h) and magnetic mixing (nominally 12 – 24 h at a time).

The particle additives tested included numerous nanoparticles, either purchased commercially or synthesized in-house. Nanoaluminum (nAl), which shows up in most of the studies presented in this dissertation, was purchased from Novacentrix with 80 nm primary particle sizes and a 2-3 nm oxide layer. Several other nanoparticle materials including CuO and MgO were purchased from Sigma-Aldrich and used as-received. In some cases when a nanoparticle material of interest was not available commercially, they could be synthesized in-house using aerosol methods in which they are sprayed from precursor solutions.

### 2.2.1 Aerosol Spray Drying

For materials such as $KIO_4$ which cannot be purchased as a reliable nanoparticle material but does dissolve in water, nanoparticles can be synthesized using aerosol spray drying which is utilized in several of the studies in this dissertation [93]. In this method, a precursor composed of the material of interest usually in an aqueous solution (but also possible in other more volatile solvents) is atomized and entrained in an aerosol flow. This stream of droplets is passed through a diffusion dryer if water is the solvent used, a cylindrical vessel filled with beads of dry silica desiccant, to absorb moisture from the flow and incite evaporation of the droplets. To complete their evaporation, the aerosol then enters a tube furnace wherein temperatures on the order

of 200 ºC at the walls heat the flow and dry the droplets to leave precipitate of the material dissolved in the precursor. Passing the flow through a membrane filter (e.g. with 400 μm pore size) enables collection of the particles. The atomized droplets are on the order of 1 μm in size but relatively polydisperse in a distribution around this nominal size and depending on the concentration of the solute, can dry to leave solid particles nanoscale in size. Furnace temperature, gas residence time, and precursor concentration are some experimental variables which can be used to tailor the nature of the particles synthesized. If a reactive solute is used which will thermally react in the furnace to leave a solid phase desired, this process is considered aerosol spray pyrolysis.

### 2.2.2 Nanoparticle Assembly into Mesoparticles by Electrospray

Reviewed previously and utilized widely in the studies presented in this dissertation, electrospray can be used to assemble existing nanoparticles into agglomerates based on evaporation of a precursor solution, similar to aerosol spray drying, except that atomization is achieved by liquid feed breakup induced by a strong electric field [94-97]. A schematic of the experimental apparatus used herein is shown in Figure 20 which was operated in a polycarbonate enclosure fitted with a fan, heater, and temperature controller for repeatable ambient temperature and continual exhaust of volatilized solvents.

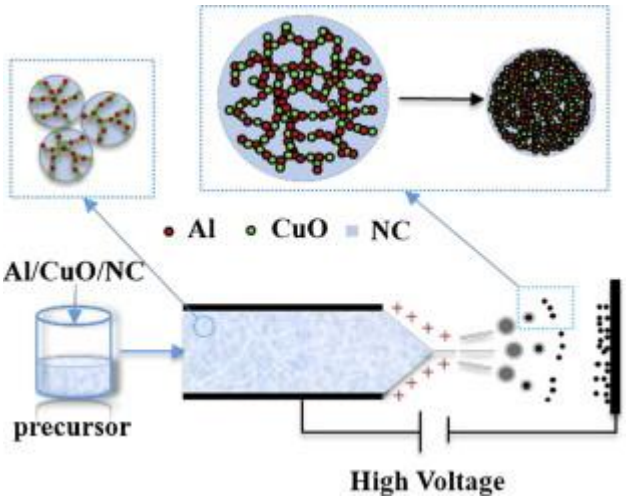


*Figure 20: Schematic of experimental apparatus constructed for electrospray assembly of nanoparticles into MPs. Reprinted from [14], with permission from Elsevier.*

A volatile solvent, usually a mixture of 3:1 ethanol:ether by volume, is used as the electrospray precursor with NC binder dissolved and nanoparticles of interest, e.g. nAl and/or CuO, in suspension. This is pumped via syringe through a steel probe needle charged to 10 kV pointed orthogonally towards a flat aluminum foil substrate charged to -10 kV. If particle suspension stability is low and prone to gravitational settling, in situ magnetic stirring can be used within the syringe reservoir. Charge concentration on the conductive precursor builds up causing the formation of a Taylor cone at the end of the needle from which the stream of precursor breaks up into a relatively monodisperse cloud of droplets which are attracted to the substrate via columbic force. As the volatile solvents evaporate in flight, suspended particles and precipitated solute agglomerate to form mesoparticles which deposit on the substrate for collection. By controlling experimental parameters such as precursor characteristics, needle-substrate separation distance, voltage potential, and ambient temperature, the drying of the

droplets to form mesoparticle composites can be tuned to vary the microstructure. The flexible nature of this general experimental setup can also be exploited to create numerous different morphologies and geometries other than mesoparticles including fibers or films. For example, with a high precursor viscosity and feed rate and lower separation distance, the fluid can hold together in a filament as it dries into fiber structures (called “electrospinning”) [98].

## *2.3 Peripheral Tools and Diagnostics*

### 2.3.1 Simultaneous Thermogravimetric Analysis and Differential Scanning Calorimetry

The thermal behaviors of energetic materials are frequently characterized in controlled temperature experiments to understand how species and formulations react to external heating. Thermogravimetric analysis (TGA) and differential scanning calorimetry (DSC) are two techniques to achieve this which are commonly employed together in commercial simultaneous DSC/TGA (SDT) instruments, such as the TA Instruments SDT Q600 used in the work of this dissertation. In both TGA and DSC, the material temperature is increased in a highly controlled manner using a sample furnace and precision Pt/Ru thermocouples with a controlled sheath gas flow while the sample weight (TGA) and heat energy required to keep the sample isothermal (DSC) are monitored relative to an empty reference sample holder (both holders adjacent on two cantilever microbalances within the furnace). The heating rate of a SDT (approximately 1-50 K/min) is significantly lower than those of combustion events and high-heating rate experiments (on the order of $10^5$ K/s) designed to more closely

emulate combustion conditions, however SDT can still elucidate important thermal behaviors including melting, thermal decomposition, oxidation reactions, and evaporation to differentiate the temperatures at which certain events can be roughly expected in practical reactions.

### 2.3.2 Thermochemical Calculations Software

When considering possible chemical effects of additives in hydrocarbon fuels, thermochemical calculations can provide context to experimental evidence regarding likely reactions, chemical products, and/or energetic and temperature effects of a certain additive. Namely, equilibrium calculations consider a set of possible reactions with an initial mixture of species with certain thermodynamic states and properties to find the most stable mixture of product species and their thermodynamic properties within a specified set of experimental constraints if reactions were allowed to progress to equilibrium. Adiabatic constraints considering zero heat loss of the system result in a comparable metric for different reactant systems and initial states: the adiabatic flame temperature (final temperature of the products at equilibrium). This is calculated by holding either volume and internal energy constant, or pressure and enthalpy constant, depending on how the experimentalist wants to model the system. In the latter case, energy is not conserved since expansion work is required to maintain the constant pressure and thusly the constant pressure adiabatic flame temperature is typically lower than that of constant volume for exothermic energetic systems. Computer programs have been developed to carry out these calculations with far more reactions and species than can be efficiently considered by manual hand calculations, including NASA's

Chemical Equilibrium with Applications (CEA) [99] and Lawrence Livermore National Lab's Cheetah 5.0. In this dissertation, calculations with these programs have most often been performed to estimate possible species formation or reactions which are thermodynamically possible, thereby supporting the proposal of certain additive mechanisms. Cheetah has also been used to perform some idealized rocket performance calculations with aluminum and silicon in rocket fuel in the motivation of this work.

### 2.3.3 Flame Emission Spectroscopy

In the most recent work described in Chapters 7 and 8, improved experimental capabilities facilitated longer observations of falling, burning droplets in a magnified view using a vertical translation stage for a high-speed camera. With the shorter viewing distance afforded by this method, a fiber optic could also be affixed to the translation stage to collect light from flame emission. The PhD work of a fellow collaborator, Rohit Jacob, has concerned the development of a time-resolved emission spectrometer useful for spectral intensity measurements on timescales relevant to energetic material reactions and this method has been applied to probe time-resolved emission of excited atomic species in droplet flames in Chapters 7 and 8.

The assembly built and operated by Rohit Jacob concurrently with the droplet experiment operated in this dissertation consists of a 1 m optical fiber collecting light from a falling droplet and transferring it to a 0.5 m spectroscope (Acton SP 500i) with a 1800 lines/mm grating to disperse the light between 473-502 nm wavelengths (different gratings are available to change wavelength ranges dispersed on the detector). The resulting spectrum is collected by a 32-channel PMT array interfaced

with a high-speed data acquisition system (Vertilon IQSP 580). The wavelength calibration was performed using a Mercury lamp (Newport) and the system sensitivity was calibrated using a black body furnace (Newport) in the range of 1200-1500 K and a high-temperature tungsten-halogen lamp (Avantes HAL-CAL) at 2440 K. The sampling rate of the acquisition system was set at 5000 Hz, sufficient to resolve the sub-millisecond disruptions in the droplet flames.

### 2.3.4 Color Camera Ratio Pyrometry

The vertical translation stage for the camera also facilitates longer videos captured of magnified burning droplets from a color high-speed camera. When atomic emissions are not significant, such videos can be analyzed to estimate spatial temperature distributions based on the collected light. This technique uses the ratios of the red, green, and blue channels of the camera to fit pixels to estimated temperatures as described in [100]. By taking ratios of raw color channel intensities, dependency on most variables associated with intensity is eliminated except for those regarding the channel gain ($\psi_i$), emissivity ($\varepsilon$), and spectral response ($\chi_i$) of the camera at individual wavelengths and channels [100]. To estimate temperature of hot soot and particles, the graybody assumption has been modified to account for an optically thin flame by assuming that $\varepsilon \sim 1/\lambda$, substituted into Planck's Law, and integrated over the entire spectrum to which the camera is sensitive [101].

$$\frac{I_i}{I_j} = \frac{\psi_i \int L(\varepsilon,\lambda,T)\chi_i(\lambda)d\lambda}{\psi_j \int L(\varepsilon,\lambda,T)\chi_j(\lambda)d\lambda} \tag{26}$$

The normalized spectral response of the camera for each color channel is provided by the manufacturer. Based on calibration with a Newport Oriel 67000 Series Blackbody Infrared Light Source, calibration factors $C_{gr}$, $C_{bg}$, and $C_{br}$ are determined to be 0.952, 0.888. and 0.847, respectively, and assumed valid from 773-4773 K. Calculation of temperature is reduced to matching of calibration factor-corrected channel intensity ratios to theoretical ratios at various temperatures.

$$\left(\frac{I_i}{I_j}\right) = C_{ij}\left(\frac{I_i}{I_j}\right)_{\emptyset} \tag{27}$$

MATLAB is used to extract raw pixel values and calculate temperatures. Black-level and saturated pixels are dilated by a factor of 3 and removed from consideration. The demosaicing routine in MATLAB is used with the Bayer color filter array (GBRG) to recover values for red, green, and blue channels at each pixel. Three color ratios (green/red, blue/green, and blue/red) were simultaneously used to estimate temperature by minimizing their summed error relative to theoretical ratios. Further thresholding eliminates summed errors corresponding to a temperature error greater than 110 K. For figures which show temperature of a video as a function of time, only unsaturated pixels above the black level and within the error threshold are used to report mean temperature of each frame for a contiguous area of at least 10 acceptable pixels.

# Chapter 3: Soluble aluminum additive to hydrocarbon fuels for droplet burning rate enhancement[1]

*Summary*

Additives to hydrocarbon fuels are commonly explored to change the combustion dynamics, chemical distribution, and/or product integrity. In this chapter, a novel aluminum-based molecular additive, Al(I) tetrameric cluster $[AlBrNEt_3]_4$ (Et = $C_2H_5$), is dissolved in a hydrocarbon fuel the resultant single-droplet combustion properties are evaluated. This $Al_4$ cluster offers a soluble alternative to nanoscale particulate additives that have recently been explored and may mitigate the observed problems of particle aggregation. Results show the $[AlBrNEt_3]_4$ additive to increase the burn rate constant of a toluene-diethyl ether fuel mixture by ~20% in a room temperature oxygen environment with only 39mM of active aluminum additive (0.16 wt % limited by additive solubility). In comparison, a roughly similar addition of nanoaluminum particulate shows no discernable difference in burn properties of the hydrocarbon fuel. High speed video shows the $[AlBrNEt_3]_4$ to induce microexplosive gas release events during the last ~30% of the droplet combustion time. This is attributed to HBr gas release based on results of Temperature-Programmed Reduction

[1] The results presented in this chapter have been previously published and are reprinted with permission from P.M. Guerieri, S. DeCarlo, B. Eichhorn, T. Connell, R.A. Yetter, X. Tang, Z. Hicks, K.H. Bowen, M.R. Zachariah, Molecular Aluminum Additive for Burn Enhancement of Hydrocarbon Fuels, Journal of Physical Chemistry a 119 (2015) 11084-11093. Copyright 2016 American Chemical Society.

(TPR) experiments of the $[AlBrNEt_3]_4$ dosed with $O_2$ and $D_2O$. A possible mechanism of burn rate enhancement is presented that is consistent with microexplosion observations and TPR results.

*3.1 Introduction*

With their high density-specific enthalpy of combustion, energetic metals can be added to propellants and explosives to drastically increase the volumetric energy density as evidenced in Figure 3. Metal nanoparticles (with diameters between 1-100nm) have demonstrated shorter ignition delays and higher burning rates than larger micron-sized particles due to their increasing surface to volume ratio as particle size decreases [4]. Nano-scale metal additives are also better suited to liquid propellant incorporation since they can replace traditionally non-energetic gelling agents and boast lower settling velocities than larger particles. However, nanoscale additives introduce new challenges. Increasing reactivity with decreasing particle size has a lower limit of potential activity because the inert native oxide on the metal particle surface comprises an increasing mass fraction of the material as the particle size decreases [4]. Colloidal stability also remains a significant challenge as nanoparticles are highly prone to aggregate and settle out of suspension before the reactive benefits of the additive can be utilized [4].

As discussed in the dissertation introduction and literature review, the precise effects of a particulate additive depend on the relative strength of competing mechanisms including particle agglomeration and physical droplet disruptions. Specific manifestations and relative strengths of such mechanisms are highly

dependent on ambient temperature, particle loading, chemical stabilizations used, and the physical characteristics of the pure solvent. Volatility and viscosity for instance will affect the relative timescales of solvent evaporation versus particle transport and aggregation in the fluid. An energetic, soluble alternative to nanoparticle additives has the potential to overcome these sensitive aggregation challenges while conserving the benefits of high-energy-density additives, thereby promoting relative dominance of the combustion-promoting mechanisms.

In this chapter, a novel aluminum-based molecular additive is utilized that for the first time enables the investigation of a directly soluble alternative to the nanometal particle dispersions that have been examined in literature. The additive is an in-house synthesized aluminum (I) bromide tetramer stabilized with triethylamine ligands, which was dissolved in a toluene-diethyl ether co-solvent matrix. Droplet combustion with and without the molecular additive was measured in a drop-tower to estimate burning rate constants. The additive was further studied by TPR-mass-spectrometry to probe reaction mechanisms and products. These results were then compared with similar experiments incorporating standard particulate nanoaluminum.

## *3.2 Experimental*

### 3.2.1 Molecular Additive

The molecular additive used in this chapter is a hydrocarbon-soluble Al(I) tetrameric cluster, $[AlBrNEt_3]_4$ (Figure 21), synthesized by Samantha DeCarlo and coworkers in the research group of Dr. Bryan Eichhorn at the University of Maryland

from the $AlBr{\bullet}NEt_3$ starting material produced from a Schnöckel-type metal-halide co-condensation reactor (MHCR) [67-69]. This tetramer is a ligand stabilized component of the $AlBr{\bullet}NEt_3$ precursor solution and contains aluminum in the 1+ oxidation state with covalent Al—Al bonds (average bond length 2.41 Å). This product is isolated from solution as a yellow crystalline solid and exhibits good solubility in the nonpolar organic solvents benzene and toluene. To maximize the concentration of aluminum in solution, the donor solvent $Et_2O$ was added to increase solubility through the use of a tol:$Et_2O$ (4:1) co-solvent mixture. This mixture allows for more concentrated samples containing ~40 mmol of aluminum, compared to ~24 mmol of aluminum in pure toluene solutions. Two concentrations of $[AlBrNEt_3]_4$ additive in the tol:$Et_2O$ co-solvent were produced and tested to study any significant effects of concentration variation. Due to the low oxidation state of the aluminum (I) tetramer and lack of an oxide passivation layer normally found on bulk aluminum metal, it is extremely air and moisture sensitive. Once an $[AlBrNEt_3]_4$ solution is exposed to air, rapid oxidation occurs causing precipitation of aluminum oxide and hydrolysis products, which necessitates the use of Schlenk techniques and gas tight syringes in the combustion studies.

The dissolution of the $[AlBrNEt_3]_4$ in the co-solvent matrix (tol:$Et_2O$) was performed in a glovebox under Ar atmosphere, and resulted in deep clear yellow solutions. Once completely dissolved, the solutions were then loaded into an Ar-purged gastight syringe. To limit exposure of the sample to air, the syringe is kept in a sealed bag under argon. Prior to being connected to the drop-tower, 6 inches of 1/16” OD x

0.040” ID PTFE Tubing is flushed with nitrogen to prevent oxidation of the product prior to tower introduction.

All reactions are performed under an argon atmosphere in a glovebox or under dry nitrogen using standard Schlenk techniques. Toluene and diethyl ether were purified by distillation from sodium benzophenone ketyl under a dinitrogen atmosphere, and triethylamine was purified through distillation over calcium hydride. All purified solvents were stored in modified Schlenk vessels over 3 Å molecular sieves under an argon atmosphere. The $^{1}H$ and $^{13}C$ NMR spectra were recorded on a Bruker DRX500 Avance spectrometer.

**AlBr•$(NEt_3)_n$:** Aluminum metal (0.8410 g, 31.1 mmol) was reacted with gaseous HBr (36.5 mmol) over 3 hours at approximately 1200 K in a modified Schnöckel-type metal halide co-condensation reactor [67, 68]. The resultant gas-phase AlBr was co-condensed with a mixture of toluene:triethylamine (3:1 v/v) at approximately 77 K. The solvent matrix was thawed to –80 °C and the resultant yellow-brown solution stored at that temperature prior to use [67, 68]. Titration of the AlBr•$(NEt_3)_n$ solution via Mohr’s method revealed a bromide concentration of 201 mM yielding an Al:Br ratio of 1:1.10. The $[AlBrNEt_3]_4$ complex was prepared through the use of a slightly modified published procedure [69] as described below.

**$[AlBrNEt_3]_4$:** A 40 mL aliquot of AlBr•$(NEt_3)_n$ was transferred to a Schlenk flask. Approximately 10 mL of solvent was removed in vacuo while warming the solution to room temperature. Solvent removal stopped upon observing the formation of yellow solid, which stood at room temperature overnight. The next day the yellow

solid was isolated, washed with copious amounts of hexanes, and crystals suitable for X-ray diffraction were obtained. $^{1}$H NMR (500 MHz, tol-d8): δ (ppm) = 1.18 (t), 3.08(q) $^{13}$C NMR (400 MHz, tol-d8): δ (ppm) = 9.80, 49.05. The overall yield of $[AlBrNEt_3]_4$, based on the parent solution $AlBr{\bullet}NEt_3$, is up to 20%.

**$[AlBrNEt_3]_4$ solution:** In a glovebox, 36.4 mg (0.0437 mmol) of $[AlBrNEt_3]_4$ was dissolved in 3.6 mL of dry toluene. After 20 minutes, 0.9 mL of dry $Et_2O$ was added to the $[AlBrNEt_3]_4$ solution for a final solution concentration of 9.7 mM $[AlBrNEt_3]_4$. The solution was then taken up in Hamilton Model 1005 SL Gastight Syringe, and sealed via syringe lock. The 5.2 mM sample was prepared in a similar manner utilizing 17.9 mg (0.0215 mmol) of $[AlBrNEt_3]_4$ and was dissolved in 4.5 mL of toluene/$Et_2O$ (4:1) mixture.

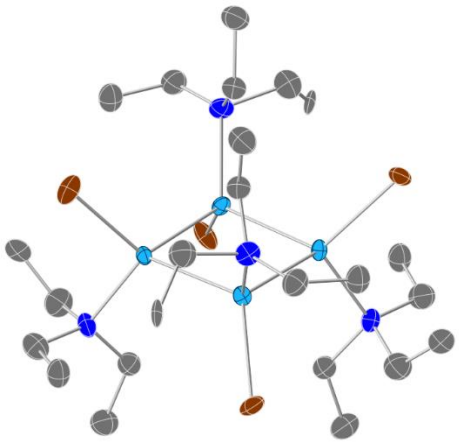

*Figure 21: Crystal structure of $[AlBrNEt_3]_4$: Al (light blue) N (dark blue) C (gray) Br (brown), hydrogen atoms omitted for clarity.*

### 3.2.2 NanoAluminum Additive

nAl sample preparations begin by adding 2.0 mg/mL of 80 nm (primary particle size) aluminum particles (Novacentrix, Inc., 80% active Al with 2-5nm oxide shell as

confirmed by TEM of as-received particles shown in Figure 22) to the toluene/$Et_2O$ (4:1) solvent mixture. As with the $[AlBrNEt_3]_4$ and control samples, the solvent mixtures are made in small batches for each sample (just before nanoparticle addition in this case) to minimize preferential evaporation of the ether component. The nanoparticles are suspended via an ultrasonication bath for 1 hour and allowed to gravitationally settle for 24 hours before decanting the stable suspension. By allowing the suspension to stand for 24 hours the largest fractal aggregates settle and are removed from the formulation to promote suspension stability and prevent needle clogging during experiments. The resultant particle concentration is determined by vacuum drying a known volume of the decantant and weighing the remaining solids. Approximately 4 mL of sample are loaded into a Hamilton Model 1005 SL Gastight Syringe connected to 6 inches of 1/16" OD x 0.040" ID PTFE Tubing. Any air is removed from the syringe and tubing before compression-fitting the tubing to the capillary tube/needle assembly and engaging the syringe in the syringe pump.

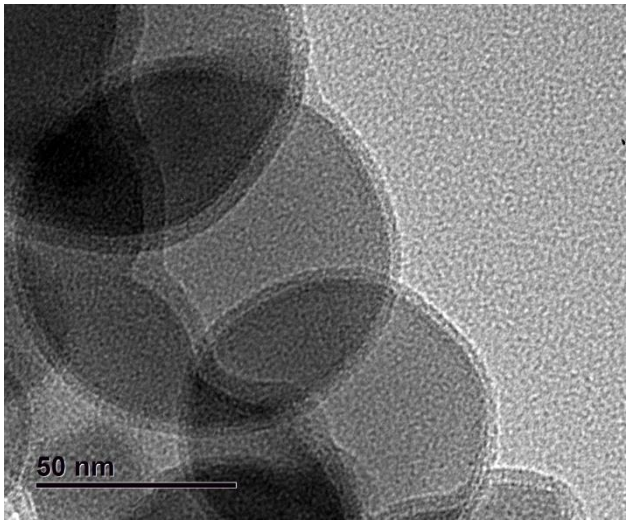


*Figure 22: Nanoaluminum particulate additive TEM showing 2-5 nm oxide shell.*

### 3.2.3 Combustion Characterization

The free-droplet combustion apparatus used in this study is described in Section 2.1.1 and reviewed briefly here for convenience. The design iteration of the apparatus used for the work in this chapter was the earliest iteration and primarily designed to prove the concept of the experimental burning rate estimation and validate it against classical droplet diameter-based estimated for single component control samples. Droplet generation is achieved with a capillary needle assembly nested in a glass sheath tube supplied with nitrogen gas flow. This design is chosen for disposability of the needles to eliminate the possibility of sample cross-contamination and for compatibility with the air and moisture sensitive samples tested in this chapter. Droplets are released to fall through an oxygen-rich tower ignited by methane pilot tubes and imaged using a tandem high-speed camera setup in two measurement configurations (for classical K measurement and effective $\overline{K}$ estimation).

Classical liquid droplet combustion theory states that, assuming the droplet is fully liquid (and therefore the volume of the droplet is directly coupled with its mass), the rate of decrease in droplet volume is linearly proportional to the diameter of the droplet [70]. By separation of variables and normalization by the initial diameter of the droplet, the governing equation for the droplet diameter as a function of time according to this theory can be written as:

$$\frac{D(t)^2}{{D_0}^2} = 1 - K\frac{t}{{D_0}^2} \tag{28}$$

While the experiments of this study do not exactly match the conditions under which the $D^2$-law is derived, it does provide a metric by which the burning rate of liquid

formulations can be characterized: K, the burning rate constant in units of $mm^2/s$, which increases for faster burning droplets. The droplet diameters and burn times measured are fit to the $D^2$-law to estimate the burning rate constant by plotting the square of the diameter versus time (both parameters normalized by the square of the initial droplet diameter) and assessing the slope of a linear best fit. Alternately, a far field camera arrangement can capture the entire combustion trajectory instead of droplet diameters measured in flight. By assuming a final droplet diameter at flame extinction and measuring the burn time with the far-field observation, a $D^2$-law burning rate constant can be estimated without the constraint that the droplet be entirely liquid according to:

$$K = \frac{1 - {D_{\text{Extinction}}}^2 / {D_0}^2}{t_{\text{Extinction}} / {D_0}^2} \tag{29}$$

Details of the two camera configurations and video-based measurements are available in Section 2.1.1. To capture residual solids remaining after termination of droplet combustion, an SEM substrate was placed in the tower so that the reaction product could impinge on the surface at a location just after combustion terminated.

*3.3 Results and Discussion*

While hydrocarbon droplets exhibit steady burning until the point of termination, fuel droplets laden with $[AlBrNEt_3]_4$ additive exhibit disruptive burning characterized by cyclical droplet inflations and eruptions or "microexplosions" presumably caused by rapid internal droplet gas release. The 9.7mM $[AlBrNEt_3]_4$ sample showed on the order of ten microexplosion events (exemplified by Figure 23) over each droplet lifetime, most commonly occurring in the last ~30% of the droplet

combustion time. The frequency and intensity of microexplosions appeared to increase with increasing $[AlBrNEt_3]_4$ concentration. In addition in many cases prior to the microexplosion, the droplet size as measured by high magnification video showed swelling of the droplet. As a result of the cyclical droplet inflations and microexplosions, droplet diameters measured in flight for the $[AlBrNEt_3]_4$ additive samples cannot be fit to classical droplet combustion modeled by Equation 28. The gas liberation decouples the mass and liquid volume of the droplets, therefore obscuring the direct burning rate constant measurement based on droplet diameter trends.

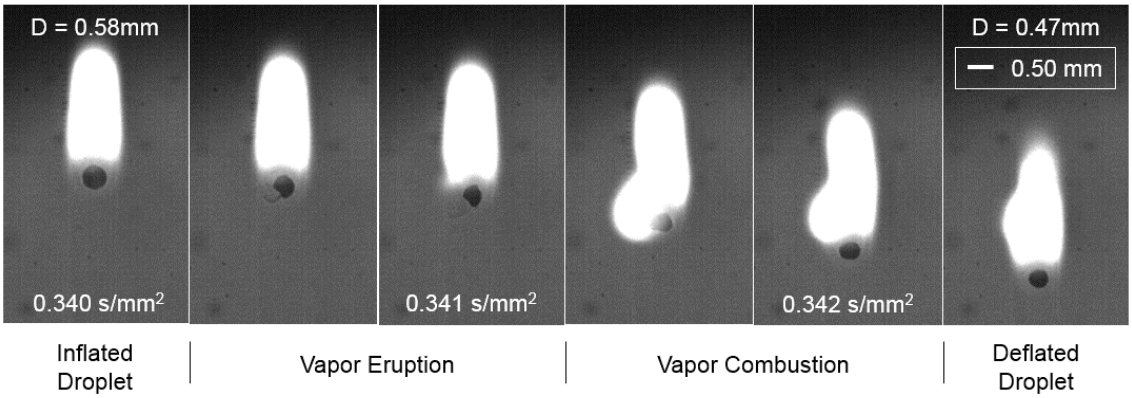


*Figure 23: Select video frames of representative 9.7mM $[AlBrNEt_3]_4$ sample microexplosion event visible by shadowgraph. Liquid-phase droplet visible as dark circle in each frame. Vapor expulsion visible in frames 2 and 3; its combustion in frame 4 and 5. Time normalized by square of initial droplet diameter = 0.65mm.*

An alternate method of estimating the fuel burning rate constant was therefore required to quantify the burning rate effect of the $[AlBrNEt_3]_4$ additive in the presence of its disruptive burning. In the far-field camera configuration, the main camera observes the trace of the entire combusting droplet trajectory from which a burn time can be measured. In order to fit a classical droplet burning model to these burn time

observations by Equation 29, a droplet size upon flame extinction is also required and therefore characteristic terminations were observed for each sample and are shown in Figure 24. Both the pure solvent and the particulate nAl additive sample terminate explosively at a critical droplet diameter of 0.1mm. On the other hand, the $[AlBrNEt_3]_4$ additive samples quench more slowly with a solid product remaining. The solid particles were collected to confirm the body observed in the termination video is the same size as the remaining solid particle. It is therefore assumed that all the liquid solvent in the $[AlBrNEt_3]_4$ samples burns and the critical diameter at flame extinction is taken to be zero.

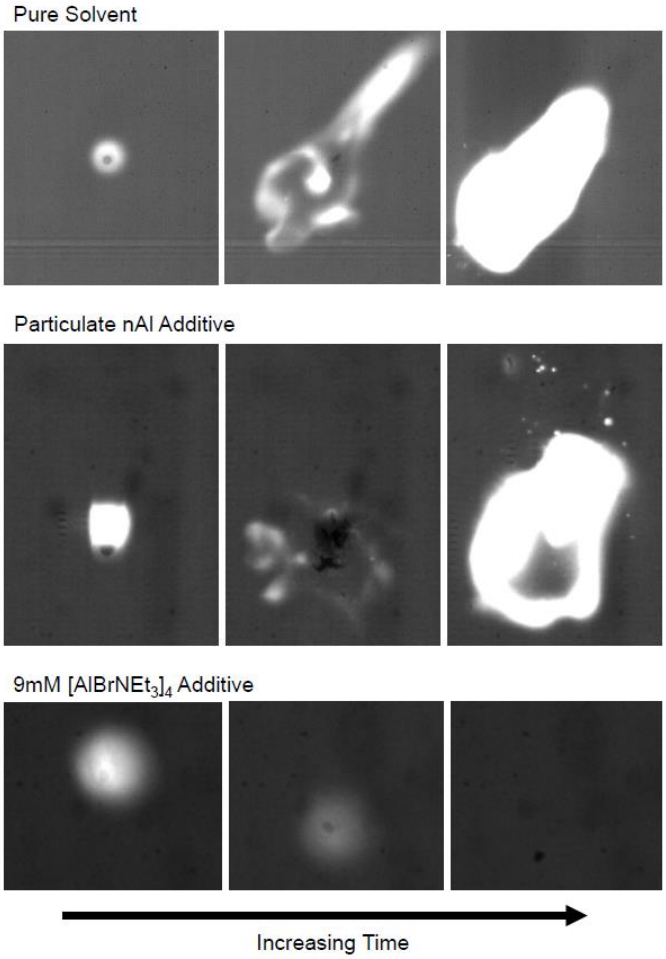


*Figure 24: Characteristic termination of droplets composed of: pure Kerosene and Kerosene with nAl additive occurring explosively at 0.1mm critical droplet diameters; Kerosene with [AlBrNEt$_3$]$_4$ additive quenching slowing as all liquid is consumed.*

Using the characteristic termination diameters, the burn times are plotted on the diameter-squared law plot in Figure 25. The classical model expressed by Equation 29 can be reasonably fit to these data by linear regression with a y=1 intercept and a burning rate constant thereby estimated by the slope of the fit (Table 3 with 95% confidence interval estimated). These model fits of the burn times (flame extinctions) are shown in Figure 25 as the linear trend lines illustrating the increased slope of the

$[AlBrNEt_3]_4$ -laden samples relative to the pure solvent and nAl-laden control samples which indicates an increased burn rate constant caused by the $[AlBrNEt_3]_4$ additive.

The variation of droplet diameters measured in flight for the pure control and nAl particulate samples as functions of normalized time from ignition are shown in Figure 25. Both control samples exhibit disruption-free burning, and therefore can fit the classical model by Equation 28 when the droplet diameters are measured in flight. The resulting burning rate constants, *K*, are derived from the slopes of linear regression fits and are tabulated in Table 3. The particulate nAl additive shows little to no effect on the burning rate. Pure solvent with triethylamine ligand added was also tested in the same manner to quantify any possible burning rate increase due to the ligand liberation or decomposition. The triethylamine concentration was adjusted to match the concentration of triethylamine contained in the solution containing the $[AlBrNEt_3]_4$ additive assuming all of the ligand was liberated. The ligand control results showed a marginal (~3%) increase in burning rate, however the combustion was qualitatively disruption-free.

The use of both fitting methods discussed to quantify the burning rate constant of the control samples allows for validation of the flame termination-based method, which employed Equation 29 to derive values of K. The resultant K values for the control experiments based on both methods agree reasonably well as evident in Figure 25 and Table 3. The flame termination-based measurement is not compromised by the disruptive nature of the $[AlBrNEt_3]_4$ additive sample combustion, and therefore yields a more accurate estimate for disruptive samples, and shows a 20% increase in burning

rate for both concentrations of $[AlBrNEt_3]_4$ additive tested compared to the pure control.

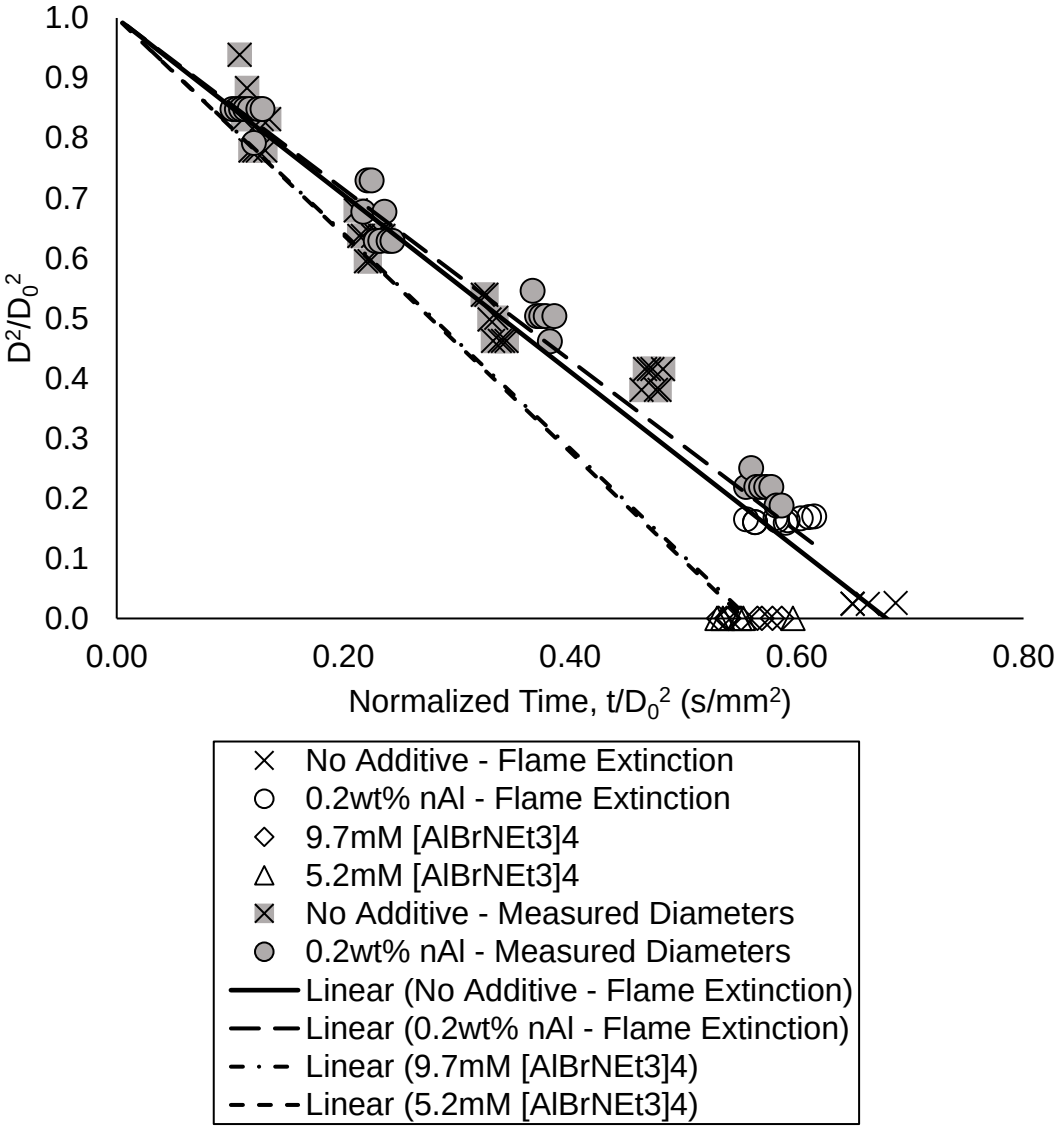


*Figure 25: Droplet diameters squared as functions of normalized time from ignition for 80% toluene / 20% ethyl with various additives. Linear fits of flame extinction data to classical droplet burning law are shown. Slopes of linear fits are tabulated in Table 3 as burning rate coefficients.*

*Table 3: Experimental samples with measured burning rate constants.*

| Additive | Active Al Conc. | Percent Increase in Energy Content | Burning Rate Constant Based On: | | |
|---|---|---|---|---|---|
| | | | $D^2$ Trend | | Time to Termination |
| | | | K ($mm^2/s$) | $R^2$ of Fit | K ($mm^2/s$) |
| None (Control) | None | None | 1.41 | 0.886 | 1.47 ± 0.10 |
| Triethylamine | None | None | 1.48 | 0.956 | 1.52 ± 0.10 |
| 0.2 wt% nAl | 50 mM | 0.14% (42 kJ/L) | 1.37 | 0.987 | 1.43 ± 0.14 |
| 5.2 mM $[AlBrNEt_3]_4$ | 21 mM | 0.06% (18 kJ/L) | (Obscured) | N/A | 1.80 ± 0.16 |
| 9.7 mM $[AlBrNEt_3]_4$ | 39 mM | 0.11% (33 kJ/L) | (Obscured) | N/A | 1.79 ± 0.18 |

Product particles remaining after the termination of $[AlBrNEt_3]_4$-laden droplets were collected and analyzed via SEM and EDX elemental analysis. A representative micrograph is shown in Figure 26. The volume of a sample droplet released into the tower is nominally ~ 9 x $10^{-4}$ $cm^3$. Based on the known aluminum concentration in the $[AlBrNEt_3]_4$-laden droplet, the maximum possible mass of product $Al_2O_3$ that can be formed from a droplet of this size is ~ 2.6 x $10^{-3}$ g. Assuming the particle captured comprises only $Al_2O_3$, the maximum density of a 100µm diameter particle such as that in Figure 26 would therefore be ~0.6 $g/cm^3$. Assuming the bulk density of $Al_2O_3$ is 4.0 $g/cm^3$, this suggests a minimum porosity of the captured particle to be ~85%. Elemental analysis of the outer surface shows an Al:O atomic ratio of ~0.3 ($Al_2O_3$ = 0.6) with ~5 atomic % carbon while an open pore shows an Al:O atomic ratio of ~1.3 with 30 atomic % carbon. Noting significant error is inherent in EDX analysis without suitable calibration standards, this result suggests that the particle may not be homogenous but is likely composed predominantly of $Al_2O_3$ and carbon species from the highly-sooting toluene fuel.

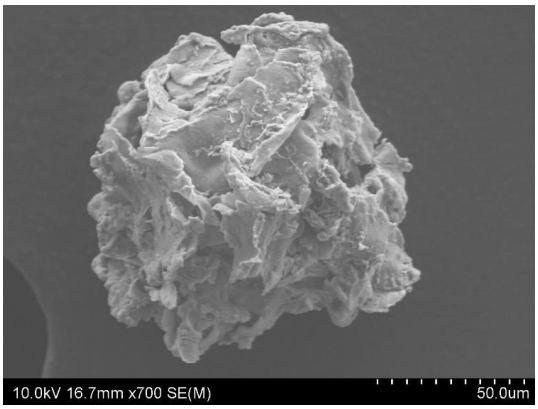


*Figure 26: SEM of product particle captured on carbon tape in-flight post-combustion from 9.7mM $[AlBrNEt_3]_4$ sample.*

A commonly argued mechanism of droplet microexplosions in multi-component droplets is that if the boiling points of the components differ enough, the lower boiling point fuel can be superheated when the droplet temperature is driven up by the higher boiling point of the other components [60-63]. This mechanism could potentially explain the explosive terminations of the control samples shown in Figure 24. However, earlier microexplosive events represented by Figure 23 were absent in all control runs and therefore are not attributed to this multiple-boiling point mechanism. Rather, the addition of the $[AlBrNEt_3]_4$ additive was clearly responsible for the internal droplet gas generation, which caused such disruptions. NASA CEA code used to estimate the flame temperature with and without the molar equivalent of aluminum added to toluene fuel (0.0050 moles Al per mole of toluene) results in less than a 10K increase [99]. This very small increase in heat release cannot account for the observations of disruptive burning.

To further explore the oxidation mechanism of the $[AlBrNEt_3]_4$ additive, temperature-programmed reaction (TPR) experiments of the crystalline solid with $O_2$

and $D_2O$ oxidants were carried out by collaborators Xin Tang and Zachary Hicks in the research group of Dr. Kit Bowen at Johns Hopkins University. Since the oxygen concentrations on the fuel side of the spherical diffusion flame are very small, the water by-product of the tol:$Et_2O$ solvent combustion process is thought to diffuse from the flame to the droplet, reacting with the $[AlBrNEt_3]_4$ cluster to generate HBr and Al-O. The control experiments showed that microexplosive gas eruptions were not a result of boiling solvent of liberated triethylamine ligand from the cluster.

TPR experiments were designed to probe the reaction chemistry of the $[AlBrNEt_3]_4$ with oxygen and water by evaluating the evolved gases and solid residues. As a control, crystalline $[AlBrNEt_3]_4$ was first studied by heating the sample in vacuum from 25 to 110 °C with a ramp rate of 10 °C/min. Analysis of the evolved gases by mass spectrometry (Hiden HAL/3F PIC quadruple mass spectrometer) shows that the complex begins to decompose at ~50°C to give $NEt_3$(101 amu), and its fragments (58, 86 amu) as the major products. A similar experiment was conducted in which crystalline $[AlBrNEt_3]_4$ was dosed with $1\times10^{-5}$ Torr isotopically labeled $^{18}O_2$ gas while heating by the same schedule described above. The $^{18}O$ isotope was used to avoid overlap with other possible products from the reaction. The resulting gases (Figure 27 (a) and (b)) are virtually identical to the in-vacuo control TPR experiment showing only $NEt_3$ and its decomposition fragments. XPS analysis of the resulting white residue showed the presence of Br and Al (III), presumably $Al_2O_3$. The TPR of the $[AlBrNEt_3]_4$ solid was repeated a third time, dosing instead with $1.0 \times 10^{-4}$ Torr $D_2O$ prior to heating to investigate possible reactions induced by the presence of water in the droplets. The

resultant spectra show that the major product is still the labile $NEt_3$ consistent with the previous two experiments with a slightly lower onset temperature (Figure 28 (a)), but closer examination of 75-84 amu mass spectrum region reveals the production of $D^{79}Br$ and $D^{81}Br$ at ~50°C (Figure 28 (b)). The presence of $D^{79}Br$ and $D^{81}Br$ from the $D_2O$ exposed sample compared to the non-exposed sample indicates $[AlBrNEt_3]_4$ undergoes a hydrolysis process to generate gaseous DBr while the slightly decreased onset temperature suggests this pathway is kinetically favorable relative to oxidation by $O_2$ species.

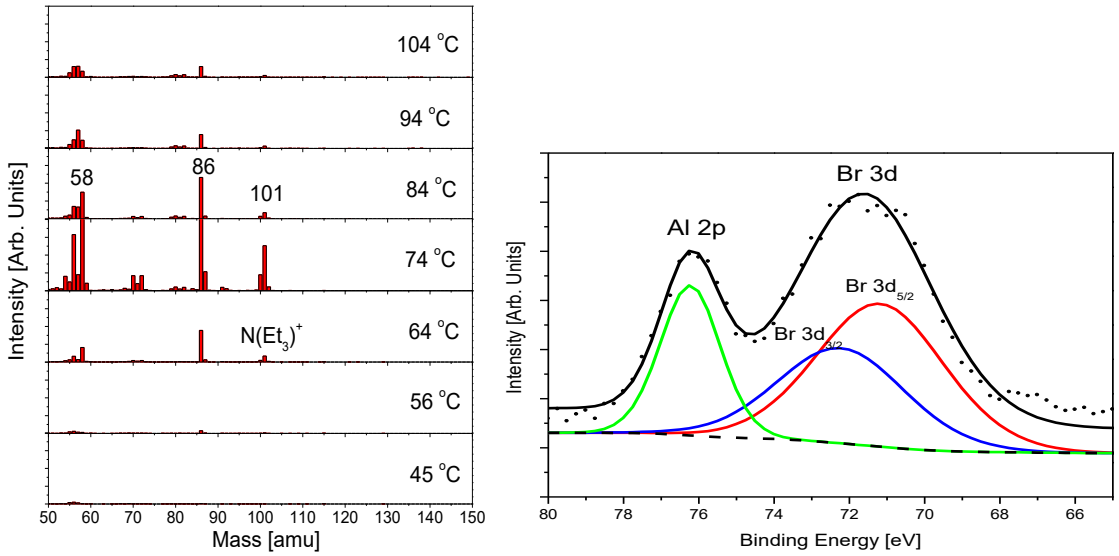


*Figure 27: (A) TPR spectra of reaction of $[AlBrNEt_3]_4$ with $^{18}O_2$ @ 1 x $10^{-5}$ Torr. peaks match $NEt_3$ and its known fragmentation pattern (Note: The intensity of 58, 86 amu at 74 °C are out of scale) (B) XPS Spectra of sample after the reaction showing Al and Br remaining.*

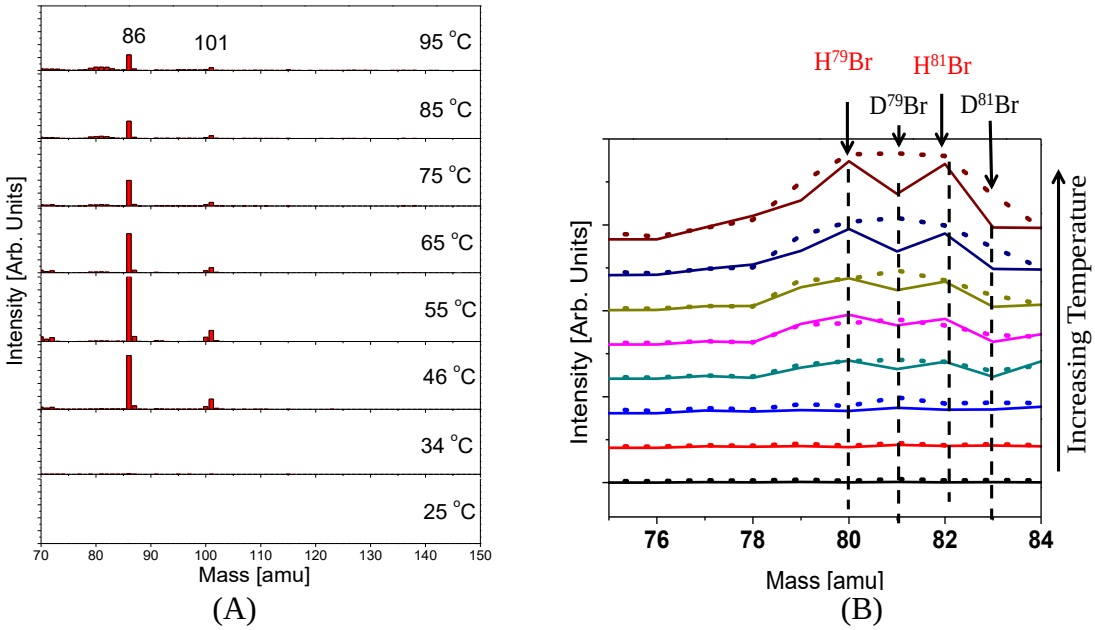


*Figure 28: (A) Temperature Programmed Reaction Spectra of $[AlBrNEt_3]_4$ exposed to $D_2O$ at 1.0 x $10^{-4}$ Torr for 1 hour. The chamber was the evacuated to 1 x $10^{-7}$ Torr and the TPR was subsequently taken. (B) Comparison of TPR Spectra of $[AlBrNEt_3]_4$ exposed to $D_2O$ (dotted line) and not exposed to $D_2O$ (solid line) in the mass 75-84 amu region.*

Breaking down these observations, the following simplified step-by-step mechanism is proposed with the help of Dr. Samantha DeCarlo and Dr. Bryan Eichhorn, described schematically in Figure 29. Early in the droplet lifetime, the $[AlBrNEt_3]_4$ concentration is considered homogenous (Figure 29 (i)). In terms of elementary reactions, it is difficult to parse the order at which reaction steps are occurring but in a global sense, combustion of the solvent yields $CO_2$ and $H_2O$ in the flame region. Upon diffusion of combustion products from the flame to the droplet, reaction of $H_2O$ with $[AlBrNEt_3]_4$, as indicated by the TPR experiments, will lead to the production of HBr gas. Early in the droplet lifetime when it is largely homogenous, $H_2O$ reaction with $[AlBrNEt_3]_4$ will occur close to the droplet surface, nearest the

source of $H_2O$ in the flame. However, liberation of HBr gas will promote convective mixing near the droplet surface and increase transport of water further into the droplet yielding HBr gas within the liquid, exemplified by the mixing evident upon gas generation in Figure 30. This enhanced mixing should promote faster $[AlBrNEt_3]_4$ decomposition and formation of HBr. At high enough concentrations, the gas nucleates to bubbles and results in the microexplosions observed (Figures 23, 29 (ii and iii), and 30). These gas release events transport more fuel to the flame region and affect the burning rate (Figure 29 (iii)). The droplet then returns to a deflated droplet form until the next visible event (Figure 29 (iv)). This process is repeated throughout the remainder of the droplet lifetime, until the solvent flame extinguishes where the major product left is alumina (according to XPS).

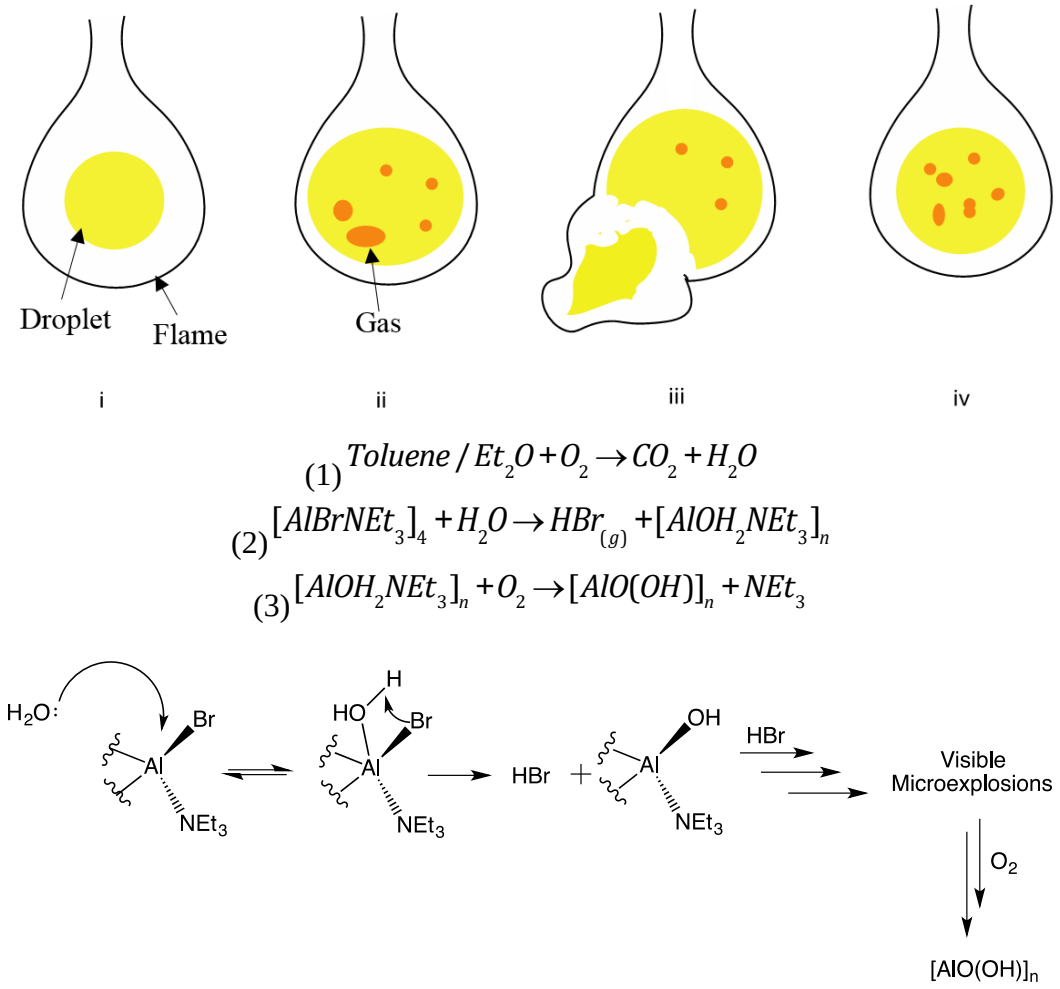


*Figure 29: Proposed reaction of $[AlBrNEt_3]_4$ dissolved in a mixture of toluene/$Et_2O$ exposed to an $O_2$ atmosphere and burned (i). The combustion of the solvents leads to the formation of $CO_2$(g) and $H_2O$(g) (1). The $H_2O$ contributes the oxidation of Al1+, the formation of HBr(g), and the expulsion of $NEt_3$(l) (ii)(2) leading to visible microexplosions (iii). This gas liberation and expulsion repeats (iv) and leads to increased mixing of the droplet and its contents with the oxidizer-rich surroundings leading to the formation of $[AlO(OH)]_n$ products (3).*

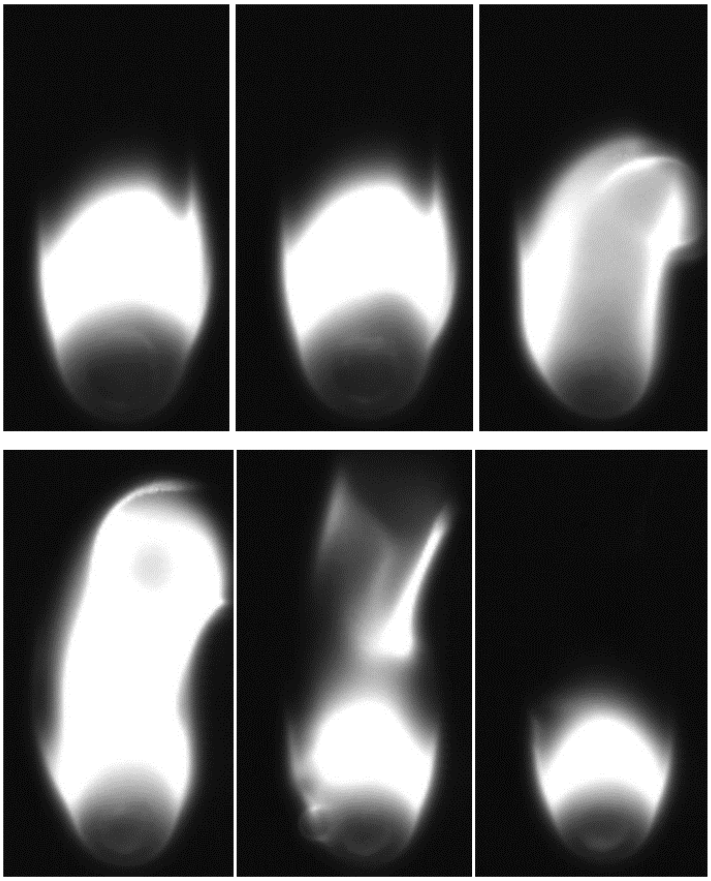

*Figure 30: Gas generation in AlBr-laden droplet. Top Row: Inflated droplet releasing gas. Bottom Row: Deflated droplet after gas release with flame perturbation. Image period = 234μs.*

The mechanism proposed is supported by the fewer incidences of visible microexplosions in less concentrated samples, wherein less $[AlBrNEt_3]_4$ is available for reaction and HBr liberation, and the observation of microexplosions only in the last ~ 30% of the droplet burn time. Since gas phase diffusion of water to the droplet will occur much faster than its condensed phase diffusion within the droplet, the timescale of this process can be conservatively estimated by considering the rate of diffusion of water from the edge to the inner region of the droplet in the absence of convective mixing. Assuming that a 0.1mm diameter sphere of HBr gas is ample to produce the

first microexplosion, $1.8x10^{-11}$ moles of water are required to diffuse into the droplet and react with $[AlBrNEt_3]_4$. Considering a static 0.5mm diameter droplet saturated with 0.33% water at its surface with a binary diffusion coefficient of $10^{-5}$ $cm^2/s$, the mean Fickian diffusion flux of water would be ~6 $x10^{-4}$ $mol/m^2$-s assuming a linear concentration gradient within the droplet. This then yields an approximate transport time for a microexplosion of ~150 ms, and presumably is a conservative estimate since convection effects are neglected. Considering a total burn time is ~250 ms, this supports the proposed mechanism wherein initial HBr liberation is produced by water diffusing within the droplet. In summary, the production of HBr causes bubble nucleation and droplet deformation to allow for increased mixing of the droplets with the oxidizing environment and thus increased reactant transport and burning rate.

### *3.4 Conclusions*

The mechanism of combustion enhancement of a soluble molecular $[AlBrNEt_3]_4$ cluster additive in liquid fuel has been studied in single droplet combustion experiments. The $[AlBrNEt_3]_4$ additive increases the burning rate constant of a toluene-diethyl ether fuel mixture by 20% in a room temperature oxygen environment with 39 mM of active aluminum additive (approximately 0.16 wt %). The primary mechanism for enhancement seems to be liquid-phase internal-droplet gas generation leading to disruptive burning. Similar experiments with nanoaluminum showed no discernable enhancement at these low concentrations. While the $[AlBrNEt_3]_4$ additive did not contain enough Al at these concentrations to appreciably increase the calorific value of the fuel, this study shows that the soluble architecture of

the Al-based additive contributes a novel mechanism to increase the burning rate of hydrocarbon fuels, proving significantly more reactivity than its particulate nanoaluminum counterpart.

*Acknowledgements*

Special thanks to the collaborators and co-authors of the work in this chapter. The $[AlBrNEt_3]_4$ material was synthesized and provided by Dr. Samantha DeCarlo and Dr. Bryan Eichhorn, both of whom cooperated on the proposed mechanism of the additive discussed. TPR experiments were executed by Xin Tang and Zachary Hicks in the research group of Dr. Kit Bowen at Johns Hopkins University.

# Chapter 4: Effects of nitrocellulose co-additive and mesoparticle composite structure on the combustion of nanoaluminum-laden kerosene droplets[2]

*Summary*

Addition of metal and metal oxide nanoparticles to hydrocarbon fuels has shown the ability to increase the volumetric energy density, decrease ignition delay, increase heat of combustion, and catalyze fuel decomposition in recent research. However, energetic metal nanoparticles are prone to aggregation, which occurs at an increased rate near the regressing surface of a burning liquid droplet where local concentrations increase and can form a transport-inhibiting shell, ultimately decreasing the droplet burning rate. Alternatively, gas ejections from the droplet can disrupt shell formation and transport nanoparticles from the droplet to the flame zone. The work in this chapter quantifies up to a 12.1% decrease in the burning rate constant of Kerosene droplets when 6.1 wt% nanoaluminum (nAl) particles are added (the maximum stable loading) with a hydrocarbon-based surfactant in a free-falling single droplet combustion experiment. Addition of nitrocellulose (NC) particles to the nanofuel diminishes or fully counteracts the burning rate decreases and provides a means of

[2] The results presented in this chapter have been previously published and are reprinted with permission from P.M. Guerieri, J.B. DeLisio, M.R. Zachariah, Nanoaluminum/Nitrocellulose microparticle additive for burn enhancement of liquid fuels, Combustion and Flame 176 (2017) 220-228. Copyright 2016 Elsevier Inc. on behalf of The Combustion Institute.

tuning the burning rate constant higher than that of pure Kerosene (maximum 13.8% increase over control with 2.3 wt% nAl and 0.6 wt% NC added). To reach stable nanofuels at higher particle loadings up to 15.0 wt% solid additives, nAl and NC were electrosprayed into composite mesoparticles (MP) before suspending with surfactant in Kerosene. These MP-based nanofuels boast increased dispersibility and additive loadings and thus higher achievable burning rates (maximum 26.5% increase over control) than physically mixed analogs. A mechanism is proposed in which droplet disruptions influenced by NC addition include cyclical inflations, during which the liquid gasification rate increases, e.g. by expanding the outer surface area of the droplet.

### *4.1 Introduction*

As described and motivated in Section 1.3.4, droplet disruptions are particularly capable of affecting burning rates by counteracting the formation of particle agglomerates, increasing physical mixing within the droplet (promoting species and thermal transport), deforming the droplet thereby changing the gas-liquid interfacial area, and causing secondary atomization of smaller droplets [59]. While dominant agglomeration depresses burning rates, physical droplet disruptions enhance it and this interplay of mechanisms is a possible reason for the variety of burning rate effects observed in literature with NP addition. Between these two, the dominating process can be dictated, and thus burning rate influenced, by modifying the additive to affect either droplet disruptions or particle agglomeration, namely by including a gas generating additive and/or modifying the particle morphology.

The work of this chapter uses the updated design of the droplet experiment apparatus to investigate the effects of chemically stabilized nAl-based additives to kerosene fuel with and without a gas-generating polymeric co-additive, nitrocellulose (NC), in a drop-tower configuration designed to estimate combustion rates in the presence of disruptive burning. Physical mixtures of the co-additives are compared with a composite mesoparticle additive of nAl electrosprayed in a NC matrix. Suspension stability is assessed and disruptive combustion is characterized by observing and measuring shadowgraphs of burning droplets suspended on a Silicon Carbide (SiC) monofilament.

## *4.2 Experimental*

### 4.2.1 Nanofuel Preparation

Nanoaluminum particles were used as-received from Novacentrix, Inc. (80% active Al with 2-5nm oxide shell; Figure 31(A)) for nAl nanofuel preparations and to assemble nAl-NC mesoparticles (MPs). The MPs, as well as NC particles for nAl-NC physical mixtures, were assembled by electrospray synthesis described by Wang et al [14]. The MP precursor consisted of 400 mg of nAl and NC solids (ranging from 5% to 20% NC) in 4 mL of 3:1 ethanol:diethyl ether while the NC precursor was mixed by dissolving 200 mg of NC solids (dried from collodion solutions of 4–8 wt.% in ethanol/diethyl ether purchased from Fluka Corp.) in 2mL of acetone. All precursors were agitated in a sonication bath for 1 h, and magnetically stirred for 24 h before electrospraying. Consistent with the electrospray procedure of Wang et al., precursors

were fed at 4 mL/h through a 0.43 mm ID stainless steel probe needle by a syringe pump. The needle was charged to (+) 10 kV and aluminum foil substrate to (-) 10kV at a distance of 10cm from the probe needle. SEM of particles produced are shown in Figure 31(B) and 1(C).

A surfactant was required to chemically stabilize the additive particles in the nanofuels. Trioctylphosphine oxide (TOPO), consisting of two long carbon chains (for compatibility with non-polar hydrocarbons) joined by a polar group (to combine with metal oxide on NP surfaces) was proposed for this purpose by E et al. to stabilize boron in JP-10 [92]. TOPO was added to all nanofuels in this study (2:1 TOPO:nAl by mass unless stated otherwise) and facilitated stable nAl suspensions up to 6.1 wt% and nAl/NC MP suspensions up to 15.0 wt%.

Nanofuels were assembled by adding specified solid loadings (either nAl, NC, nAl and NC, or nAl/NC MPs) to 0.5 mL of premixed TOPO in Kerosene (reagent grade from Sigma-Aldrich Co. LLC.) solutions. The same TOPO/Kerosene solutions were used as control fuels without additives for each loading. To promote suspension, nanofuel mixtures were agitated in a sonication bath for 1 h and magnetically stirred continuously until use (at least 24 h). 1 minute of sonication also preceded all combustion experiments. MP nanofuels, which showed generally higher suspension stability than nAl or NC particle nanofuels and therefore required less agitation for suspension, were only sonicated for 5 min before stirring to prevent MP damage.

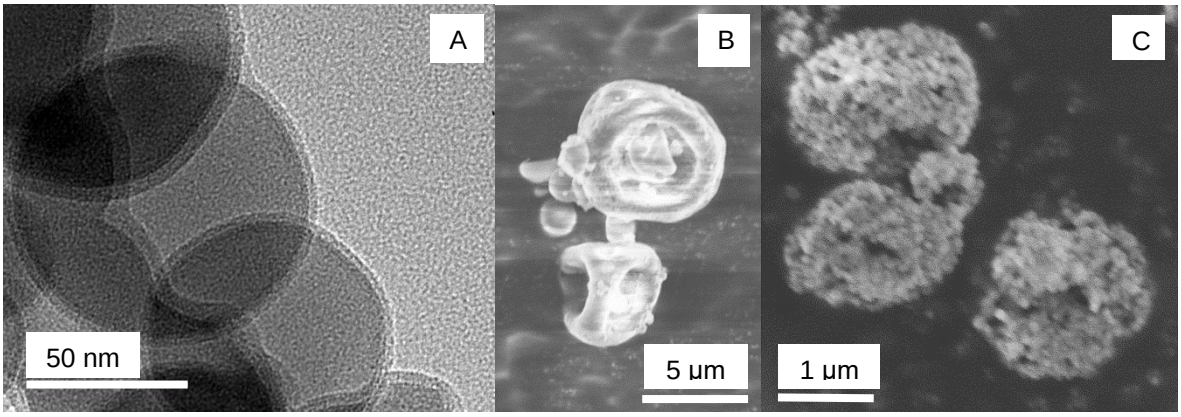


*Figure 31: (A) Nanoaluminum particulate additive TEM showing 2-5nm oxide shell. (B) SEM of electrosprayed NC particles ranging from 1-6 µm in diameter. (C) nAl/20%NC Mesoparticle SEM showing 1-2 µm diameter assemblies of ~80 nm nAl primary particles.*

### 4.2.2 Combustion Characterization

Burning rate constants are evaluated using a drop tower configuration described in Section 2.1.2 in which a ~0.6 mm diameter fuel droplet is generated and released to fall past two counter-flow methane pilots and through 20 vertical inches of pure oxygen at room temperature. This method avoids interference of any suspending filaments and the nonphysical assumption that the droplet volume indicates the mass of unburnt fuel remaining, which is otherwise required for classical burning rate measurements (using the slope of $D^2$ versus time). One high speed camera records a magnified shadowgraph (generated with an expanded HeNe laser and lens train) of the droplets passing the pilots to measure the initial droplet size (4-5 frames per droplet) while a second synchronized camera records the droplet flame falling through the tower. MATLAB image processing is used to measure the cross-sectional pixel area of droplets passing the igniters, calculate the equivalent circular diameter, and evaluate the eccentricity of the droplet. Calibrating for camera magnification with the known-diameter igniter

tubes and eliminating frames of deformed droplets with eccentricity greater than 0.6 (where 0 is a circle and 1 in a line), each initial droplet diameter is calculated from the average of at least 3 admissible frames collected. The uncertainty of this average is estimated to be ±0.01mm (an improvement upon method of Chapter 3 with higher camera magnification). MATLAB image processing also detects the first light and last light of each droplet flame falling through the tower to assess burning time with an estimated uncertainty of ±3ms for the most faintly emitting samples (pure kerosene). The burning time and initial droplet diameter are used to estimate a burning rate constant by assuming all initial reactive material has burned upon flame extinction (i.e. $D_{Extinction}=0$) using Equation 25 with a measurement uncertainty of ±0.02 $mm^2/s$. This assumption has been supported by TGA and XRD analyses of solid residues collected from falling droplets in Chapter 3 and TGA of oxidized nAl residues from suspended droplet experiments discussed later. By averaging K estimates of approximately 8-12 droplets per trial, K is evaluated for each sample with an estimated experimental uncertainty of ±0.1 $mm^2/s$ according to Equation 25.

To further assess droplet disruptions during combustion, an alternative configuration employs a horizontal SiC monofilament (0.1mm diameter; Goodfellow USA) to suspend a droplet in the center of the tower by pipetting a drop manually onto the filament. A methane pilot is then swept past the droplet for ignition and the same camera/laser shadowgraph setup described previously records a magnified image of the droplet combusting in place. The tower atmosphere used in suspended droplet experiments is air instead of oxygen to prevent the filament from igniting. MATLAB

is used to measure the cross-sectional area of the droplet (with the filament subtracted) every two frames (334 μs), from which an equivalent spherical droplet diameter can be estimated. The initial droplet diameter is measured over at least 100 frames prior ignition and an ignition time is estimated using the inflection point of the initial increase in droplet diameter which occurs upon heating. The droplet diameter evolution over time can then be plotted to visualize the droplet disruptions over its entire combustion lifetime. While insight into the disruptive nature of each formulation is provided by this method to facilitate comparisons, quantitative burning rates are obscured by gas generation and solid combustion products within the droplets and are incomparable to the drop tower configuration due to the oxidizer change and conductive filament interference. Residue remaining on the filament after each sample burns is transferred to carbon tape on an SEM substrate for analysis and the filament is cleaned with Acetone before the next trial.

## *4.3 Results and Discussion*

### 4.3.1 Suspension Stability

Particle loading ranges for all samples were maximized based on their propensity to pump through the droplet generation capillary reliably. nAl particle suspensions clogged the delivery needle at loadings >6.1 wt% and NC suspensions at >2.3 wt%. MPs suspensions however can be mixed up to 15.0 wt% particles for MPs composed of 80 wt% nAl and 20 wt% NC ("nAl/20%NC MPs") before clogging begins. In order to electrospray particles instead of fibers, the binder content of the MP

composite is limited to 20% or less NC polymer and thus four MP types were used (nAl/5wt%NC, nAl/10wt%NC, nAl/15wt%NC, and nAl/20wt%NC). nAl+NC physical mixture suspensions were chosen to match the constituent loadings of the MP samples up to 6.0 wt% nAl NPs + 0.7 wt% NC particles ("6.7wt% nAl+10%NC PM"), with higher loadings causing clogs. Based on these limits, Table 4 summarizes the samples formulated and tested and the theoretical change in volume and mass-based energy densities (enthalpies of combustion with oxygen per volume or mass) the additives would cause in dodecane without TOPO surfactant considered.

*Table 4: Nanofuel Suspension Loading Ranges*

| Sample | wt% nAl | wt% NC | % Change in Energy Density | |
|---|---|---|---|---|
| | | | by Volume | by Mass |
| nAl NPs | 2.3 to 6.0 | N/A | 1.1 to 3.3 | -0.59 to -1.7 |
| NC NPs | N/A | 0.13 to 1.3 | 0.06 to 1.0 | -0.10 to -1.8 |
| nAl + NC NP Phys Mix | 2.3 to 6.0 | 0.13 to 0.70 | 1.1 to 3.0 | -0.69 to -2.2 |
| nAl/5%NC MPs | 2.3 to 12.4 | 0.13 to 0.65 | 1.1 to 8.1 | -0.69 to -4.6 |
| nAl/10%NC MPs | 2.3 to 12.4 | 0.23 to 1.4 | 1.0 to 7.6 | -0.79 to -5.3 |
| nAl/15%NC MPs | 2.3 to 12.4 | 0.40 to 2.1 | 0.94 to 7.0 | -0.90 to -6.0 |
| nAl/20%NC MPs | 2.3 to 12.4 | 0.57 to 3.0 | 0.86 to 6.4 | -1.0 to -6.9 |

Long term stability of the nanofuels was assessed qualitatively by allowing the suspensions to gravitationally settle for 1 week following combustion testing and visualizing the suspension quality. Representative suspensions of 6.1 wt% nAl, nAl/5%NC MPs, and nAl/20%NC MPs were also sonicated and stirred in kerosene without surfactant before pouring into clean vials and allowing to gravitationally settle for 1 day to illustrate dispersibility without chemical stabilization. With TOPO, all physical mixture nanofuels settled out of suspension within 1 week while MP samples

maintained suspension (photographs available in Appendix A). Without surfactant, nAl failed to suspend at 6.1 wt% with most of the nAl and kerosene gelling during the magnetic stirring and adhering to the mixing vial. The MP samples do suspend but gravitationally settle more without surfactant after 1 day. The presence of NC polymer in the MPs with the nAl is the likely cause of increased dispersibility of MPs relative to nAl with and without TOPO. NC has polar and nonpolar sections but overall has a lower dielectric constant (~6.2-7.5) than the alumina surfaces of nAl (~9.3-11.5). Since kerosene has a low dielectric constant (~1.8-2.8), the NC will disperse better than alumina in kerosene. MPs have more alumina surfaces covered in NC than do nAl particles (with or without NC particles added) and therefore will disperse better than nAl. Adding TOPO surfactant will increase the stability of both nAl physical mixtures and MPs since it has a polar end which is compatible with any exposed Alumina and hydrocarbon chains compatible with the kerosene.

### 4.3.2 Nanofuel Falling Droplet Combustion

Figure 32 depicts time-lapse images of five representative samples combusting in the falling droplet experiment. When applicable, the samples shown include the same mass loading of TOPO surfactant (B-E), nAl (C-E), and NC (D-E). Disturbances in the trace of visible flame radiation are attributed to droplet disruptions during which gas is ejected from the droplet, on occasion carrying condensed phase reactants or causing a fission event, and usually preceded by droplet inflation. Suspended droplet experiments discussed later provide detailed evidence for and analysis of these disruptions. The falling motion of the droplets, deviations of their trajectories from the centerline, and

apparent stochastic disruption events render magnified videography and classical $D^2$ burning rate analysis on the falling droplets unviable.

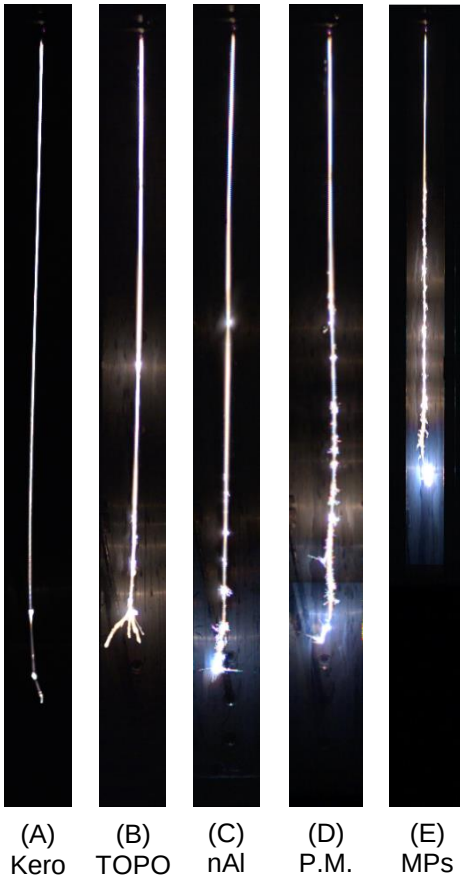


*Figure 32: Time-lapse images of falling, combusting Kerosene droplets with 120mg/mL TOPO surfactant, unless noted otherwise, and various nanoparticle additives. (A) Kerosene Only (no TOPO). (B) 120 mg/mL TOPO Control. (C) 6.1 wt% nAl. (D) 6.7 wt% nAl+10%NC Physical Mixture. (E) 6.7 wt% nAl/10%NC Mesoparticles.*

Any nAl added combusts predominantly in the final stage of combustion, when little to no liquid fuel remains (indicated by obvious color temperature increase in Figure 32(C)-(E) characteristic of Al combustion). While slurry fuels behave similarly [20], their slow-burning micron-particles comprise a significantly larger fraction of the overall burning time compared to the rapid combustion of nAl in liquid fuels. When

disruptions liberate secondary small droplets, minute amounts of nAl can also combust near their termination, before the final stages of the parent droplet combustion. Presumably nAl could escape unburned from a system without ample energy to ignite the solids; however, TGA data confirms that residues collected from suspended droplet experiments contain little to no reactive aluminum suggesting near-complete nAl combustion here in kerosene-air. Flame temperatures of the kerosene-oxygen system in falling droplet trials are even higher than those of kerosene-air which together with evident emission characteristic of nAl in the color videos suggests thorough combustion of nAl in the fuels.

### 4.3.3 Burning Rate Measurements

Because the TOPO surfactant concentrations vary among the samples tested with the nAl additive concentration, the surfactant effect on the burning rates must be assessed so additive effects can be normalized with respect to TOPO control data. Addition of the surfactant increases the burning rate linearly with an R-squared fit value of 0.955 (plot of absolute burning rates versus surfactant concentration with TOPO control trendline shown in Figure 33). Time-lapse images of falling droplet trials show increased visible flame radiation and onset of a characteristic late explosion which can disperse small secondary droplets with increasing TOPO concentrations. All subsequent burning rates are represented as percent change relative to the burning rate of the corresponding TOPO solution measured on the same day to eliminate environmental variations. Considering the estimated experimental uncertainty of the

burning rate constant, the maximum uncertainty of the percent change in burning rate is estimated to be ±8%.

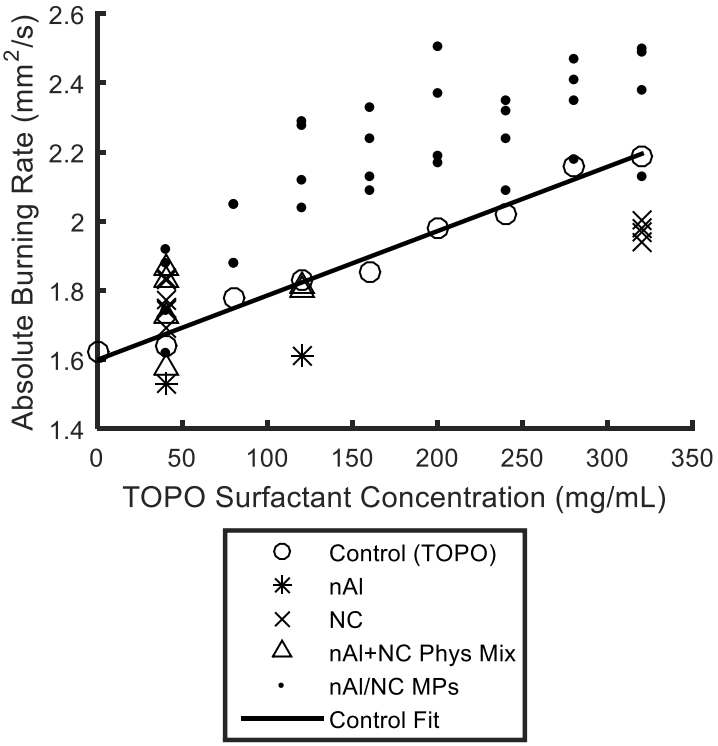


*Figure 33: Absolute Burning Rate Constants versus Control Surfactant Concentration*

Nitrocellulose addition is of interest due to its preexisting role as a composite particle binder and its expected role as a gas generating additive to incite droplet disruptions for burning rate enhancement. To investigate its influence without nAl present, NC is assembled into microparticles and added to kerosene fuels with two TOPO concentrations (the minimum and maximum surfactant loadings used in the study). Flame trace observations depict little to no significant qualitative effects of added NC on visible flame radiation or apparent droplet disruptions relative to

respective TOPO solution controls (representative time-lapse images available in Appendix A). Resultant burning rate effects are plotted in Figure 34 as functions of NC particle loading. At low surfactant concentration, NC addition causes burning rate enhancement up to a critical loading (12.9% increase at 0.5 wt% NC) beyond which the enhancement decreases. However, at high surfactant loadings, the NC enhancement is masked by the burning rate increase of the TOPO. 320 mg/mL TOPO causes a 33.5% increase in burning rate relative to 40 mg/mL TOPO. If the mechanisms of the NC and TOPO additions without nAl were mutually exclusive, thereby counteracting each other, a decrease much greater than the observed 5% would be expected with NC addition to 320 mg/mL TOPO. This shows that instead, the mechanisms of NC and TOPO added without nAl to kerosene are likely similar, such that relatively small NC addition to an already highly TOPO-laden sample simply incites no further enhancement. Despite this, NC added to kerosene can clearly increase the burning rate and even provide means of tuning with NC concentration.

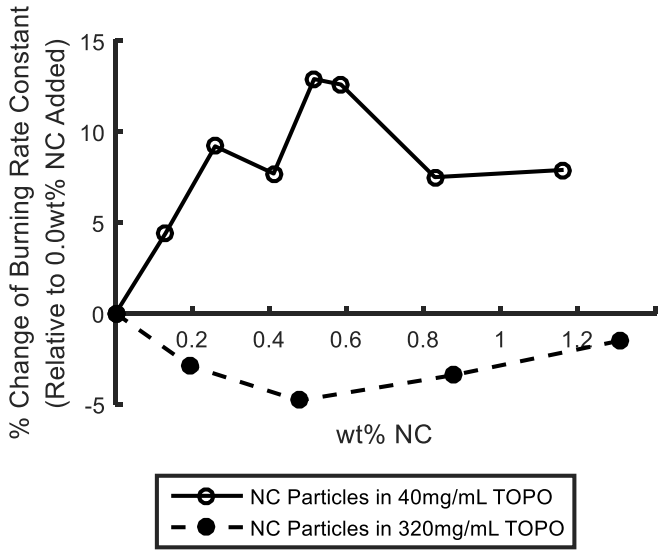


*Figure 34: Effect of Nitrocellulose Particles on Droplet Burning Rates*

nAl was added to the fuel in two forms: as-received NPs and within mesoparticle composite assemblies with NC. The effects of these configurations can be directly compared up to the maximum loading of nAl NPs (6.1 wt%). To do so, physical mixtures of nAl + NC particles and MPs of equal constituent loadings were formulated and their burning rate effects are plotted in Figure 35 as functions of each nanofuel's NC concentration. The two y-intercepts denote as-received nAl without NC added in all cases (since MPs cannot be assembled without a polymeric binder). While nAl addition alone decreases the burning rate with increasing concentration, this decrease can be counteracted by adding NC to increase the burning rate. The net effect is a nanofuel that burns with the same or higher burning rate as the control with the added theoretical energy density of the nAl component. At low loadings (2.3 wt% nAl), the physical mixture and MPs behave the same showing no benefit of one architecture over the other. At higher loadings however, the MPs follow the same trend as low

loadings while the burning rate of the physical mixtures are depressed by the increased nAl addition. The MP architecture with 6 wt% nAl also facilitates higher stable NC loadings (>0.7 wt%). In the analogous 6 wt% nAl physical mixtures, NC loadings >0.7 wt% cause sample agglomeration and needle clogging. Consistent with its effect without nAl, NC provides a means of tuning the burning rate and compensating for decreases caused by nAl addition. Assembly into MPs expands the range of tuning available.

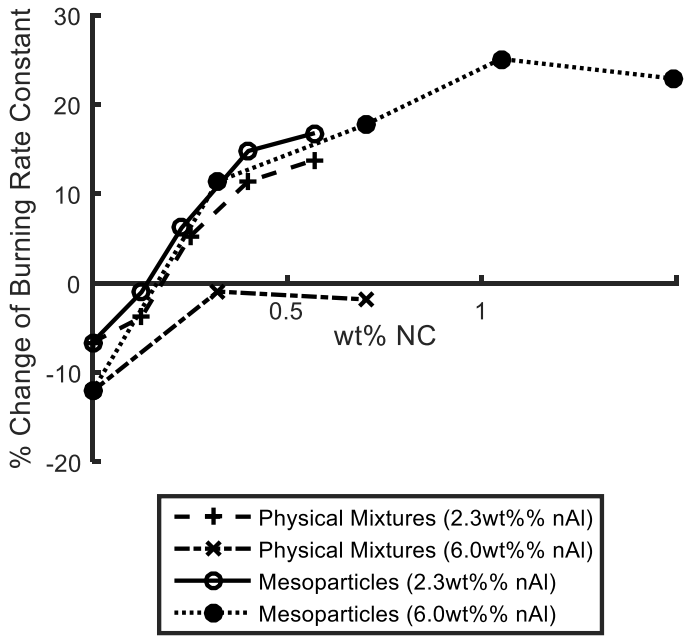


*Figure 35: Burning Rate Effects of nAl/NC Physical Mixture and Mesoparticle Additives. Y-intercepts are nAl particle suspensions in all cases. Burning rate % changes are relative to the TOPO surfactant-only control solution for each data point (2:1 TOPO:nAl by mass).*

Recalling that assembling the NC and nAl into MPs maintains suspension stability at higher loadings than physical mixtures, the burning rate enhancement of such higher loadings are shown in Figure 36 plotted versus total particle loading and

organized by the nAl:NC ratio (i.e. MP type). Note that in all cases, the absolute burning rates increase with particle loading when the TOPO effect is considered. When normalizing by this effect, it is evident that (similar to NC particle addition) MPs cause burning rate increases up to critical loadings beyond which the burning rate enhancements diminish. Higher NC content in most cases also increases the enhancement as expected; however, 15% and 20% NC burning rates are similar indicating minimal marginal benefit of increasing the NC content beyond 15%. In all but two data points, addition of nAl/NC MPs increased the burning rate to some extent and since they can be used to reach higher loadings, a greater maximum burning rate enhancement over controls is also observed compared to physical mixtures (MP maximum 26.5% burning rate increase; physical mixtures maximum 13.8% burning rate increase). NC addition decreases the net volumetric energy density of the fuel, an effect opposite to that observed with nAl addition. Figure 36 quantifies this effect theoretically over the range of MP loadings studied based on calculating the change in enthalpy of combustion per unit volume that results from adding the corresponding quantities of Al and NC to dodecane. Added NC content can increase the burn rate of the composite particles while the nAl content increases the theoretical enthalpy of combustion per volume relative to the liquid fuel; however, since NC has a lower volumetric energy density than that of kerosene, this increase in burn rate incurs a penalty in the resultant energy density increase as illustrated in Figure 36. Both MP additive loading and NC percentage in the MPs provide a fuel designer with means of tuning the burning rate and energy density increases of the composite fuel.

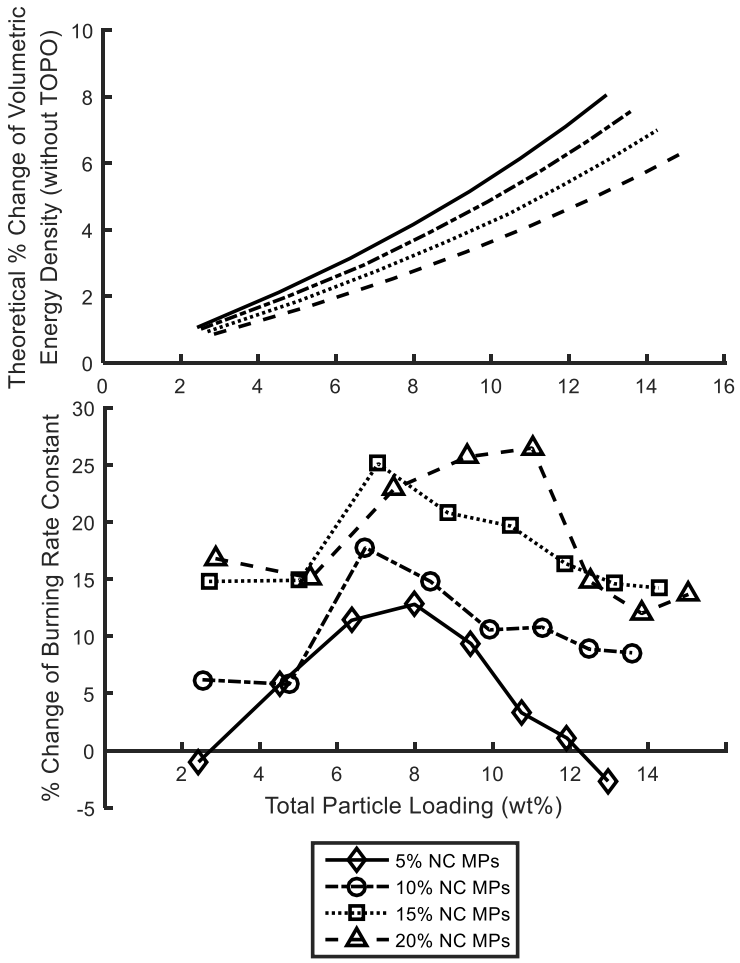


*Figure 36: (Top) Theoretical increase in volumetric energy density of kerosene fuel as functions of composite mesoparticle additive loading based on enthalpy of combustion with oxygen per volume of nanofuel. (Bottom) Effect of composite mesoparticle loadings on droplet burning rates. Burning rate % changes are relative to the TOPO surfactant-only control solution for each data point (2:1 TOPO:nAl by mass).*

### 4.3.4 Droplet Disruption Analysis

Direct observation of burning clearly shows that a classical $D^2$-type analysis is not applicable since significant fission events during burning are observed. Figure 37 depicts a representative plot of droplet size evolution during its burning on a horizontal SiC filament in air with time-lapse images of falling droplets with and without MP

additive (plots and time-lapse images for all thirteen representative samples tested as suspended droplets are available in the Appendix A). The filament is not completely insulating (with slight preferential boiling observed near the droplet-filament interface) and air is required rather than oxygen to prevent combustion of the filament. Gas generated during disruptions and solid products in the droplets also obscure any burning rate measurements by decoupling the cross-sectional area observed from the mass of unreacted fuel remaining [59, 102]. As such, the stationary experiments are not quantitatively equivalent to the falling droplet experiments but facilitate comparison of the disruptions caused by various additives. Appendix A includes suspended droplet data next to falling droplet time-lapse images for various samples illustrating that qualitatively, the disruptive natures of the fuels are approximately preserved between the two experiments and thus the suspended droplet experiments can provide insight into disruption effects.

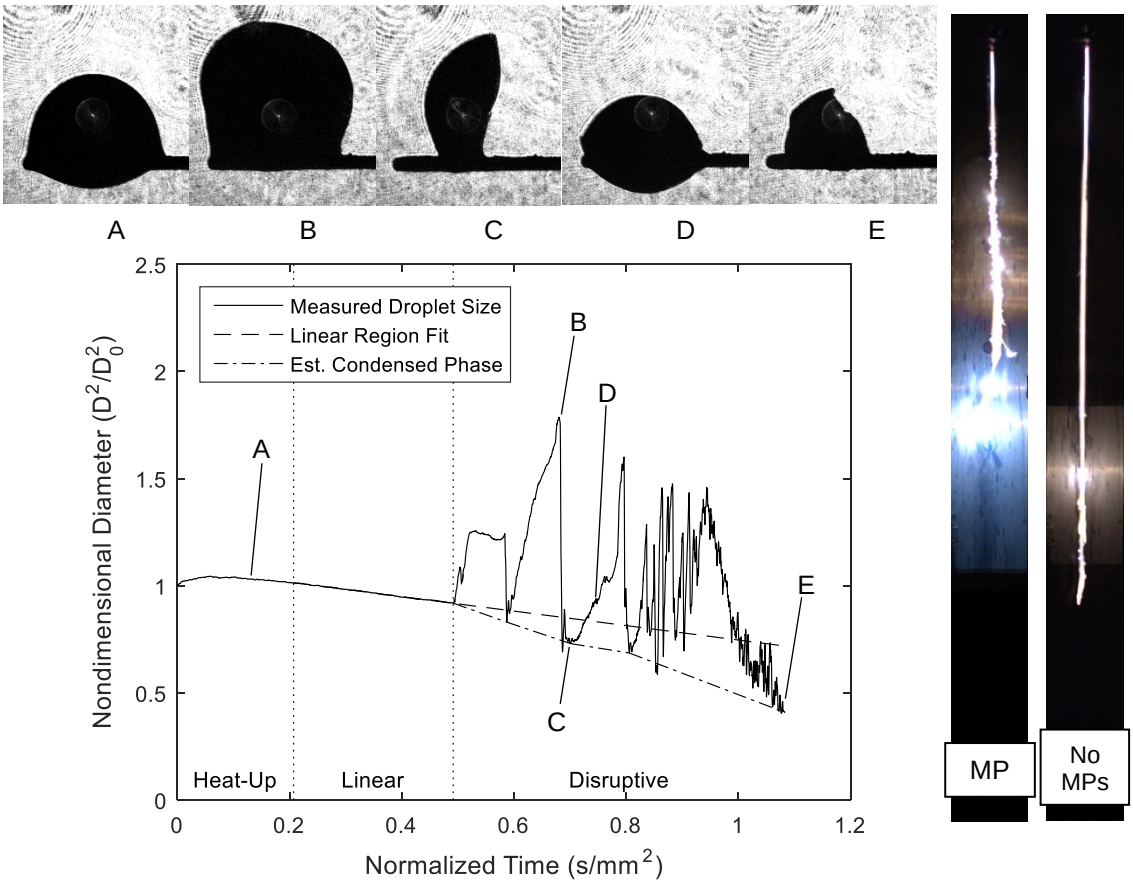


*Figure 37: 10.4 wt% nAl/15%NC MPs in 200mg/mL TOPO/Kerosene. (LEFT) Representative annotated data of suspended droplet size evolution during combustion on a SiC filament in air. (RIGHT) Time-lapse images of 200mg/mL TOPO/Kerosene with and without MPs added. Plots for all thirteen samples tested as suspended droplets with representative falling droplet time-lapse images available in Appendix A.*

Three distinct combustion regimes are evident in the stationary droplet evolution plots: an initial non-linear heat up region during which flame energy heats the droplet to its boiling point (expanding it); a subsequent linear combustion region akin to classical droplet combustion; and ultimate disruptive regions characterized by deviations from classical (linear) droplet burning by repeated inflations, deflations, and shape perturbations from momentum transfer upon gas or condensed phase ejections. Shorter times (normalized by square of initial droplet diameter) to the first of these

disruptive regions in suspended droplet experiments roughly correlate ($R^2$=0.829) with faster burning rates measured in falling droplet experiments (plotted in Appendix A). The surface area increase due to inflation can be estimated from this data during the disruptive regimes. Disruptive regions are subdivided by local minimums which roughly represent the droplet with little to no internal gas. The approximate volume of condensed phases in the droplet can therefore be interpolated between these two points for each sub-region (shown as dash-dot lines in Figure 37) and by comparison with the actual volume measured, the difference provides an estimate of droplet inflation volume that results from internal gases. Assuming constant values of vapor diffusion coefficients, vapor mass fractions at the droplet, and vapor mass fractions in the ambient environment, the rate of phase change per surface area at the droplet is inversely proportional to the droplet diameter. By fitting the proportionality constant to data obtained for pure kerosene which is devoid of any disruptions ($\alpha$ = 0.963), the added volume gasified due to increases in droplet surface area by inflations over the droplet lifetime is estimated and normalized by initial droplet volumes (expressed as volume percent) and residue volumes (final solid product volumes measured are assumed to form within the droplet linearly over their lifetimes and are subtracted) and given by the equation below, plotted in Appendix A.

$$\left(\frac{\Delta V}{V_0}\right)_{\text{Inflation}} = \alpha \int_0^{\frac{t}{D_0^2}} \left(\frac{D_{\text{Inflated}}}{D_0}\right) - \left(\frac{D_{\text{Deflated}}}{D_0}\right) dt \tag{30}$$

By assuming that a hypothetical droplet burning in the tower without this enhancement will do so at the rate observed for pure kerosene droplets in falling droplet

experiments ($\overline{K}_{\text{Kerosene}} = 1.62$), the effect of this added volume loss by increased surface gasification from inflations on the burning rate constant can be estimated theoretically by the equation below and compared with the actual burning rate constants observed in Figure 38.

$$K_{\text{Inflation}} = \frac{\overline{K}_{\text{Kerosene}}}{1-\left(\frac{\Delta V}{V_0}\right)^{1.5}_{\text{Inflation}}} \tag{31}$$

The linear correlation observed suggests that inflation is a strong mechanism by which these disruptive samples affect overall burning rates. The theoretical burning rate constants that would result from this effect are similar to the actual burning rate constants observed, proving that the magnitude of this mechanism can be large enough to account for much of the enhancements observed. However, since the proportionality constant is less than one (exact agreement), inflations also likely enhance the burning rate by mechanisms other than outer droplet surface area increase.

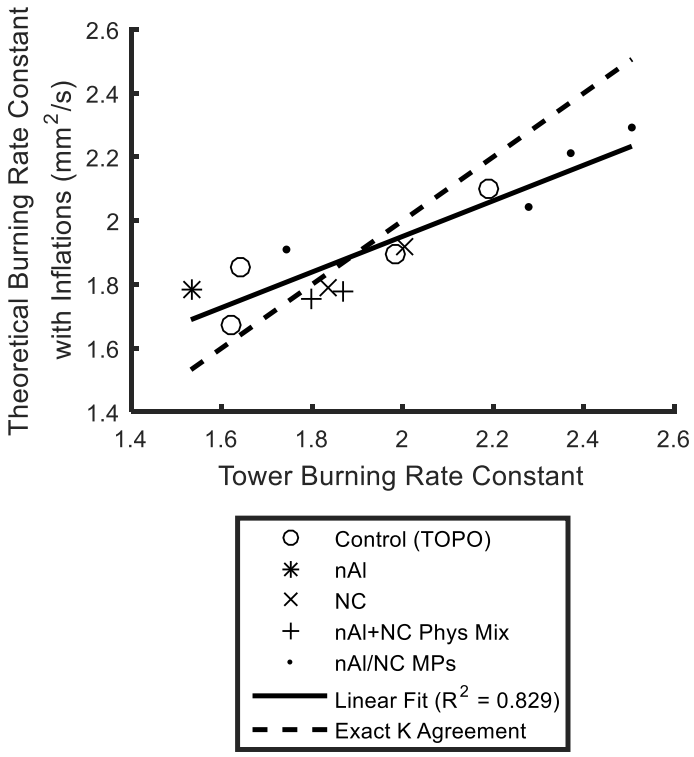


*Figure 38: Theoretical burning rate constants based on enhancement of surface gasification caused by droplet inflations in suspended droplet experiments versus burning rate constants measured in falling droplet experiments.*

### 4.3.4 Proposed Additive Mechanisms

Based on evidence from the suspended droplet experiments, droplet inflations are thought to be directly related to burning rate increasing mechanisms of disruptively burning droplets. A schematic of an inflation-deflation event is shown in Figure 39. Inflations increase the outer surface area thereby promoting the gasification rate (II – V), facilitate internal gasification at newly formed liquid-gas interfaces (II – III), and can eject material upon deflation (IV).

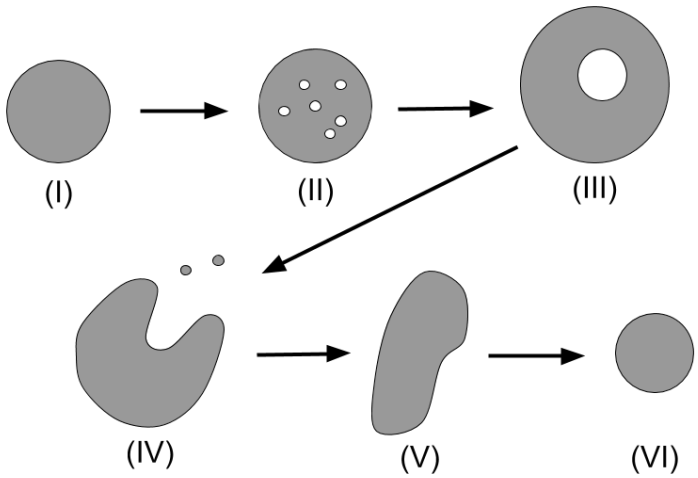


*Figure 39: Schematic of cyclical droplet inflation and deflation. Increased surface area during inflations promote gasification at outer surfaces and promotes burning rate. (I) Undisturbed droplet. (II) Gas bubbles nucleate by radiative heat absorption gasifying local fluid, thermal decomposition of NC, and/or multicomponent superheating [60-63]. (III) Gas bubble coalescence. (IV) Ejection. (V) Momentum transfer and shape deformation (VI) Droplet equilibration and repeat.*

The propensity of a droplet to inflate is affected by internal gas generation and effective surface tension. The equilibrium inflation volume is that which balances inward atmospheric pressure and Laplace pressure with outward gas pressure. This outward pressure is a function of the gas's mass, temperature, and volume. For constant internal gas mass and temperature, its volume will increase with decreasing Laplace pressure given by Equation 32, where $\gamma$ is surface tension, $R_b$ is the radius of the internal bubble, and $R_d$ is the radius of the droplet. Therefore, as surface tension decreases, inflations would be expected to increase for the same amount of internal gas generated. As the mass of gas liberated within the droplet increases, inflations also increase since the equilibrium inflation size ($R_b$ and $R_d$) that balances the inward and outward forces on the condensed phase becomes larger.

$$\Delta P_{\text{Laplace}} = \gamma\left(\frac{1}{R_b}+\frac{1}{R_d}\right) \quad (32)$$

The soluble TOPO surfactant can both decrease the surface tension of the kerosene and increase gas generation since multicomponent combustion droplets with differing boiling points are known to generate gas internally [60-63]. This is consistent with the observed increase in both droplet inflations and burning rate with increasing TOPO concentration. Agreeing with multiple examples of increasing burning rates with increasing NC content, NC addition will also increase gas generation and consequential inflations since it is known to thermally decompose beginning at ~195 C which is lower than the boiling point of kerosene (the temperature that the droplet can be expected to reach and maintain in the ignition stage of its combustion). nAl can also promote inflations since it is known to increase radiative heat transfer from the flame to the droplet which can accelerate internal gasification and thermal decomposition processes [27, 53-55]. Therefore, all additives studied herein have mechanisms by which droplet inflations (and burning rates) can increase with increasing additive concentration.

However, inclusion of solid particles also adds the effects of particle transport and agglomeration to the inflation dynamics. As particle-laden droplets burn and the particle mass fraction increases, particle agglomeration increases, especially near the receding droplet surface resulting in shell formation. The characteristic time for a particle to diffuse the radius of the droplet is $\tau_{\text{Diff}} \approx \frac{(0.3\text{mm})^2}{D}$ where by the Stokes-Einstein equation, $D = \frac{k_B T}{3\pi\mu d_{\text{p}}}$. Assuming the viscosity of the droplet is approximately

that of dodecane ($\mu = 1.34$ mPa-s), MP diameters are 1 μm, and NP diameters are 80 nm, the characteristic times are $\tau_{\text{Diff,MP}} \approx 1.6 \times 10^7$s and $\tau_{\text{Diff,NP}} \approx 1.3 \times 10^6$s which are much longer than the characteristic time of surface regression (equal to the burning time which is approximately 250 ms). Therefore, the surface will regress during combustion much faster than particles can diffuse inward, thereby forming a shell. Agglomerate shells will inhibit liquid and gas transport and therefore add an inward component to the force balance on a growing internal gas bubble. Similar to the effect of weak versus strong surface tension, an agglomerate held together with weak minimum interparticle forces will change shape and size and permit multiphase transport more easily (and thus induce less inward pressure on a growing bubble) than an agglomerate shell with strong minimum interparticle forces. Considering an agglomerate forming of nAl NPs (e.g. Figure 31(A)) versus one forming of MPs (e.g. Figure 31(C)), the top-level assembly particles are an order of magnitude different in size (nAl agglomerates are assembled of ~80nm nAl NPs; MP agglomerates are composed of ~1 μm mesoparticle sub-assemblies). Thus, the overall strength of MP agglomerates is limited by the smaller contact areas and larger interparticle distances between individual MPs, a level of interparticle weakness which does not limit the strength of a nAl agglomerate. Figure 40 shows SEM of the inner surfaces of agglomerate residues recovered from suspended droplet experiments of nAl/NC MP (A) and nAl+NC physical mixture (B) nanofuels respectively. The porosity of the MP nanofuel residue is noticeably higher than that of the physical mixture nanofuel, providing further evidence of smaller contact areas and larger interparticle distances in

MP agglomerates. Therefore, MPs are expected to facilitate increased inflations relative to physically mixed analogs which is consistent with experimental observations. Particle agglomeration inhibiting droplet inflation can also explain decreases in burning rates observed at high particle loadings and in samples of nAl without NC.

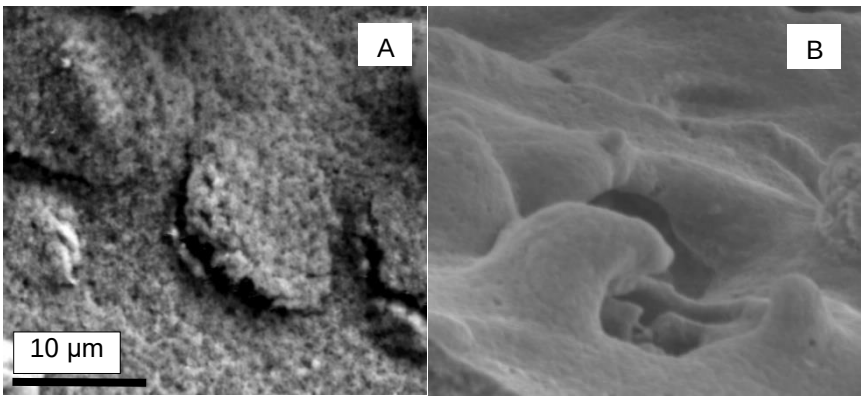


*Figure 40: SEM (1.8kX) depicting inner surfaces of residues of (A) 10.4wt% nAl/15%NC MPs in 200mg/mL TOPO and (B) 2.9wt% nAl+20%NC Physical Mixture in 40mg/mL TOPO suggesting higher porosity of MP agglomerates relative to physical mixture agglomerates.*

## *4.4 Conclusions*

Nitrocellulose is shown to be a suitable gas generator capable of increasing the burning rates of hydrocarbon droplets laden with nAl particles, which without this gas-generating co-additive would otherwise decrease the burning rate of the fuel. Physical mixtures of NC and nAl particles in kerosene are limited by poor stability with increasing particle loading, even with the use of TOPO, a hydrocarbon surfactant. However, composite nAl/NC mesoparticles can be used to create stable nanofuels with over twice the maximum particle loadings of physically mixed nanofuels without clogging the droplet generation capillary (analogous to propellant/fuel handling

infrastructure). The MP additives also promote higher burning rates at increased loadings where detrimental agglomeration effects are more severe for physically mixed additives relative to MP additives. Cyclical droplet inflations and deflations are found to be an important mechanism whereby increased gasification rates, e.g. by enlarged droplet surface area exposed to the flame, promote the overall burning rate of the fuel which can be promoted by lowering fluid surface tension, increasing internal gas generation with absorbing particles or thermally decomposing additives, or by weakening particle agglomerates that form using the MP composite architecture.

# Chapter 5: Activity of oxygen-containing nanoparticle additives in combusting kerosene droplets[3]

*Summary*

Metallizing and gelling hydrocarbons has received attention since the 1960s, but slurry fuels utilizing micron particles suffer from long particle burning times and problematic agglomeration. This study investigates single droplet combustion of kerosene with oxygen-containing nanoparticle additives, assembled by electrospray into nitrocellulose(NC)-bound composite "mesoparticle" (MP) structures (on the order of 5 μm). Significantly improved dispersion properties of these materials are demonstrated compared to unassembled nanoparticles. Droplet combustion is characterized with a free-falling droplet experiment utilizing high speed videography. The MP pre-assembly strategy demonstrated previously by this group to improve burning rate effects and suspension stability of nanoaluminum is extended to oxygen-containing nanoparticles of CuO, $KIO_4$, MgO, and $Al_2O_3$ added to kerosene as NC-bound MPs. Burning rate enhancements of up to 40% are seen for CuO and $KIO_4$ MPs. Direct observation of droplet combustion disruptions is used to propose active mechanisms for each additive.

---

[3] The results presented in this chapter have been previously published and are reprinted with permission from P.M. Guerieri, R.J. Jacob, J.B. DeLisio, M.C. Rehwoldt, M.R. Zachariah, Stabilized microparticle aggregates of oxygen-containing nanoparticles in kerosene for enhanced droplet combustion, Combustion and Flame 187 (2018) 77-86. Copyright 2017 Elsevier Inc. on behalf of The Combustion Institute.

*5.1 Introduction*

As discussed in Section 1.1.2, nitrocellulose can be used to assemble nanoparticles into porous agglomerate "mesoparticles" (MPs) on the order of 1-10 μm in size which exhibit enhanced combustion compared to nAl [13]. This strategy has been extended to thermite mixtures demonstrating a three-fold increase in constant volume combustion pressure rise and pressurization rate for nAl/CuO MPs compared to physical mixtures [14]. This effect was attributed to more intimate contact of the fuel and oxidizer and gas generation by NC decomposition dispersing the reactant particles thereby mitigating reactive sintering [14]. The mechanism of primary particle dispersion to mitigate sintering and promote high burning rates was supported by aerosol-based combustion observations in [17] and MPs were employed in solid rocket propellant in [16].

In Chapter 4, this MP architecture is used to preassemble nAl for addition to kerosene, showing significantly increased suspension stability, higher maximum stable loadings, and therefore greater maximum burning rate increases versus physical mixtures of nAl and NC nanoparticles. This chapter evaluates effects of oxygen-containing solid particles of CuO, $KIO_4$, MgO, and $Al_2O_3$ on the single-droplet combustion of kerosene in a drop-tower configuration when the same gas-generating NC co-additive and MP preassembly strategy is employed to promote droplet disruption, agglomerate break-up, and suspension stability.

## *5.2 Experimental*

### 5.2.1 Nanofuel Preparation

Samples tested were chosen to investigate oxide compounds of various natures: CuO, a metal oxide commonly used in thermite mixtures which thermally decomposes to release oxygen [103]; $KIO_4$, a periodate salt more recently demonstrated as a strong oxidizer of reactive metals which also releases oxygen by thermal decomposition [104]; MgO, a metal oxide expected to be more stable than CuO but which has some possibility of oxidizing combustion species; and $Al_2O_3$, a stable metal oxide expected to be inert.

Nanopowders of CuO, MgO, and $Al_2O_3$ were used as-received from Sigma-Aldrich which specified <50 nm particle sizes for all three materials (Sigma-Aldrich 544868, 549649, and 544833 respectively). SEM images shown in Figure B.1 (in Supporting Information) confirm primary particle sizes on the order of 50 nm, but show secondary particle agglomerate sizes of 0.5-5 μm for CuO and 1-10 μm for MgO and $Al_2O_3$ within tertiary fractal aggregates on the order of 50-100 μm. $KIO_4$ nanoparticles were synthesized by spray-drying as-received $KIO_4$ (Sigma-Adlrich 210056) dissolved at 4 mg/mL in deionized water from a venturi-style collision atomizer through a silica diffusion dryer into a tube furnace at 200 C and was collected with an in-line 400 μm membrane filter [105]. Resulting particles are on the order of 0.1-1 μm primary particles in agglomerates of 0.5-10 μm. NC nanoparticles required for NC-only control samples were assembled by spray drying precursor, composed of NC collodion (Fluka Analytical 09986) diluted with acetone to approximately 25 mg/mL NC solids, into

two in-line tube furnaces at 80 C and collecting the particles in a 400 μm membrane filter heated to 90 C to prevent solvent condensation.

Nitrocellulose-bound mesoparticles were assembled using electrospray particle synthesis described by Wang et al. [13] wherein precursors of solid particles suspended in NC solutions (3:1 ethanol:ether solvent) are agitated in a sonication bath for 1 h and magnetically stirred for 24 h before injection via syringe at 2.5 mL/hr through a 0.43 mm ID stainless steel probe needle charged at 10 kV. 10 cm from and perpendicular to the probe needle, an aluminum foil collection substrate is charged to -10 kV to induce fluid breakup at the needle exit into microdroplets of precursor which dry in flight before deposition on the foil.

Nanofuel suspensions are mixed by adding NPs or MPs to 0.3 mL of kerosene (Sigma-Aldrich 329460, reagent grade) with 15 mg of trioctylphosphine oxide (TOPO) surfactant, agitating by sonication bath, and magnetically stirring for 24 h. Sonication bath times were 1 h for NP suspensions and 5 min for MP suspensions to limit possible MP damage while maximizing NP aggregate disassembly and suspension. TOPO surfactant is required to chemically stabilize particles in suspension and was proposed for this purpose by E et al. to stabilize boron in JP-10 in [92] and has successfully stabilized nAl/NC MPs in Chapter 4. To simplify comparison of nanofuel burning rates using one common control, constant TOPO concentration (50 mg/mL), nanofuel batch size (0.3 mL), and mixing/storage vial size (0.5 Dr) was maintained for all samples in this study. Each sample was sonicated for 1 min prior to combustion experiment trials to ensure particle dispersion. The loadings of samples tested are shown in Table 5,

which were based on equal oxygen content of the additives, constant for each loading category A-D (except for NC binder-only control samples which do not include oxides). NC binder mass throughout the study is five weight percent of the theoretical reactive mixture, i.e. 5 wt% of a stoichiometric mixture of the oxygen-containing nanoparticles and nAl fuel for direct comparison with results of Chapters 4 and 7.

*Table 5: Sample mass loadings tested by mixing with 0.3 mL of kerosene including 50 mg/mL TOPO surfactant. Control samples (not shown) included neat kerosene, kerosene with TOPO surfactant, and NC nanoparticles in kerosene/TOPO at loadings of 2-10 mg/mL. Oxygen Molarity defined by the oxygen content of the oxides in the final nanofuel suspensions.*

| | | A | B | C | D |
|---|---|---|---|---|---|
| | Oxygen Molarity | 0.44 | 0.89 | 1.33 | 1.78 |
| | | Mass Loadings (mg/mL) | | | |
| 1 | CuO NPs | 35.4 | 70.8 | 106.1 | 141.5 |
| 2 | KIO4 NPs | 25.6 | 51.1 | 76.7 | 102.3 |
| 3 | MgO NPs | 17.9 | 35.9 | 53.8 | 71.7 |
| 4 | $Al_2O_3$ NPs | 15.1 | 30.2 | 45.3 | 60.5 |
| 5 | CuO/NC MPs (6.4wt% NC) | 37.8 | 75.5 | 113.3 | 151.1 |
| 6 | $KIO_4$/NC MPs (6.7wt% NC) | 27.4 | 54.9 | 82.3 | 109.8 |
| 7 | MgO/NC MPs (7.7wt% NC) | 19.4 | 38.8 | 58.2 | 77.6 |
| 8 | $Al_2O_3$/NC MPs (8.1wt% NC) | 16.4 | 32.9 | 49.3 | 65.8 |

### 5.2.2 Combustion Characterization

Measurements of burning rate constants were taken consistent with the apparatus and methodology of Chapter 4, as described in Section 2.1.2. For further characterization of droplet disruptions, select samples were observed in this Chapter with magnified high-speed video at the height of the red line in Figure 43. Point spectroscopy was also taken using an Ocean Optics USB2000+UV-VIS spectrometer with a fiber optic focused at the same height as the camera on the falling droplets. The integration time of the spectrometer was longer than the time of a droplet falling

through the field of view resulting in one spectra per falling droplet. Representative spectra are shown in Figures B.6-B.11.

## *5.3 Results and Discussion*

### 5.3.1 Material Characterization

Electrosprayed MPs are shown in SEM images in Figure 41. MP sizes are on the order of 5 μm and generally round in shape which, compared to the ~1-10 μm amorphic secondary aggregates of the source oxide particles shown in Figure B.1, suggests that sonication and mixing of the electrospray precursors successfully breaks secondary soft aggregates to intimately mix NC binder with collections of primary particles <5 μm in size, which reform round MPs as precursor droplets evaporate during electrospray.

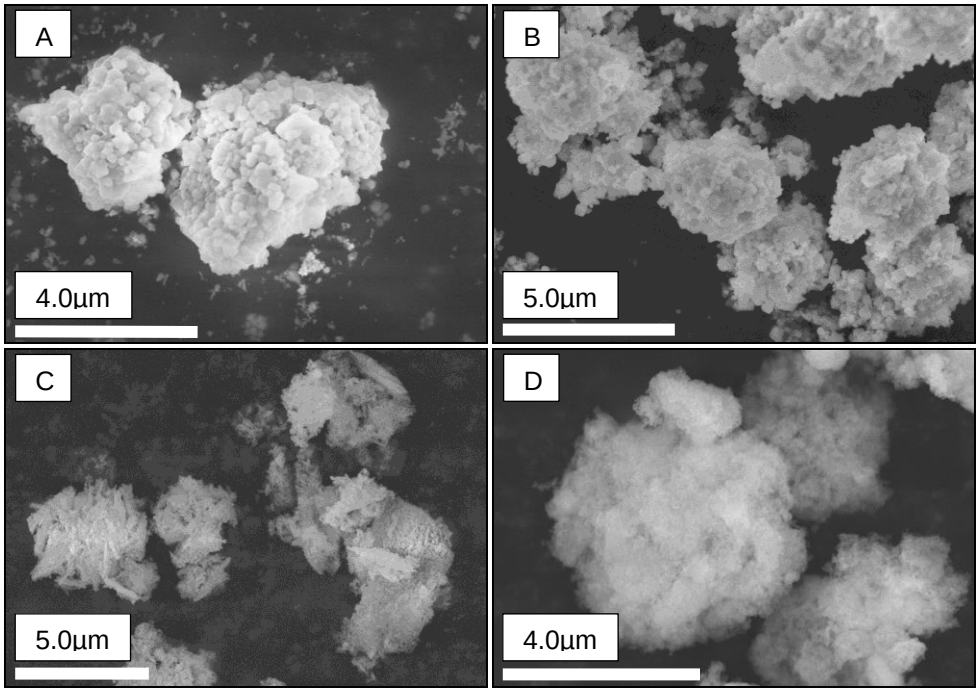


*Figure 41: SEM of electrospray assembled mesoparticles (A) CuO, (B) $KIO_4$, (C) MgO, and (D) $Al_2O_3$.*

Simultaneous thermogravimetric analysis and differential scanning calorimetry (TGA/DSC) was conducted to assess the thermal behavior of the MP constituent materials, shown in Figure B.3. The NC binder decomposes exothermically at ~485 K. TGA/DSC on the specific CuO nanoparticles used in this study under 10 K $min^{-1}$ heating in argon shows onset of endothermic oxygen release at ~1100 K. Jian et al. showed this CuO decomposition temperature is heating rate dependent and identified $O_2$ release temperatures between approximately 925 K and 1020 K for heating rates of ~$1.5x10^5$ and ~$6x10^5$ K $s^{-1}$ respectively [103]. TGA/DSC of $KIO_4$ closely matches the results of [104] with two decomposition steps at 604 K and 830 K. Conversely, TGA/DSC of MgO nanoparticles revealed only a ~2.5% weight loss near 580 K, likely decomposition of impurities in as-received MgO, with no obvious thermal

decomposition of the oxide below 1200 C. NC-bound MP samples show superimposed activity of both the NC binder oxide particle, exhibiting no effect of one component on the thermal behavior of the other.

The suspension stabilities are shown in Figure 42 as a function of time after sonication. The important result here is that mesoparticles offer considerably greater colloidal stability than the corresponding unassembled materials, consistent with our observations for nAl/NC MPs in Chapter 4.

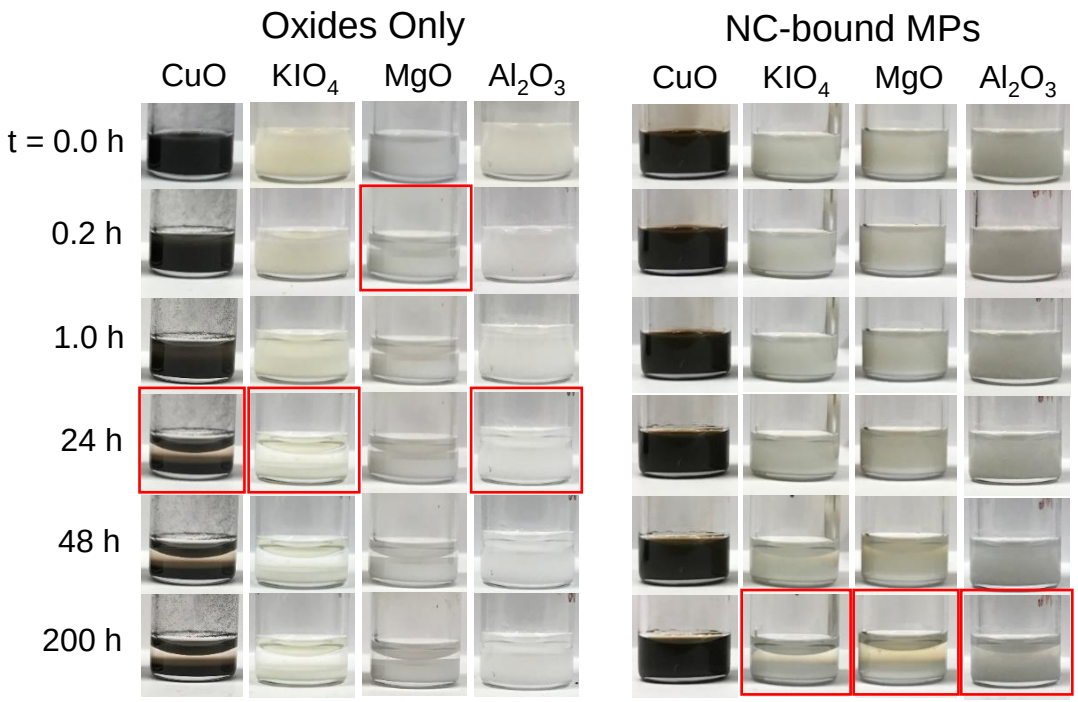


*Figure 42: Nanofuel suspension photographs at various elapsed times from dispersion by sonication. Red boxes indicate suspensions which have visibly gravitationally settled.*

### 5.3.2 Nanofuel Falling Droplet Combustion

Figure 43 depicts representative time-lapse images of a single combusting droplet for the highest loading class of each sample (including neat kerosene without

surfactant which was artificially brightened for visibility). The droplet position is not linearly related to its burning time and the initial droplet diameters can vary +/- 0.1 mm, therefore the length of the traces only loosely illustrates the burning rate of each sample (more accurately quantified in Section 5.3.3). Traces A-C depict the control samples of neat kerosene, kerosene with TOPO surfactant, and NC particles added with surfactant. Notably, the burning rate is only marginally affected by NC addition alone and visible effects of the surfactant and NC particles are limited to the end stage of droplet combustion.

Combustion traces D-G in Figure 43 illustrate the effects of oxide addition as nanoparticles. Longer traces suggest slower burning rates but quantification in Section 5.3.3 shows near zero effect, with slight burning rate increases (most significant for $KIO_4$). Slightly longer traces are thought to be from small density variations with the solid additives which, with constant droplet volume, decreases the significance of drag compared to droplet inertia. It is possible that such slightly higher droplet velocities near termination marginally increase burning rates when solid additives are included by promoting aerodynamic mixing compared to liquid-only samples. This effect is estimated to be small relative to the effects of MP additives and comparable to the experimental error. The droplet combustion of all oxide-only formulations remains unaffected for the first approximately 50% of their lifetimes. CuO incites droplet disruptions at the earliest point in the droplet lifetime with the most widely dispersed activity and increased flame emission. Initial disruptions of $KIO_4$, while appearing to occur later and with less flame emission expansion, are of a similar nature to those of

CuO, characterized by asymmetrical flame plume expansions. As $KIO_4$-laden droplets approach termination, they demonstrate a more swollen emission profile. MgO also incites highly emitting disruptions, however they typically only occur in less than ten events in the last roughly 80% of the combustion time, are more symmetrical, high emission, and most prevalent near droplet termination. This is the first indication that CuO and $KIO_4$ may affect flame chemistry with emerging gas phase agents while MgO activity may be limited to when flame and solid particles interact. $Al_2O_3$ shows very small perturbations in the flame but generally only lengthens flame emission near droplet termination, consistent with emission from heated $Al_2O_3$ solid particles remaining as liquid burnout completes.

The last of the combustion traces, H-K, depict NC-bound oxide MPs added to kerosene with surfactant. The drastic shortening of traces H-J demonstrates the significant effect of NC inclusion via MP assembly versus NPs-only. The onset of any droplet/flame disruptions are significantly earlier for NC-bound MP samples in H-J, consistent with observations of nAl MPs in Chapter 4. The resulting disruptions are also exaggerated, featuring more widely expanded flame emission for CuO and more frequent and brighter emission for $KIO_4$ and MgO compared to traces D-G. $Al_2O_3$ is the notable exception, showing little to no effect of the NC-bound structure on the activity of the additive, except for added trajectory perturbations consistent with NC-only (in trace C) wherein NC gas generation perturbs the trajectory immediately before droplet termination.

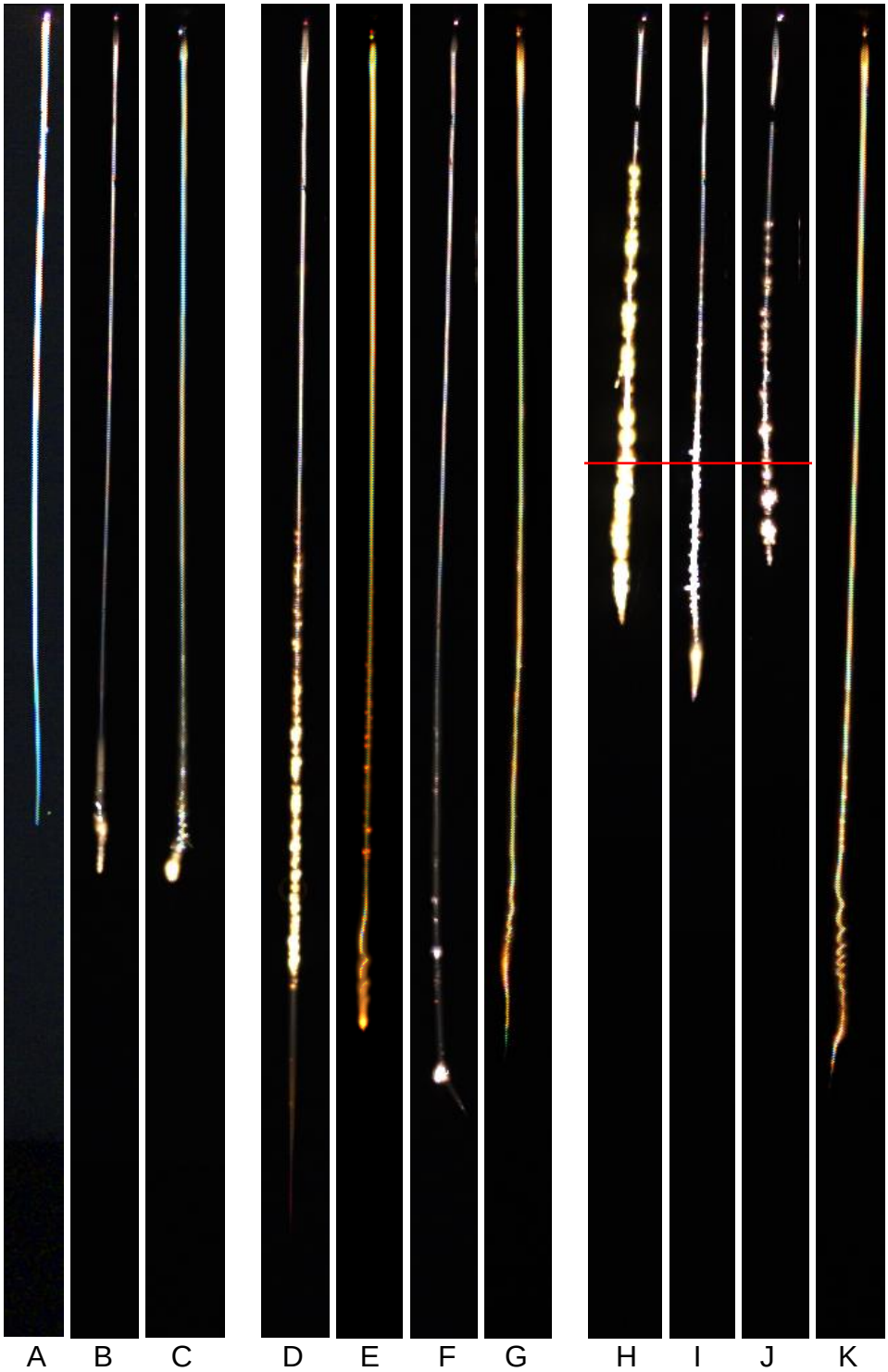


*Figure 43: (A) Kerosene Only, (B) Kerosene with TOPO Sufactant (base liquid for C-H), (C) NC Particles Only, (D) CuO Only, (E) $KIO_4$ Only, (F) MgO Only, (G) $Al_2O_3$ Only, (H) CuO/NC MPs, (I) $KIO_4$/NC MPs, (J) MgO/NC MPs, (K) $Al_2O_3$/NC MPs.*

*Red line corresponds to the height at which the magnified videos shown in Section 5.3.4 (and flame emission spectra discussed in 5.3.5) were taken: 4.5 inches below the ignition point.*

### 5.3.3 Burning Rate Measurements

The kerosene/TOPO fuels with MP additives studied include up to 1.15 wt% NC. The burning rates of NC nanoparticle-laden samples up to this loading were assessed without oxides and are shown in Figure B.2. All burning rate data is presented as percent changes in the burning rate constant compared to surfactant-only kerosene ($K = 2.21$ mm$^2$/s with 50 mg/mL TOPO surfactant). NC NPs increase the burning rate linearly by approximately 7% per wt% of NC, agreeing with observations in Chapter 4 which proposed that NC thermal decomposition, beginning below 200 C, generates gas within the droplets since combusting liquid droplets heat quickly to the boiling point of the fluid (approxiamtely 220 C for Kerosene). Such generated gas inflates the droplets, thereby increasing liquid surface area for evaporation, and significantly increasing physical mixing of the system. Trace C in Figure 43 shows these disruptions are most active near droplet termination for NC-only samples. This late disruption onset relative to MP samples in part explains the relatively lower order of magnitude of the burning rate increases for NC alone.

Burning rate effects of the oxide additives are assessed relative to the baseline effects of NC-only and plotted relative to oxygen content for the four oxides in Figure 44. The calibration curve of NC-only is overlaid on each plot to show the burning rate of NC-only, relative to MP samples with the same amount of NC. With this frame of reference, an obvious benefit of NC-bound MPs is evident for CuO, $KIO_4$, and MgO

based formulations. Consistent with the combustion traces in Section 5.3.2, $Al_2O_3$ is the exception to this effect with little to no discernable benefit of the NC-bound MP architecture. Oxide-only NP samples without NC (solid points of Figure 44) generally increase or minimally affect burning rates. This is in stark contrast with observations of nAl NPs added alone in Chapter 4 which decreased the burning rate with added nAl loading. $KIO_4$ stands out with the highest burning rate increases at and above 0.9 M oxygen (5.6 wt% $KIO_4$ NPs) among the oxide-only samples.

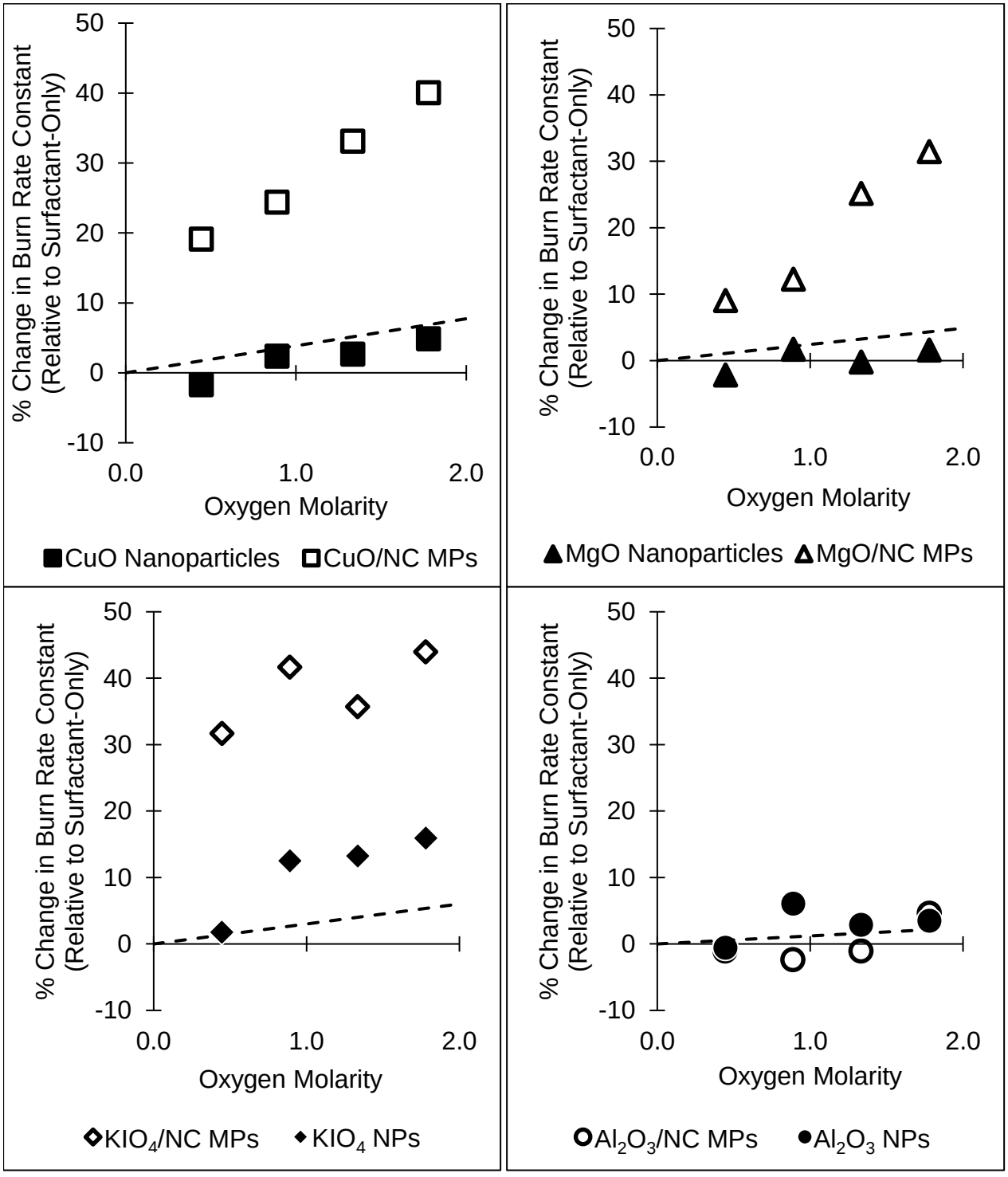


*Figure 44: Burning rate effects of CuO, MgO, $KIO_4$, and $Al_2O_3$ nanoparticles and NC-bound MPs. Dotted lines are the NC-only control fit scaled to correspond to NC content in the MPs at those oxygen molarities. NC oxygen content is not considered.*

The effect of mass loading of MPs is shown in Figure 45 with the various oxygen contents of the four oxides. With respect to burning rate, $KIO_4$ clearly provides the highest overall rate increase. The oxides with the most significant burning rate increases in MPs ($KIO_4$ and CuO) are also the two least efficient oxygen carriers by mass. MgO and $Al_2O_3$ boast higher oxygen per mass ratios, however, only MgO MPs achieve significant burning rate increases.

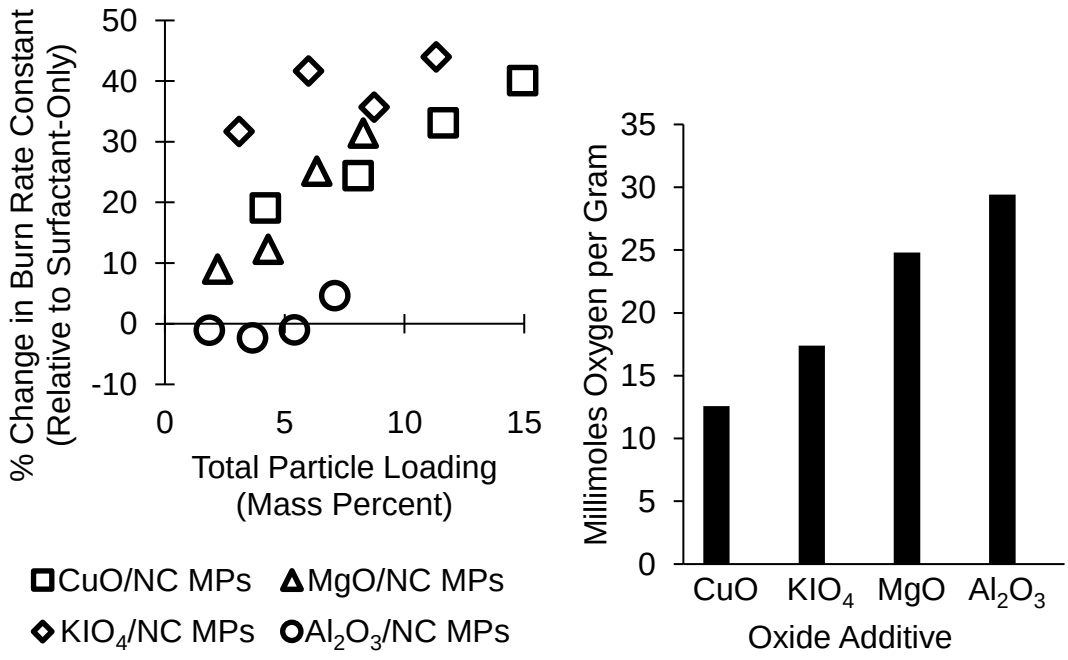


*Figure 45: Burning rate effects of all mesoparticle additives versus mass percent particle loading and oxygen carrying efficiency of each oxide.*

5.3.4 Direct Observation of Droplet Disruptions

To further investigate the droplet combustion disruptions that emerge upon CuO, $KIO_4$, and MgO MP addition, magnified high speed video was taken at the height of the red line in Figure 43. A representative disruption event for CuO/NC MPs is shown in Figure 46. Image gains are artificially adjusted to keep the droplet frames

visible throughout the event. The CuO/NC MP disruption initiates in the second frame of Figure 46 with a small region of decreased emission in the flame, and spotted spot of orange emission expansion. The region of lower emission behaves like low temperature gaseous species released from within the droplet since in the following frames, it expands upward through the flame and increases emission consistent with the combustion of gaseous species. Concurrently, the initial spot of orange emission first expands outward in the direction of its ejection for 2-3 frames before veering upward, suggesting nontrivial inertia of the emitting species. Predominantly orange emission plumes with faint regions of green near the edges are observed in frames 5-17 in Figure 46 accompanying the ejection event.Such emission is consistent with that of copper-containing species, confirmed by emission spectroscopy of a passing CuO MP-laden droplet shown in Figure B.6 to likely be excited CuO and CuOH (orange 608nm and 618nm doublet, and green 525-555 nm band respectively. In the fifth frame, this presumed copper species liberation occurs again at a secondary site on the left side of the droplet and together these releases overall create the widespread orange/green emission attached to the droplet flame which is visible on the order of 3 ms. A possible explanation is ejection of particulate CuO which decomposes and reduces near and in the flame region thereby affecting gas phase reactions causing the emission increase which lingers around the droplet flame.

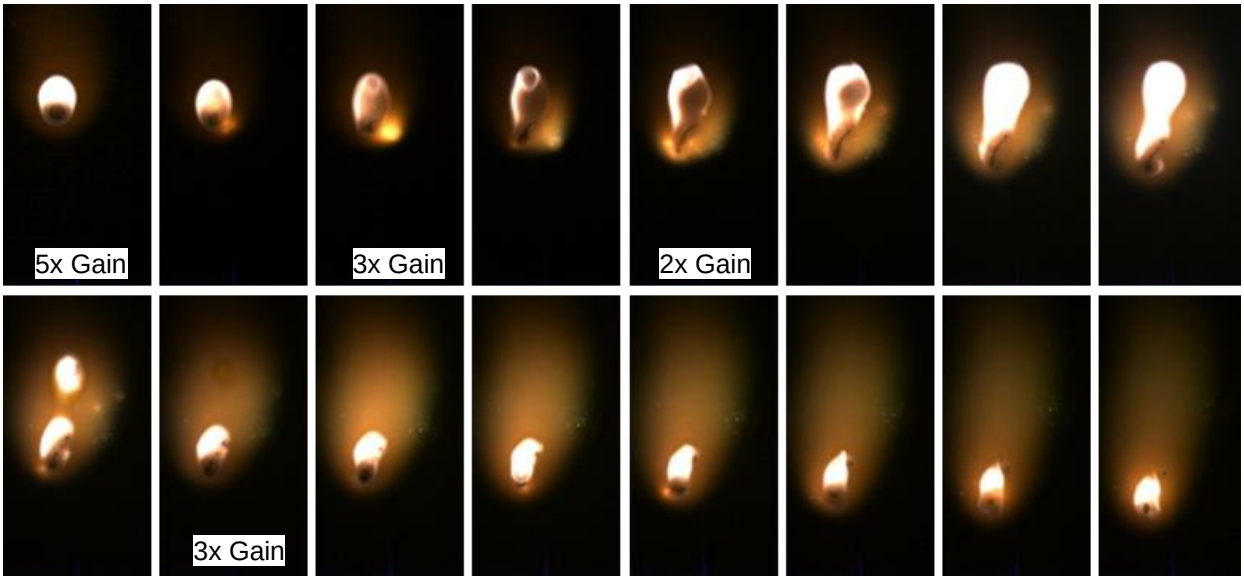


*Figure 46: Representative swelling/eruption event during combustion of CuO/NC MPs in Kerosene/TOPO. Brightness is artificially increased for visibility as labeled on the first frame of each gain adjustment setting. 166 μs image period).*

Disruptions of $KIO_4$/NC MPs, represented by Figure 47, contain notable differences relative to those of CuO MPs. First, the droplet flame in the absence of a large disruption is unsteady compared to the flame with CuO MPs (seen steady in the first frame of Figure 46 compared to the deformed flame shape for $KIO_4$ MPs shown in the first frame of Figure 47). The timescale of these small flame perturbations for $KIO_4$ MPs is short, on the order of one frame or less (166 μs), and are possibly due to heterogeneous oxygen release from the droplet by $KIO_4$ decomposing near the droplet surface. Larger disruptions occurring concurrently are similar to gas ejections observed for CuO MPs and in Chapter 4, exemplified in the seventh frame of Figure 47 at the bottom right of the droplet. However, compared to those of CuO MPs these events are smaller, occur more frequently, and have little to no spectral effect on the flame emission. Orange-violent emission beginning in the ninth frame is not attached to the

droplet flame (like the emission expansion of the CuO MP disruption), but rather seems to emanate from a small companion droplet visible left of the main drop in the first three frames. This companion droplet, formed from a prior disruption, enters the flame zone near frame nine and incites the increased emission above the flame. Two other examples of companion droplet liberation and combustion are seen in frames 13 and 15.

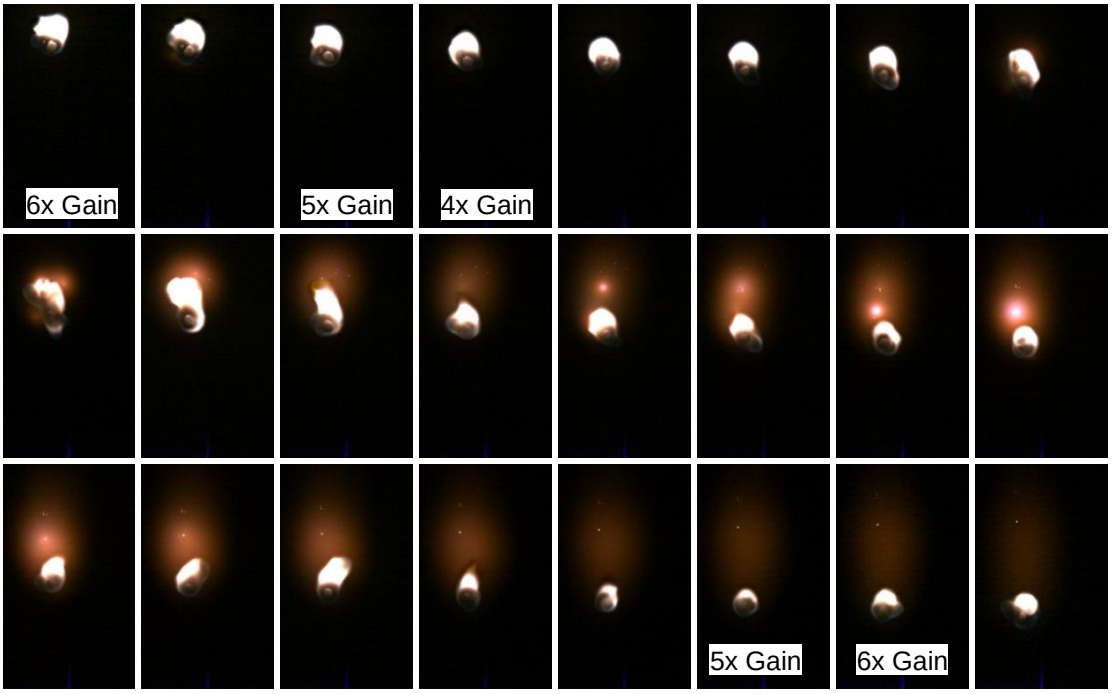


*Figure 47: Combustion of $KIO_4$/NC MPs in kerosene/TOPO. Brightness is artificially increased for visibility as labeled on the first frame of each gain adjustment setting. First two frames show a companion microdroplet to the left and above the main droplet, which generates the orange emission detached from the main droplet flame as it combusts fully. 166μs image period.*

MgO/NC MP disruptions, such as those depicted in Figure B.4, resemble those of CuO MPs in that the droplet flame is steady in the absence of a disruption and the perturbations are characterized by significant gas eruptions, albeit with significantly

smaller flame emission expansions. However, MgO MPs show small spots of emission consistent with particle release more prevalently than CuO MPs, shown in Figure B.5. These particle emissions survive in the flame zone significantly longer than any particle emission observed for CuO or $KIO_4$ MPs.

### 5.3.5 Thermodynamic Considerations

To assess possible reduction of the oxides by reaction with combustion species, NASA CEA was used to generally investigate thermodynamic equilibrium species of stoichiometric combustion of RP-1 and $O_2$ with small amounts of CuO, MgO, or $Al_2O_3$ added ($KIO_4$ thermodynamic properties unavailable in CEA) [99]. Results of these calculations are given in Table 6. Equilibrium calculations show that the addition of the metal oxides is insufficient to appreciably impact the adiabatic flame temperature. Considering the concentration of the reduced metal vs. its parent metal oxide shows that while CuO undergoes significant decomposition at flame temperatures, alumina is relatively inert and MgO is in between. This is consistent with the observed effect on burning rate and the visual observations of droplet combustion and disruptions.

*Table 6: Results of NASA CEA equilibrium calculations for constant enthalpy, constant temperature stoichiometric RP-1/O2 with additives (added as 1% of the oxidizer by mass).*

| Additive | None (RP-1/O2) | CuO | | MgO | | $Al_2O_3$ | |
|---|---|---|---|---|---|---|---|
| Equil. T (K) | 3110 | 3105 | | 3097 | | 3103 | |
| Equil. Mole Fractions Containing Additive Metal | | Cu | 2.3E-03 | Mg | 2.2E-03 | $Al_2O_{3(L)}$ | 1.1E-03 |
| | | CuO | 3.8E-05 | MgO | 1.9E-03 | AlOH | 1.0E-03 |
| | | CuOH | 1.0E-05 | MgOH | 3.4E-04 | AlO | 3.0E-04 |
| | | | | $Mg(OH)_2$ | 2.4E-04 | $Al(OH)_2$ | 3.9E-05 |
| | | | | | | $AlO_2$ | 3.0E-05 |
| | | | | | | $HAlO_2$ | 2.9E-05 |
| | | | | | | $Al(OH)_3$ | 2.5E-05 |
| | | | | | | Al | 1.5E-05 |

Another way of considering this is to assess the likelihood of redox reaction between the oxides and major reducing gases expected in the rich zone of the diffusion flame (i.e. CO and $H_2$). For reactions with positive free energies at room temperature, the temperature at which the free energy equals zero is listed in Table 7. These reduction reaction onset temperatures show that $Al_2O_3$ reduction by combustion species is not thermodynamically favorable at reasonably physical temperatures (<6600 K). $KIO_4$ and partial CuO reduction by combustion species is thermodynamically favored down to room temperature, with full CuO reduction to Cu favored above 1300 – 1600 K. MgO reduction is only thermodynamically spontaneous above 2820 K for reduction by $H_2$ (3381 K for CO). This is interestingly near possible flame temperatures for kerosene/oxygen as suggested by flame spectroscopy fits to Planck's Law in Figures B.7-B.11 and Table B.1. Most reduction reactions are endothermic except for those of $KIO_4$.

*Table 7: Reaction thermodynamics of oxide reduction by CO and $H_2$.*

| | ΔH kJ/mol | ΔS kJ/mol-K | ΔG(300K) kJ | T(ΔG=0) K |
|---|---|---|---|---|
| **Reduction by CO** | | | | |
| $CuO_{(s)} + CO = Cu + CO_2$ | 210 | 0.1395 | 169 | 1508 |
| $CuO_{(s)} + CO = Cu_2O_{(l)} + CO_2$ | -83 | 0.0601 | -101 | |
| $MgO_{(s)} + CO = Mg + CO_2$ | 466 | 0.1378 | 425 | 3381 |
| $Al_2O_{3(s)} + CO = AlO + CO_2$ | 1460 | 0.1835 | 1405 | 7954 |
| $KIO_{4(s)} + CO = KIO_{3(s)} + CO_2$ | -326 | -0.0081 | -324 | |
| **Reduction by $H_2$** | | | | |
| $CuO_{(s)} + H_2 = Cu + H_2O$ | 252 | 0.1815 | 197 | 1386 |
| $CuO_{(s)} + H_2 = Cu_2O(l) + H_2O$ | -42 | 0.1021 | -72 | |
| $MgO_{(s)} + H_2 = Mg + H2O$ | 507 | 0.1798 | 453 | 2820 |
| $Al2O3_{(s)} + H_2 = AlO + H_2O$ | 1501 | 0.2255 | 1433 | 6655 |
| $KIO_{4(s)} + H_2 = KIO_{3(s)} + H_2O$ | -285 | 0.0339 | -295 | |

Flame emission spectroscopy results shown in Figure B.6 reveal emission peaks attributed to CuOH/CuO, K, MgOH/MgO/Mg for CuO, $KIO_4$, and MgO, respectively. Peaks near 589nm and 767nm are strong sodium and potassium lines, the potassium in the CuO spectra attributed to slight contamination by $KIO_4$ in the droplet generation assembly. Atomic lines of CuO and MgO support the notion that the additives reach the high temperature flame region, despite the expectation that CuO also undergoes concurrent thermal decomposition. Mg emission is evidence of MgO reduction reactions to a small degree considering the weak intensity of the Mg peak. Both CuO and MgO form hydroxides in the flame by reaction with H. Flame temperatures estimated by fitting plank's law to the collected spectral intensity are shown on the respective spectral plots in Figures B.7-B.11, suggesting flame temperatures in the range of 2900 K – 3300 K. However, the uncertainty in this measurement is estimated to be at least 200K and the model does not consider non-blackbody emissivity of the

flame species and emitting particulates. The estimate does however provide evidence that the MgO reduction reactions considered in Table 7 are possible in the combustion of the kerosene droplets in oxygen.

### 5.3.7 Proposed Mechanisms: Role of NC in MP Additive Effects

The NC-bound mesoparticle architecture has been shown in Chapter 4 to be beneficial for burning rate enhancement by addition of energetic solids to kerosene. This nanoparticle preassembly controls the primary particle agglomeration in a structure that is bound by NC which itself can decompose at low temperature (~200 C) exothermically releasing gas and dissembling the agglomerate. This architecture also demonstrated much improved colloidal stability enabling longer particle settling times and higher maximum testable loadings. In this study, CuO, $KIO_4$, and MgO additives all exhibit drastically higher burning rate constants in kerosene when incorporated into NC-bound MPs. These observations can be explained by the notion of a positive feedback loop first presented in Chapter 4. As NC within the combusting droplets decomposes, generated gas swells the droplet. The resulting enlargement of liquid surface area exposed to the flame contributes to higher gasification rates of the droplet (and therefore higher burning rates). Both magnified videography in this study and results of Chapter 4 show clear disruptions caused by gas releases in MP samples. Once the first of these disruptions occurs, the resulting droplet deformation and increased mixing promote mass and thermal transfer rates. Disruptions also transport additive particles or decomposition products to the flame region. For CuO, $KIO_4$, MgO, and nAl in Chapter 4, these additives are shown to have combustion promoting effects by

releasing oxygen on the fuel rich side of the flame or adding to the calorific output (for nAl). Increased mass and heat transfer together with faster combustion reaction rates or calorific output would increase the rate at which NC within the condensed phase decomposes to repeat this cycle. Therefore, this primary mechanism forms a self-accelerating positive feedback loop consistent with the earlier and more frequent disruptions observed for NC-bound MP-laden droplets.

Notably, $Al_2O_3$ MPs had minimal effect on burning rates and showed no added droplet disruptions relative to NC-only control samples, therefore representing a physical control group. Two factors likely contribute to this lack of an apparent NC decomposition feedback loop mechanism in this case: the high thermal stability of $Al_2O_3$ and its high heat capacity, approximately twice that of CuO, MgO, or nAl ($KIO_4$ has a higher heat capacity than $Al_2O_3$ but easily decomposes before surviving in the flame for appreciable time). Both such characteristics of $Al_2O_3$ likely slow or interrupt the chain of events proposed necessary to form a feedback loop between a gas ejection, the resulting droplet and combustion disruption effects, and subsequent occurrences of gas ejection brought on by those effects.

### 5.3.7 Proposed Mechanisms: Oxide-Specific Activity

With an oxygen release temperature (~1000K depending on heating rate) significantly below the flame temperature, CuO will act as an oxygen donor. Furthermore, reduction of CuO to Cu by CO and $H_2$ is thermodynamically favored in the flame. Therefore, CuO likely undergoes both thermal decomposition and direct reduction once it enters the flame region upon droplet disruptions. Such decomposition

effectively delivers gas phase oxygen to the fuel rich side of the flame. These two pathways fit droplet disruption observations discussed in Section 5.3.4 wherein evidence of both gas phase reaction (suggested by emission attached to the droplet flame) and particle existence within the flame at disruption onset are attributed to the CuO additive.

While onset of $KIO_4$/NC MP disruptions are consistent with gas ejections caused by phase change and/or NC decomposition within the droplet, the $KIO_4$ seems most active either in the absence of such an event (likely by perturbing the droplet flame upon releasing decomposition products) or by entering the flame in a companion droplet generated by secondary atomization during a gas ejection. Such companion droplets combust quickly due to their small size and add to the surface area of condensed species exposed to flame, thereby increasing burning rates. Overall, these disruption characteristics suggest that solid $KIO_4$ particles likely don't survive decomposition as long as those of CuO. TGA results confirm a lower oxygen release temperature for $KIO_4$ relative to CuO, in two decomposition steps at 604K and 830K. This first oxygen release step would occur in lower temperature regions of the system compared to CuO i.e. closer to the droplet surface, which can explain the steady flame perturbations observed. The second decomposition step can account for the added emission from combusting companion droplets, as any remaining $KIO_4$ or $KIO_3$ in such droplets decomposes rapidly upon liquid burn-off releasing excited KI species and $O_2$.

MgO is unlikely to thermally decompose to release any oxygen at the temperatures reached in this system and instead is thought to only be partially reduced

in the flame by high temperature reducing species such as $H_2$, as supported by CEA calculations and thermodynamic consideration of redox reactions considered in Section 5.3.5. This activity agrees with the observations of MgO MP disruptions in that the emission increase around the flame is significantly smaller and lower intensity than that of CuO, which both thermally decomposes and reduces in the flame. The significant presence of emitting point sources during such disruptions can be explained by condensed phase MgO undergoing reduction in the flame followed by any resulting Mg reoxidizing in the oxygen rich atmosphere outside of the flame while it sustains enough thermal energy to do so from the exothermicity of Mg oxidation.

## *5.4 Conclusions*

CuO/NC, $KIO_4$/NC, and MgO/NC mesoparticles loaded up to 14.9%, 11.3%, and 8.3% by weight in kerosene fuel with TOPO surfactant have been shown to increase burning rates 40%, 44%, and 31% respectively compared to the surfactant-only control, while inactive $Al_2O_3$/NC MPs were shown to have minimal effects. These materials also show significant improvement in colloidal stability compared to unassembled nanoparticles. The mechanism by which the NC-bound MP architecture facilitates these effects, presented first in Chapter 4, is supported by these results, in which NC binder decomposes within the droplet to generate droplet-deforming gas ejections, increasing mass and thermal transfer rates, promoting gasification rates, and transporting additive to the flame.

# Chapter 6: Influence of mesoparticle morphology on nanofuel stability and droplet burning rates

*Summary*

Preassembly of energetic nanoparticles into nitrocellulose-bound clusters ("mesoparticles") by electrospray is a recent strategy which promotes higher energy release rates and greater stability of nanofuels composed of these MPs stabilized in a hydrocarbon with TOPO surfactant. Stability observations however have previously been anecdotal and little is understood regarding the effects of the wide tuning available in electrospray on these observed benefits in nanofuels and their isolated droplet combustion. Kerosene/TOPO nanofuels of MPs composed of nanoaluminum (nAl) and nitrocellulose binder are compared to those of as-received nAl using TGA/DSC to characterize relative gravitational settling by testing nAl loading near the fluid meniscus over time. Significantly lower settling rates are quantitatively shown with the MP preassembly strategy. A tuning parameter available in electrospray, precursor loading, is also varied and a free-droplet combustion experiment contextualized by SEM and TGA-based settling trials are used to suggest that as increased precursor loading causes larger and more spherical MPs, these are broken into sub-MP clusters during nanofuel mixing and the morphology differences affect the resultant sub-MP sizes and survival rate of parent MPs. The properties of these suspended clusters cause varying burning rates of nanofuels, which are higher with lower precursors (and less MP break-up), but only slightly affect settling stability.

*6.1 Introduction*

Electrospray assembly of energetic nanoparticles into nitrocellulose (NC)-bound mesoscale structures has shown potential in Chapters 4 and 5 to facilitate higher free liquid droplet burning rate constants when such materials are suspended in hydrocarbons compared to suspensions of unassembled nanoparticles. Specifically, this strategy could be useful for metallizing hydrocarbons for increased energy density without depressing the burning rate of the modified fuel to a degree at which a larger combustion chamber is necessary for complete fuel oxidation, which would increase the dry weight of a vehicle negating the higher payload capabilities made possible by metallizing propellants. Greater colloidal stability of particle additives has also been observed in these studies but so far in this dissertation, such observations are anecdotal or only qualitatively made from photographs of settling suspensions. Preventing or slowing particle settling is required for future application of nanofuels to ensure product consistency. Therefore, a quantitative measure of how the gravitational settling of electrosprayed mesoparticles in a hydrocarbon compares to that of unassembled nanoparticles to better assess the merit of this added production step. To quantitatively visualize gravitational settling of nanoaluminum (nAl) suspended in kerosene with chemical stabilization as both as-received nanoparticles and electrosprayed NC-bound mesoparticles, suspensions made in this study are left to gravitationally settle for various times before sampling from the top meniscus of the nanofuel for thermogravimetric analysis (TGA) and aluminum content measurement.

Opportunities to tune a propellant additive can also be useful to realize desired properties of the resultant nanofuel. Electrospray assembly adds variables to the production process which could be exploited to provide means of tuning combustion and suspension properties. Wang et al. showed that higher particle loading in the electrosprayed precursor yields larger resultant MPs [13]. To further investigate tuning potential with respect to liquid propellant modifications, work presented in this chapter also varies the nAl and NC concentrations of the electrosprayed precursor used to compose the nAl-based mesoparticle additives. Effects on the resulting morphologies are investigated with scanning electron microscopy while suspension stability is assessed with TGA after prescribed settling times and a free-droplet combustion experiment is used to estimate the droplet burning rate constants with the different precursor concentrations.

## *6.2 Experimental*

### 6.2.1 Particle Assembly and Nanofuel Mixing

Electrospray mesoparticle assembly, described in detail in Section 2.2.2 and first published for used with energetic materials by Wang et al. [13], consists of a syringe of volatile precursor pumped through a metal probe needle which is charged to high voltage and separated from a metal foil collection substrate oriented orthogonal to the needle and charged to opposite voltage. As the conductive precursor fluid exits the probe needle, the charge difference between the fluid and distant substrate builds like charges on the liquid surface while extending columbic attractive force between the

precursor and substrate. As a result, a Taylor cone forms at the end of the needle from which fluid droplets break off as the repulsive force between like charges on the surface overcomes surface tension to shatter the liquid flow into a fine mist of droplets, thereby reducing the charge density on the liquid surface as the specific surface area increases with smaller droplet sizes. Attraction of the droplets to the foil substrate and the needle/foil separation allows the volatile carrier fluid to evaporate in-flight before depositing the resulting particle precipitates on the foil for collection. When the sprayed precursor is composed of energetic nanoparticles of fuel and/or oxidizer suspended in an ethanol/ether co-solvent with dissolved NC, the formation of energetic nanoparticle composites can be controlled and this strategy has been shown to improve nAl and nAl/CuO combustion performance in dry formulations [13, 14].

In this chapter, nAl nanoparticles (Novacentrix, Inc., 80% active Al with 2-5nm oxide shell) are used with 5% NC binder (received as 4-8% Collodion solution from Sigma-Aldrich 09986) by mass relative to the nAl in a 3:1 mixture of ethanol and diethyl ether which is necessary to dissolve the NC binder. The concentration of this precursor, held constant at 100 mg/mL in Chapters 4, 5, and 7, is varied between 50 mg/mL and 150 mg/mL in 25 mg/mL increments and the mixed precursors are sonicated for 1 h before magnetically stirring for 12 h. The formulations are electrosprayed from a 0.43 mm ID probe needle charged to 10 kV and separated by 10 cm from an approximately 6 in. square aluminum foil substrate charged to -10 kV between 2.0 and 2.5 mL/h. The pumping rate is set as high as possible while maintaining stable formation of a fine spray without visible droplet deposition on the

foil which occurs at unacceptably high flow rates. To make the nanofuel suspension samples according to Table 8, collected mesoparticles are mixed with kerosene (Sigma-Aldrich 329460, reagent grade) and 50 mg/mL of trioctylphosphine oxide (TOPO) surfactant (Sigma Aldrich 223301; use of TOPO surfactant is necessary for chemical stabilization of particles based on its application to Boron suspensions in JP-10 by E et al [92] and has been used in nAl, metal oxide, and mesoparticle nanofuels in kerosene in Chapters 4 and 5). The nanofuel mixtures are agitated in a sonication bath for 5 min and magnetically stirred for 24 h for initial suspension. Samples for gravitational settling measurement by TGA are mixed in 2 mL batches (so ~20 μL used for TGA negligibly affects the sample volume) and resuspended after each settling and TGA trial by 1 min of sonication and 12 h of magnetic stirring. Nanoaluminum particle suspensions in kerosene with TOPO surfactant are mixed in the same fashion except that 30 min of sonication is used to break up primary particle aggregates. For droplet burning rate estimation, the same mesoparticles and nAl are used and mixed in 0.3 mL batches in 0.5 Dr vials with 50 mg/mL TOPO surfactant, except as noted in Table 8 where one series of 15 wt% particles samples was made with 168 mg/mL of surfactant to test a constant TOPO to particle mass ratio as 5 wt% particles in 50 mg/mL of TOPO (i.e. 1:1.18 TOPO:particles by mass).

*Table 8: Experimental samples composed of either as-received nAl nanoparticles or 95%nAl/5%NC by mass mesoparticles with electrospray precursor concentration (if applicable), nanofuel weight % particles, and surfactant loading.*

| *Sample* | *Particles and Loading (Weight %)* | | *TOPO Loading (mg/mL)* |
|---|---|---|---|
| *nAl-5* | Nanoaluminum | 5 | 50 |
| *MP50-5* | MPs: 50 mg/mL Precursor | 5 | 50 |
| *MP75-5* | MPs: 75 mg/mL Precursor | 5 | 50 |
| *MP100-5* | MPs: 100 mg/mL Precursor | 5 | 50 |
| *MP125-5* | MPs: 125 mg/mL Precursor | 5 | 50 |
| *MP150-5* | MPs: 150 mg/mL Precursor | 5 | 50 |
| | | | |
| *nAl-15* | Nanoaluminum | 15 | 50 |
| *MP50-15* | MPs: 50 mg/mL Precursor | 15 | 50 |
| *MP75-15* | MPs: 75 mg/mL Precursor | 15 | 50 |
| *MP100-15* | MPs: 100 mg/mL Precursor | 15 | 50 |
| *MP125-15* | MPs: 125 mg/mL Precursor | 15 | 50 |
| *MP150-15* | MPs: 150 mg/mL Precursor | 15 | 50 |
| | | | |
| *MP50-15** | MPs: 50 mg/mL Precursor | 15 | 168 |
| *MP75-15** | MPs: 75 mg/mL Precursor | 15 | 168 |
| *MP100-15** | MPs: 100 mg/mL Precursor | 15 | 168 |
| *MP125-15** | MPs: 125 mg/mL Precursor | 15 | 168 |
| *MP150-15** | MPs: 150 mg/mL Precursor | 15 | 168 |

### 6.2.2 Gravitational Settling Measurement by TGA

Quantitative measurement of gravitational settling is conducted using TGA to observe the aluminum loading in the top-most layer of settled suspensions after prescribed quiescent times post-mixing. The thermal behavior of the components in the nanofuels must be appropriate for the removal of all constituents other than aluminum for the measurement. To ensure this, TGA of kerosene, TOPO surfactant, NC binder, and nAl particles is taken at 10 ºC/min and shown in Figure 48. Kerosene and kerosene/TOPO are held at 160 ºC for 20 min to ensure complete kerosene evaporation which occurs below its boiling point of 190-250 ºC due to the dry Argon flow through

the instrument (after the 160 ºC hold for nanofuels and for nAl, the Argon flow is changed to air to oxidize any active aluminum). TOPO evaporates below 260 ºC, NC decomposes leaving no condensed phase weight at 194 ºC, and nAl only loses moisture weight below 400 ºC before oxidizing in two steps fully by approx. 880 ºC. Based on these behaviors, the nAl content of a nanofuel composed of nAl/NC MPs stabilized by TOPO in kerosene can be measured by ramping a sample of the suspension in the TGA at 10 ºC/min up to 160 ºC under Argon flow, holding isothermal for 20 min, then changing to air flow and ramping at 10 ºC/min to 1000 ºC. The weight remaining at 450 ºC then represents the nAl content and the final weight at 1000 ºC should be near 150% of that nAl content if that weight is only due to nAl remaining at 450 ºC (since 150% weight increase would occur upon conversion of 80% active nAl to $Al_2O_3$). An example TGA/DSC result is shown in Figure 48 for MP100-15 nanofuel and kerosene/TOPO/NC showing that the only weight remaining after 260 ºC is nAl. For gravitational settling plots, data points are compiled by mixing the appropriate sample, allowing it to settle at the TGA instrument for the prescribed time, and pipetting approximately 20 µL of sample collected from the meniscus of the sample in its mixing vial.

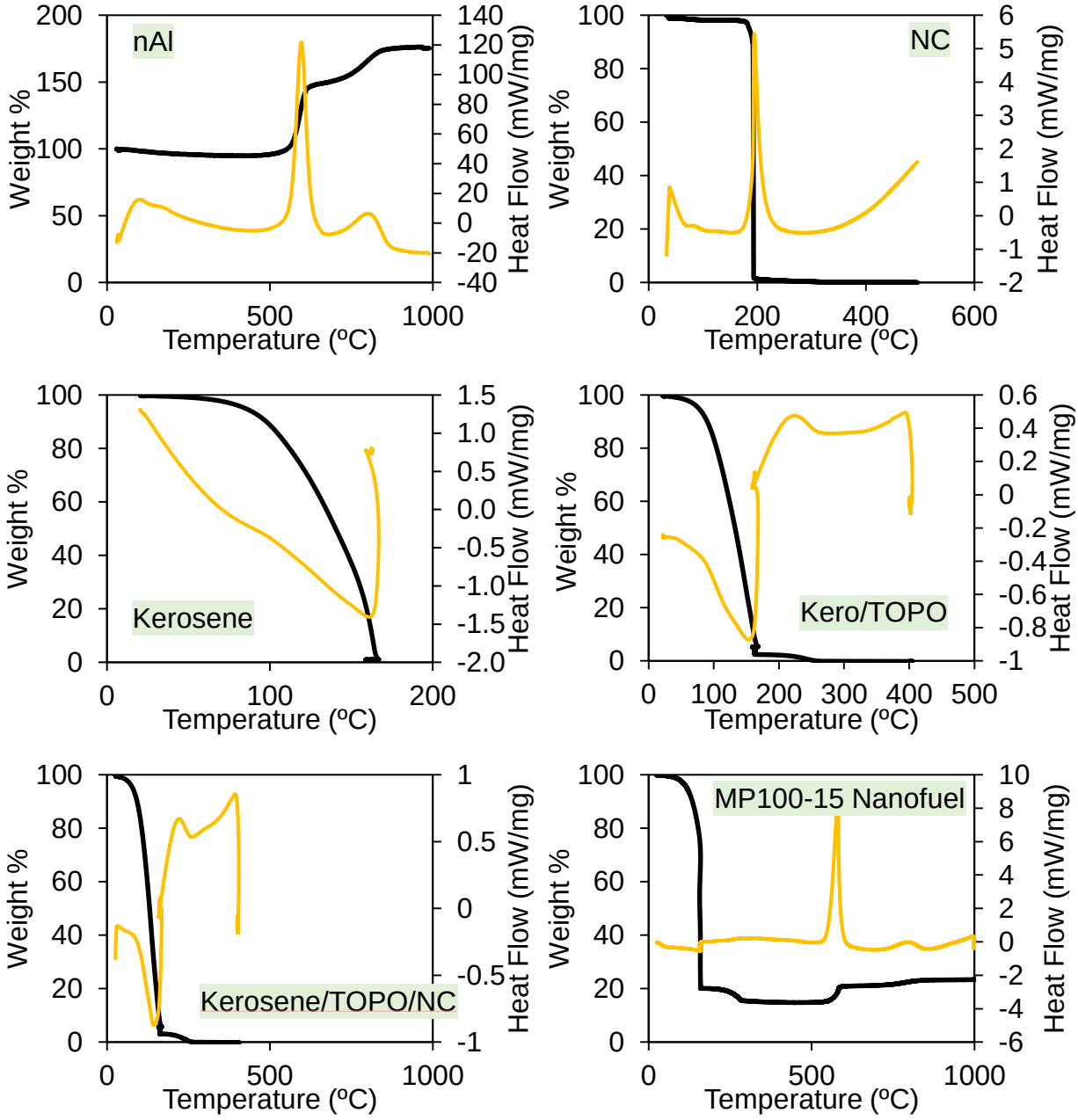


*Figure 48: Thermal behavior of nAl/NC nanofuel and its components characterized by simultaneous TGA/DSC. TGA plotted in black, DSC plotted in yellow. 10 ºC/min heating rate. Kerosene, kerosene/TOPO, kerosene/TOPO/NC, and MP100-15 nanofuel are held at 160 ºC for 20 min to ensure full kerosene evaporation.*

### 6.2.3 Free Droplet Combustion Characterization

Estimation of burning rate constants and visualization of falling droplet flame traces are performed using a free droplet combustion apparatus described at length in in Section 2.1.2. Aerodynamic shedding of droplets from a vertically oriented capillary nested in a laminar nozzle with nitrogen flow generates droplets of sample 600 µm in diameter ±50 µm at the top of a 20 in tall tower filled with oxygen gas. Falling past two methane pilot flames, the droplets ignite and are imaged with two high speed cameras, a far field camera to capture the entire droplet flame trajectory and a magnified camera which observes the generated droplet size to estimate the burning rate constant according to $K \cong {D_0}^2/t_{\text{burn}}$ within an estimated error of ±0.1 $mm^2/s$. This methodology is necessary to estimate burning rates for nanofuels which cause droplet deformations, disruptions, and gas generations since the diameter of the droplet does not represent the mass of unreacted fuel and therefore the classical $D^2$-law is not applicable.

## *6.3 Results and Discussion*

### 6.3.1 Gravitational Settling of nAl MPs versus Unassembled nAl

The default electrospray precursor concentration used in Chapters 4, 5, and 7 corresponds to MP100 samples (100 mg of particles and solute per mL of precursor). Gravitational settling of MP100-5 and MP100-15 are plotted as nAl content versus settling time near the sample meniscus in Figure 49 compared to nAl-5 and nAl-15 (same weight loadings of nAl as-received without the electrospray preassembly).

Consistent with the anecdotal findings in Chapter 4 for nAl/NC MPs in kerosene with TOPO and the photographic evidence in Chapter 5 for oxidizer/NC MPs in kerosene with TOPO, the electrospray preassembly strategy of nAl into nAl/NC MPs is directly responsible for lower gravitational settling rates compared to as-received nAl. At 24 hours of settling time, MP100-15 remains 85% suspended near the sample meniscus while MP100-5 remains 60% suspended. In both loading cases, nAl had completely settled to effectively zero particle loading near the meniscus well before 24 h from mixing (at 4 h for nAl-15 and 7.5 min for nAl-5). Noting the significantly higher settling rate of nAl versus MPs suggests, in the absence of columbic or van der Waal forces, that the ratio between mass of the settling particles (directly related to downward gravitational force) and their drag in the fluid (force opposing the downward motion affected by surface area or morphology) is greater for nAl. Possible explanations for this slower settling of MPs include a lower mass to surface area ratio from lower agglomerate density and/or size, or a morphology which increases drag in the fluid. In an aerosol particle sizing experiment, Jacob et al. have shown that the agglomerate sizes in the same commercial nAl used in this study has agglomerate sizes larger than those nAl/NC MPs made consistently with MP100 samples here, with log-normal distributions centered near 2.5 μm and 1 μm respectively [17].

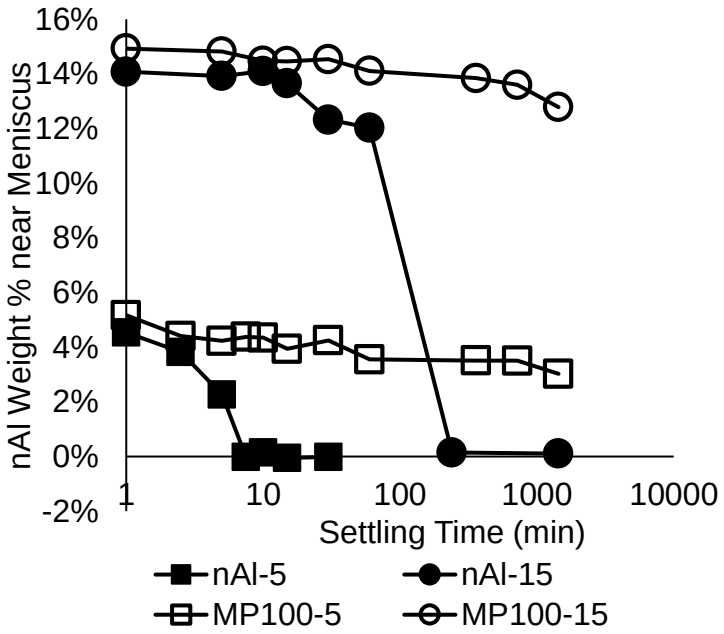


*Figure 49: Gravitational settling of nAl in kerosene stabilized by 50 mg/mL TOPO surfactant compared to nanoaluminum preassembled into NC-bound mesoparticles by electrospray before stabilization.*

6.3.2 Collection and Microscopy of MPs with Various Precursor Concentrations

Scanning Electron Microscopy is first used to compare the nAl/NC MPs electrosprayed with differing precursor concentrations and three representative images for each concentration tested are shown in Figure 50. Assuming the precursor droplet size distribution is unaffected by particle concentration variations in this range, varying the loading of the particles would change the number density per droplet and thusly increase the resultant mesoparticle size with increasing precursor concentration. Wang et al. in this group characterized the resultant MP size as nAl concentration was increased in [13], wherein MPs varied from about 3 μm in diameter to 13 μm in diameter with 50 mg/mL of nAl and 150 mg/mL of nAl in the precursor respectively. The significant difference in observed MP sizes between [13] and this work can be

attributed to the higher NC loading used by Wang et al. (10% by mass relative to nAl) which significantly effects precursor viscosity and thusly generated droplet size. Based on the evidence of [13] and the images shown in Figure 50, increasing MP size distribution with increasing precursor concentration is likely present here but cannot be conclusively shown without more precise characterization of size distributions such as those available using aerosol methods.

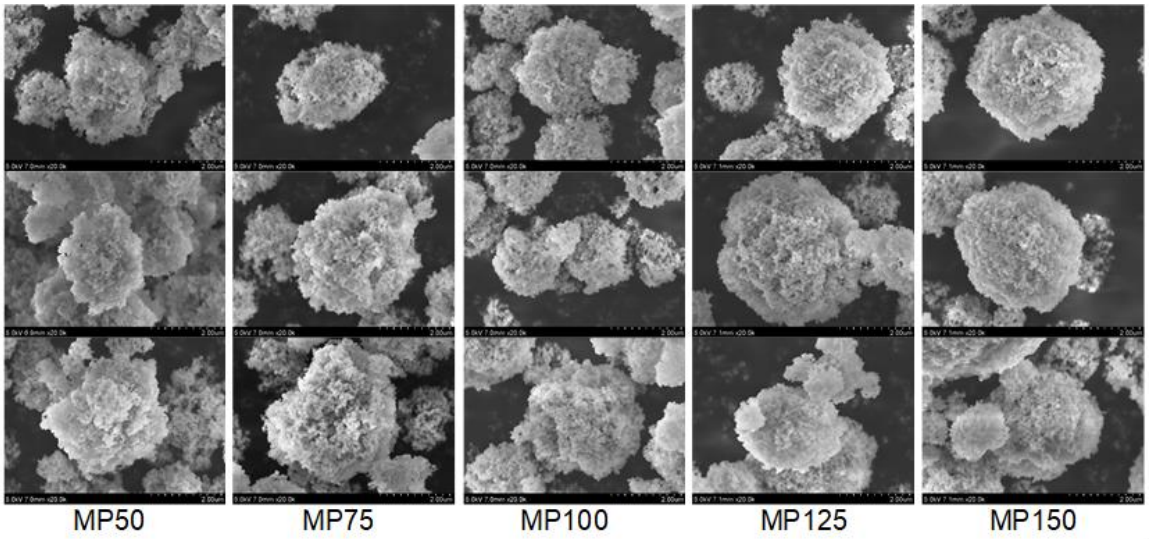


*Figure 50: Representative SEM images of nAl/NC MPs made from different precursor concentrations between 50 mg/mL and 150 mg/mL (3 images of each sample at equal magnification of x20k).*

Qualitatively evident from the SEM images in Figure 50, lower precursor concentrations accompany less spherical MPs with more irregular agglomerate shapes and higher surface roughness compared to MPs sprayed from higher concentration precursors. A possible mechanism by which this relationship results is differing evaporation times of the electrosprayed droplets. Longer evaporation times have been shown to result in smoother MP surface morphologies based on the added time for particle diffusion to organize a lower surface energy state of the resulting MP [106]. If

the higher precursor concentrations cause slightly larger electrospray droplets to form (due to slightly higher viscosity of the precursor), or if the greater particle concentration per droplet lowers the evaporation rate as has been shown for nAl particles suspended in evaporating heptane [43], then the longer evaporation time for higher precursor concentration samples can be responsible for the smoother MP surface morphology of MP150 relative to MP50.

Once the particles are collected from the foil into a sample vial, they pack together by gravity as a powder and any widespread characteristics of MP size and morphology will affect their packing density. The lower eccentricity and higher surface roughness of MP50 would cause lower packing density compared to more spherical and smoother MPs in MP150 if the specific density of the MPs themselves is consistent enough. To roughly test for differences in packing density, MP50 and MP150 were collected, weighed to measure their mass, placed in glass sample vials of known cross-sectional area, and tapped vertically against a rigid surface approximately ten times until the level of the powder stopped decreasing. This methodology roughly allowed both samples to pack according to their equilibrium packing densities under the same conditions. By measuring the height of the powders, their volume and powder density could be estimated. A photograph of the settled samples is shown in Figure 51 with density results in Table 9 showing a higher packing density of MP150 compared to MP50, thereby supporting that the higher eccentricity and surface roughness of lower precursor concentrations observed in Figure 50 are widespread throughout the samples.

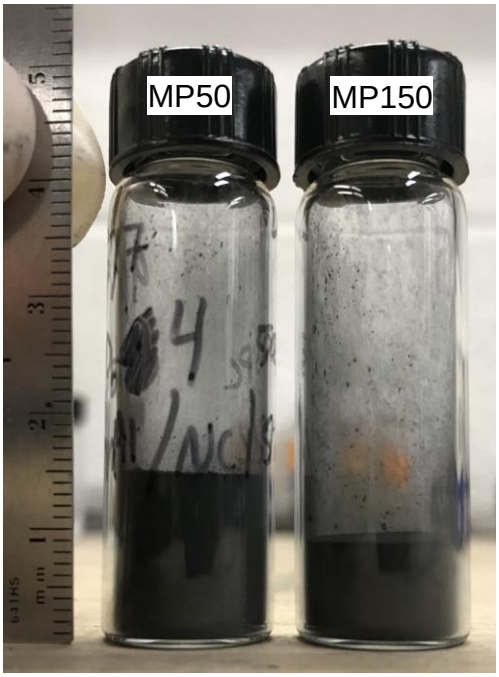


*Figure 51: Settled MP powders for packing density estimation.*

*Table 9: Estimated packing densities of MP50 and MP150 samples.*

| Sample | ES Precursor Loading | Collected Powder | | |
|---|---|---|---|---|
| | | Mass | Volume | Density |
| MP50 | 50 mg/mL | 427 mg | 1.55 mL | 0.276 g/mL |
| MP150 | 150 mg/mL | 380 mg | 1.01 mL | 0.377 g/mL |

### 6.3.3 Burning Rate and Gravitational Settling Effects of Precursor Concentration

The electrospray preassembly strategy has been shown to facilitate significantly higher droplet burning rates when NC is used as the binder in nAl MPs and the particles are suspended in kerosene with TOPO surfactant compared to burning rate declines observed with nAl mixed into the nanofuel as-received in Chapter 4. Those results linked the burning rate promotion to the presence of physical disruptions during droplet combustion during which gas is generated within the droplet from NC decomposition which swells the drop before the gas erupts, causing significant droplet deformation

and vigorously mixing the system, speeding up the usually diffusion-limited process. Relationships between MP morphology and burning rate effects are sought by changing the nAl/NC MP morphology using various electrospray precursor concentrations herein. Samples of 5 wt% and 15 wt% nAl/NC MPs are mixed into kerosene nanofuels with TOPO surfactant and time-lapse images of the falling combusting droplets are shown in Figure 52. Increased blue-white emission near droplet terminations in 15 wt% samples indicates more nAl combustion at that late stage than in 5 wt% samples. Spots along the flame trace in MP…-5 samples indicate discrete microexplosions (disruption events observed in Chapter 4) while these events in the higher loading samples are more frequent and not individually discernible. Finally, the TOPO surfactant is known to cause an orange surfactant flame and disruptive gas release events of its own as shown in Chapter 4. In MP50-15*, the mid-height orange flash is attributed to TOPO surfactant however this emission diminishes as the electrospray precursor concentration is increased up to the MP150-15* sample. Other than these small variations noted, the droplet combustion traces are generally very similar and indicate the same overall disruptive behavior across the MP samples tested.

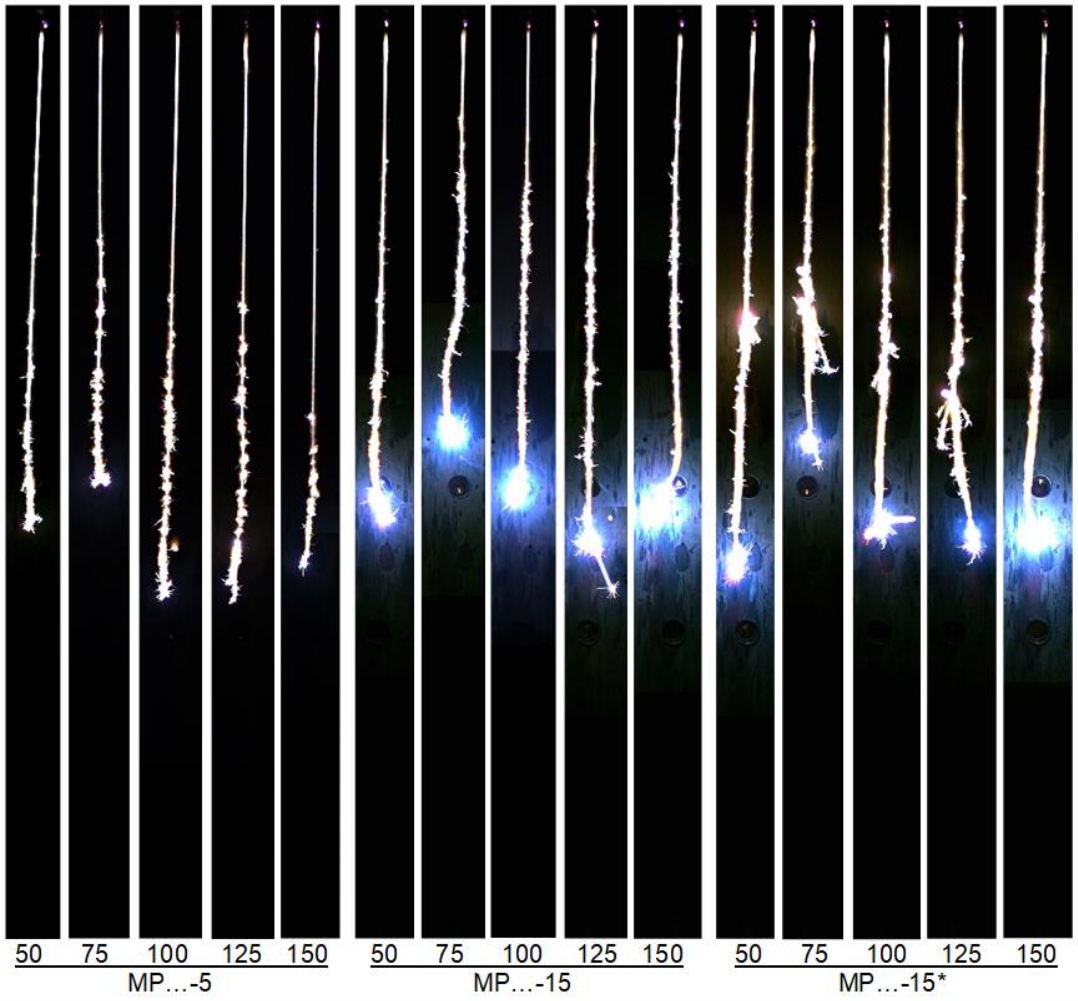


*Figure 52: Representative time-lapse images of kerosene with 95% nAl / 5% NC by mass MPs suspended using TOPO surfactant. Electrospray precursor concentrations used for each sample are listed under the images with the loading code corresponding to Table 8. "-5" signifies 5 wt% MPs and "-15" signifies 15 wt% MP with 50 mg/mL of TOPO surfactant. *168 mg/mL TOPO used to equal the TOPO:MP mass ratio = 1.18 of the MP…-5 samples*

Burning rate constants estimated for each MP nanofuel sample are plotted in Figure 53. Both MP…-5 and MP…-15* sample groups show a general decline in burning rate with increasing electrospray precursor concentration. These sample groups share the same mass ratio of TOPO surfactant to MPs (1.18). MP…-15 which has a TOPO:MP ratio of 0.39 shows no clear trend in burning rate constant relative to

precursor loading, however MP100-15 stands out with the highest burning rate of the set. Overall, each set varies within approximately 10% burning rate changes, a small range relative to changes caused by different MP compositions in Chapter 5 or particle preparation in Chapter 4.

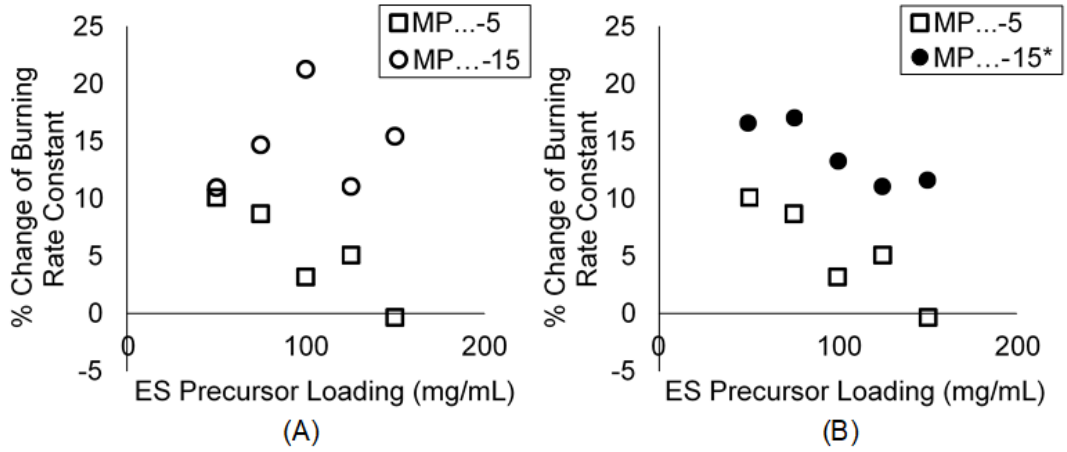


*Figure 53: Measured burning rate constants of 95% nAl / 5% NC MPs electrsprayed with various precursor concentrations suspended in kerosene using (A) 50 mg/mL TOPO surfactant and (B) a constant TOPO:MP ratio = 1.18 by mass. Burning rate change is relative to surfactant-only controls. *168 mg/mL TOPO surfactant loading.*

Gravitational settling of these nanofuel samples with different MP precursor concentrations was characterized by TGA and the nAl content versus settling time is plotted in Figure 54 for 5 wt% and 15 wt% MP loadings in the nanofuels with 50 mg/mL TOPO surfactant using nAl/MPs electrosprayed from precursors loaded to 50 mg/mL, 100 mg/mL, and 150 mg/mL. For the 5 wt% nanofuels, settling rate appears to increase with lower precursor loadings indicating slightly higher colloidal stability of MP150-5 over MP50-5. However, significant differences in suspended concentrations do not arise before 24 h suggesting that this difference in settling rate is not responsible for the trend observed in burning rate constants of MP…-5 samples. By

comparing the curves of MP50-15 and MP150-15, the same can be said regarding the settling rates indicated by the downward curvature of the data (lesser for MP150). However, data points at 1 min show that small fractions of these 15 wt% nanofuels failed to colloidally suspend at all (1.3 wt% failure in MP50-15 and 2.3 wt% failure in MP150-15).

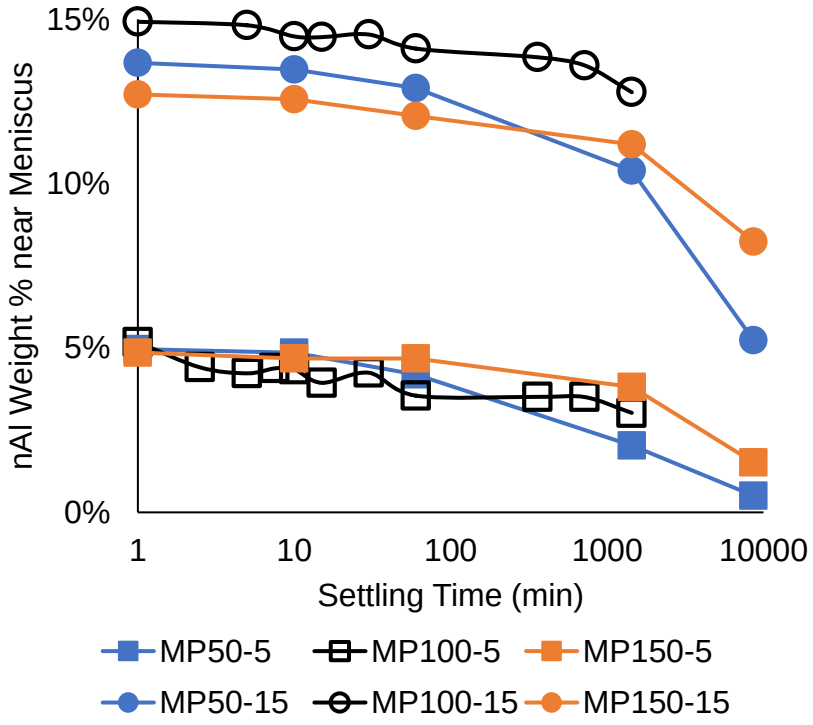


*Figure 54: Gravitational settling of nAl/NC MP nanofuels at 5 wt% and 15 wt% MP loadings with 50 mg/mL TOPO surfactant in kerosene and differing electrospray precursor concentrations of 50 mg/mL, 100 mg/mL, and 150 mg/mL.*

### 6.3.4 Microscopy of Dried Nanofuel Suspensions

Examination of solids which remain after nanofuel samples are dried can elucidate the presence and morphology of aggregates or nanoparticles suspended in these samples. In particular, samples from nAl-5, MP50-5, and MP150-5 were placed on aluminum foil during the 1 min TGA gravitational settling trials and SEM was

performed once these samples dried to examine the status of the particle suspended near the fluid meniscus shortly after stirring and SEM images of these are shown in Figure 55. Attempts were made to perform the same analysis of 15 wt% samples however SEM of these simply revealed continuous mats of overlapping settled particles owing to the high particle loading in those nanofuels and as such, information on particle aggregation was unclear. For 5 wt% samples, sections of the sample did feature similar thick mats of deposited particles but the sample concentration was low enough that in other disperse areas, particle aggregates were discrete and not stacked allowing their observation. Particle aggregation of as-received nAl the in nAl-5 sample is far more severe compared to the nanofuels made from electrosprayed nAl/NC MPs, MP50-5 and MP150-5, which explains the faster gravitational settling observed for nAl-5 and nAl-15 compared to mesoparticles. As the aggregate sizes increase in the nanofuels, their ratio of mass to surface area increases which promotes gravitational settling by favoring gravitational downward force over fluid friction forces. Both MP samples shown exhibited significant agglomerate break-up as evidenced by the presence of small nAl clusters down to a few nAl primaries compared to the nominal 1 μm diameter of electrosprayed MPs in Figure 50. Notably, MP50-5 featured direct evidence of MP survival as recognizable MP structures are observed and widespread in addition to the smaller broken pieces of MPs, which both have example images shown in Figure 55. While it cannot be conclusively determined that categorically no MPs were able to survive in the MP150-5 sample, no truly recognizable MP agglomerates were found

suggesting at the least that their survival through nanofuel mixing and drying was far less likely than for the MP50-5 sample.

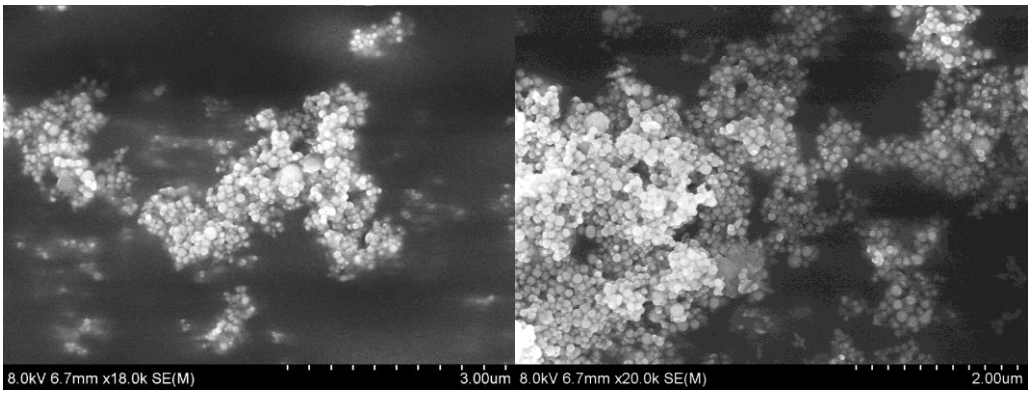


"nAl-5" (as-received nAl)

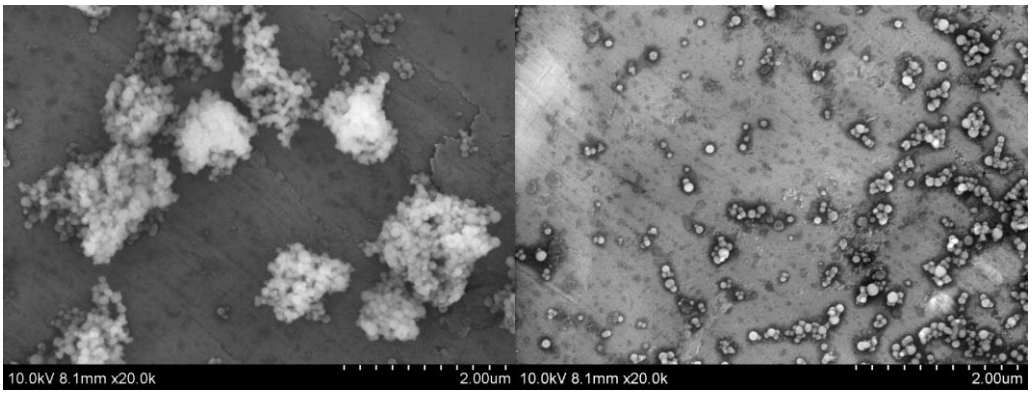


"MP50-5" (nAl/NC MPs, 50 mg/mL ES Precursor)

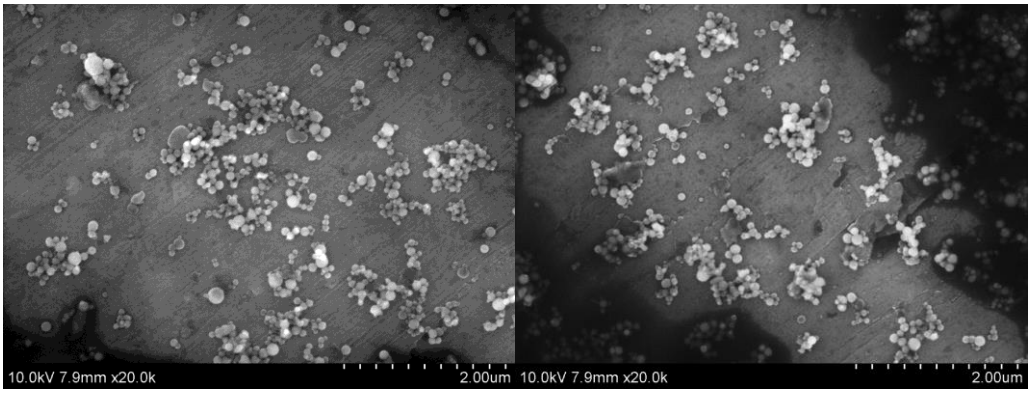


"MP150-5" (nAl/NC MPs, 150 mg/mL ES Precursor)

*Figure 55: SEM of dried nanofuels after 1 min of gravitational settling sampled near the fluid meniscus.*

### 6.3.5 Discussion

A variety of different observations were made to determine any prominent effects of varying the precursor concentration when electrospraying nAl/NC mesoparticles for kerosene nanofuel formulation with TOPO surfactant stabilization. SEM of collected powders from electrospray showed higher eccentricity and surface roughness with lower precursor loading and supported previous evidence that lower precursor loading yields smaller MP sizes [13]. A possible explanation for this is the higher precursor loadings extending the evaporation time of electrosprayed droplets which can yield smoother and more spherical MPs [106]. Longer evaporation can result from larger electrosprayed droplets caused by higher precursor viscosity with greater NC loading, or from the evaporation rate decreasing as higher nAl loadings slow solvent mass transfer rates within the evaporating droplets [43]. These differences in MP morphology and size are also supported by greater estimated powder packing density for MP150 versus MP50 herein.

Such effects of the precursor loading on the resulting MP structures could also be related to the observations made on burning rate and gravitational settling effects with the different MP precursor loadings. While the droplet combustion behavior did not drastically change qualitatively with precursor loading as seen in Figure 53, MP…-5 and MP…-15* both showed a declining burning rate with increasing MP precursor concentration while SEM of dried nanofuels suggest that the lower MP precursor loading made the MP structure more likely to survive through nanofuel mixing. The greater degree of MP break-up in the higher precursor loading MP nanofuels explains

the slightly higher long-term stability of MP150 nanofuels versus MP50 nanofuels. Namely, the smaller size of broken nAl clusters in MP150 compared to more intact MPs in MP50 would decrease their gravitational settling rate since the ratio of their mass to surface area (and thus gravitational force to viscous drag) would be lower.

The prevalence of more MP structures is also thought to promote burning rates by increasing the availability of the nAl/NC composite structures near the combusting droplet surface at an earlier time. As a combusting droplet evaporates and its surface recedes, a radial concentration gradient will form driving diffusion of particles towards the center of the droplet. This is thought to be why images like those in Figure 53 show most blue-white aluminum combustion near droplet termination because much of the additive can continue diffusing inward to remain in the droplet until liquid burn-off, something which is mitigated by vigorous mixing of gas eruption events. However, slower diffusion caused by larger particle sizes will promote more interaction of the receding droplet surface and these slower diffusing particles. Since MPs include NC which decomposes to release gas near the boiling point of kerosene, radiative heating from the flame of these outer particles nearest the droplet surface is likely to incite gas generation to cause droplet disruptions/microexplosions as discussed in Chapters 4 and 5. Once this begins to occur rigorously it is thought to create enough mixing of the entire system to accelerate further NC decomposition and repetition of the process forming a positive feedback loop. However, slower initial diffusion of agglomerates creating more interaction between the NC-bound MPs and receding liquid surface where this process was likely to begin would promote its emergence and initial rate of

occurrence which could be the reason for slower burning rates with higher electrospray precursor loadings. Comparing MP-5 samples in Figure 53 does suggests that disruptions appear to occur later for the higher precursor loading samples, as would be the case with larger MP structures surviving more in the MP50-5 sample relative to MP150-5.

To consider the magnitude of these differences between diffusion of MP50 versus MP150 suspended agglomerates, the timescale of diffusion of a 300 nm nAl sphere (meant to represent smaller broken clusters of nAl more common in MP150-5 in Figure 55) is compared to that of a 1000 nm nAl sphere (meant to represent an intact MP seen more commonly in MP50-5 in Figure 55) and the rate of droplet surface regression (a similar analysis was carried out in Chapter 4). Using the Stokes-Einstein equation for the diffusion constant, $D = \frac{k_B T}{3\pi\mu d_{\mathrm{p}}}$ and assuming the droplet viscosity is near that of dodecane ($\mu = 1.34$ mPa-s), the characteristic time for a particle to diffuse the radius of the droplet is $\tau_{\mathrm{Diff}} \approx \frac{(0.3\mathrm{mm})^2}{D}$. Resulting characteristic times are $\tau_{\mathrm{Diff,300nm}} \approx 4.8 \times 10^6 \mathrm{s}$ and $\tau_{\mathrm{Diff,1\mu m}} \approx 16 \times 10^6 \mathrm{s}$ versus approximately 0.2 s for droplet regression (equal to droplet burning times). As noted in Chapter 4, since surface regression is orders of magnitude faster than particle diffusion, interaction of the particle and droplet surface will occur. For the larger MP aggregates in MP50-5 compared to smaller broken nAl clusters in MP150-5, the diffusion of the particles is approximately three times slower, supporting the idea that the intact MPs more common in lower precursor loading samples will interact with the receding liquid surface sooner and incite droplet disruptions earlier to increase burning rate.

Lastly, a physical mechanism is proposed by which precursor loading can contribute to the propensity of MPs to break-up in mixed nanofuels. The preparation step prior to drying and observing the agglomerates in Figure 55 with the most energy imparted to the particles is the physical agitation of the nanofuels upon mixing to achieve suspension and therefore this step is the most likely to have caused particle break-up. Precursor concentration has already been shown to cause morphological differences in the MPs, most notably causing less spherical agglomerate shape, higher surface roughness, and likely smaller MPs as precursor loading diminishes. How these factors relate to drag forces on the particles depends on their flow regime. Assuming the dynamic viscosity and density of the fluid to be 0.00164 N-s/$m^2$ and 810 kg/$m^3$ respectively, Stokes' flow is valid for $Re_P$<0.1 which is valid for a 1 μm particle if the fluid velocity is below 20 cm/s which is a reasonable assumption for the fluid motion by magnetic stirring herein. The Stokes number of the particles, given by the ratio of characteristic particle relaxation time to fluid flow relaxation time, represents their propensity to follow fluid streamlines (higher likelihood for lower Stokes number). In the presence of similar flow conditions at low $Re_P$, the Stokes number of the MPs is affected by particle relaxation time $t_p = {\rho_p {D_p}^2}/{18\mu}$ where $\rho_p$ and $D_p$ are the particle density and diameter and μ is the fluid dynamic viscosity. With their irregular shape, higher surface roughness, and likely smaller size distribution, the MPs made with low precursor loadings will have lower stokes numbers than the MPs from high precursor loadings and will follow fluid streamlines more closely during mixing, thereby minimizing their motion relative to the fluid. This will decrease Stokes' drag force on

the particles given by $F_{\mathrm{D}} = 3\pi\mu D_p v$ where v is the relative velocity between the fluid and particle both by the lesser relative motion and the likely slightly smaller particle size distribution of low precursor loading MPs. Therefore, the drag forces experienced by the larger, smoother, and more spherical MPs like those in MP150 will be greater than those experienced by MP50 and the higher precursor loading MPs will be more likely to break apart, consistent with the observations made in Figure 55.

*6.4 Conclusions*

Nanoaluminum is prepared for incorporation into kerosene by electrospray with 5% by mass nitrocellulose binder to assemble "mesoparticles" of NC-bound nAl agglomerates which are suspended in kerosene with TOPO surfactant. By varying the loading of nAl and NC in the electrosprayed ethanol/ether precursor, the morphology of the resultant MPs has been affected and experiments were conducted to determine the effects of morphological changes on gravitational settling and burning rate effects of the MPs in the nanofuels including scanning electron microscopy, free-droplet combustion burning rate estimation, and thermal gravimetric analysis estimating nAl loading versus settling time. The key findings of this study are:

- Significantly lower gravitational settling rates observed when nAl is assembled into MPs before nanofuel mixing compared to as-received nanoaluminum.
- Lower precursor loadings yield higher MP eccentricity and surface roughness, likely from slightly shorter evaporation times of electrosprayed droplets.

- Such morphological differences promote more break-up of MPs made from high loading precursors during nanofuel mixing, as evidenced by SEM of dried nanofuels post-mixing, likely due to higher Stokes' drag force experienced in mixing.
- When TOPO:MP loading ratio is kept constant, burning rate constants generally decrease with increasing electrospray precursor concentration, thought to be due to easier and earlier onset of disruptive microexplosion events and resulting disruption runaway.
- An expense of the improved combustion from MPs of lower precursor loadings is slightly faster gravitational settling rates compared to those of high precursor loadings owning to their lower degree of MP breakup and thusly larger suspended particle size distribution.

*Acknowledgements*

Special thanks to fellow student Rui Xu for collecting TGA gravitational settling data for nAl and MP100 samples.

# Chapter 7: Combustion effects of nanoaluminum/oxidizer composite mesoparticles stabilized in kerosene

*Summary*

Inclusion of energetic and chemically active nanoparticles into liquid fuels and propellants is known to affect combustion dynamics of the resulting nanofuels. Recently, the activity of such nanoparticle additives has been promoted by using electrospray to preassemble such particles into nitrocellulose-bound mesoparticle (MP) clusters, of either nanoaluminum (nAl) or oxygen-carrying nanoparticle primaries. In either case, stability in kerosene with TOPO surfactant and isolated droplet burning rates estimated in a free-droplet experiment increase substantially using the MP architecture. Burning rates benefit from violent physical mixing of droplet systems which occur when the carried nanoparticles are energetic and/or chemically active, causing gas generation, additive transport to the flame, energy or oxygen release, and further gas liberation accelerating the process. In this study, this same physical underlying mechanism is seen superimposed with the effects of another advantage of electrospray: flexible control of MP composition. By mixing nAl with oxide nanoparticles to form composite MPs, these novel additives for hydrocarbons are employed to modify kerosene and their effects are found to be dependent on the oxidizer chosen. Most notably, nAl/CuO MPs show evidence of interparticle thermite reaction in the droplet system yielding a cooperative benefit of the two constituents relative to either alone in MPs. Use of oxidizer co-additives and the MP architecture

with nAl represents a flexible and promising method of overcoming low burning rates of hydrocarbons with high as-received nAl loadings and provides expansive means of tunability to tailor nanofuel properties.

*7.1 Introduction*

Improved colloidal stability and significantly higher burning rate constants have been demonstrated for nanofuels composed of both nanoaluminum (in Chapter 4) and oxygen-containing nanoparticles (in Chapter 5) specifically when such additives are prepared for kerosene inclusion by electrospray assembly into nitrocellulose-bound clusters of nanoparticles in the range of 1-5 μm nominal diameter. Similar mechanisms were also identified for both classes of nanomaterial additives: namely that the marriage of chemical benefits of the additives (either energy density of nAl or oxygen release of oxidizers) with physical droplet disruptions caused by gas generation and erupts during free-droplet combustion creates a positive feedback loop between the release of the active particles into the flame zone by these eruptions and the subsequent acceleration of further disruptions. While nAl represents added fuel density and is thought to increase the heat of combustion of the base fuel, oxidizer additives were hypothesized to be beneficial chemically because the most active candidates (e.g. $KIO_4$ and CuO) release gas-phase oxygen on the fuel-rich side of the droplet diffusion flame thereby causing faster fuel oxidation and vigorous physical mixing.

Considering the similar nature of the physical droplet disruption mechanism of both nAl and oxidizer based mesoparticle (MP) additives and the complementary aspect of their chemical roles as fuel and oxidizer respectively, these two systems

represent a prime opportunity to formulate composite particle additives with both nAl and oxidizer components. In this chapter, nAl is mixed with various oxidizer nanoparticles in a volatile precursor with dissolved NC which is electrosprayed to form composite NC-bound MPs which have previously exhibited improved combustion rates in dry powder experiments versus physically-mixed analogs [13, 14, 16, 17, 107]. These "thermite" MPs are added to kerosene and stabilized with TOPO surfactant to assess effects on the free-droplet combustion by direct observation and estimation of burning rate constants relative to those of MPs with only nAl or oxidizers presented in Chapters 4 and 5. The role of the MP preassembly strategy is also evaluated for such thermite nanoparticle mixtures by comparing their activity in kerosene nanofuels with that of non-electrosprayed nanoparticles.

## *7.2 Experimental*

### 7.2.1 Particle Additives and Nanofuel Preparation

Energetic nanoparticles are prepared for kerosene (Sigma-Aldrich 329460, reagent grade) incorporation in this study using electrospray to generate a relatively monodisperse cloud of volatile precursor solution as described at length in Section 2.2.2 and first utilized for energetic nanoparticle modification by Wang et al. [13]. The precursor consists of a 3:1 mixture of ethanol and ether by volume with the particles of interest suspended by in-situ magnetic stirring within the syringe and NC binder dissolved in solution (5% NC binder by mass relative to nanoparticles). nAl, CuO, $Al_2O_3$, and MgO are purchased commercially as nanoparticles and utilized as-received

(nAl: Novacentrix, Inc., 80% active Al with 2-5nm oxide shell; CuO, MgO, and $Al_2O_3$: Sigma-Aldrich 544868, 549649, and 544833 respectively with <50 nm particle size shown in Figure C.1). $KIO_4$ (Sigma-Aldrich 210056) and AP (Sigma-Aldrich 208507) are purchased as solid powder reagents and are reformed into nanoparticles by spray drying aqueous solutions of each (4 mg/mL $KIO_4$ and 50 mg/mL AP) from a venture-style collision atomizer through a silica desiccant diffusion dryer and into a tube furnace at 200 C for $KIO_4$ and 150 C for AP before collecting in an in-line 400 μm membrane filter [105]. Resulting $KIO_4$ nanoparticles on the order of 0.1-1 μm primary particles in agglomerates of 0.5-10 μm are shown in Figure B.1. Stoichiometric mixtures of nAl and each oxidizer were added to the electrospray precursor solutions at 95 mg/mL (with 5 mg/mL of NC binder for a constant electrospray precursor loading of 100 mg/mL), sonicated for 1 h, and magnetically stirred overnight. Pumping the precursor though a probe needle charged to 10 kV situated 10 cm from a -10 kV aluminum foil substrate generates a cloud of precursor droplets as repulsive charge accumulation on the fluid overcomes surface tension and the cloud is electrostatically attracted to the substrate. Evaporation of the precursor solvent in-flight leaves the aggregated mesoparticles bound by precipitated NC binder. Representative SEM images of nAl/Oxidizer/NC MPs made for this study are shown in Figure 56.

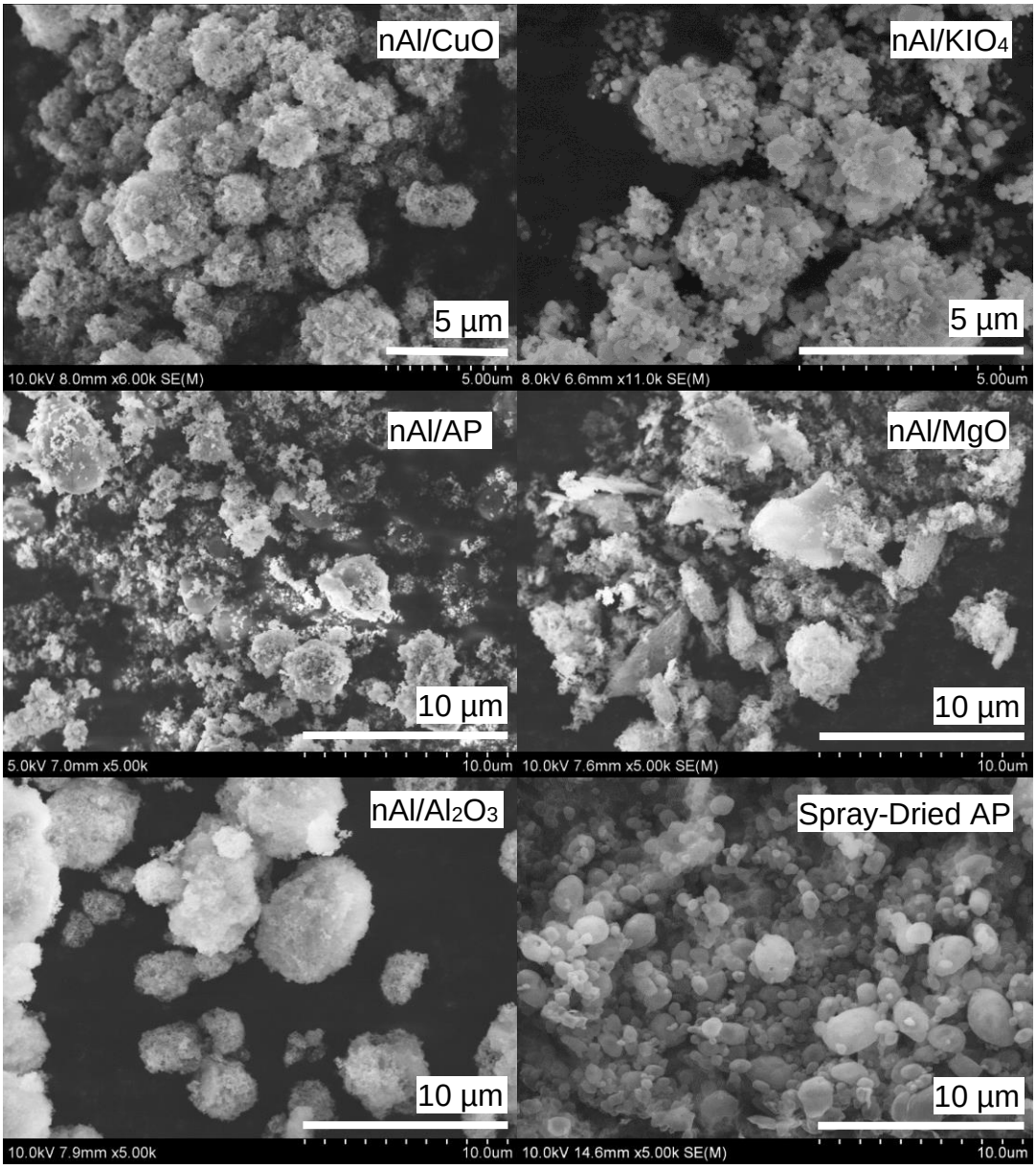


*Figure 56: SEM images of MP samples collected from electrospray of nAl with various oxidizers and NC binder (and spray dried AP nanoparticles).*

The electrosprayed MPs are added to kerosene in 0.3 mL batches at the concentrations shown in Table 10 with 50 mg/mL of TOPO surfactant (Sigma-Aldrich 223301) which has been necessary to stabilize nAl and nAl MP nanofuels in kerosene. The surfactant loading is not varied with particle additive loading so as not to modify

the combustion characteristics of the base kerosene/TOPO fuel. With MPs and TOPO added to the kerosene, the nanofuels are sonicated for 5 min and magnetically stirred 24 h before droplet combustion experiment are carried out. Nanofuel particle loadings were based on equal nominal loadings of the nAl component and the appropriate oxidizer loading to comprise a stoichiometric mixture as determined by considering full conversion of the 80% active nAl to $Al_2O_3$ and kept just low enough to prevent capillary clogging of the nAl/CuO samples (which feature the highest mass loading). To compare each of these four loading classes to each other, data are plotted against "oxygen demand" referring to nAl loadings and/or "oxygen concentration" referring to an oxidizer loading. Physical mixtures were also formulated from the as-received commercial nAl with either CuO, MgO, or $Al_2O_3$ for comparison with their MP analogs by mixing of the nanoparticles with kerosene and TOPO in the same proportions as the MP nanofuels. Data on nAl-only and Oxidizer-only MPs is available from Chapters 4 and 5 for all samples except AP. Therefore, nanofuels were also tested herein with AP-only MPs and spray-dried AP nanoparticles as shown in Table 10.

*Table 10: Sample compositions and loadings for nanofuels of nAl/Oxidizer/NC MPs, nAl/Oxidizer physical mixtures, and AP-only MPs or nanoparticles tested.*

| | **Particle Compositions by Mass** | | **Particle Loadings in Nanofuels (wt%)** Each Column Based on Nominal nAl Concentration (mg/mL) of: | | | |
|---|---|---|---|---|---|---|
| | % nAl | % Ox. | 10 | 20 | 30 | 40 |
| **NC-bound MPs** | | | | | | |
| nAl/CuO/NC | 21 | 74 | 5.6 | 10.6 | 15.0 | 19.1 |
| nAl/$KIO_4$/NC | 27 | 68 | 4.4 | 8.5 | 12.2 | 15.6 |
| nAl/AP/NC | 41 | 54 | 2.9 | 5.7 | 8.3 | 10.7 |
| nAl/MgO/NC | 34 | 61 | 3.5 | 6.8 | 9.8 | 12.7 |
| nAl/$Al_2O_3$/NC | 38 | 57 | 3.2 | 6.1 | 8.9 | 11.5 |
| nAl/NC (for CuO) | 81 | 0 | 1.5 | 3.0 | 4.4 | 5.8 |
| nAl/NC (for $KIO_4$) | 84 | 0 | 1.4 | 2.8 | 4.2 | 5.5 |
| nAl/NC (for AP)***** | 89 | 0 | 1.4 | 2.7 | 4.0 | 5.3 |
| nAl/NC (for MgO)***** | 87 | 0 | 1.4 | 2.8 | 4.1 | 5.4 |
| nAl/NC (for $Al_2O_3$)***** | 88 | 0 | 1.4 | 2.7 | 4.0 | 5.3 |
| AP/NC | 0 | 92 | 1.7 | 3.4 | 5.0 | 6.6 |
| **Physical Mixtures** | | | | | | |
| nAl+CuO | 22 | 78 | 5.3 | 10.1 | 14.4 | 18.3 |
| nAl+MgO | 36 | 64 | 3.3 | 6.5 | 9.4 | 12.1 |
| nAl+AP | 43 | 57 | 2.8 | 5.4 | 7.9 | 10.2 |
| AP | 0 | 100 | 1.6 | 3.1 | 4.6 | 6.1 |

7.2.2 Free-droplet Combustion Characterization

As described in Section 2.1.2, combustion of the nanofuels is studied utilizing a free-droplet burning apparatus in which droplets are ignited at the top of a 20-inch-tall tower filled with oxygen as they fall past two methane igniter pilots. This experimental framework avoids the interference of a suspension filament used in stationary droplet burning experiments and facilitates estimation of a burning rate constant despite the presence of gas generation within droplets and disruptive gas eruption events common upon energetic solid addition which obscures the classical droplet-diameter-based measurement of burning rate. This is accomplished by the approximation for the burning rate constant $K \cong {D_0}^2/t_{\mathrm{burn}}$, recorded by a one high-speed camera capturing the flame trace to measure burn time and another zoomed on

the initially generated droplet size to account for small variations in the size droplets formed by aerodynamic shedding from a vertical capillary (600 ± 50 μm).

An alternative camera configuration to collect magnified videography of burning droplets as they fall past a high-speed camera as used in Chapter 5 to garner information on droplet deformations and disruptions to better understand mechanisms of the additives. However, that configuration with a stationary camera suffered from short viewing times as the droplets enter and exit the static field of view. An updated apparatus variation is utilized herein and shown in Figure 18 in which the color high-speed camera with a macro lens is attached to an aluminum vertical translation stage which slides free on two linear bearings. With foam below to safely decelerate the stage and camera, they are repeatedly raised and dropped while a train of droplets fall and combust. When the heights of the camera and a falling droplet are similar, the viewing time of the droplet is drastically increased compared to static camera tests, as far as some trials in which the entire droplet lifetime from ignition to termination is imaged.

Emission spectroscopy of excited flame species can identify specific compounds reacting and/or heating in the droplet flames. Further utility of such information is available if the spectra collected is time-resolved on a scale relevant to droplet disruption events. As described in Section 2.3.3, a fiber optic cable and collection lens is affixed to the camera's vertical translation stage to collect emission spectra from droplet flames in the field of view of the camera (fiber collection diameter in the plane of the droplets is approximately half the vertical height of the camera field of view and is oriented to collect spectra when droplets are in the top half of the camera

frame). To achieve high time resolution, the spectrometer was designed and assembled in-house using a spectroscope (Acton SP 500i) and a 32 channel PMT array interfaced with a high-speed data acquisition system (Vertilon IQSP 580) to acquired intensities of light in the wavelength range of 473 – 502 nm. The sample rate on the acquisition system was set at 5000 Hz, sufficient speed to resolve effects of sub-millisecond disruptions in the droplet flame.

## *7.3 Results and Discussion*

### 7.3.1 Droplet Burning Rates and Observations

Effects of thermite additives are assessed first by examining far-field color images of the burning droplets, shown as representative time-lapse images of a full droplet flame trace for each sample in Figure 57, including those of oxide/NC MPs reproduced from Chapter 5 for comparison. Qualitatively, thermite MP additives cause similar droplet disruptions to both nAl/NC MPs and oxide/NC MPs characterized by stochastic expansions of the flames and ejected emitting particles. Each thermite type also appears similar to its respective oxide MP in general flame color and disruption timing with respect to the lifetime of the droplet. However, relative to either nAl or oxides alone in MPs, thermites generate feature larger amplitudes of the flame expansions with disruptions and the added nAl is specifically to blame for more widespread brilliant white emission and more significant brilliant while termination bursts characteristic of aluminum combustion in these droplet experiments. Noted in Chapter 5, CuO, $KIO_4$, and MgO are all active oxides which increase kerosene burning

rates when added as MPs compared to adding the oxides as nanoparticles. $Al_2O_3$ MPs were observed to cause trivial effect as evident in its time-lapse, and AP MPs tested here in kerosene/TOPO also cause little droplet disruption. While the nanofuels of $Al_2O_3$ thermite MPs still appear to burn relatively slow evidenced by the long flame trace, they do exhibit a few more emission flares and the nanofuels of nAl/AP MPs appear to burn significantly more disruptively than those of AP/NC MPs, more resembling nAl/NC MPs.

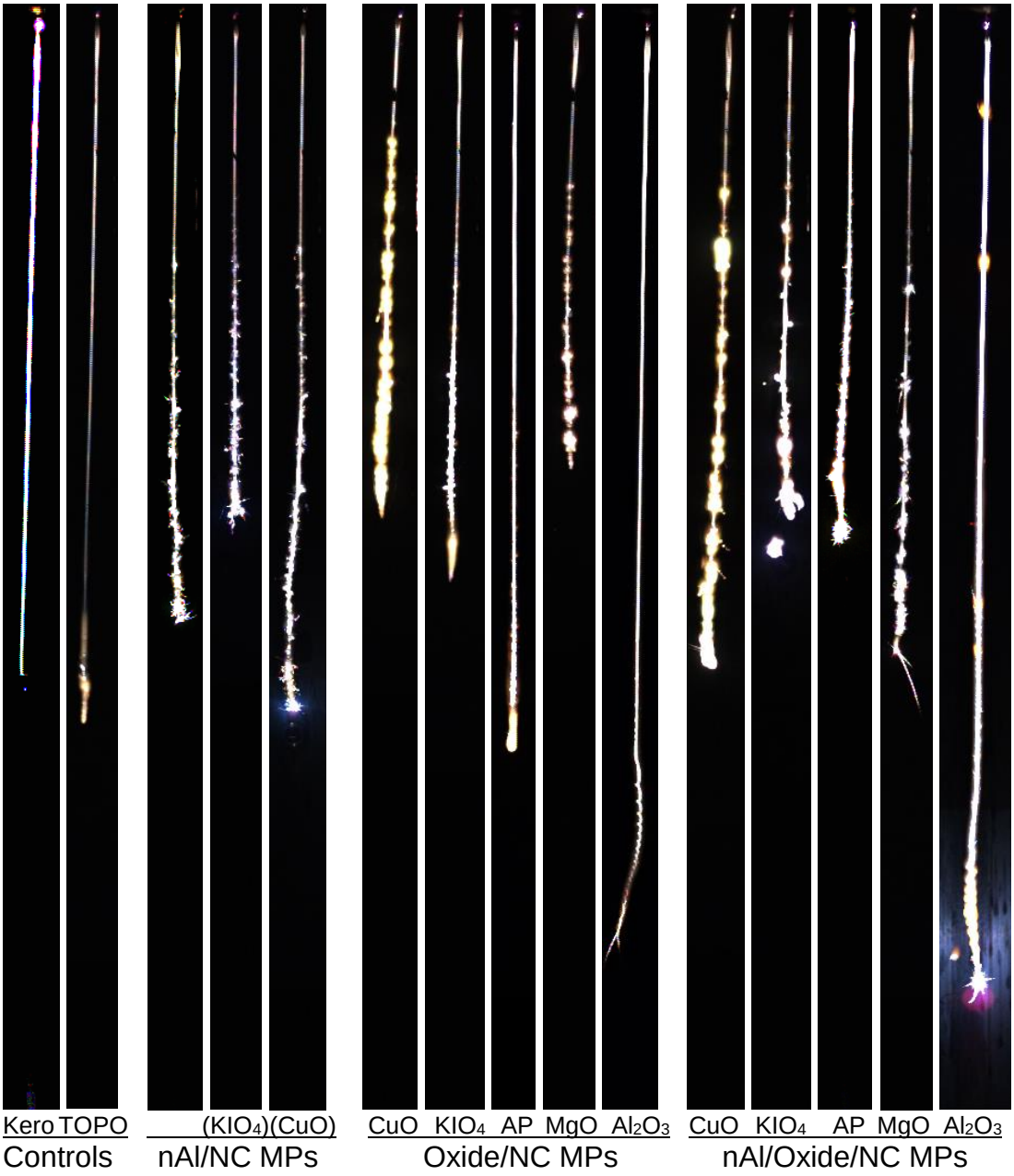


*Figure 57: Representative timelapse images of flame traces from nanofuels composed of various additive particle types including control samples (no particle additives), nAl/NC MPs and Oxide/NC MPs (from Chapter 5) with NC% to match content in respective thermite MPs, and the nAl/Oxide/5%NC Thermite MPs.*

Burning rate constants estimated based on the generated droplet size and burning times of multiple droplets per sample provide a more quantitative basis to

compare effects of the various thermite additives. Data for thermite MPs tested are shown in Figure 58 plotted relative to each other and shown as MP samples relative to physically mixed samples of nAl and oxides (for CuO, MgO, and AP systems). In both cases, estimated burning rate constant changes compared to surfactant-only droplets are shown versus oxygen demand/content, i.e. the four particle loading levels shown in Table 10. nAl/$Al_2O_3$ MPs in the highest loading class was not tested as it repeatedly clogged the sample delivery capillary. Overall, thermites of CuO and $KIO_4$ with nAl exhibited the highest burning rate increases which follows observations of oxide/NC MPs in Chapter 5. AP thermites showed a positive trend between loading and burning rate increase while MgO thermites showed a generally negative trend with this respect and both burned slower than CuO and $KIO_4$. Lastly, $Al_2O_3$ thermites has not discernible trend and hovered around zero effect. For the three thermites tested as both MPs and physical mixtures, a primary finding of Chapters 4 and 5 is further supported: that the MP architecture facilitates significantly higher burning rates than unassembled particles added to kerosene with TOPO surfactant.

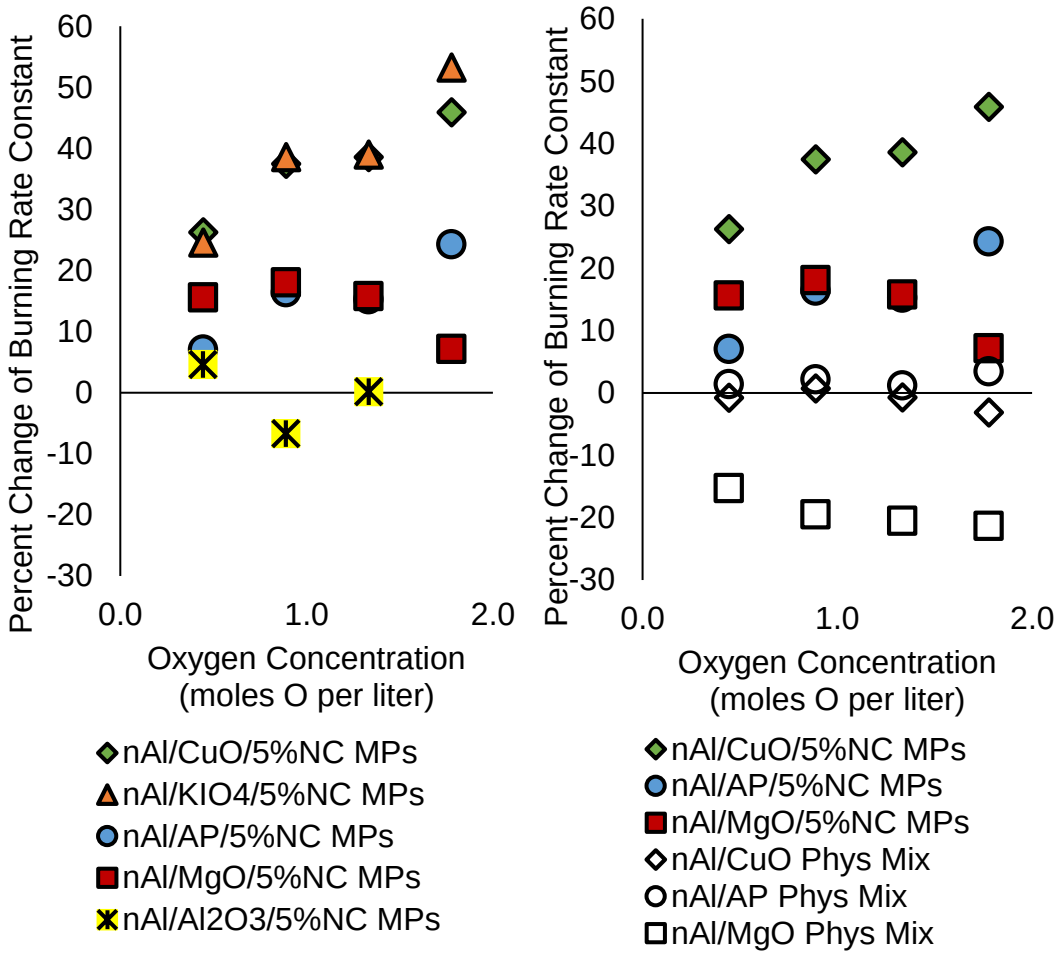


*Figure 58: Burning rate constants of nAl/Oxide/5%NC MPs of various oxide composition and comparison with physical mixtures*

This data is further deconvoluted by considering the different oxides individually as shown in Figure 59 for all except $Al_2O_3$ (shown in Appendix C to be cause minor change compared to control burning rates). CuO thermites burn faster than both nAl-only and oxide-only MPs suggesting that neither fuel nor oxidizer is individually dominant in the composite system and instead they may feature a cooperative effect which follows from their frequent use as nanothermite components. $nAl/KIO_4$ also constitutes an energetic nanothermite formulation [104, 108], but the

nanofuel composed of MPs of this thermite show burning rate constants overall similar to oxide-only MP nanofuels (with a slight but inconclusive benefit of the thermite at high loadings only). Compared to the nAl/CuO thermite, this suggests that nAl and KIO4 in this combusting droplet system is not as reactive or has less of a cooperative effect of the two components and instead the droplet burning is dominated by the activity of the oxidizer. AP/NC MP nanofuels cause a relatively low burning rate increase around 10% which does not appear to scale with particle loading. The burning rate improvements are increased when nAl is added in the thermite MPs however both AP-containing MP additives cause lower burning rate increases than nAl/NC alone suggesting that the metal fuel is the most active component which compensates for the less active oxide. A contributing factor to the lower activity of AP compared to the other proven oxidizers, CuO and $KIO_4$, is its poor particle morphology, i.e. the significantly larger size of AP particles which decreases their interfacial contact with fuel species (as seen in Figure 56). MgO thermite MPs show a fourth possible effect such additives: a negative relationship between nAl/MgO MP loading in the nanofuel and realized burning rate increases. MgO also features large particle sizes like AP, however, MgO is also not thermodynamically expected to react with the nAl fuel, unlike the other three oxidizers discussed above. As such, no possible exothermic interparticle reaction is present to compensate for lower mass diffusion rates caused by increased solid particle loadings and the MgO and nAl have a cooperatively negative effect on burning rate increases observed for one component or the other in MPs.

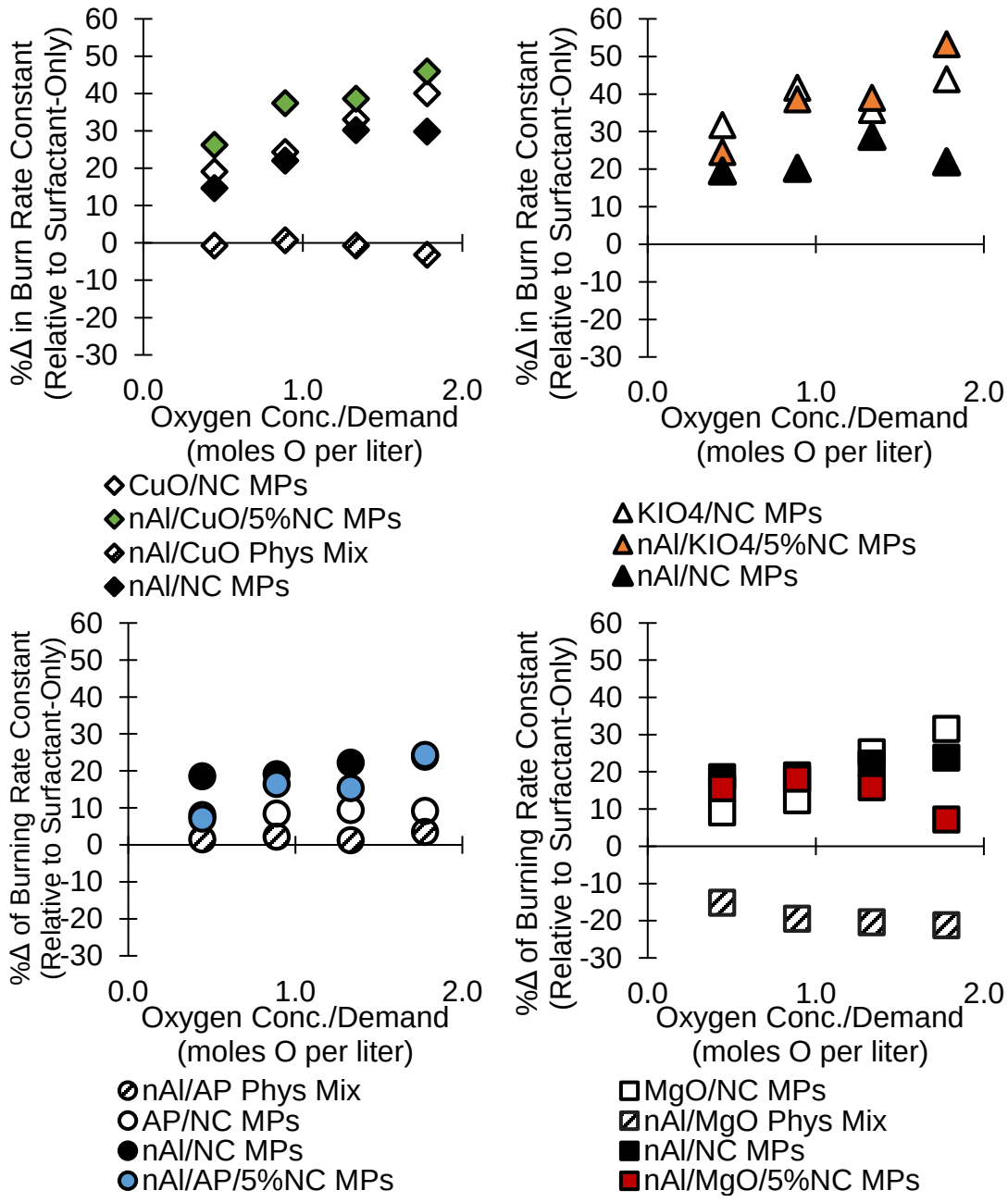


*Figure 59: Burning rate constants of various nanofuel types sorted by respective oxide composition with Oxide/NC MP data from Chapter 5.*

7.3.2 Magnified Videography and Flame Emission Spectroscopy

The alternate configuration of the high-speed cameras together with an emission spectrometer discussed previously yields added information about the way each additive studied here perturbs kerosene droplet combustion (which is seen in Chapters 4 and 5 to be otherwise steady and disruption-free). Select frames from magnified videos of combusting droplets with various additives are made available in Appendix C. Observations for nAl/CuO MPs and nAl/$KIO_4$ are exemplified by Figures 60 and 61.

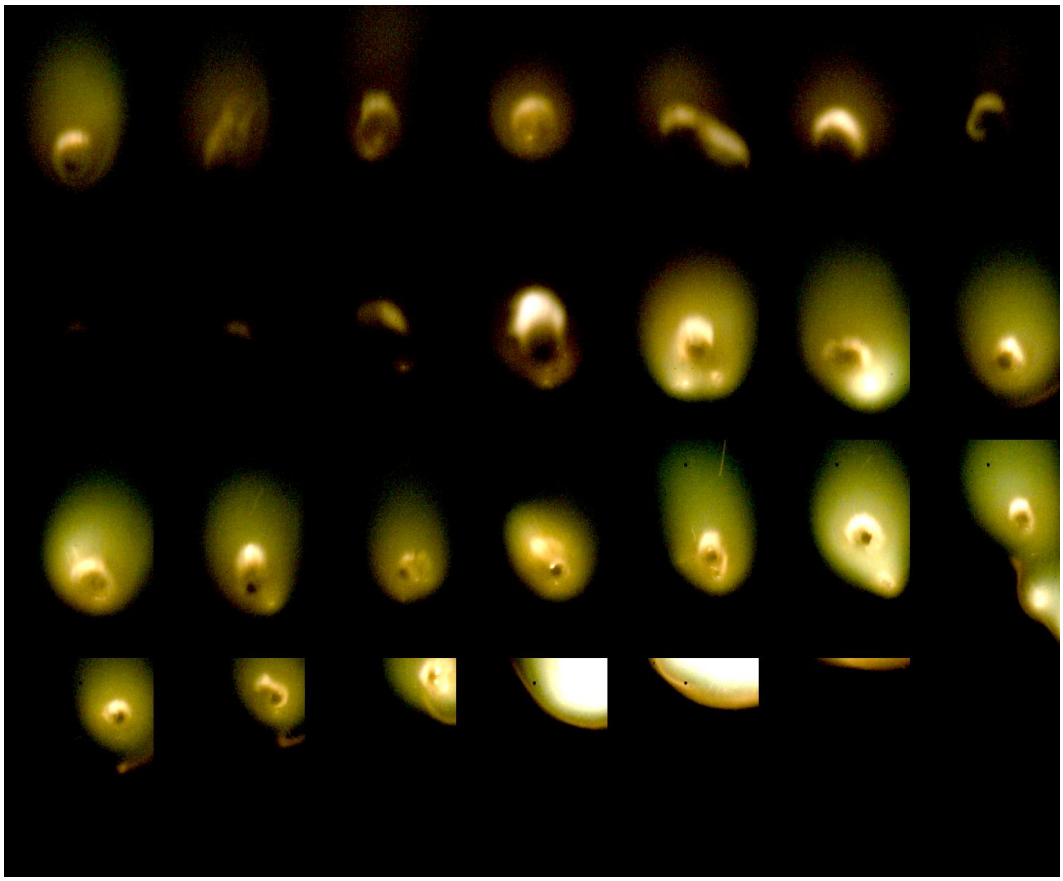

*Figure 60: nAl/CuO/5%NC MPs in kerosene/TOPO (Droplet D). 114.0 to 137.6 ms burning time shown with 0.909 ms period. 3X brightness shown.*

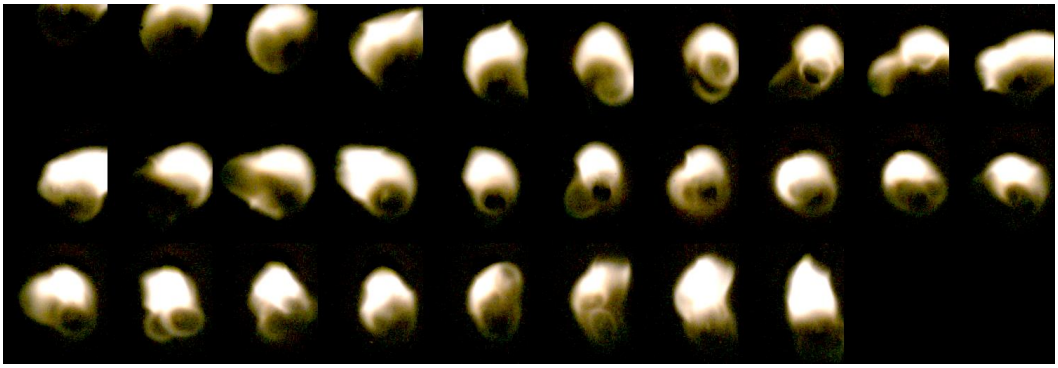

*Figure 61: nAl/$KIO_4$/5%NC MPs in kerosene/TOPO (Droplet H). 104.4 to 112.6 ms burning time shown with 0.303 ms period. 3X brightness shown.*

nAl/CuO MP-laden droplets exhibit gradually accelerating and increasingly violent "microexplosion" events consistent with eruptions seen with CuO/NC MPs in kerosene (Chapter 5) characterized by droplet shape deformations, flame perturbations with significant added green and orange emission from copper species. Meanwhile, nAl/KIO4 MP nanofuels also exhibit disruptions consistent with those of the oxide-only MPs studied previously which are higher frequency and lower amplitude than those of CuO without a large component of atomic emission readily visible in camera footage. In Chapter 5, these differences were proposed to be caused by the lower oxygen release temperature of $KIO_4$ which promoted its activity in the gas phase more evenly in time compared to CuO which survived into the flame region as a solid to rapidly release its oxygen content more stochastically and violently in time. Both additives featured their most violent and brightest disruption at the termination of the droplet with large bursts of emission (shown in Appendix C). This termination burst with nAl/CuO MPs maintains the orange and green dominant emission color while the nAl/$KIO_4$ instead show a high degree of brilliant white/blue emission with widely

dispersed particles suggesting a high degree of nAl combustion in this termination event. Nanofuels with MgO-based thermite MPs burn disruption-free for an initial period before slowly causing gas eruptions from the droplet which are accompanied by particles spot emissions also seen with MgO/NC MPs suggesting this is primarily MgO heating and emitting in the flame, possibly with some surface reduction by high-temperature reactive flame species like CO and $H_2$. Termination of nAl/MgO MP-laden droplets feature the brilliant white/blue emission of combusting nAl with significant orange spot emissions around and attached to the droplet likely caused by hot MgO particle agglomerates. nAl/AP MPs in kerosene burn with a short initial disruption-free period soon followed by onset of small gas eruptions with consistent release of emitting particles. In general, these droplets are significantly less violent than those of CuO and $KIO_4$ but release far more discrete emitting particle tracers. Their terminations also do not feature a large burst but instead a gradual fade of the flame. Based on these observations nAl and AP seem to react with each other throughout the disruptive period of the droplet combustion (evidenced by the lack of large nAl combustion burst upon termination), but do so relatively slowly which cause the particle tracer emissions and follows from the large primary particle size of the AP. Notably, the disruptions are significantly lower amplitude than say those of nAl/CuO MPs possibly owing to a weaker feedback loop formed between NC decomposition to droplet gas release, disruption, particle transport into the flame, and chemical activity of the particles in the flame which cause further disruptions (by increased physical mixing or combustion heat release locally). Finally, nAl/$Al_2O_3$ thermites in kerosene/TOPO burns steadily for

an extended period with infrequent bursts of particle emission from the flame before a bright particle burning flash upon termination. This behavior alludes to a complete breakdown of the aforementioned feedback loop in which the infrequent particle releases, which in the other systems would start the feedback loop, fail to incite the acceleration of subsequent disruptions. Agreeing with conclusions of Chapter 5, this result supports the requirement that the particles carried in the NC-bound MP structure be inherently active in the droplet flame system in such a way that their release perturbs the system enough to directly cause further disruptions, so that the process is self-accelerating.

Figure 62 depicts sample emission spectra collected during high-intensity events for thermites of CuO, $KIO_4$, and MgO. No appreciable atomic emission was collected by the spectrometer for thermites of AP and $AL_2O_3$ and thusly only the spectroscopy of the former three is discussed. The atomic species noted in the emission spectra and highlighted in the sample spectra shown are CuO at 477 nm, AlO at 484 nm, $Cu_2$ at 490 nm, KH at 480 nm, $Na_2$ at 492-496 nm (a common contaminant), and MgO at 500 nm [109]. To track the occurrence of these emissions in time during droplet combustion observations, baselines for each spectrum are fit to the data outside the windows of atomic emission of interest. Comparing the actual data to the interpolated data on the baseline in each window of atomic emission, the peak areas are integrated using the trapezoid method in MATLAB and these integrated peak intensities can be plotted versus burning time of the droplet in view for multiple droplets observed at separate times as shown in Figure 63. The overlaid emission signals of different

droplets are labeled by letters corresponding to video frame montages shown in Appendix C.

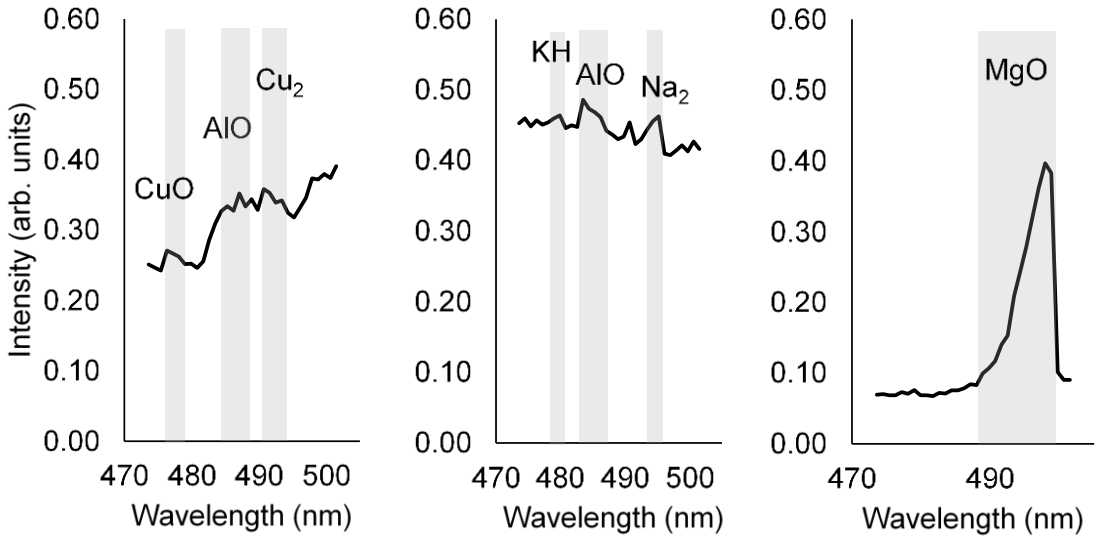


*Figure 62: Sample spectra collected between 473 nm and 502 nm (over 32 channels) from flame emission of nAl/CuO/NC MPs, nAl/KIO4/NC MPs, and nAl/MgO/NC MPs. Shaded regions denote expected atomic emissions based on [109].*

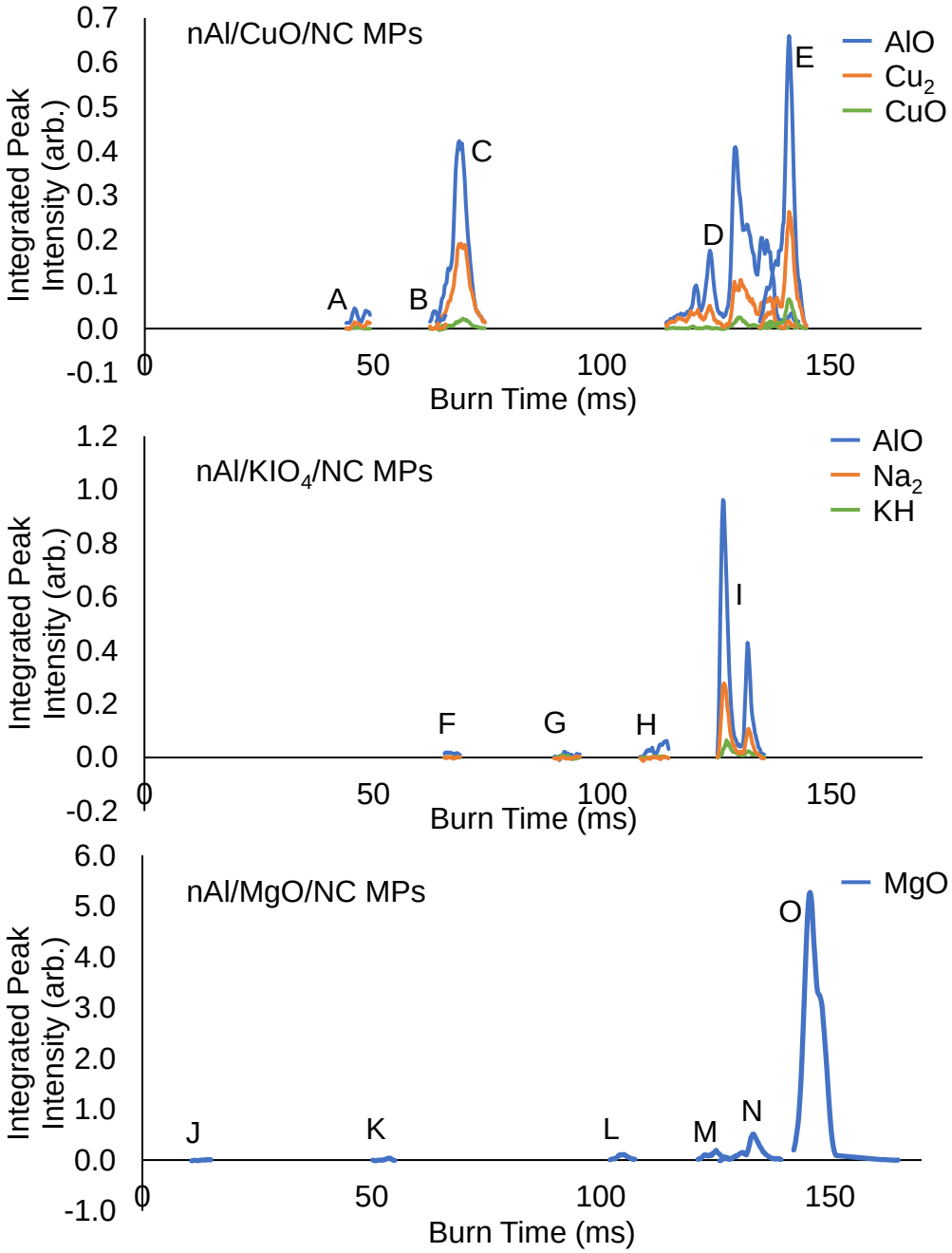


*Figure 63: Integrated emission peaks for atomic emission of nAl/CuO/NC MPs, nAl/KIO4/NC MPs, and nAl/MgO/NC MPs flames plotted versus droplet burning time for multiple droplets tested (labeled alphabetically). Droplets E, I, and O terminated in the field of view. All droplets are seen burning disruptively except J (K only slightly). Frame montages shown in Appendix C.*

nAl/CuO/NC MP-laden droplets (A-E) shown in Figure 63 with video frames in Appendix C (except droplet D which is depicted in Figure 60) spanned various droplet burning times and the emission detected for each is compared to the qualitative nature of the combustion observed in video. Droplets A and B feature 2-3 slight flame perturbations each with relatively small flame expansions, otherwise burning steadily disruption-free. In both cases, AlO, $Cu_2$, and CuO emission levels were very low indicating relative low metallic reaction rates. Droplet C is undergoing a moderate microexplosion/eruptions with green/orange color emission attached around the flame tail with 2-3 spots of particle emission as it passes (similar to microexplosions in Chapter 5) and notably, this droplet released significantly higher atomic emission intensities suggesting that the more stochastic high-volume gas eruption events or "microexplosions" are a primary vehicle transporting metal species into the flame zone. This idea is reinforced by droplet D which shows multiple moderate microexplosions transitioning into more rapid disruption repetition cycles immediately preceding a termination burst. The emission signals for this droplet can be seen fluctuating based on the occurrence of microexplosions. A strong droplet termination burst is directly imaged in droplet E after remnants of moderate microexplosions and of the five droplets captured for this sample, the termination point exhibited the greatest atomic emission intensity providing evidence that significant particle loadings still remain in the droplet prior to liquid burn-off before they ignite, similar to nAl-only per Chapter 4. In all these droplets, the three atomic emissions scale directly with each other suggesting a coupling of the chemical activity or at least the presence of nAl and CuO

in the flame. The significant $Cu_2$ emission further proports oxidation of the CuO by either nAl or flame species.

Droplets captured in this manner loaded with nAl/$KIO_4$/NC MPs generally featured lower relative emission levels for AlO than nAl/CuO/NC MPs prior to the final termination stage. Droplets F, G, and H show the small scale, high frequency flame perturbations characteristic of $KIO_4$/NC additives with increasing intensity for each droplet which are captured over increasing droplet burning times (H shown in Figure 61). Atomic emission intensities increase slightly with the increasing disruption amplitudes of these three droplets, but remain very low compared to emission near termination as shown in droplet I. Images of this droplet show detailed termination characterized by large outbursts of brilliant combusting particle emission in all directions 3 times including divergence of the droplet into two drops upon the second burst. The vast majority of AlO, $Na_2$, and low levels of KH are observed during these termination bursts showing that contrary to CuO-based thermite MPs, the earlier disruptions incited by these nAl/$KIO_4$/NC MPs are not a strong particle transport mechanism and instead most of the nAl at least reaches the flame near termination. Sodium is a common contaminant which emits strongly in flames, seen often with KIO4 additives here and in Chapter 5. KH is a strong base which reacts with oxygen to form KOH and $H_2$ and therefore is likely a reaction intermediate after $KIO_4$ decomposition sensed only slightly during the high intensity termination bursts.

Lastly, MgO-based thermite MPs in kerosene/TOPO feature a large emission peak from excited MgO which dominates the spectra in the wavelength range tested.

No AlO emission was detected either due to a lack of its presence, or more likely signal dominance by the stronger MgO peak. Droplets J-N demonstrate a progression through steady droplet burning, emergence of few slight flame perturbations with emitting particle release, acceleration and growing intensity of these gas release events with more emitting particle ejections, to continuous bright particle ejection with some small to moderate microexplosions, and continuous particle release with regular moderate microexplosions immediately before a termination burst. In all these stages, the atomic emission of MgO grows from zero, seemingly as the prevalence of emitting particle release increases. Droplet O demonstrates a relatively long termination flash (compared to short lived bursts of other nanofuel terminations like $KIO_4$ and CuO) with some large emitting particle releases before degrading into a cluster of high emitting solid particles. The highest MgO emission signal by far is seen during this termination suggesting that MgO is likely the glowing emitting solids released more slowly in Droplets L-N and seen prominently during the termination. This provides evidence that first, earlier gas eruption events are a good vehicle for particle transport into the flame from NC-bound MP additives and second, that MgO is largely inert and survives as a solid as it heats near the flame and emits heavily as MgO. Mg emission was sensed in Chapter 5 so it is likely that some surface reduction reactions happen on the MgO surface in the presence of high-temperature reactive flame intermediates and the particles continue to glow as the hot particles reach the O2 atmosphere and reoxidize.

7.3.3 Discussion

Overall, NC-bound MP mechanisms seen in Chapters 4 and 5 are reinforced by these results, particularly regarding behavior caused by the nature of these composites preassembled with NC gas generator by electrospray. Most droplets viewed herein featured gas release from the liquid droplet which perturbed the system, even with relatively inert MgO oxidizer and least so with fully inert $Al_2O_3$ oxide. This is theorized to be a physically disruptive characteristic of NC-bound MPs underlying the additives studied which can incite the first system perturbations/droplet disruptions as NC decomposes in and around the droplet, as proposed in Chapter 4. Increased physical mixing from these events can cause further NC decomposition and a self-acceleration of the process. However, larger eruption events transport particles into the flame zone (as seen from atomic emission in CuO and MgO thermite nanofuels and in videos of AP and $Al_2O_3$ thermite nanofuels), so the behavior of the particles thrown into the flame do play a role in the emergence of this physical disruption feedback loop and can accelerate it, largely propagate it, or seemingly suppress it. To explain further, each thermite additive is considered by the oxidizer composition.

*Table 11: Estimated reaction enthalpy change and Gibbs' Free Energy change for full Al oxidation to $Al_2O_3$ by CuO, MgO, or AP (calculated from heats of formation and standard enthalpies available in the NIST Webbook [110]).*

| **Aluminum "Thermite" Reaction** | **$\Delta H_r$ (kJ/mol)** | **$\Delta G_r$ (kJ/mol)** |
|---|---|---|
| $Al + 3/2\ CuO \rightarrow 1/2\ Al_2O_3 + 3/2\ Cu$ | -601 | -596 |
| $Al + 3/2\ MgO \rightarrow 1/2\ Al_2O_3 + 3/2\ Mg$ | 67.5 | 65.7 |
| $Al + 3/2\ NH_4ClO_4 \rightarrow 1/2\ Al_2O_3 + 3/2\ HCl + 3/4\ N_2 + 9/4\ H_2$ | -759 | -791 |

**nAl/CuO/NC MPs:** Microscopy showed thorough interparticle mixing of the nAl and CuO both as relatively small nanoparticle primaries. Burning rate constants

are promoted by the thermite compared to either component alone as MPs (nAl/NC MPs and nAl/CuO MPs) and physical droplet disruptions observed show characteristics of the self-accelerating process discussed above. Based on Chapter 5, CuO is expected to survive further outside the droplet without decomposition compared to $KIO_4$ and TGA shows its oxygen release temperature (~1000 K) is just above the melting point of nAl (~970 K based on TGA in Figure 48), indicating availability of the oxygen near the point at which Al fuel is increasingly mobile for reaction. Intermetallic reaction of nAl/CuO is also thermodynamically favorable as seen in Table 11. Orange/green emission visible attached to the flame and atomic emission of AlO, $Cu_2$, and CuO further suggest significant reaction with these species in the gas phase. These atomic emission signals are tied to gas eruptions/microexplosions, reinforcing the presence of a feedback loop entraining physical disruptions, particle transport and reaction, and process repetition. The emission is noted in mid- and late-burning time disruptions and slightly more heavily at termination suggesting that while a disproportionally high amount of thermite likely remains at termination, appreciable thermite mass also reaches the flame though microexplosions at earlier burning times. The likely mechanism of this additive is therefore a classical thermite reaction between the nAl and CuO particles as they are ejected into the flame zone by physical disruptions, releasing locally high heats of combustion and feeding back into the propagation of the process by inciting more disruptions with this released heat which continues to throw more particles into the flame.

**nAl/KIO4/NC MPs:** Like CuO thermites, microscopy shows a beneficial microstructure with well-mixed small primary particles. However, burning rate constants resemble oxide-only MPs shown in Chapter 5 suggesting dominance by the activity of the $KIO_4$ component. Disruptions observed prior to termination are characteristic of the high-frequency low-amplitude flame gas perturbations seen in Chapter 5 and attributed to gases released as $KIO_4$ decomposes in two steps at 604 K and 830 K, significantly lower than the melting point of aluminum at ~970 K. Even though the nAl/$KIO_4$ thermite reaction has been demonstrated to be thermodynamically favored in dry nanothermite reactions [104, 108], a mismatch exists between the lower oxygen release temperature and higher melting point of aluminum which is not present for nAl/CuO. Discussion in Chapter 5 set forth that $KIO_4$ primarily does not survive into the flame zone as a solid and instead decomposes near the droplet surface. Atomic emission of AlO is lacking for most of the droplet burning times, even with $KIO_4$ disruptions, until the latest stages immediately before and during termination, when the particles are presumably the largest fraction of the remaining fuel and react as thermite and/or nAl/$O_2$. As such, this additive is proposed to react less so as an intermetallic thermite like nAl/CuO MPs and instead in mostly separated occurrences of $KIO_4$ decomposition and nAl oxidation, owing to the lower heating rate of the droplet combustion framework compared to dry thermite experiments. Rather, $KIO_4$ and NC decomposition causes higher frequency but lower intensity disruptions which provide a weaker vehicle for solid particle transport to the flame zone than the stochastic gas bursts from CuO thermites. Thusly, solid nAl particles primarily remain inside the

droplet until near termination when they burn either with remaining solid $KIO_4$ as a thermite or with atmospheric $O_2$. Burning rate effects follow those of $KIO_4$/NC MPs tested in Chapter 5, wherein $KIO_4$ introduces oxygen to the otherwise fuel rich side of the diffusion flame.

**nAl/MgO/NC MPs:** Microstructure is shown by microscopy is less favorable due to larger MgO particles and thusly lower interfacial contact. Burning rate constants decrease with higher loadings of the thermite suggesting possibly a negative competition of the two components. Disruptions follow the modus operandi of NC-bound MPs caused by gas release from NC, but with a generally slower acceleration of the disruption frequency relative to CuO and $KIO_4$ thermites and with accompanying emitting particle traces (resembling MgO/NC MP nanofuel droplets in Chapter 5). Notably specific to this additive, intermetallic thermite reaction between nAl and MgO is not thermodynamically favored as seen in Table 11 and based on the results of Chapter 5, reaction of MgO in this droplet system is likely limited reduction to Mg on the surface of MgO particles by high-temperature flame species (e.g. CO or $H_2$) and re-oxidation of this Mg by atmospheric $O_2$. This is supported by atomic emission herein showing significant excited MgO species and either an absence AlO emission or its wash-out by dominating MgO signal. MgO emission scales with the prevalence of emitting particle tracers further suggesting they are MgO particles heating in the flame. Most of this emission, along with video evidence of some likely Al combustion, is concentrated during the termination suggesting a low rate of particle emergence from the droplet before termination. Therefore, it is proposed that the usual NC

decomposition mechanism of MPs is active but that the nAl/MgO thermite does little to accelerate it as the two components compete for heat energy without an intermetallic thermite reaction favored thermodynamically. nAl and surface reduced Mg will also compete for oxygen to form respective oxides (of which MgO is more stable than $Al_2O_3$). The weaker physical disruption feedback loop transports less solid particles to the flame region and a majority fraction of the emission and particle reaction is seen instead upon termination and liquid burn-off.

**nAl/AP/NC MPs:** Performance of this additive was already expected to suffer based on microscopy alone which showed large AP particle sizes and poor mixing of the fuel and oxidizer. Wang et al. used alternate electrospray solvents to assemble nAl/AP/NC MPs wherein the AP instead dissolved into the precursor and thereby incorporated into the binder phase of the composite, which also featured higher NC loading (>17% instead of 5% by mass) [107], to overcome the otherwise poor microstructure. However, those particles were not stable in kerosene/TOPO when considered for this study and AP had to be added conventionally following electrospray procedures of the other thermites studied (this is anecdotal evidence that NC binder presence and characteristics significantly affect MP stability in kerosene/TOPO). Burning rate constants of the AP thermite MP nanofuels are relatively poor and below those of nAl/NC MPs which dominate the burning rates at higher thermite loadings, suggesting the rate increasing mechanism of nAl is the most active. While thermodynamics does favor thermite reaction of nAl/AP (Table 11), kinetics will suffer from the poor microstructure. In addition, the simple stoichiometry considered

ubiquitously for thermites in this study (i.e. defined by full conversion of nAl to $Al_2O_3$) is not fitting for the complex AP oxidizer. NASA CEA calculation of equilibrium species from the Al/AP O/F ratio used in this study (tabulated in Appendix C) suggests alternate products forming towards $AlCl_3$ instead of complete conversion of $Al_2O_3$ rendering the nAl/AP ratio used in this study more correctly called fuel-rich. Magnified videography shows the usual onset of gas eruptions characteristic of NC-bound MPs and reveals appreciable particle release into the droplet in the process. However, compared to CuO and KIO4 thermites, the disruption frequency and intensity is overall lower, seen primarily via less droplet deformation, suggesting the nAl/AP thermites released poorly accelerated the aforementioned physical disruption feedback loop. The unique lack of a large termination burst supports the observation of significant particle transport into the flame at earlier times, possibly due to added gas generation from the AP, but their poor microstructure and mixture ratio limits the benefit of their earlier presence in the flame. While the nAl/AP thermite system could be promising as liquid propellant additives, the greatest burning rate effects are only realized with a proper marriage of appropriate physical disruption behavior and additive combustion performance, the latter of which is lacking for this additive herein.

**nAl/$AL_2O_3$/NC MPs:** Magnified video of this inert control group showing rare gas perturbations with particle release suggests the underlying NC MP physical disruption mechanism exists, but no acceleration or growing intensity of such disruptions is observed and so the phenomena is not self-propagating and the feedback loop discussed previously fails to form. The vast majority of the additive particles

therefore remain within the droplet until the termination burst which features overwhelming bright particle emission presumably from nAl oxidation and $Al_2O_3$ heating. The activity of this additive is like that of MgO thermites wherein no intermetallic reaction is possible, except that with $Al_2O_3$, zero chemical activity of the oxide is present and this "thermite" completely breaks the disruption feedback loop.

Lastly, a loose correlation is observed between measured burning rate increases and energy release that would result from full redox from the nAl and oxide among the CuO, KIO4, and MgO thermites as plotted in Figure 64 (excluding the AP thermite with its effects from poor microstructure and complex stoichiometry). The thermodynamic energy release is calculated based on the net enthalpy change from complete nAl oxidation to $Al_2O_3$ and metal oxide reduction to the base metal. Since MgO is not thermodynamically favored to reduce to Mg by oxidation of Al, this case is merely hypothetical and provides a basis to penalize for the absorbed heat by the inactive MgO oxidizer. The relationship observed reinforces the supposition that combustion heat could be a method by which active particle additives promote or suppress the physical disruption feedback loop process to varying degrees. Namely, the additives most thermodynamically favored to release combustion heat inside the flame radius near the droplet are most likely to incite further disruptions, propagate the feedback loop, and thusly increase droplet burning rates.

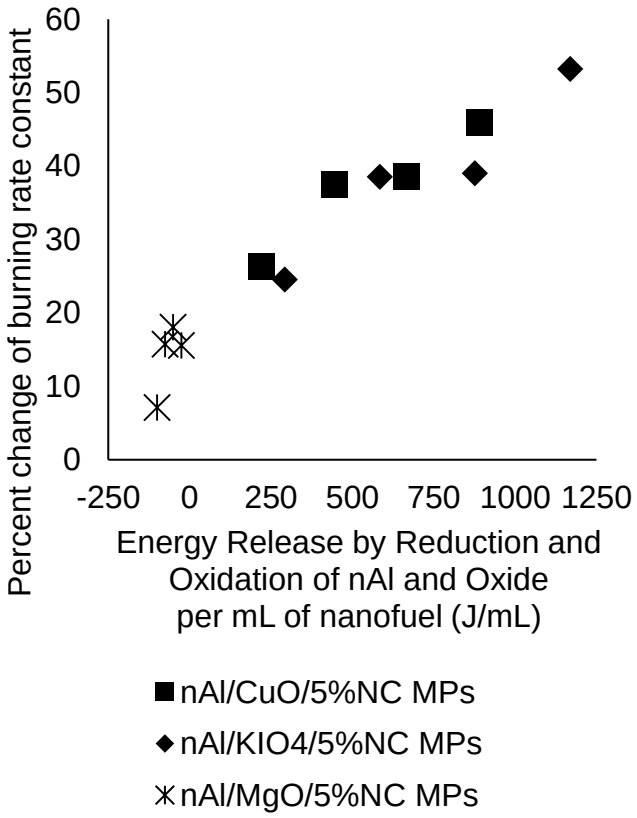


*Figure 64: Experimentally estimated burning rate constants of CuO, $KIO_4$, and MgO based thermite MPs with active oxides relative to theoretical enthalpy release of Al oxidation reaction by the particulate oxide.*

*7.4 Conclusions*

Building upon prior work which identified significant modification of solid particle additive effects on kerosene with TOPO surfactant when said particles are preassembled into NC bound MPs of nAl fuel (per Chapter 4) or various oxidizers (per Chapter 5), work in this chapter surveyed and investigated droplet combustion effects upon addition of nAl/Oxidizer/5%NC thermite MPs to kerosene/TOPO. An ensemble of diagnostics coupled to a free-droplet combustion apparatus was employed including droplet burning rate constant estimation, direct videography of burning droplet

trajectories and magnified burning droplet details, and time resolved flame emission spectroscopy to probe certain excited species in order to establish which thermite compositions incited the most beneficial combustion effects and to probe the possible mechanisms of each formulation's activity. As expected, the most typically reactive and exothermic thermite MPs, those of nAl/CuO and nAl/$KIO_4$, exhibited the highest burning rate increases. Based on the observed activity of each thermite tested and mechanisms proposed, droplet burning rates are found to be increased most when the underlying physical disruption cycle facilitated by the NC-bound MP structure (caused by NC gas generation and characterized in Chapters 4 and 5), cooperates with a chemical mechanism of the carried particle additive, whether that is highly exothermic intermetallic reaction (e.g. nAl/CuO), or relatively low temperature oxygen release (e.g. $KIO_4$). Each of these two coupled processes are shown to affect the precise manifestation of each other and so far reach optimal burning rate increase only when their cooperation results in a self-accelerating pattern of gas generation, physical disruptions, particle liberation into the flame, heat or diffusion benefits from the additive, and further gas generation/disruptions: a powerful physical disruption feedback loop.

*Acknowledgements*

Special thanks to Rohit Jacob for his lead role assembling and operating the flame emission spectrometer and Haiyang Wang for inspiring and providing the spray-dried AP nanoparticles.

# Chapter 8: Droplet burning rate improvements with triisobutylaluminum dissolved in toluene

*Summary*

Metallizing hydrocarbons has received renewed research attention with improved control and characterization of nanoscale metals with novel properties and effects in combustion systems. Particle agglomeration is always relevant in such applications and threatens practical road blocks for application like system fouling with particle deposition. Achieving a metallized hydrocarbon without nanoparticles in suspension would avoid particle agglomeration problems. Previous proof-of-concept work with highly reactive organometallic Al-based clusters stabilized by ligands and dissolved in a hydrocarbon showed such a scheme is not only possible, but the decreased size of the cluster molecules relative to nanoparticles substantially increases reactivity and at least an order of magnitude less active aluminum in a dissolved cluster caused similar isolated droplet burning rate increases by gas eruption and physical mixing compared to nanoaluminum. To increase understanding of how such burning rate effects manifest with dissolved aluminum, a higher valency alkyl aluminum historically used as a hypergol, triisobutylaluminum (TiBAl), is dissolved in toluene and isolated droplet combustion is characterized showing up to 60% burning rate increase with 810 mM TiBAl relative to pure toluene attributed specifically to the aluminum content of the additive molecule. Flame emission spectroscopy supports the vital role of gas eruption and droplet disruption to transport additives into the flame.

*8.1 Introduction*

Metallizing liquid fuels and propellants has the potential to increase their net volumetric energy density thereby improving payload capabilities in volume-limited systems [6]. Addition of micron-sized metal particles to hydrocarbons however proved to be detrimental to combustion efficiency and burning rates as the relatively slow-burning metal particles tend to ignite near liquid burn-out and two-phase losses can decrease specific impulse [20, 111]. Research into metal/hydrocarbon incorporation has been revitalized with the emergence of nanoscale control of metal particles and the resulting improvements in the reaction rates and ignition delays of nanometals versus micron-sized analogs [4]. This demonstration that the physical form of the metal drastically affects its combustion behavior has motivated consideration of metallizing hydrocarbons with soluble aluminum-containing molecules. To prove this concept in Chapter 3, AlBr clusters stabilized by triethylamine ligands with aluminum in a low valency state ($[AlBrNEt_3]_4$) were dissolved in a toluene/ether co-solvent and combusted as free-droplets showing that relatively low amounts of the material notably increase the burning rate of the fuel droplets compared to nanoaluminum.

Organoaluminum compounds comprise a similar opportunity to dissolve an aluminum molecule into a hydrocarbon and have been used to formulate hypergolic fuels [64]. Aluminum based metal clusters like $[AlBrNEt_3]_4$ are difficult to synthesize and maintain since they suffer from air and temperature sensitivity. While they are similarly air-sensitive and pyrophoric, alkylaluminum compounds, e.g. triisobutylaluminum (TiBAl), are readily available commercially and thermally stable,

therefore comprising an opportunity to contextualize the demonstrated effects of $[AlBrNEt_3]_4$ despite the higher oxidation number of Al in TiBAl (3+ versus 1+ in $[AlBrNEt_3]_4$). In this chapter, TiBAl is dissolved in Toluene to investigate the effects of this Al-centered hydrocarbon-compatible molecule on the free-droplet burning rate and combustion behavior relative to a Nitrogen-centered control molecule, triisobutylamine (TiBam).

*8.2 Experimental*

A free-droplet combustion apparatus described in Section 2.1.2 facilitates burning characterization in which a 600-micron droplet is released from a capillary needle to free-fall passed two methane pilot flame igniters into a 100% oxygen environment. Droplet shedding off the end of the vertical capillary is achieved with nitrogen flow through a ~2mm diameter glass shroud around the capillary at the top of the tower. Relative to the tower oxygen flow (15 LPM), this nitrogen flow (0.25 LPM) is negligible and used for all droplet experiments. Droplets are generated approximately 3 times per second and maintain separation of approximately 6 in. to prevent combustion interference. Two high-speed cameras are used to record the flame emission of the falling droplet (to measure burning time) and initial diameter of the droplet at ignition, from which a burning rate constant for each droplet can be estimated by the ratio of initial droplet diameter squared to the burning time according to eq. 1 and the rate of 10-20 droplets averaged to estimate the burning rate of the fuel.

$$K \cong \frac{{D_0}^2}{t_{\text{Burn}}} \tag{33}$$

An alternative camera configuration has also been used here to gather magnified video of combusting droplets with a color high-speed camera concurrently with time-resolved emission spectroscopy between 475nm and 500nm. In this configuration, the camera and collection fiber are mounted on a vertical translation stage which is free to fall parallel to the length of the tower. Releasing this diagnostics stage to fall into foam padding in front of sequentially falling and burning droplets significantly lengthens the data collection time relative to static diagnostics mounting with droplets passing by. The second camera is used to image the falling diagnostic stage and falling droplets relative to the tower axis so that the ignition time of any droplet captured in the field of view of the magnified camera and spectrometer is known. The initial diameter of the droplets is not measured in this configuration and therefore burning time data is not normalized by droplet diameter which can fluctuate +/- 50 microns. Magnified videos are used to estimate spatially resolved temperature with a three-color ratio pyrometry method described in Section 2.3.4. Emission spectroscopy data is used to seek atomic emission of excited AlO species in the droplet flames as an indication of aluminum oxidation consistent with the experimental setup described in Section 2.3.3.

Dissolution of triisobutylaluminum (TiBAl) (Sigma Aldrich 257206 CAS 100-99-2, prepared in toluene by collaborator Dr. Andrew Kerr), triisobutylamine (Sigma Aldrich 374989 CAS 1116-40-1), and Benzene (Sigma Aldrich 319953) used in this study was performed in a glovebox under an Ar atmosphere and the Toluene

solvent was purified with the help of collaborator Dr. Dennis Mayo by distillation from sodium benzophenone ketyl under a dinitrogen atmosphere and stored over 3 Å molecular sieves. To prepare samples for combustion experimentation consistent with strategies utilized for air-sensitive $[AlBrNEt_3]_4$ in Chapter 3, ~0.5 mL are loaded into gastight syringes and sealed in bags with the syringe value closed under an Ar atmosphere. The 3 in. PTFE 1/16 in. OD x 0.040 in ID tubing syringe lead is flushed with nitrogen immediately before connecting to the sample delivery capillary and pumping the sample into the combustion experiment. A key benefit of TiBAl versus $[AlBrNEt_3]_4$ is its higher solubility limit and compatibility in toluene without ether co-solvent. As such, higher concentrations of TiBAl are tested here: 280 mM, 440 mM, and 810 mM. Equal molar concentrations of the nitrogen-centered control (TiBam) and similar boiling point control (Benzene) were used to elucidate the role of the Al atom in TiBAl versus the lower boiling point of TiBAl and Benzene compared to Toluene.

*Table 12: Samples tested with estimated burning rate constants and percent change relative to pure toluene control.*

| Sample | None | 280 mM | | 440 mM | | 810 mM | |
|---|---|---|---|---|---|---|---|
| | K ($mm^2/s$) | K ($mm^2/s$) | % Δ | K ($mm^2/s$) | % Δ | K ($mm^2/s$) | % Δ |
| Toluene | 2.33 | | | | | | |
| TiBAl | | 3.16 | 35.7 | 3.68 | 57.8 | 3.75 | 61.0 |
| TiBam | | 2.28 | -2.1 | 2.30 | -1.4 | 2.28 | -2.1 |
| Benzene | | 2.21 | -5.1 | 2.17 | -7.0 | 2.27 | -2.7 |

*8.3 Results and Discussion*

Time-lapse images shown in Figure 65 depict representative complete droplet lifetimes for each sample type at the highest concentration unless noted otherwise. TiBam and Benzene control trials closely resemble the disruption-free burning of the toluene carrier fuel (the appearance midframe in the Benzene trace of what appears to be a small disruption is an artifact caused by reflection off residue on the inside of the cover glass and was visible in the same location for every droplet imaged in that trial). Consistent with Toluene/Ether controls in Chapter 3, small flashes occur upon termination of the control group droplets as a critical droplet size is reached and the remaining liquid fuel rapidly gasifies.

Four shown depict combustion behavior with TiBAl for the three concentrations tested including two common profiles for the highest 810 mM loading. Generally for TiBAl, an initial disruption-free burning period precedes discrete strong and bright disruptions which have the potential to generate companion droplets, change the main droplet trajectory, and/or catastrophically disassemble the main droplet into smaller sub-droplets. As the concentration is increased from 280 mM to 440 mM, disruptions occur earlier and with more frequency, with neither concentration catastrophically dispersing the droplet with a single disruption event. At 810 mM loading however, a usual strong initial disruption commonly generates companion droplets while the main droplet survives, or catastrophically breaks the main droplet into a number of sub-droplets. The disruptive nature of the combustion with TiBAl

additive is similar to microexplosions observed with ~10mM $[AlBrNEt_3]_4$ in Toluene/Ether co-solvent in Chapter 3.


*Figure 65: Representative time-lapse images of free-falling droplets combusting with and without 810 mM TiBAl additive or TiBam/Benzene control additives. (A) Pure Toluene, (B) 810 mM Triisobutylamine in Toluene, (C) 810 mM Benzene in Toluene, (D-E) Two types of disruptions from 810 Triisobutylaluminum in Toluene. The mid-height emission expansion in (C) is an artifact caused by reflection off a spot of residue on the experiment cover glass and is not a disruption.*

To quantify the effect of the disruptive combustion behavior which emerges upon TiBAl addition, estimated burning rate constants are plotted in Figure 66 versus additive concentration. While the control TiBam and Benzene have slight negative to no effect on the burning rate constant relative to Toluene, increases up to 61% are measured upon TiBAl addition, surpassing the ~20% increase measured with ~10mM $[AlBrNEt_3]_4$ in Toluene/Ether. No conclusive difference in the burning rates is detected between 440 mM and 810 mM TiBAl despite the appearance if differing combustion disruption behavior. Notably, the standard deviation of the data collected increases substantially with the disruptive TiBAl additive, from 3.5% or less for control groups to 10%, 14%, and 16% for 280 mM, 440 mM, and 810 mM TiBAl respectively, suggesting that the mechanism by which TiBAl increases burning rate is relatively stochastic either in occurrence or effect on burning rate.

Multi-component liquid fuels are known to feature disruptive "microexplosion" events which can increase burning rate when the components have differing enough boiling points to superheat the lower boiling point fuel during droplet combustion [60-63]. Since the boiling point of TiBAl (359 K per supplier) is lower than that of Toluene (384 K [110]), it is necessary to test a control additive with a similar boiling point (TiBam control is unsuitable for this since it has a boiling point of 465 K [110]). Benzene has a similar chemical structure to Toluene and a boiling point (353 K [110]) close to that of TiBAl but failed to generate combustion disruptions or affect the burning rate of Toluene thereby suggesting the mechanism of TiBAl activity is not due to superheated component microexplosions.

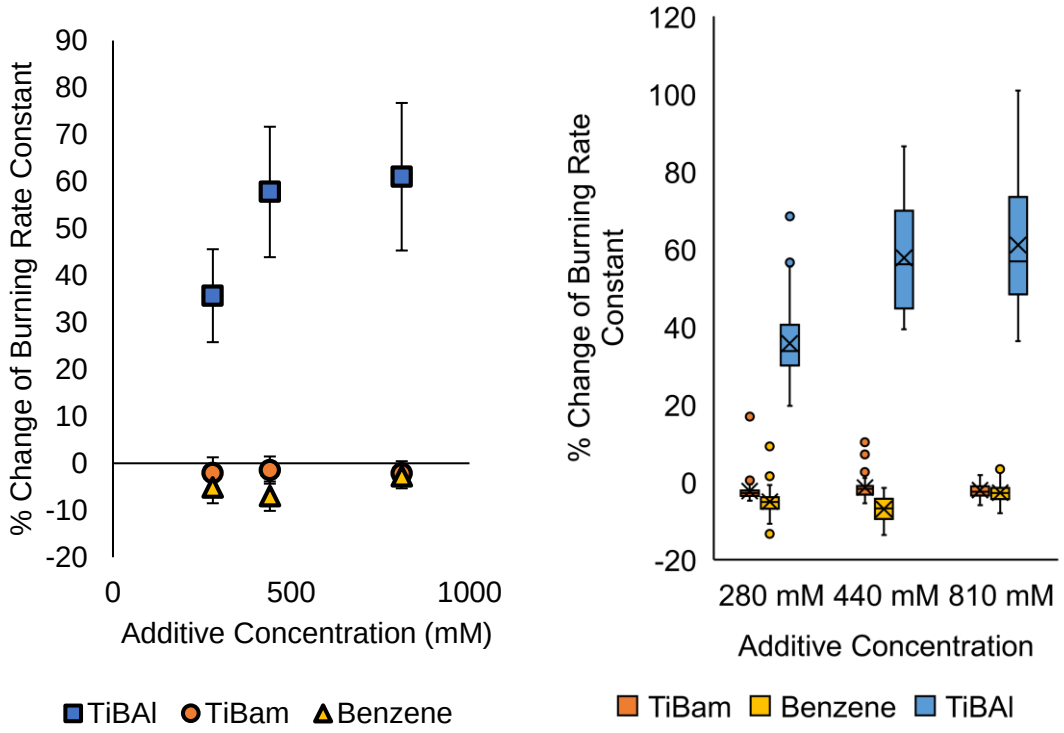


(A) (B)

*Figure 66: Measured changes of burning rate constant relative to Toluene (K = 2.33) with Triisobutylaluminum, Triisobutylamine, and Benzene additives. Error bars in (A) represent one standard deviation in each direction.*

Magnified color high-speed video of combusting droplets with accompanying pyrometric temperature estimation and concurrent emission spectroscopy between 474 nm and 502 nm wavelengths is available for toluene, 810 mM TiBam in toluene, and 810 mM TiBAl in toluene to better observe droplet combustion behavior, estimate flame temperature effects, and detect the $\Delta v = 0$ emission band of AlO which indicates reaction of gas-phase aluminum with an oxidizer [112, 113]. Figure 67 depicts select frames from magnified videos of TiBam control droplets and TiBAl test droplets. No difference is noticed between the magnified videos of toluene and TiBam controls which both burn steadily without disruptions.

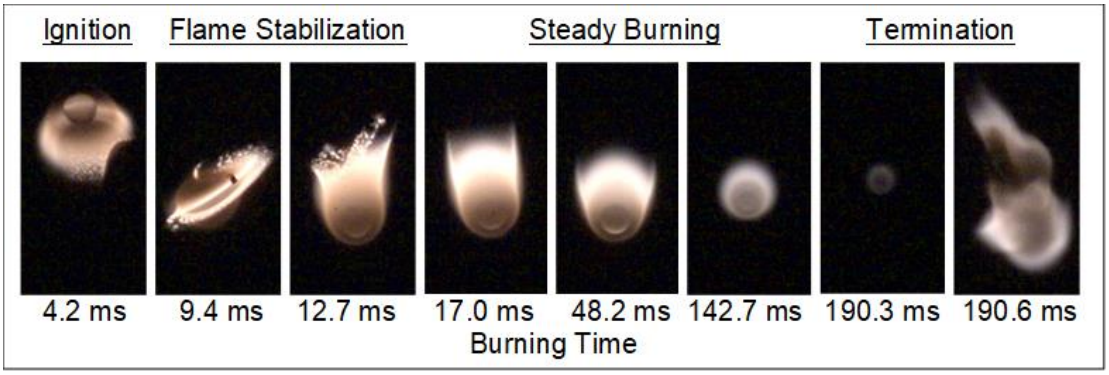


*Figure 67: Representative combustion profile from magnified videography of 810 mM TiBam in Toluene with time from ignition noted per frame.*

Droplet disruptions caused by the TiBAl additive are shown in Figure 68, in which the primary droplet survives, and Figure 69, in which the main droplet is broken up into multiple sub-droplets. Such disruptions are characterized by rapid release of gas phase reactants from the droplet which expand the flame zone and combust as they mix with ambient oxidizer and at times release sub-droplets. Visible in the last two frames of Figure 68 and first two frames of Figure 69, the additive also causes high frequency and low intensity flame perturbations throughout the droplet lifetime contrasting with the steady flame shape of the control samples suggesting continuous anisotropic and stochastic gas release from the droplet. Companion droplets released are visible in frames 5 and 6 of Figure 68 showing the significant propensity of TiBAl to release sub-droplets during disruptions. Frames 2-4 in Figure 69 also show substantial droplet swelling prior to the inception of the violent eruption and droplet breakup which resembles the cyclical inflation and eruption events seen with $[AlBrNEt_3]_4$ in Chapter 3 and nanoaluminum/nitrocellulose composite mesoparticles in Kerosene in.

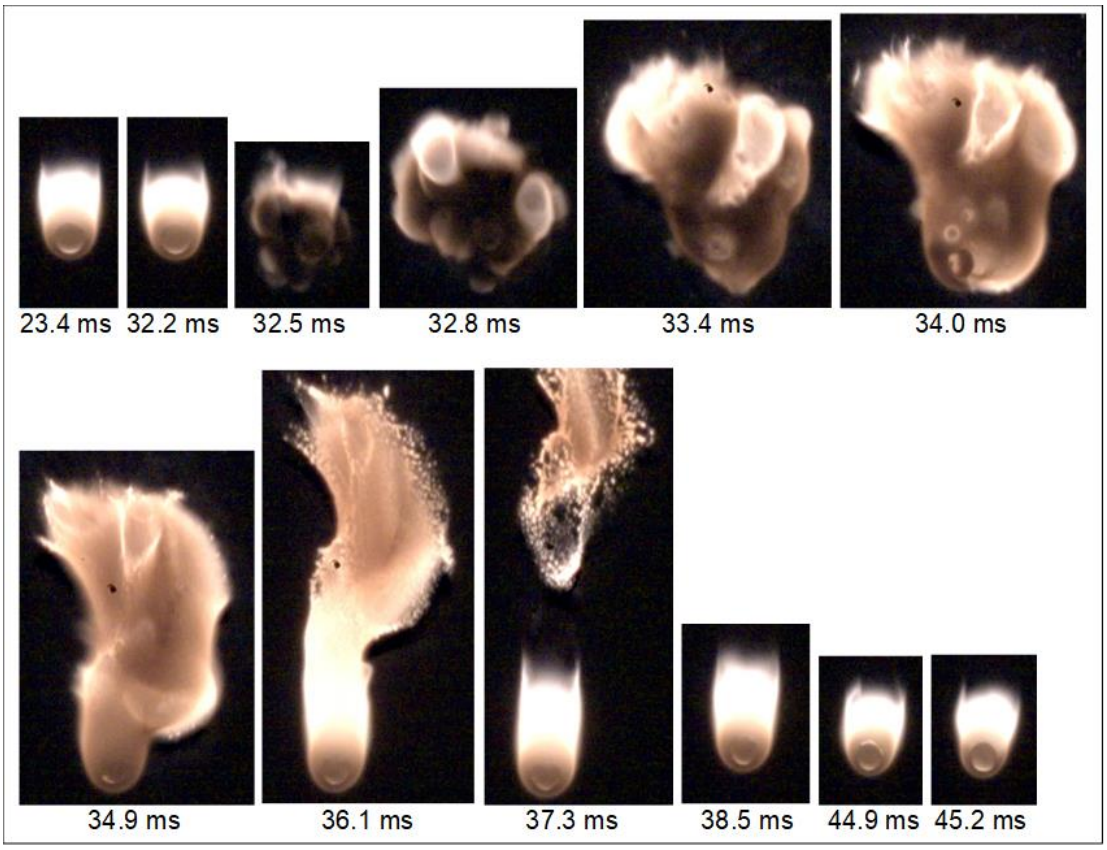


*Figure 68: Representative combustion disruption of 810 mM TiBAl in Toluene in which the primary droplet survives intact with time from ignition noted per frame.*

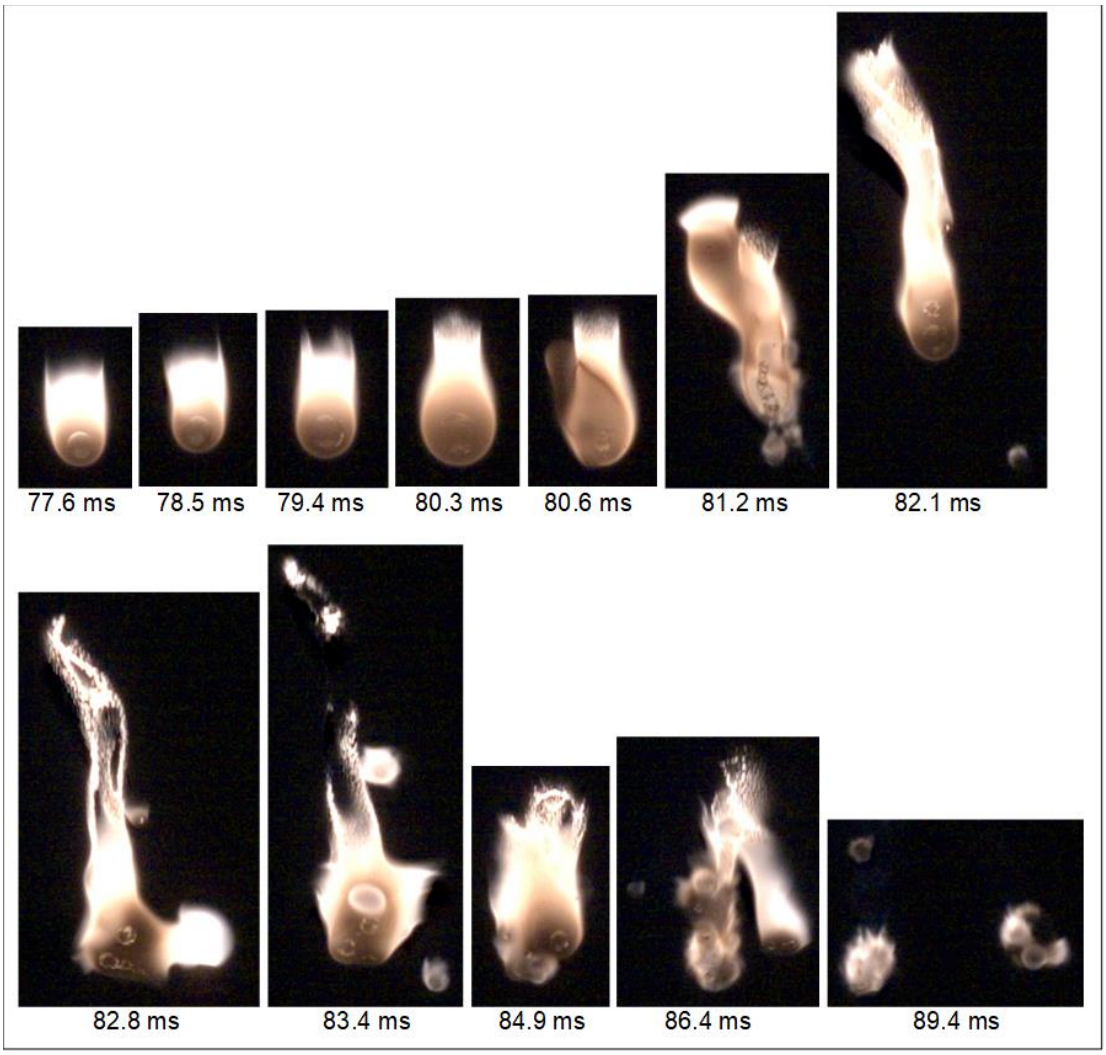


*Figure 69: Representative combustion disruption of 810 mM TiBAl in Toluene in which the primary droplet is catastophically disassembled into sub-droplets with time from ignition noted per frame.*

Spatially averaged temperatures given by ratio pyrometry of the magnified color videos are plotted versus droplet burning time in Figures 71-76 with accompanying video frame montages available in Appendix C. As droplets burn and their flame shrinks in size, this spatial average is biased towards the highest temperature regions as depicted in Figure 71, leading to a linearly increasing mean temperature profile. A linear regression fit to the toluene control temperature after 23 ms (lower

temperature prior to this time is during the droplet heat-up period) shown in Figure 71 with the perturbation near 100 ms resulting from the droplet slightly emerging out of the camera frame. This fit provides the basis of comparison of the experimental temperature profiles and is relatively repeatable for toluene as evidenced in Figure 72. The flame temperature measured with TiBam control additive is approximately 150 K greater than the toluene control throughout its lifetime owing to its higher boiling point and greater heat of combustion considering the reactions in Table 13.

*Table 13: Boiling points, stoichiometric combustion reactions and combustion energies for Toluene, TiBam, and TiBAl fuels with Oxygen.*

| **Fuel** | **$T_B$ (K)** | **Stoichiometric Combustion Reaction** | **$\Delta H_c$ (kJ/mol)** |
|---|---|---|---|
| Toluene | 383 | $C_7H_8 + 9\ O_2 \rightarrow 7\ CO_2 + 4\ H_2O$ | -3672 |
| TiBam | 465 | $C_{12}H_{27}N + 18.75\ O_2 \rightarrow 12\ CO_2 + 13.5\ H_2O$ | -7654 |
| TiBAl | 359 | $C_{12}H_{27}Al + 19.5\ O_2 \rightarrow 12\ CO_2 + 13.5\ H_2O + 0.5\ Al_2O_3$ | -8531 |

Representative emission spectra collected for toluene, TiBam, and TiBal samples are shown in Figure 70. Blackbody emission from soot particles comprises the majority of the electromagnetic radiation measured, however AlO atomic emission can be sensed at a strong $\Delta v = 0$ emission band near 484 nm – 488 nm [112, 113]. The TiBAl emission spectra shown includes a departure from the blackbody emission at these wavelengths indicating AlO emission. To estimate the presence and relative strength of this emission per spectra measured in time, a least-squares polynomial fit is generated for each spectrum omitting data between 483 nm and 489 nm and the area between this baseline and the measured data in this range is integrated to estimate the intensity of the AlO peak. The integrated intensity of this peak, representing AlO emission spectroscopy is plotted with pyrometrically estimated flame temperature in

Figures 71-76. AlO emission was not detected in any toluene nor TiBam control trials but was observed for TiBAl samples near droplet gas eruptions.

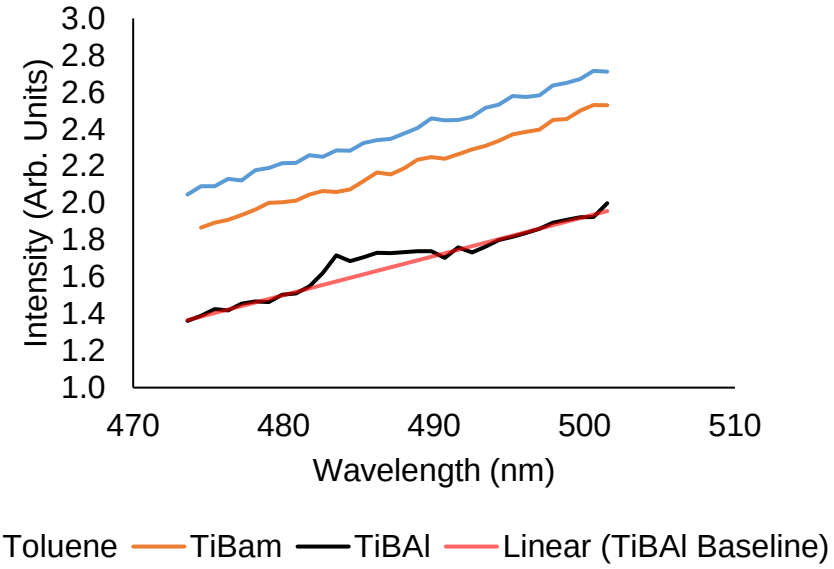


*Figure 70: Representative spectra collected from the emission of combusting droplets of Toluene, TiBam in Toluene, and TiBAl in Toluene. Reference line is the least-squares fit of the TIBAl spectra omitting data between 433 nm and 439 nm. Data in that range is integrated over that baseline fit to measure AlO emission intensity.*

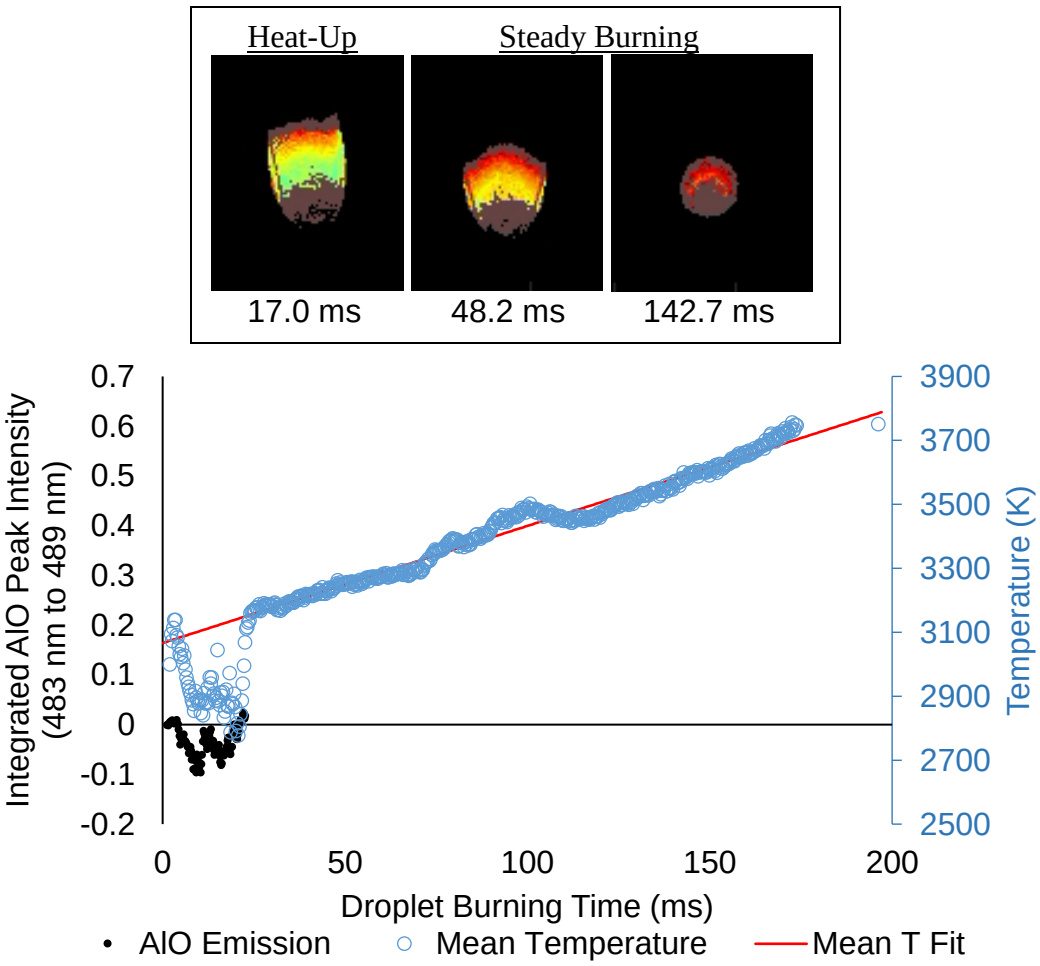


*Figure 71: Toluene Control. (Top): Sample pyrometry results for select frames showing low-temperature initial heat-up period followed by a shrinking droplet flame which increases the spatial mean. (Bottom): Spatial mean of temperature and integrated size of AlO emission peak. Droplet falls out of spectrometer view at 21 ms. Temperature perturbation at 100 ms is an artifact as the droplet leaves the camera frame slightly.*

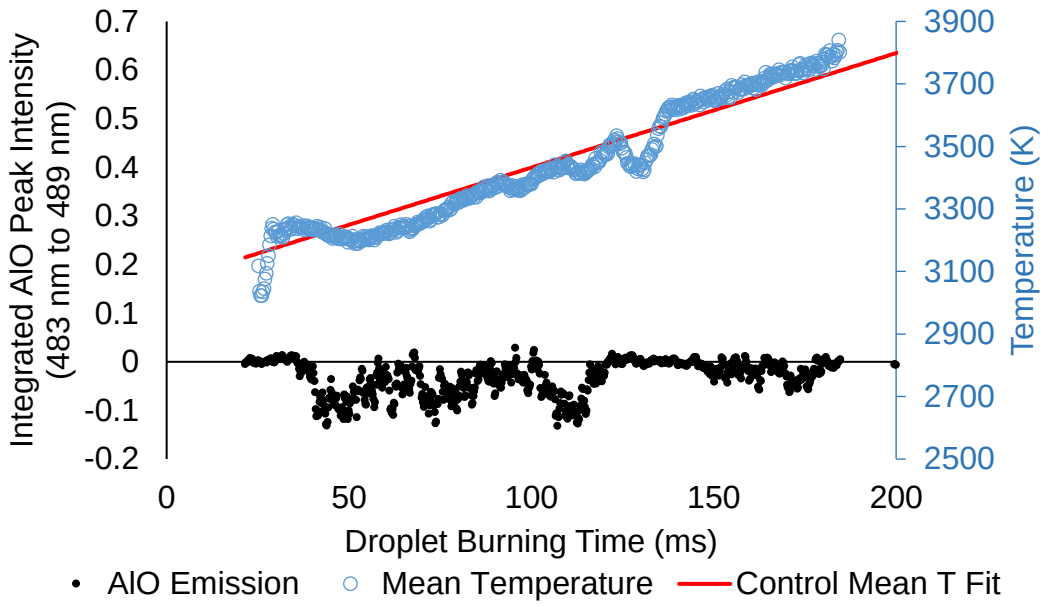


*Figure 72: Toluene. Spatial mean of temperature and integrated size of AlO emission peak. Reference line corresponds to linear fit of Toluene Control temperature in Figure 71. Temperature perturbation at 130 ms is an artifact as the droplet leaves the camera frame slightly.*

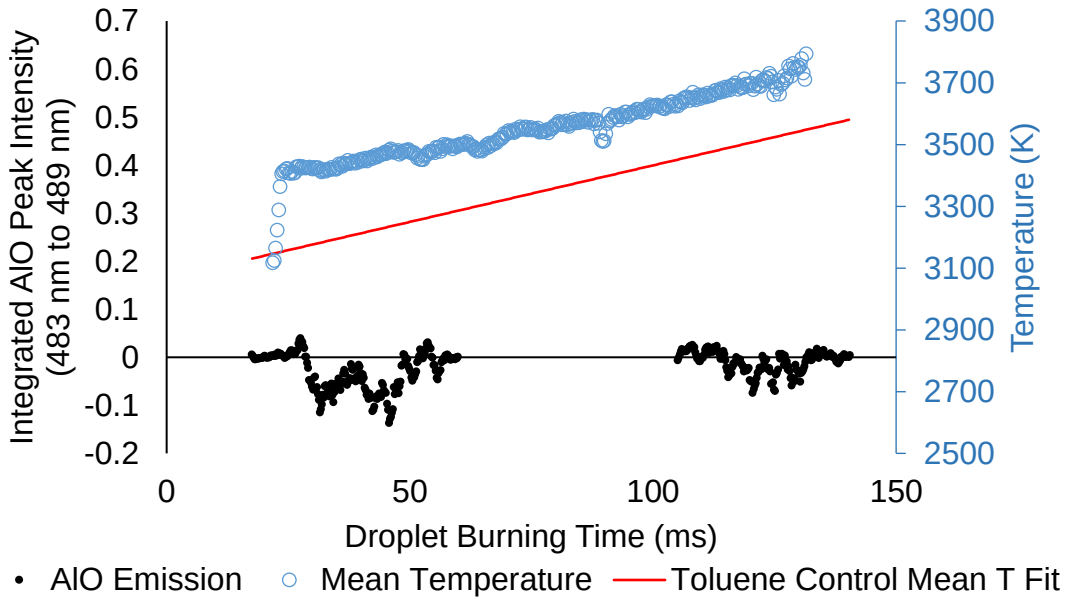


*Figure 73: 810 mM TiBam. Spatial mean of temperature and integrated size of AlO emission peak. Reference line corresponds to linear fit of Toluene Control temperature in Figure 71. Droplet leaves spectrometer view between 60 ms and 105 ms.*

Figure 74 shows the pyrometrically estimated temperature profile and AlO emission signal for 810 mM TiBAl during ignition and heat-up. No AlO is detected in the first 10 ms of droplet burning. After the heat-up period, the droplet reaches a temperature approximately 50 K greater than the toluene control profile suggesting that in the presence of the lower boiling point of TiBAl compared to toluene, its higher combustion heat as listed in Table 13 is ample to maintain a similar or slightly higher flame temperature than pure toluene droplets. The effect of disruptive microexplosions with TiBAl additive is evident in Figures 75 and 76 wherein microexplosions occur at 35 ms, 55 ms, and 73 ms in Figure 75 and at 31 ms in Figure 76, corresponding with sharp decreases in temperature as the flame mixes with cool ambient oxygen and prominent spikes in AlO emission indicating gas-phase Al combustion during such events.

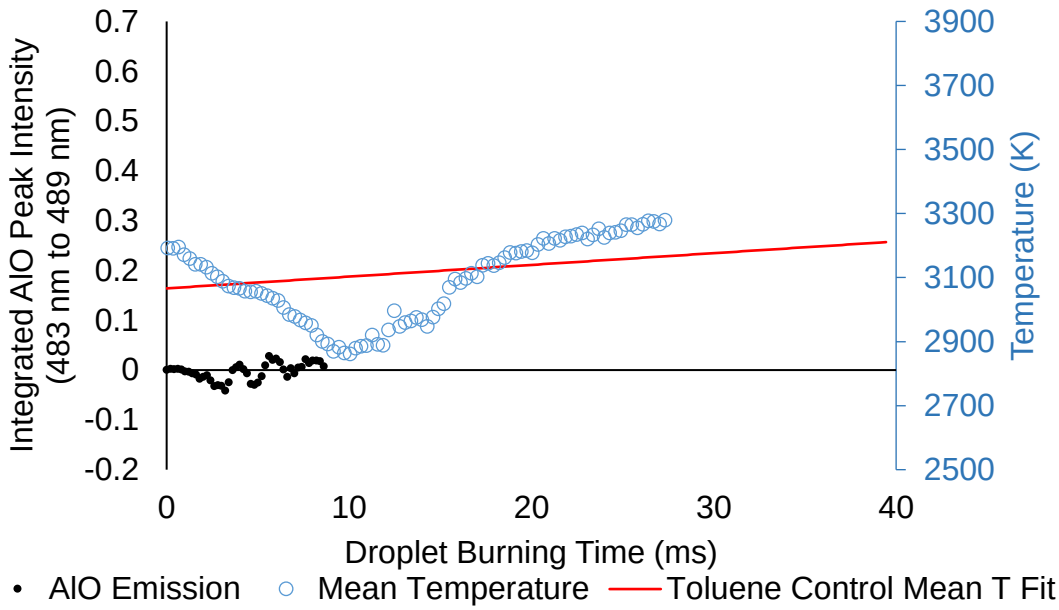


*Figure 74: 810 mM TiBAl ignition. Spatial mean of temperature and integrated size of AlO emission peak. Reference line corresponds to linear fit of Toluene Control temperature in Figure 71. Droplet leaves spectrometer view at 9 ms and camera view at 27 ms.*

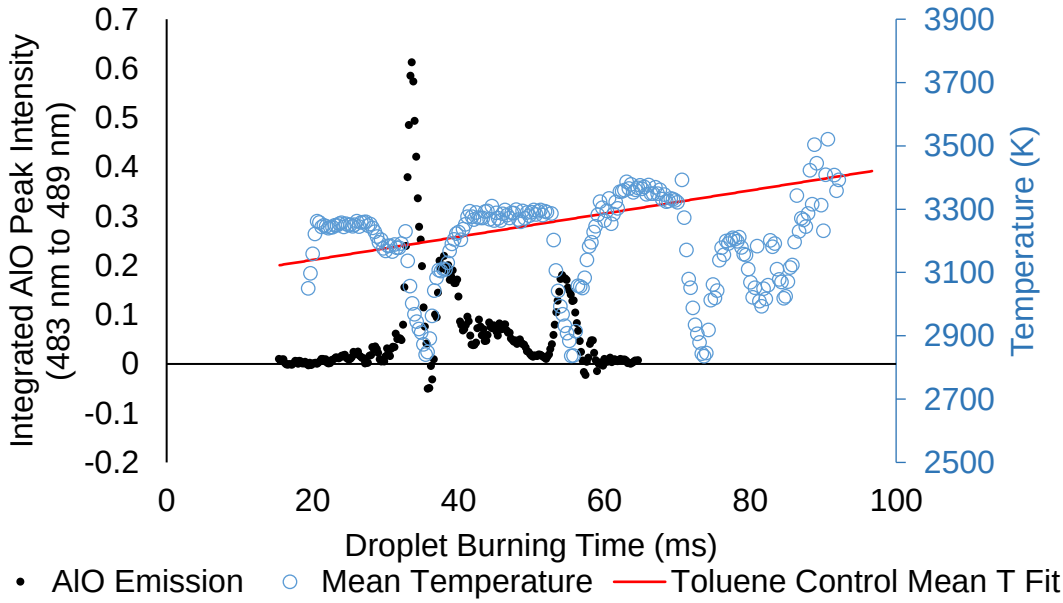


*Figure 75: 810 mM TiBAl. Spatial mean of temperature and integrated size of AlO emission peak. Reference line corresponds to linear fit of Toluene Control temperature in Figure 71. Droplet leaves spectrometer view at 65 ms. Disruptions at 35 ms, 55 ms, and 73 ms.*

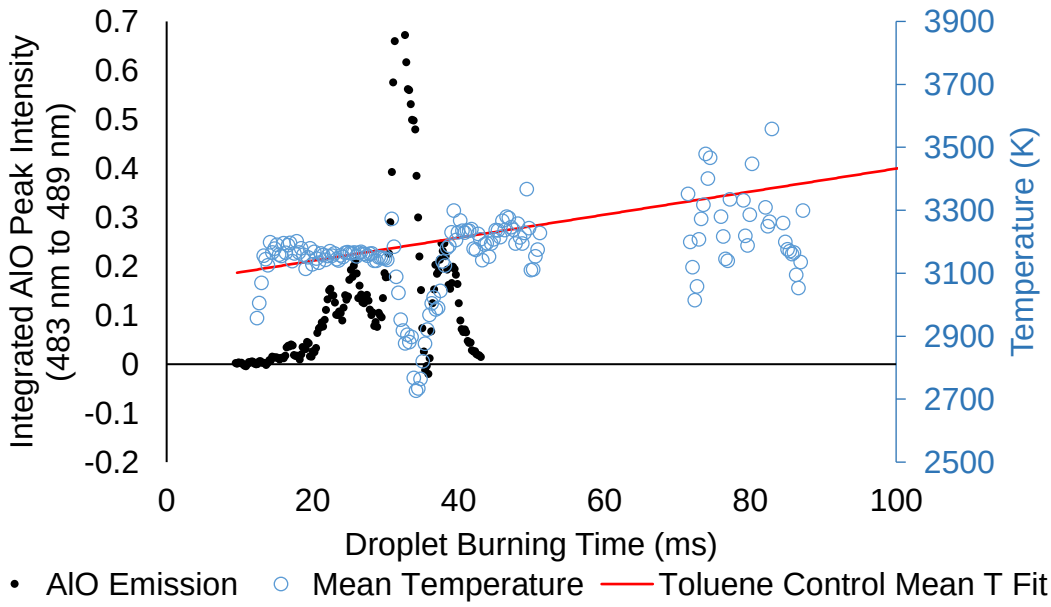


*Figure 76: 810 mM TiBAl. Spatial mean of temperature and integrated size of AlO emission peak. Reference line corresponds to linear fit of Toluene Control temperature in Figure 71. Droplet leaves spectrometer view at 43 ms and camera view between 51 ms and 72 ms. Disruption at 31 ms.*

Direct observation of microexplosions/disruptions upon TiBAl addition to toluene suggest a gas phase product formed in the droplet expands outward from the liquid into the flame zone where it combusts. This liberation is rapid enough to significantly deform the shape of the droplet and/or generate companion sub-droplets or catastrophically disassemble the primary droplet into smaller components. Similar observations of combusting droplet effects were made when $[AlBrNEt_3]_4$ was added to toluene/ether in Chapter 3 and nanoaluminum/nitrocellulose composite mesoparticle were added to kerosene in Chapter 4. In the latter case, the shape deformation of the droplet alone was shown to be a likely mechanism by which such events increase gasification and burning rates by increasing droplet surface area exposed to the flame. Burning a particular quantity of liquid fuel as multiple smaller droplets instead of one

large droplet would also increase the gas-liquid interface area having a similar effect. Therefore, the mechanism by which TiBAl addition increases the burning rate is proposed to be volatile fuel gas evolution within the droplet followed by expansion and eruption of this vapor to combust in the flame zone, promote physical mixing of the system promoting diffusion-limited oxidation reaction, and increasing liquid gasification rates by increasing the gas-liquid interface surface area by droplet deformation and/or breakup.

Upon heating for chemical vapor deposition, TiBAl is known to decompose into aluminum, isobutene, and hydrogen and when this occurs in the presence of water, this process is observed with evolution of AlOx species above 300 K [114]. Since the toluene droplet temperatures are limited to 383 K by the boiling point of toluene, decomposition of TiBAl and its reaction with water diffusing into the droplet from the flame zone is proposed to be the primary pathway to internal droplet gas generation by evolution of isobutene and hydrogen gases. To assess the feasibility of such a mechanism, the volume of only isobutene vapor available from one 600-µm toluene droplet of 280 mM TiBAl is estimated to be $2.98 \times 10^{-3}$ mL by the ideal gas law at 1 atm and 383 K (estimated droplet temperature) assuming 3 moles of $C_4H_8$ are available per mole of TiBAl, $C_{12}H_{27}Al$. Comparing this to the $1.13 \times 10\text{-}_4$ mL volume of such a droplet reveals 26 times the volume of the droplet is available as isobutene vapor which is more than ample to generate disruptive events as this gas is gradually released. Like the mechanism set forth for $[AlBrNEt_3]_4$ disruptions in Chapter 3, water can also be considered as a diffusion-limited reactant of the gas generation reaction to estimate a

time-scale to an initial disruption. Assuming a 100-μm diameter sphere of isobutene in a 600-μm droplet of 280 mM TiBAl in toluene would cause a microexplosion, 5.5 x $10^{-12}$ moles of water are needed to react with TiBAl and generate 1.67 x $10^{-11}$ moles of isobutene. Following the analysis of Chapter 3 with a 600-μm diameter droplet saturated with water at its surface (0.33 % water), a binary diffusion coefficient of 6 x 10-$^{4}$ mol/($m^2$-s), and a linear concentration gradient, enough water will reach one half-radius into the droplet to cause a microexplosion in approximately 30 ms. This closely resembles the time to the first microexplosions seen in Figures 75 and 76.

*8.4 Conclusions*

The droplet combustion behavior of triisobutylaluminum dissolved in toluene has been investigated to elucidate microexplosive droplet disruption events caused by this additive which are absent in pure toluene, triisobutylamine in toluene, and benzene in toluene controls. Estimations of burning rate constants show the TiBAl additive increases toluene burning rates by 36%, 58%, and 61% with 280 mM, 440 mM, and 810 mM of TiBAl additive respectively while control additives have no appreciable effect. Direct observation of incited droplet microexplosions with pyrometric temperature estimation of color videos and concurrent measurement of AlO emission supports a mechanism proposed in which decomposition of TiBAl and reaction with water within the droplet evolves isobutene and hydrogen gases which increase the burning rate by physical mixing, droplet breakup, and droplet shape deformation similar to findings for $[AlBrNEt_3]_4$ in toluene/ether in Chapter 3 and nanoaluminum/nitrocellulose composite mesoparticles in kerosene in Chapter 4.

*Acknowledgements*

Thanks to Rohit Jacob and Dylan Kline for their primary roles assembling and operating the AlO emission spectrometer and pyrometry computational analysis code respectively. Thanks to Andrew Kerr, Dennis Mayo, and Edward Foos for suggesting use of and providing the TiBAl in toluene.

# Chapter 9: Summary

## *9.1 Findings and Impact*

This dissertation presents research conducted which has resulted in a number of impactful findings. A custom experimental apparatus was developed along with extensive automation algorithms to estimate the burning rates of liquids with energetic additives which can be highly reactive and air sensitive, and/or cause disruptions and gas generation which invalidate classical droplet burning rate measurement methods. A proof-of-concept study has been presented demonstrating promising burning rate increases achieved with aluminum clusters and molecules soluble in hydrocarbons. The lack of a particle morphology makes such materials highly attractive for increasing energy density of liquid fuels with high energy release rates and without particle agglomeration. Regarding particulate nAl and similar nanoscale additives, a promising preparation method has been identified to significantly improve droplet combustion performance with suspended energetic particles and drastically increase stability of the suspensions against settling. This electrospray preassembly of nanoparticles into NC-bound mesoparticles also provides flexible means of tuning reactivity with morphology or composition including facilitation of composite additives with different nanoparticle ingredients intimately mixed.

Soluble Al(I) tetrameric clusters stabilized by triethylamine ligands, $[AlBrNEt_3]_4$, are dissolved a toluene/ether co-solvent and burned as single droplets in Chapter 3 as a proof of concept for the first design iteration of the experimental

apparatus. This study validates the approximation methodology for burning rate constant based on total burning time and initial droplet size and proves the apparatus is suitable for highly sensitive and reactive air-sensitive liquids. The $Al_4$ cluster material exhibits high burning rate increases ~20% considering its comparatively low active aluminum content of 0.16 wt% which when added as nAl has no discernible effect on the carrier fuel. Microexplosive events resulting from HBr gas evolution in the droplet are proposed to be the primary mechanism of burning rate increase.

Chapter 4 builds upon the observation of burning rate increases from gas generation in the prior chapter and investigates nitrocellulose (NC) as a gas generating co-additive for nanoaluminum in kerosene droplets stabilized with trioctylphosphine oxide (TOPO) surfactant. Both physical mixtures of nAl and NC along with electrosprayed MPs of nAl with NC binder are considered, demonstrating the NC co-additive to be capable of counteracting burning rate decreases seen with nAl alone, and identifying significant benefits of higher burning rate increases and greater maximum stable suspension loadings made possible by the electrospray preassembly strategy. The condensed phase of filament stabilized droplets are imaged by shadowgraph to assess the influence of droplet disruptions and deformations on the burning rates estimated.

In Chapter 5, the NC-bound MP architecture is put to use for incorporation of oxygen-containing particles into kerosene/TOPO. The benefits of the MP structure identified in Chapter 4 with nAl are reinforced and burning rate increasing mechanisms unique to different oxide particle compositions are studied and proposed. CuO and

$KIO_4$ are shown to be promising for burning rate enhancement by releasing oxygen on the fuel rich side of the diffusion-limited droplet flames. Emission spectroscopy of the droplet flames is utilized to probe the chemical effects of the oxides.

With benefits of preparing nanoenergetic particles for liquid incorporation by electrospray with NC binder made clear by the work in the two preceding chapters, Chapter 6 quantitatively demonstrates the greater stability in kerosene/TOPO afforded to nAl by this preparation method. The tunability of electrospray is also demonstrated as precursor concentration in varied and effects on the morphology, particle gravitational settling, and burning rates are assessed and modes of interactions between these factors are discussed.

As an extension of Chapters 4 and 5 and demonstration of flexible capabilities of electrospray particle assembly, Chapter 7 employs composite nAl/oxidizer mesoparticles as additives for kerosene/TOPO. Burning rate constants are assessed and mechanisms proposed based on the nature and activity of the oxides as they relate to the nature of the nAl fuel and MP architecture. Atomic emission spectroscopy is used to probe the chemical mechanisms of the additives and show that physical disruption effects caused by the MP structure are a powerful vehicle for transporting additive particles into the flame zone before liquid burn-off.

Another soluble aluminum additive is considered in Chapter 8, albeit in a higher oxidation state than the cluster material demonstrated in Chapter 3. Commonalities between the two materials highlight unique activity and benefits of air-sensitive additives and drastic burning rate increases are realized even with the higher oxidation

state aluminum in the additive. Color camera ratio pyrometry is employed to characterize droplet flame temperature effects of the additive and control additives and emission spectroscopy of AlO is used to prove direct chemical activity of the Al in the additive and highlight its strongest emergence during microexplosive disruptions.

## *9.2. Recommendations for Future Work*

### 9.2.1 Improvements to Droplet Combustion Apparatus

In the latest design iteration of the experiment, initially generated droplet size is estimated to vary up to ±50 μm in most cases and less so during a specific trial. On occasion, especially high viscosity samples have been seen to cause up to 100 μm variation (usually an increase) of the nominally generated droplet size relative to other samples. These variations are currently monitored and minimized in each experimental set to ensure that any compared data is within the prescribed ±50 μm variation but this inconsistency represents the primary source of non-repeatability risks and uncertainty. To improve this, alternative droplet generation methods can be (and have been) considered including most notably ultrasonic vibration of an orifice orthogonal to the plane of the orifice created by a piezoelectric actuator with sample pumped through the orifice, e.g. as employed by the Tanvir and coworkers in the Qiao research group at Purdue University [55]. Such a method can produce more monodisperse droplets with more repeatable trajectories but has not been used because the separation between droplets is usually low and difficult to increase, and the setup is not usually employed with disposable/replaceable surfaces exposes to the sample (a significant practical

benefit of the aerodynamic shedding method used in this research). However, even without changing the operating principle of the current droplet generation system, it stands to benefit highly from a top-end redesign of the apparatus to improve needle/nozzle alignment and capillary length. Better repeatable concentricity and alignment of the nozzle and needle as shown in Figure 12 would help to maintain more consistent initial droplet size by mitigating effects of varying misalignments. Achieving acceptable alignment is also practically one of the most difficult steps of the operation procedure for the experimentalist and data collection rates would benefit from minimizing such difficulty. Shorter capillary lengths can not only help to make this step easier, but also lessens the operating cost of the experiment by requiring less needle materials and would decrease prevalence of needle clogging with a lower syringe pressure required to pump sample through a shorter capillary. In the current apparatus, most of the needle length is required to traverse height of the assembly provided for the alignment systems which can be significantly shortened with a mechanical redesign. The alignment system also has a zero position near one end of the X-Y limits and therefore can only appreciably make alignment compensations in one direction for each axis. If the needle is misaligned in the other direction it has to be reseated before alignment can be achieved, a problem which should be fixed with a redesign. Overall, a more user-friendly droplet generation assembly using significantly shorter needle assemblies is likely to increase data collection rates and decrease uncertainty from varying initial droplet size.

Another limitation of this instrument's precision is the size of the tower relative to the droplet and its trajectory. Creating a larger tower so that the ambient environment is more semi-infinite relative to each droplet is a non-trivial redesign compared to a simpler redesign of only the top-end assembly, but would minimize effects of droplet combustion on the oxidizing environment, possibly decrease some turbulent trajectory variations, and facilitate use of less oxygen-concentrated purge gases which lengthen the burning time. The current experiment requires oxygen so that droplets do not risk impinging on the screen at the bottom on the tower.

Considerable evidence has been gathered in the more recent investigations undertaken as the ability to image moving droplets in high magnification has improved experimentally. Notably, this capability improved when the vertical translation stage was added to drop a high-speed camera alongside combusting droplets. However, this method is passive and numerous repetitions are usually required to collect a video with long viewing times (or imaging of full droplet lifetimes), repetitions which are not always possible based on sample quantity limitations. The vertical translation stage can be used with a custom designed motion controller to control the descent of the camera using video output (and the position of the droplet in the frame) to increase or decrease a controller input force. Design concepts based on a belt drive or electromagnetic braking have been considered. Motion tracking of droplets would drastically improve data collection rates and efficiencies for magnified video collection and other optical diagnostics like spectroscopy which can be mounted on the vertical translation stage.

### 9.2.2 Alternate Droplet Combustion Experiment and Analysis Techniques

Analysis MATLAB code used to take video-based measurements for burning rate constant estimation could benefit from optimization to be more user-friendly and/or addition of a graphical user interface. While the burning rate calculation program can be learned by a new MATLAB user, formation of time-lapse images and frame montages using MATLAB tools created during this research currently requires the user to understand MATLAB programming to make code adjustments as necessary. Therefore, these tools can also benefit from code optimization to be more user-friendly. Such improvement would facilitate independent operation of this experiment by users who are less proficient in MATLAB analyses and programming.

Qualitatively, differences in ease of ignition has been observed during experiment operation but this evidence is purely anecdotal. In the current experiment, ignition facilitated by methane diffusion flame pilots is poorly controlled for precise energy input compared to resistive or radiative heating by current flow in a wire or a focused laser source. Slow degradation of the ceramic methane delivery tubes limits exact repeatability of the relationship between methane flow and ignition energy delivered over time. Thusly, the current design is not suitable for ignition delay measurement but could be adapted to measure this using another ignition method either by a hot wire coil or focused laser beam. A costlier redesign would be required to characterize autoignition by releasing the droplets to fall into a vertical tube furnace.

Prevalence of soot formation and flame standoff ratio can be sensitive to the chemical mechanism of combustion occurring. Most of the additives considered in this

dissertation are thought to be chemically active and therefore could be affecting the sooting properties or flame standoff ratio of the base fuel. Experiments can be designed to use the droplet combustion apparatus to observe possible effects with some adjustments of the current apparatus and methodology. Aforementioned improvements to droplet motion tracking would facilitate more reliable collection of magnified flame videos. From these the flame size and position can be assessed over the lifetime of the droplet more precisely which could be related to sooting behavior and flame standoff ratio thereby providing insight. The backlighting method used to make initial droplet sizing measurements (with the expanded HeNe laser) has also been seen to image larger soot particles in igniting Toluene droplets (when flame emission is filtered using a HeNe line filter). Employing this backlighting apparatus with optical techniques allowing height variation of the camera, or tracking of the backlight with a falling camera on the translation stage, could facilitate direct imaging of soot and the condensed droplet boundary as the droplet burns down the length of the tower.

Free-droplet combustion is a relevant research topic as it relates to spray combustion of fuels and propellants in practical systems. A logical extension of single droplet experimentation is therefore scale-up to spray-based experiments which more closely emulate the practical systems of interest. Achieving this transition with nanoscale additives is non-trivial as the additives introduce practical complications such as particle deposition and rheology effects. The single droplet combustion experiment developed in this dissertation is valuable in part because it tolerates liberal particle deposition in the system by using strategically disposable components,

primarily the droplet delivery needle. A spray combustion experiment which may incorporate similar design features could be used to study collective effects of droplets in a spray and characterize metrics such as atomization efficiency, burning time, combustion enthalpy, or even specific impulse.

### 9.2.3 Further Studies of Additives for Hydrocarbons

The research in this dissertation primarily concerns experiment development and additive identification with some context provided by probing additive mechanisms. The basic nature of this work has identified as many new questions as new answers. Several avenues of possible research continuations are now clear. The scope of this work limited chemical stabilization to the used of TOPO surfactant in kerosene. Numerous alternatives have already been identified including sorbitan olelate, oleic acid or surface functionalization of additive particles [37-39]. The interaction of such techniques with the mesoparticle preassembly strategy demonstrated in this work could yield more effective methods of stabilization. The nature of such stabilization as it relates specifically to MPs is poorly understood beyond the higher stability observed in this work. Colloidal studies could identify the beneficial nature of MPs for chemical stabilization in order to exploit those features and extend them to other particle systems. Innumerable constituent alternatives exist to replace the fuel, oxidizers, and NC binder utilized herein. Namely, silicon and boron fuels incorporate similar energy density benefits as aluminum, albeit with their own specific complications (namely inhibition of boron ignition by HOBO formation). Considering the demonstrations here that morphology and strategic co-additives can drastically

change additive behavior, problems with the combustion of nanoscale silicon or boron could be mitigated with novel liquid addition and particle synthesis techniques. MP binders other than NC like PVDF, PTFE, or HTPB are worth investigating for improved thermal stability of the additives or effects of direct reaction between particle constituents and the binder. Lastly, the soluble additives investigated in this dissertation largely constitute a proof-of-concept for exploitation of soluble organometallic cluster materials as hydrocarbon additives. Significant loading improvements, stability increases, synthesis simplifications, and performance increases are possible upon continued research of aluminum or silicon-based metastable molecular clusters soluble in hydrocarbons.

# Appendix A: Supplemental Material for Chapter 4

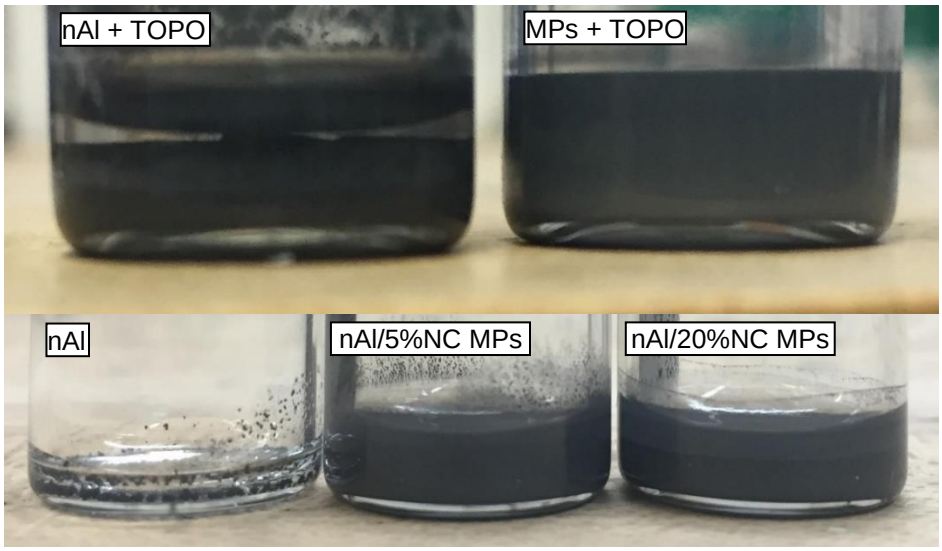


*Figure A.1: (Top) nAl versus MP representative suspension quality after 1 week with TOPO surfactant. (Bottom) Suspension quality of 6.9 wt% nAl, nAl/5%NC MPs, and nAl/20%NC MPs after 1 day without TOPO surfactant.*

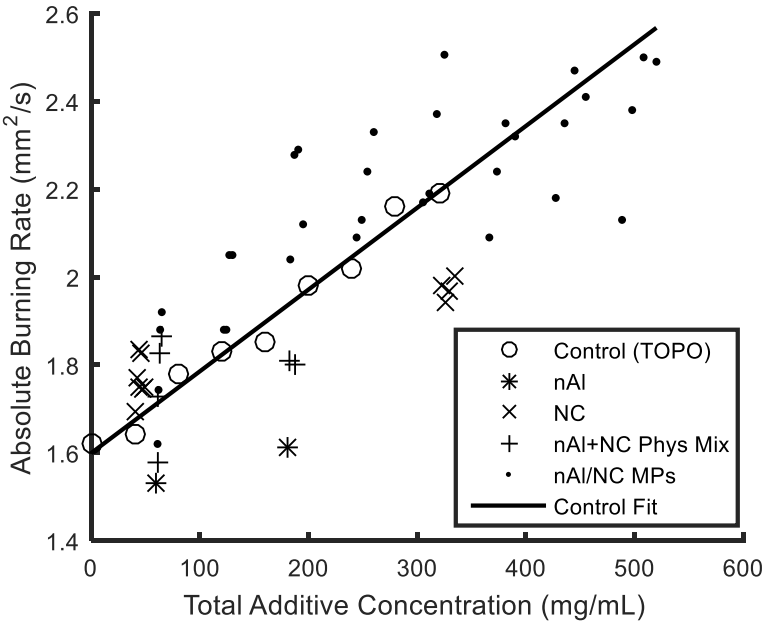


*Figure A.2: Absolute burning rate constants measured in falling droplet experiments versus total additive concentration. Linear trendline shows correlation between surfactant concentration and burning rate (subsequent burning rate data normalized by respective TOPO control burning rates).*

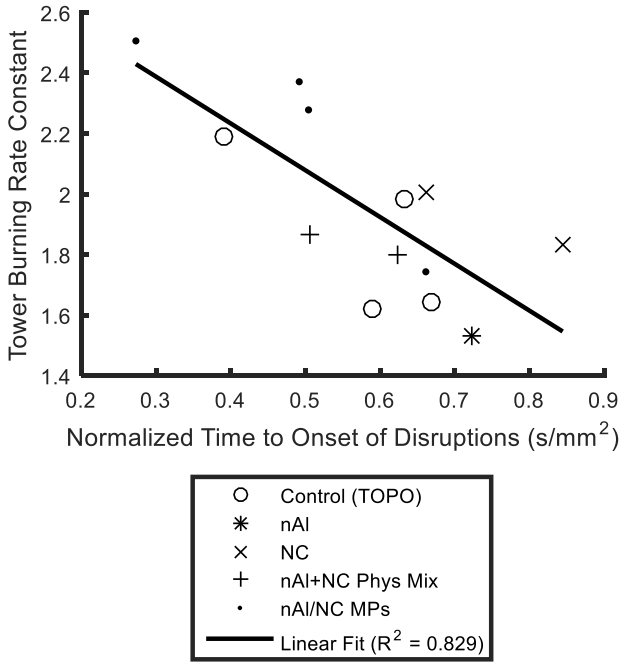


*Figure A.3: Burning rate constants measured in falling droplet experiments versus normalized time to first disruptive region in suspended droplet experiments.*

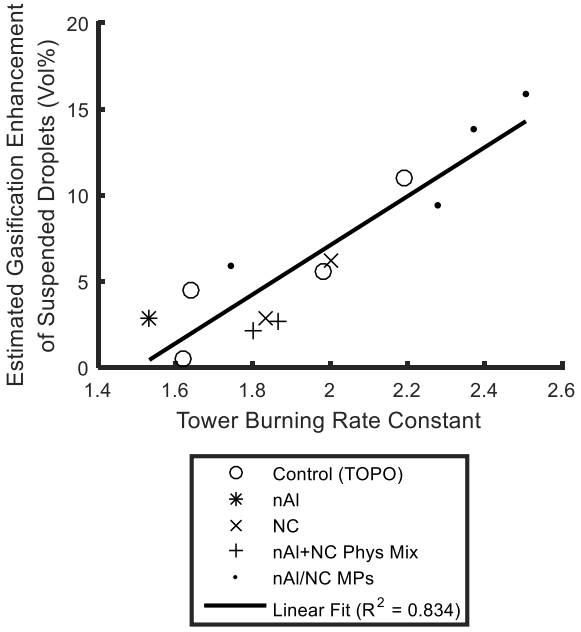


*Figure A.4:* $\left(\frac{\Delta V}{V_0}\right)_{Inflation}$ *(Estimated enhancement of surface gasification caused by inflated droplet surface areas in suspended droplet experiments) versus burning rate constants measured in falling droplet experiments.*

Each figure below depicts the droplet diameter evolution versus time measured from suspended droplet experiments for each sample listed. For qualitative comparison, adjacent images depict the same sample in a time-lapse of a representative droplet combusting in the falling droplet configuration. Vertical position is not always an accurate depiction of time from ignition, but merely an approximation.

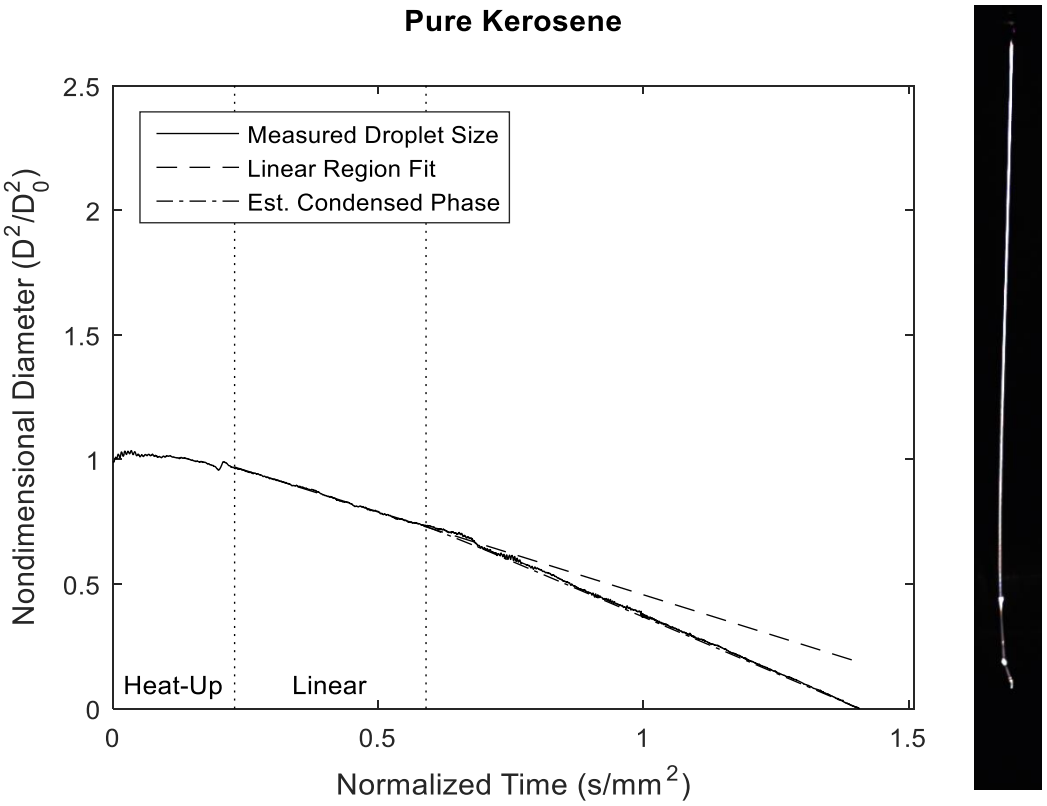

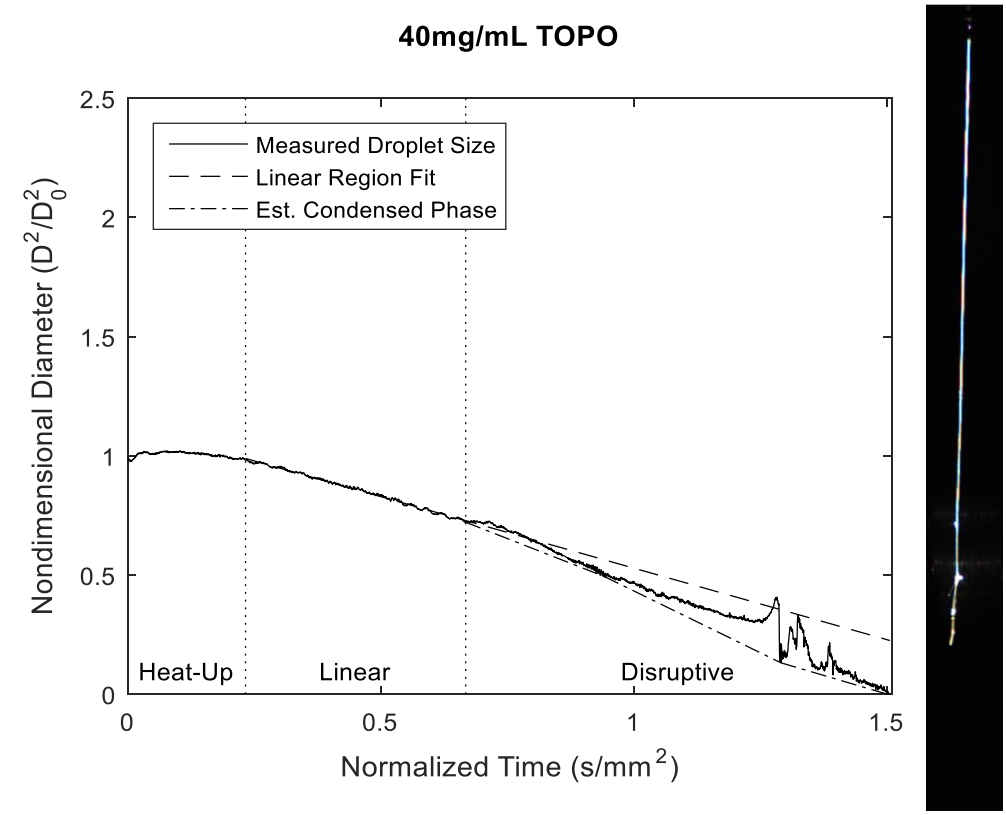
40mg/mL TOPO
Measured Droplet Size
Linear Region Fit
Est. Condensed Phase
Nondimensional Diameter (D²/D₀²)
Normalized Time (s/mm²)
Heat-Up
Linear
Disruptive
0
0.5
1
1.5
2
2.5

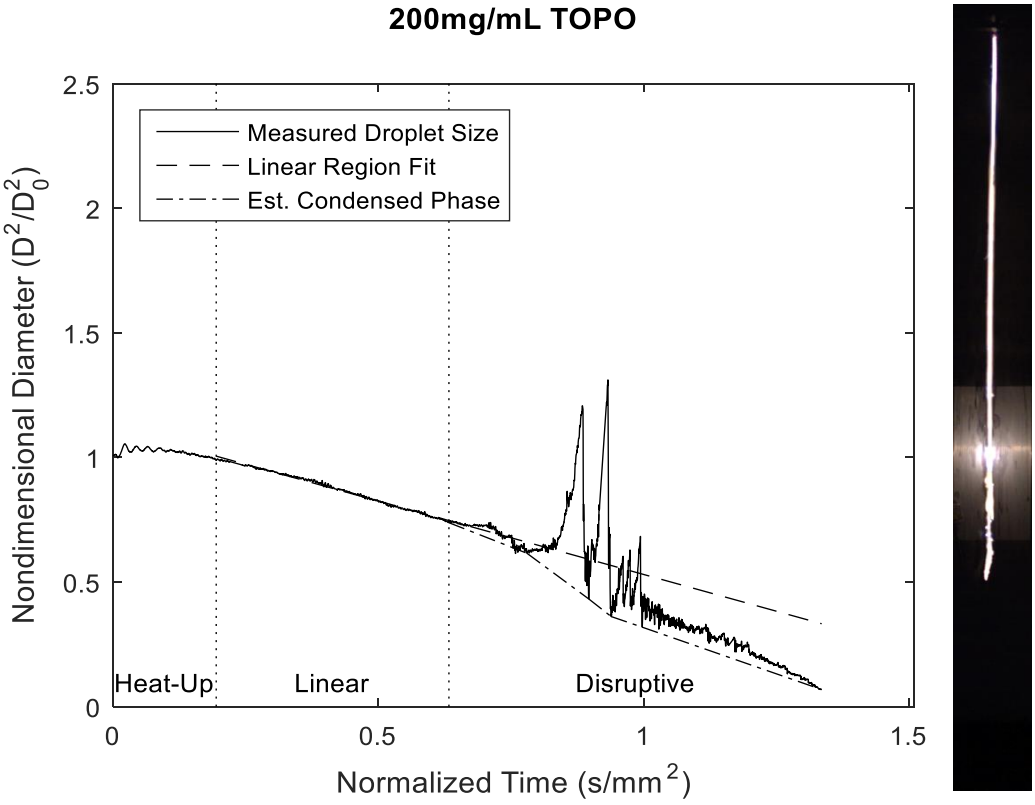
200mg/mL TOPO
Measured Droplet Size
Linear Region Fit
Est. Condensed Phase
Nondimensional Diameter (D²/D₀²)
Normalized Time (s/mm²)
Heat-Up
Linear
Disruptive
0
0.5
1
1.5
2
2.5

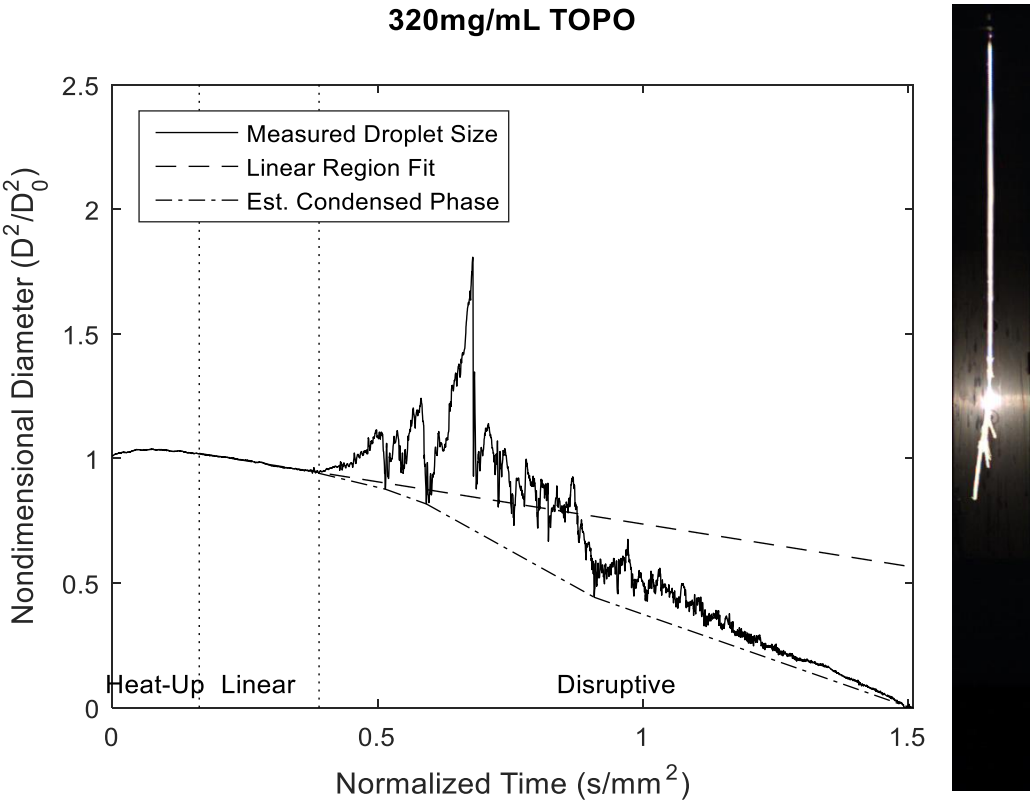
320mg/mL TOPO
Measured Droplet Size
Linear Region Fit
Est. Condensed Phase
Nondimensional Diameter ($D^2/D_0^2$)
Normalized Time ($s/mm^2$)
Heat-Up
Linear
Disruptive
0
0.5
1
1.5
2
2.5

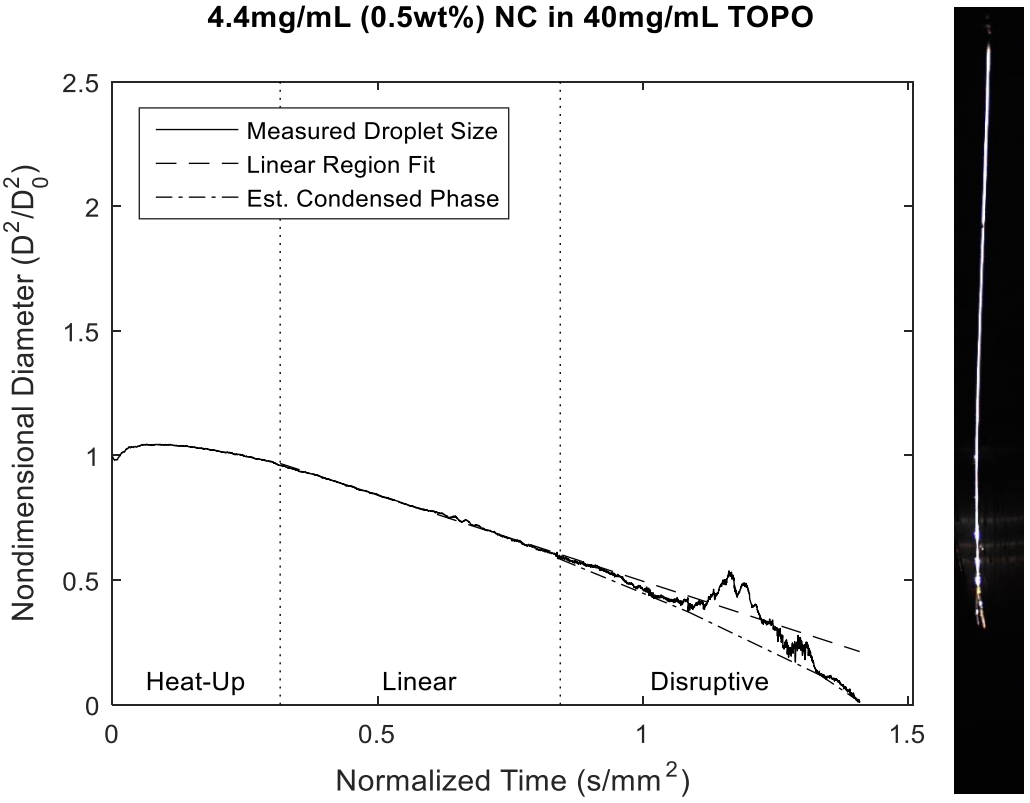
4.4mg/mL (0.5wt%) NC in 40mg/mL TOPO
Measured Droplet Size
Linear Region Fit
Est. Condensed Phase
Nondimensional Diameter ($D^2/D_0^2$)
Normalized Time ($s/mm^2$)
Heat-Up
Linear
Disruptive
0
0.5
1
1.5
2
2.5

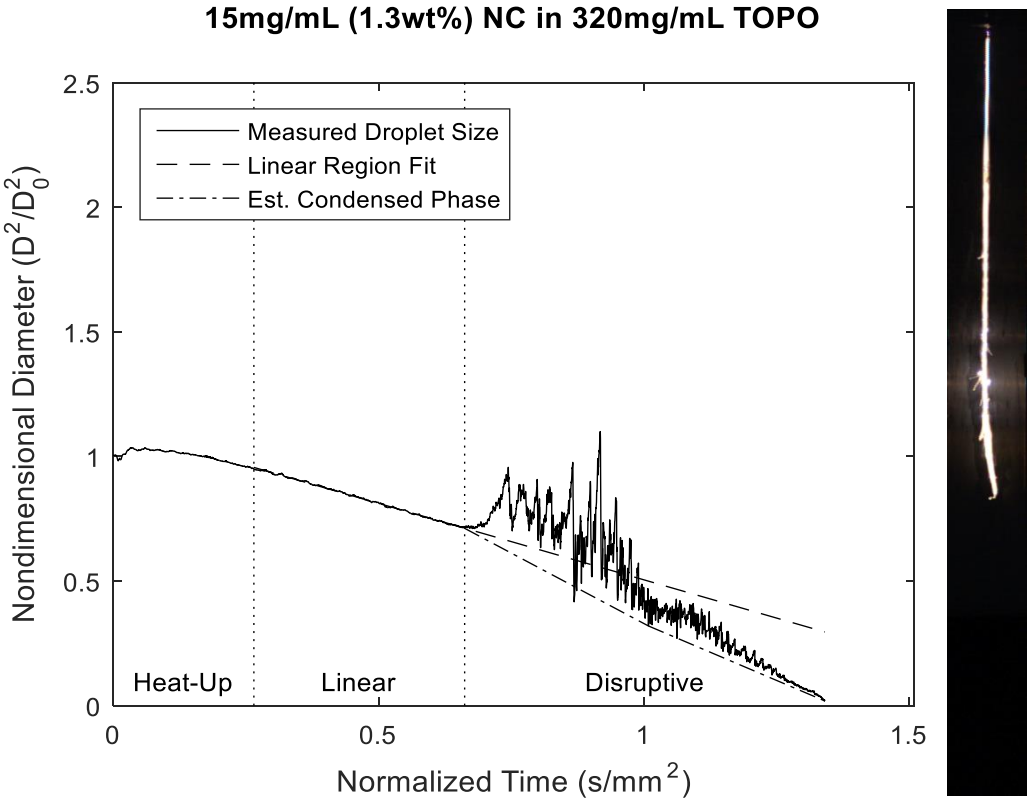
15mg/mL (1.3wt%) NC in 320mg/mL TOPO
Measured Droplet Size
Linear Region Fit
Est. Condensed Phase
Heat-Up
Linear
Disruptive
Nondimensional Diameter (D²/D₀²)
Normalized Time (s/mm²)
0
0.5
1
1.5
2
2.5

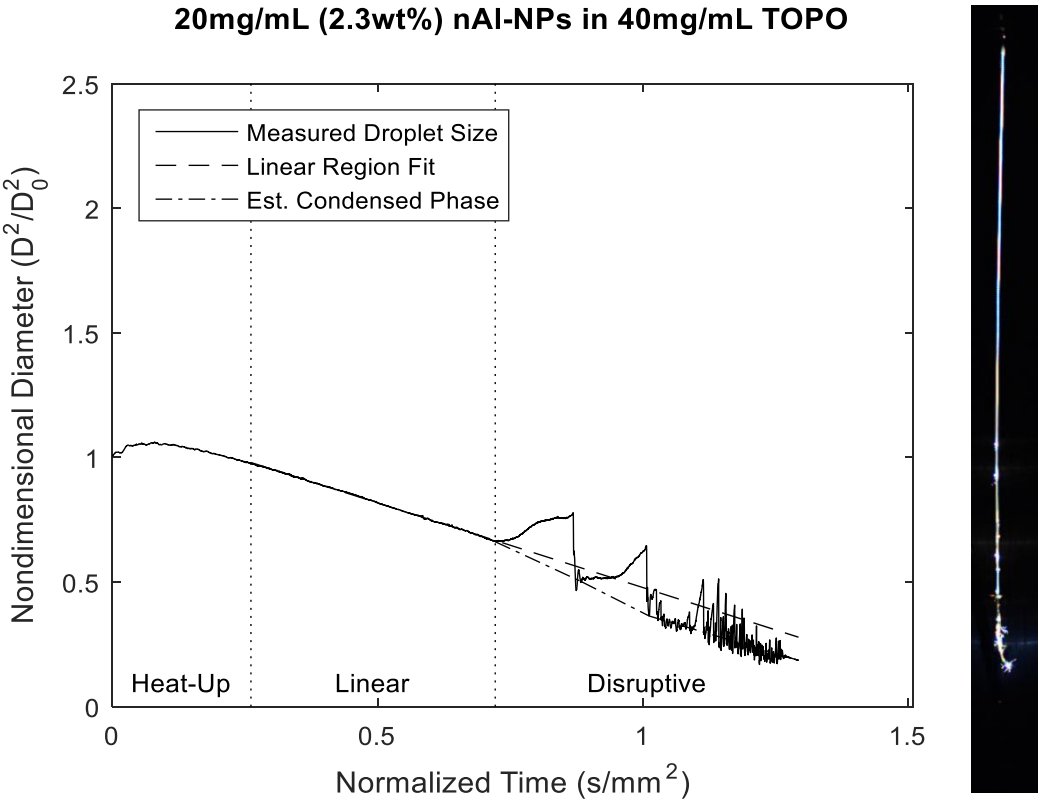
20mg/mL (2.3wt%) nAl-NPs in 40mg/mL TOPO
Measured Droplet Size
Linear Region Fit
Est. Condensed Phase
Heat-Up
Linear
Disruptive
Nondimensional Diameter (D²/D₀²)
Normalized Time (s/mm²)
0
0.5
1
1.5
2
2.5

**25mg/mL (2.9wt%) nAl-NPs + 20%NC Phys Mix in 40mg/mL TOPO**

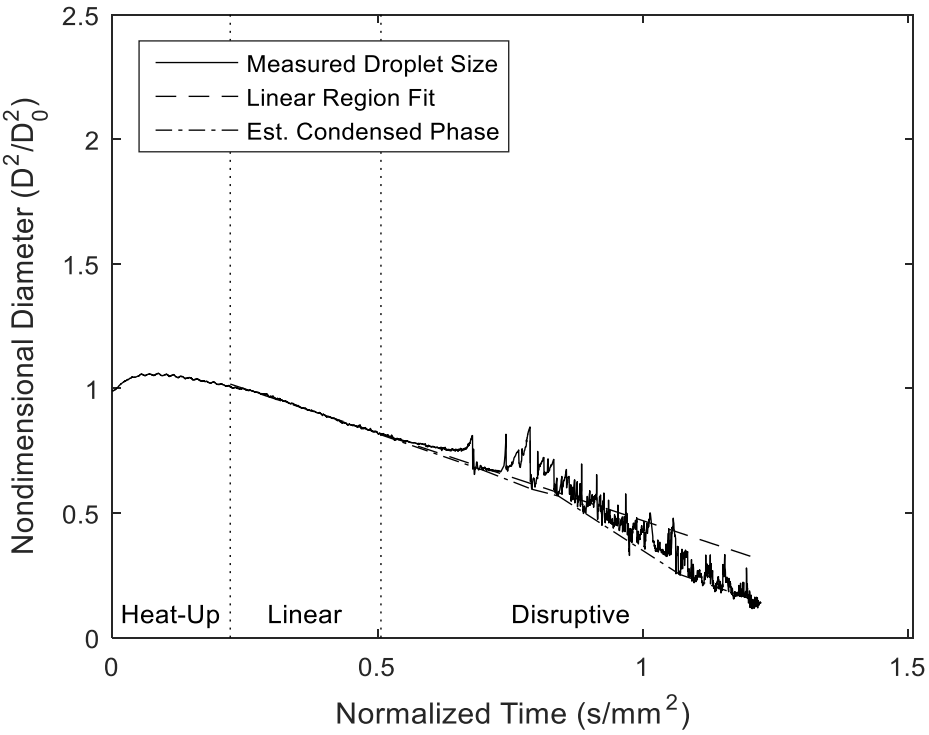


**67mg/mL (6.7wt%) nAl-NPs + 10%NC Phys Mix in 120mg/mL TOPO**

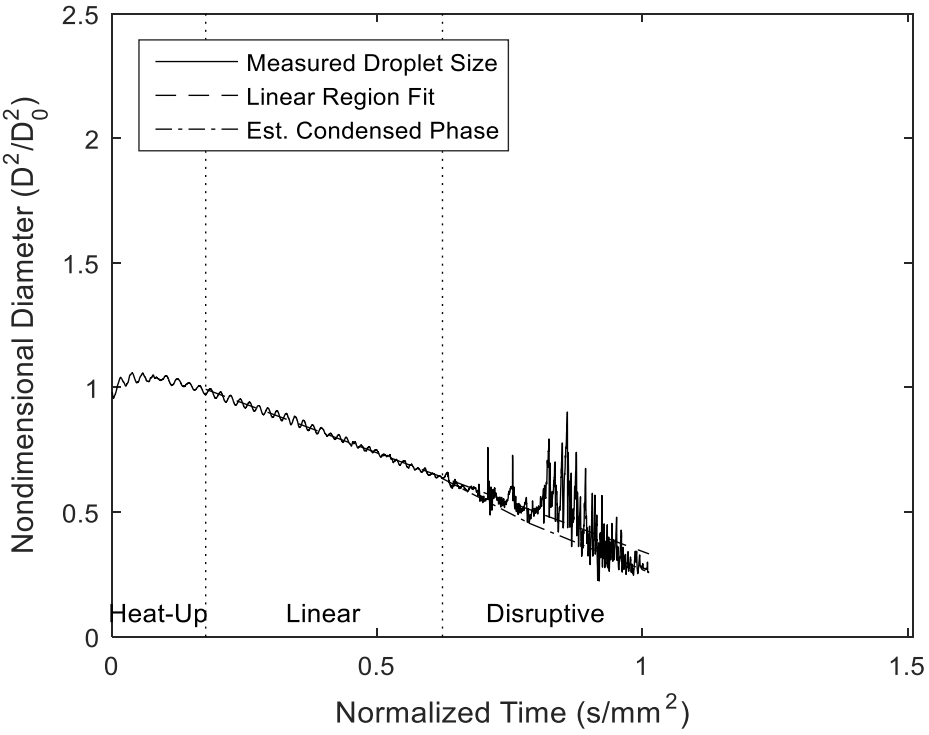


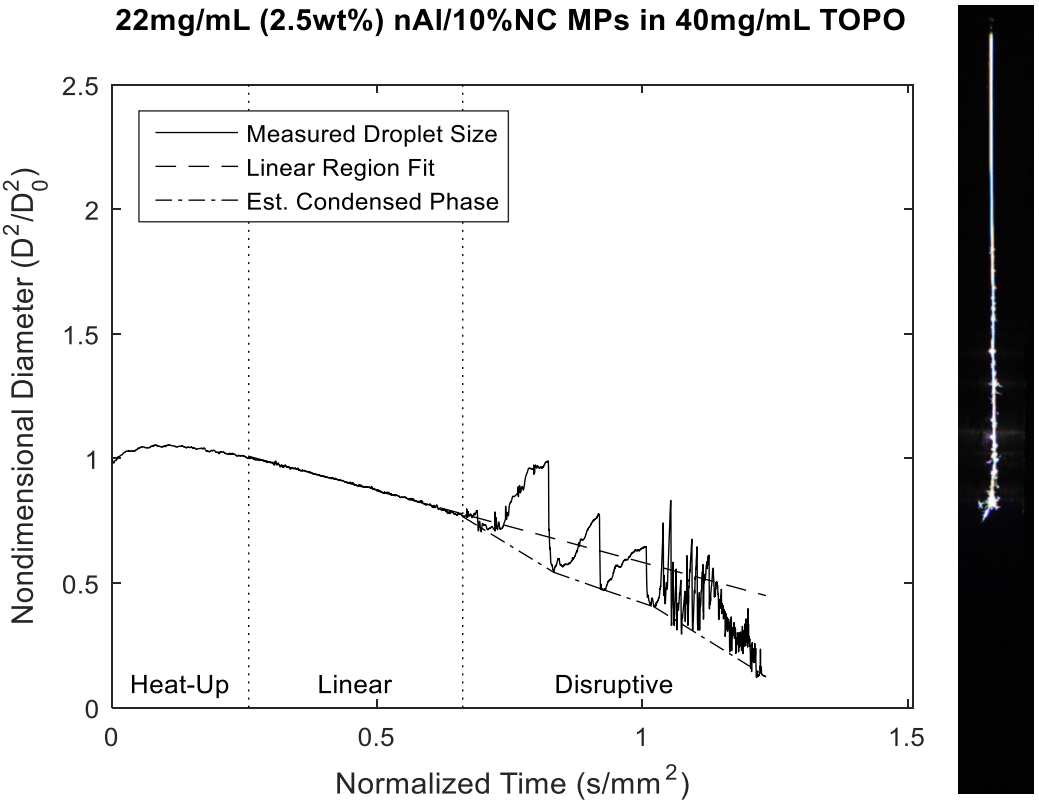
22mg/mL (2.5wt%) nAl/10%NC MPs in 40mg/mL TOPO
Measured Droplet Size
Linear Region Fit
Est. Condensed Phase
Heat-Up
Linear
Disruptive
Nondimensional Diameter ($D^2/D_0^2$)
Normalized Time ($s/mm^2$)
0
0.5
1
1.5
2
2.5

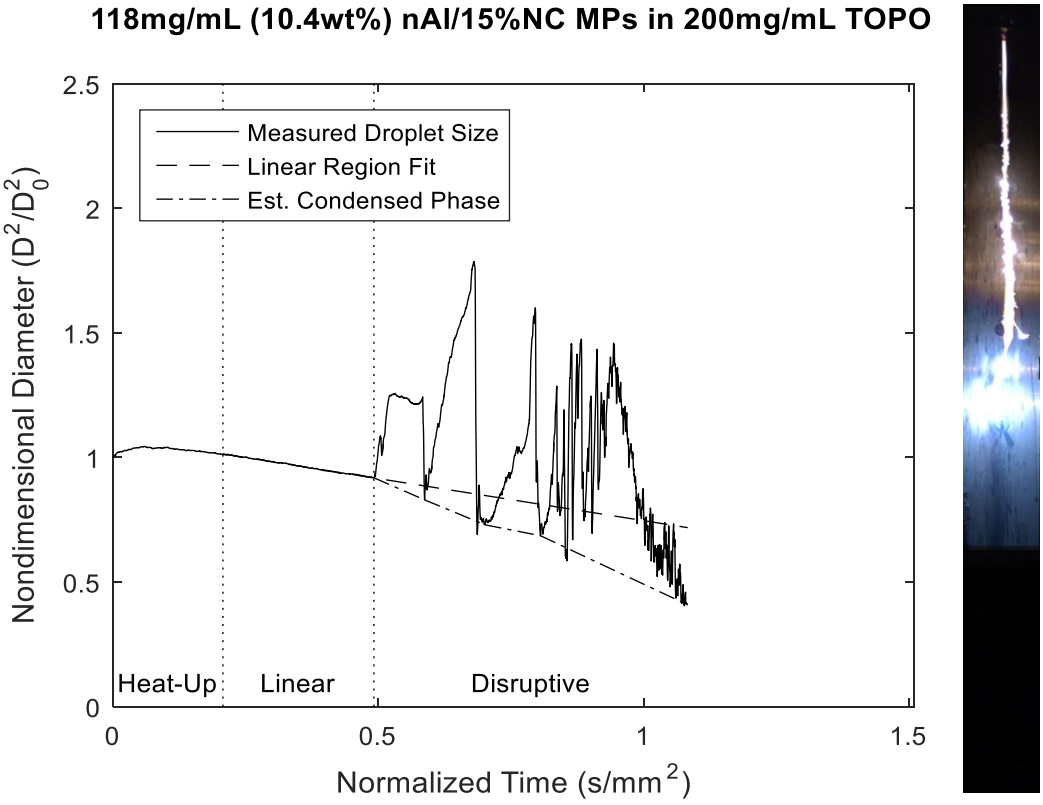
118mg/mL (10.4wt%) nAl/15%NC MPs in 200mg/mL TOPO
Measured Droplet Size
Linear Region Fit
Est. Condensed Phase
Heat-Up
Linear
Disruptive
Nondimensional Diameter ($D^2/D_0^2$)
Normalized Time ($s/mm^2$)
0
0.5
1
1.5
2
2.5

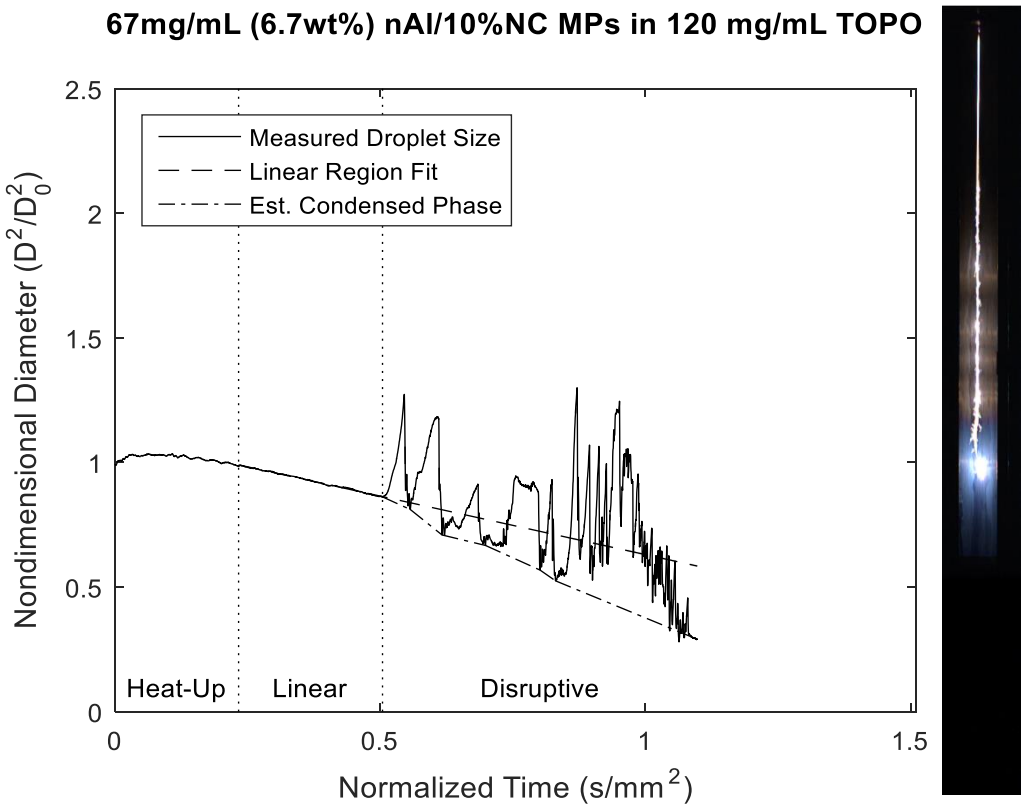
67mg/mL (6.7wt%) nAl/10%NC MPs in 120 mg/mL TOPO
Measured Droplet Size
Linear Region Fit
Est. Condensed Phase
Heat-Up
Linear
Disruptive
Nondimensional Diameter (D²/D₀²)
Normalized Time (s/mm²)
0
0.5
1
1.5
2
2.5



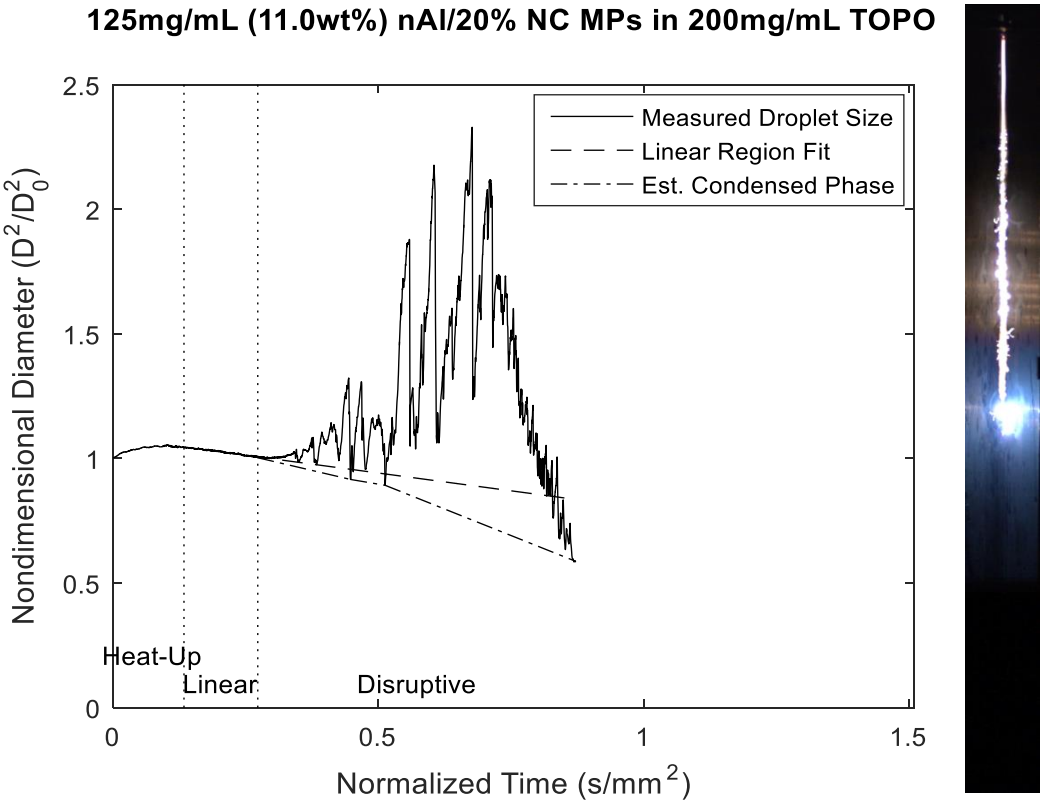
125mg/mL (11.0wt%) nAl/20% NC MPs in 200mg/mL TOPO
Measured Droplet Size
Linear Region Fit
Est. Condensed Phase
Heat-Up
Linear
Disruptive
Nondimensional Diameter (D²/D₀²)
Normalized Time (s/mm²)
0
0.5
1
1.5
2
2.5

# Appendix B: Supplemental Material for Chapter 5

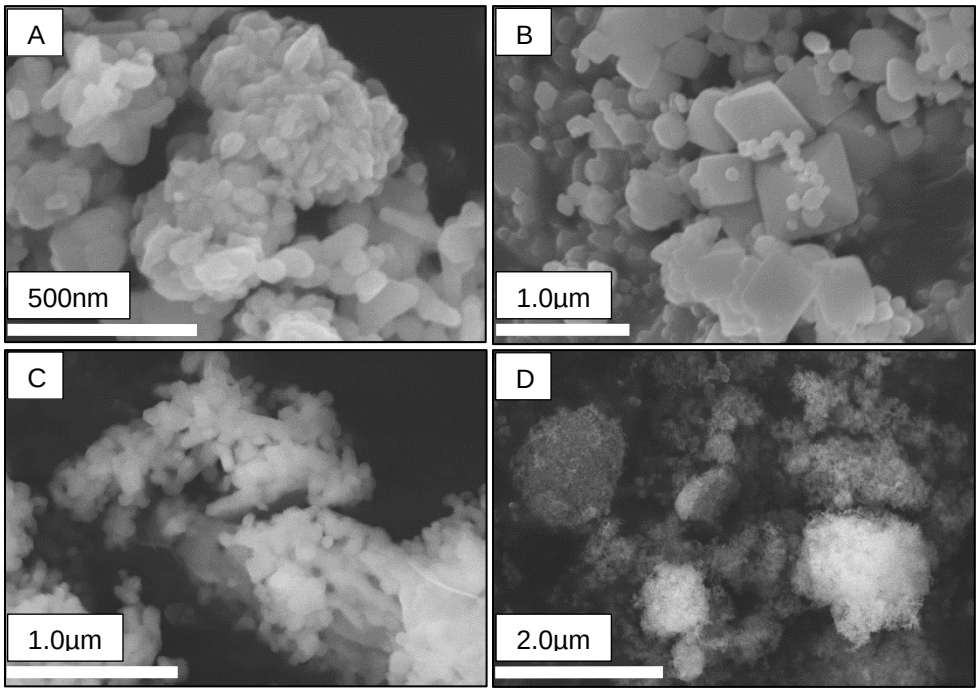


*Figure B.1: SEM of (A) CuO, (B) $KIO_4$, (C) MgO, and (D) $Al_2O_3$ Nanoparticles.*

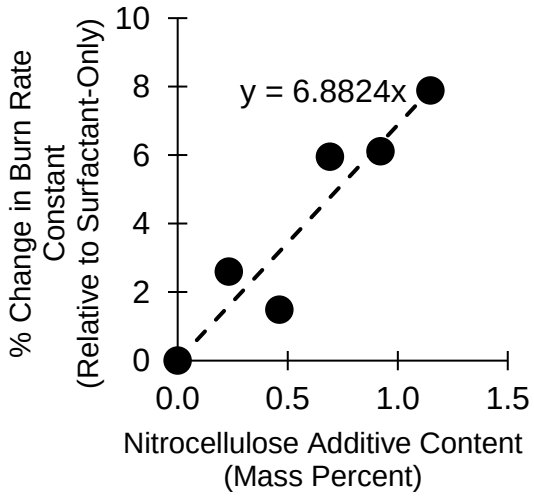


*Figure B.2: Effect of pure NC nanoparticles on burning rate constant of Kerosene/TOPO.*

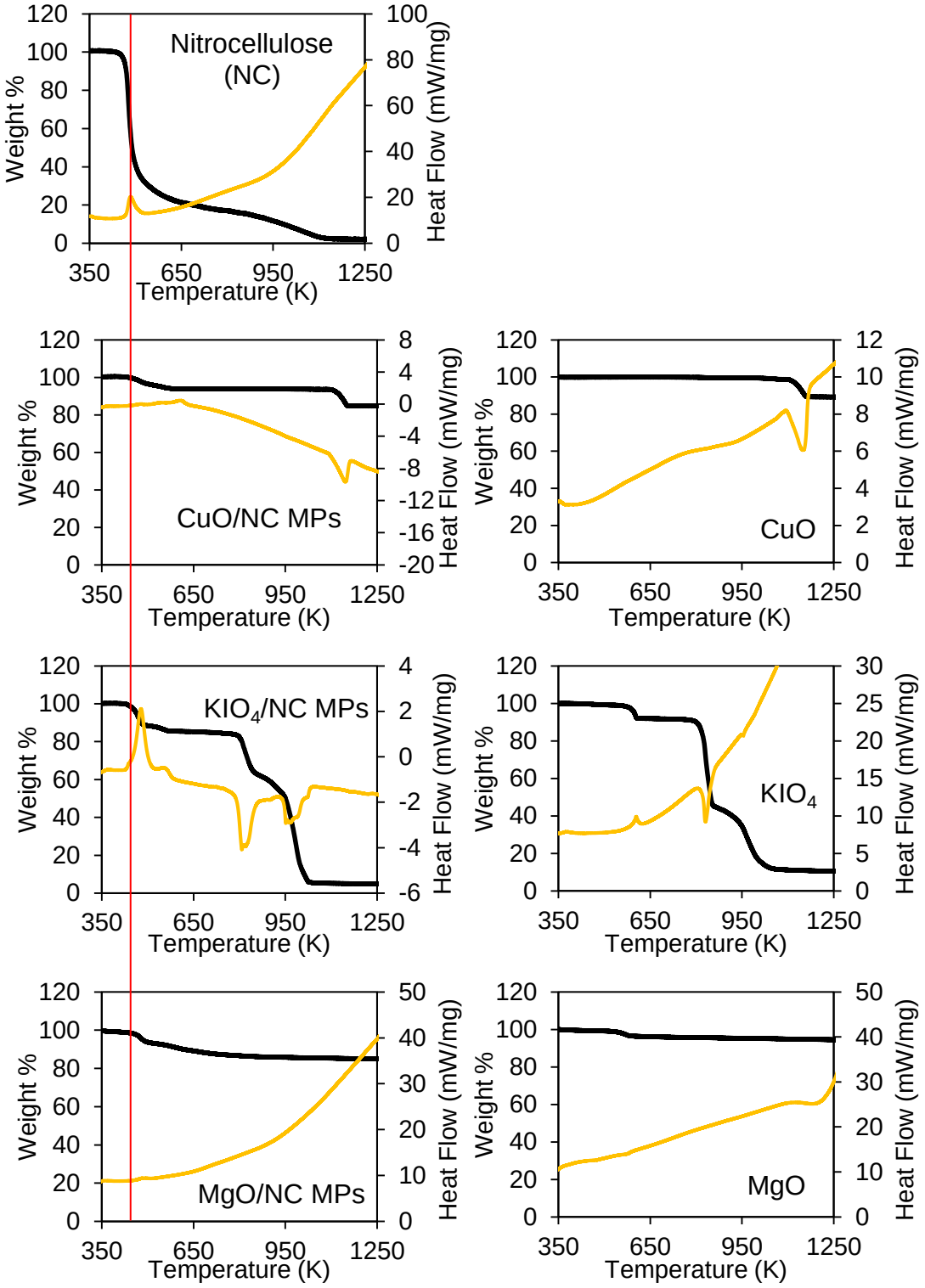


*Figure B.3: TGA/DSC of additives with interplot reference line for NC decomposition temperature.*

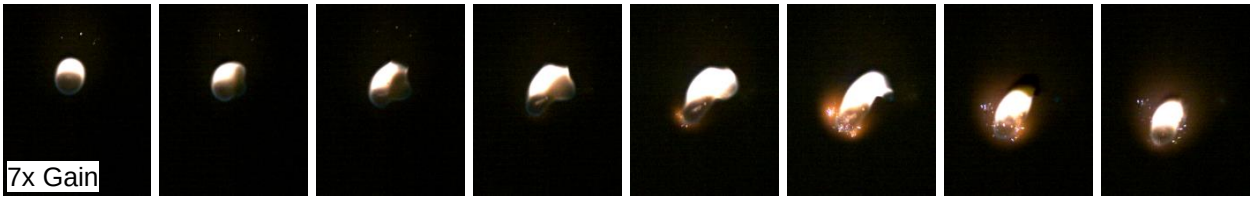


*Figure B.4: Representative swelling/eruption event during combustion of MgO/NC MPs in Kerosene/TOPO. Brightness is artificially increased for visibility as labeled on the first frame of each gain adjustment setting. 166μs image period.*

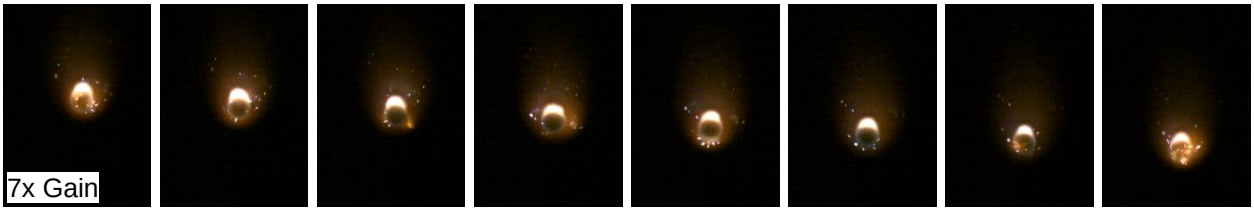


*Figure B.5: Representative particle emission release during combustion of MO/NC MPs in Kerosene/TOPO. Brightness is artificially increased for visibility as labeled on the first frame of each gain adjustment setting. 166μs image period.*

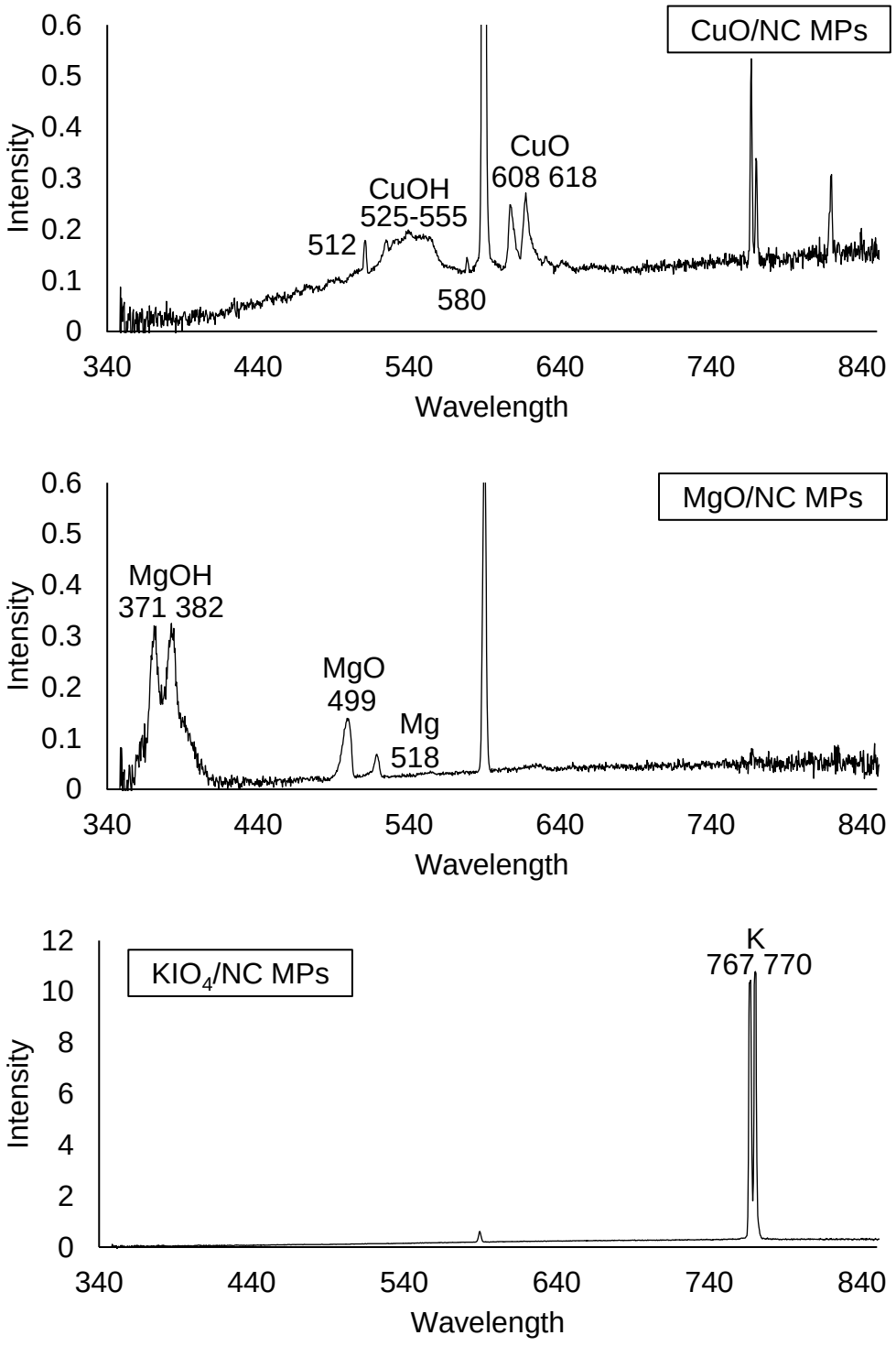


*Figure B.6: Representative spectra measured during CuO/NC MP, MgO/NC, and $KIO_4$/NC MP-laden droplet combustion.*

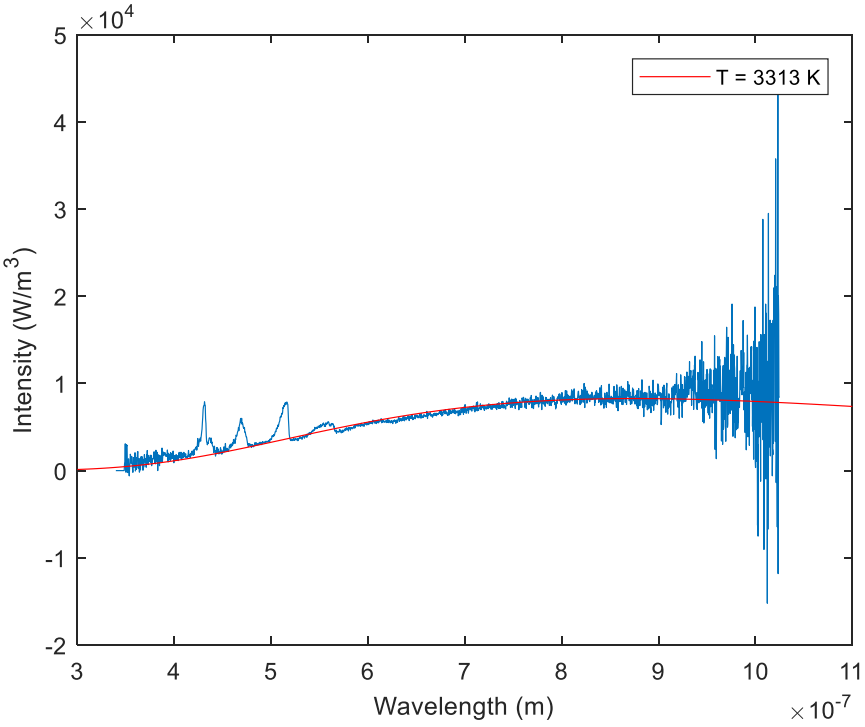


*Figure B.7: Kerosene Flame Spectra with Planck's Law fit.*

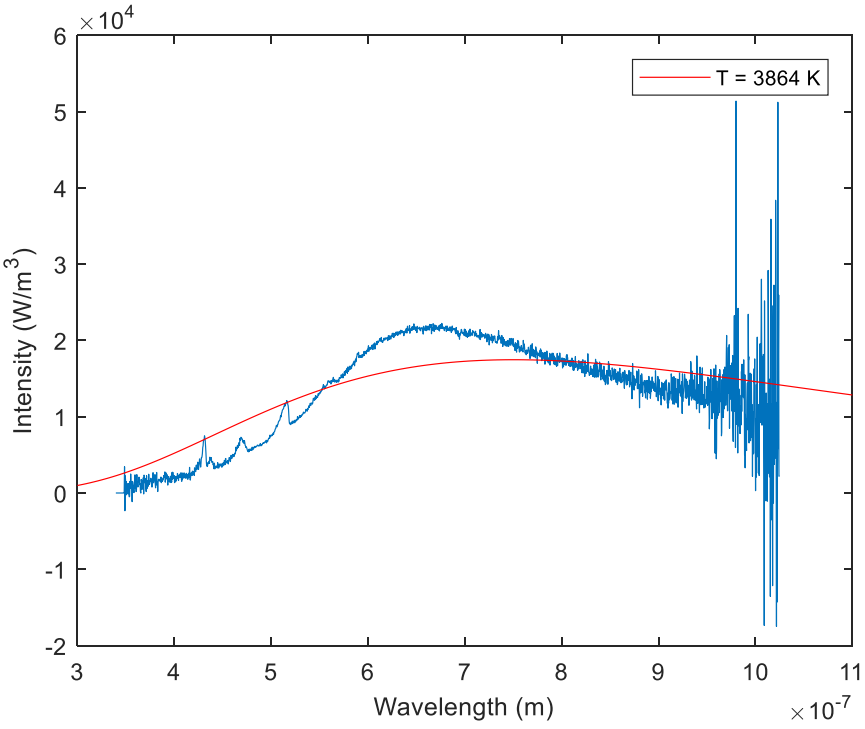


*Figure B.8: Kerosene/TOPO Flame Spectra with Planck's Law fit.*

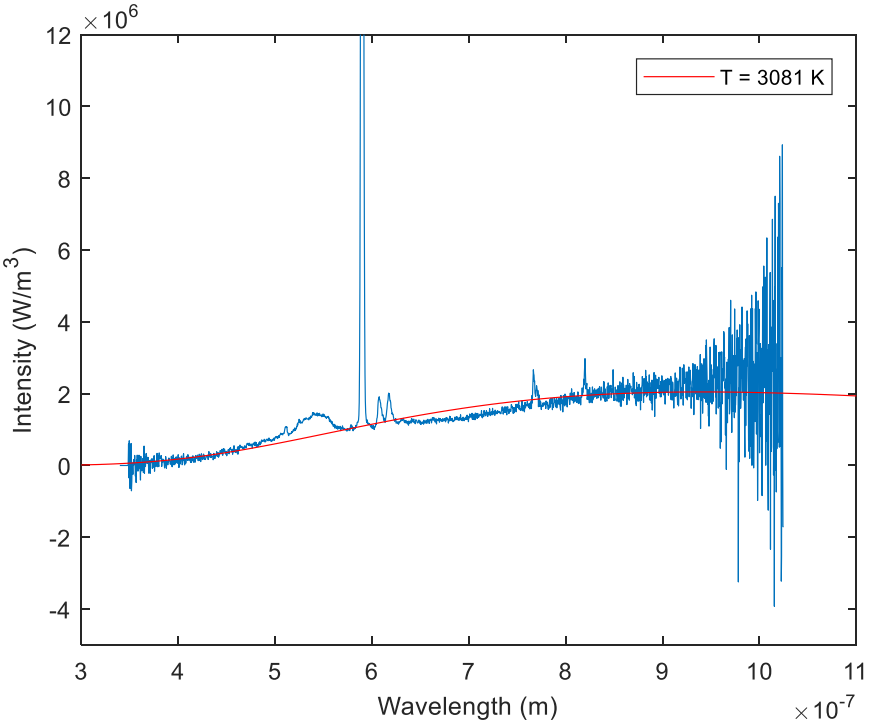


*Figure B.9: CuO/NC MPs in Kerosene/TOPO Flame Spectra with Planck's Law fit.*

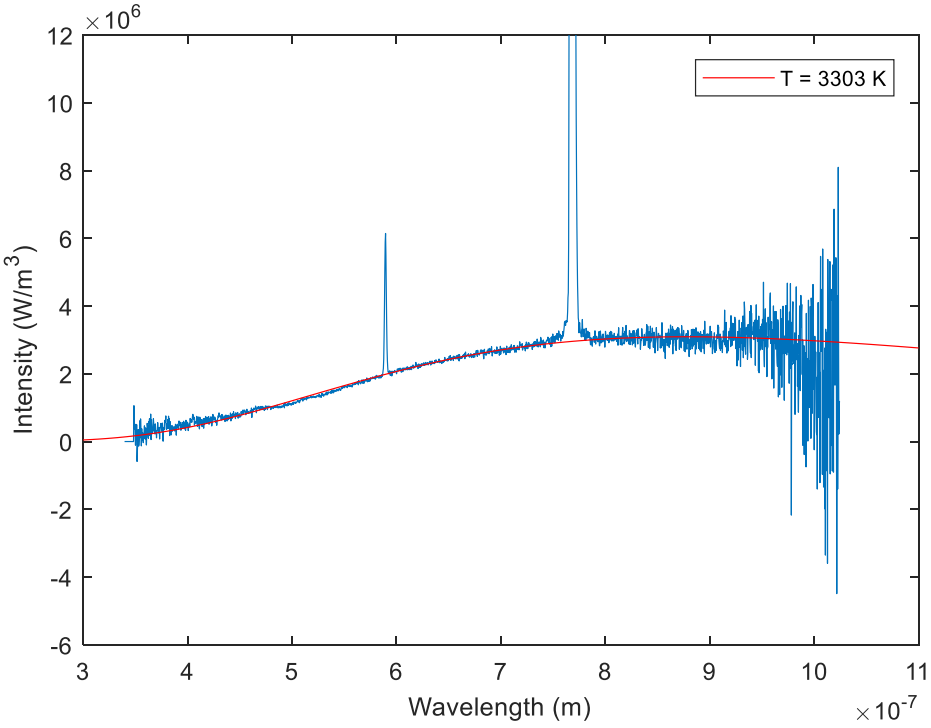


*Figure B.10: $KIO_4$/NC MPs in Kerosene/TOPO Flame Spectra with Planck's Law fit.*

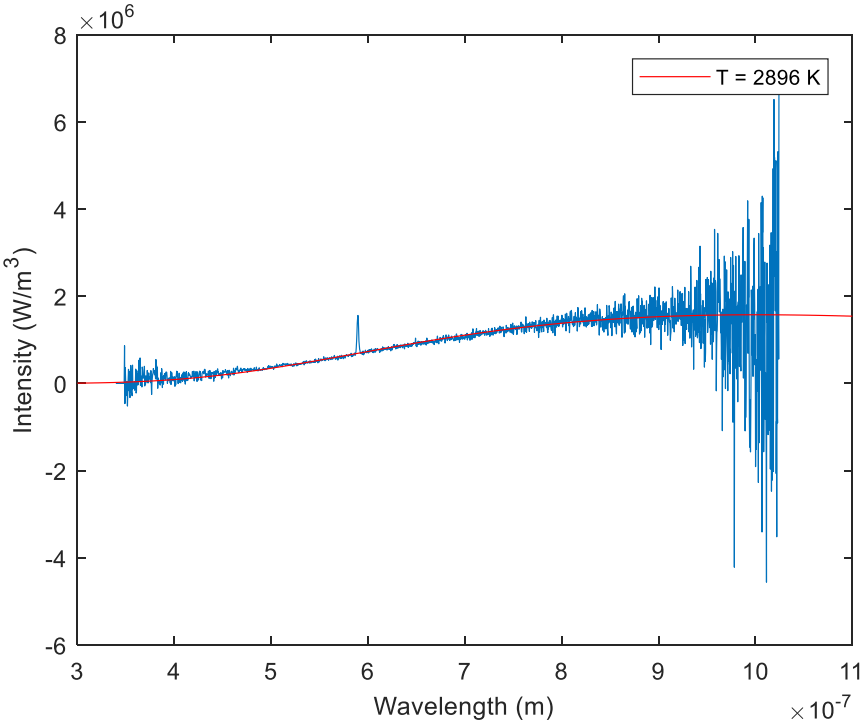


*Figure B.11: MgO/NC MPs in Kerosene/TOPO Flame Spectra with Planck's Law fit.*

*Table B.1: Flame temperatures fit to emission spectra recorded during droplet combustion.*

| Sample | Est. Flame T |
|---|---|
| Kerosene | 3313 K |
| Kerosene/TOPO | 3864 K* |
| CuO/NC MPs | 3081 K |
| $KIO_4$/NC MPs | 3303 K |
| MgO/NC MPs | 2897 K |

*Poor temperature fit quality

# Appendix C: Supplemental Material for Chapter 7

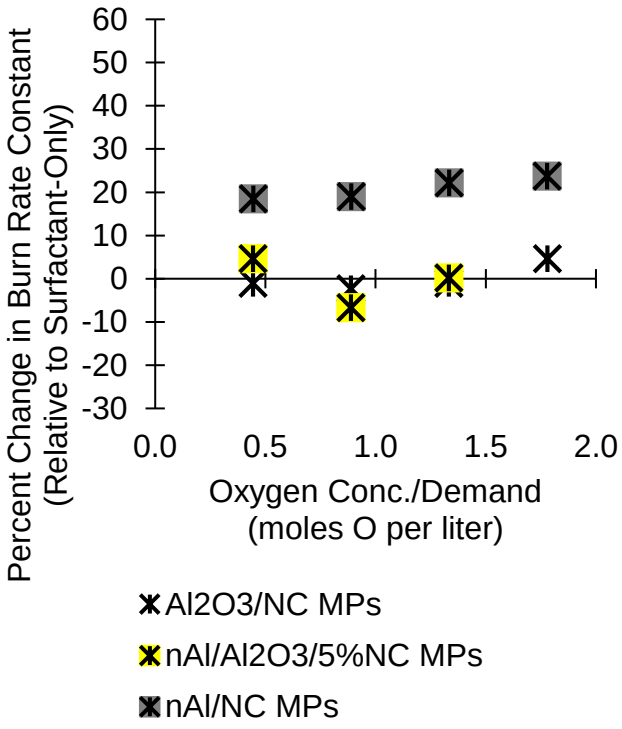


*Figure C.1: Burning rate constants of MP nanofuels containing $Al_2O_3$.*

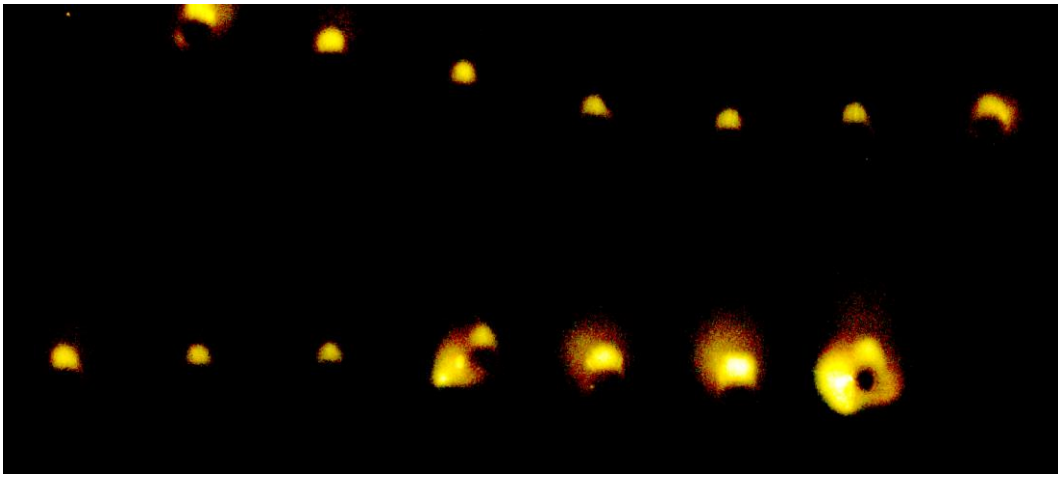

*Figure C.2: nAl/CuO/5%NC MPs in kerosene/TOPO (Droplet A). 40.1 to 48.6 ms burning time shown with 0.303 ms period. 10X brightness shown.*

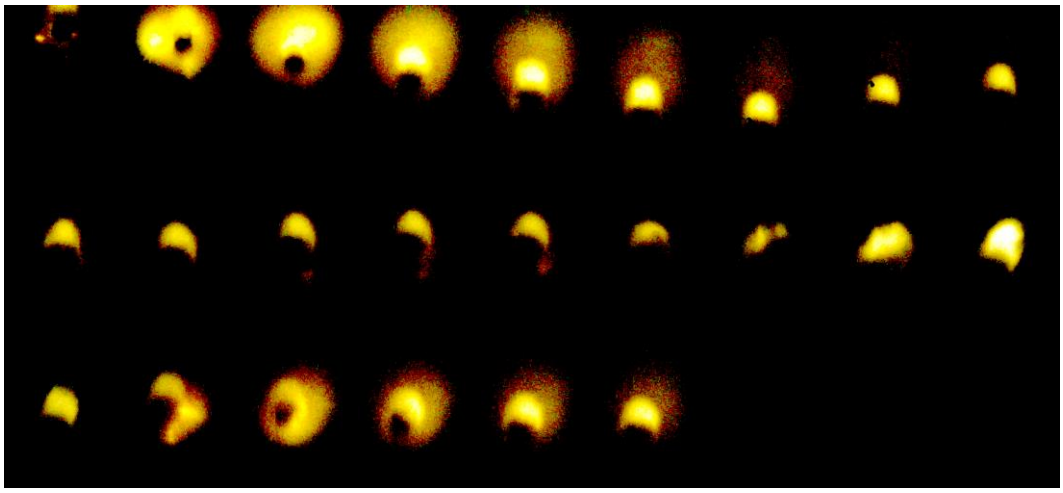

*Figure C.3: nAl/CuO/5%NC MPs in kerosene/TOPO (Droplet B). 57.6 to 64.6 ms burning time shown with 0.303 ms period. 10X brightness shown.*

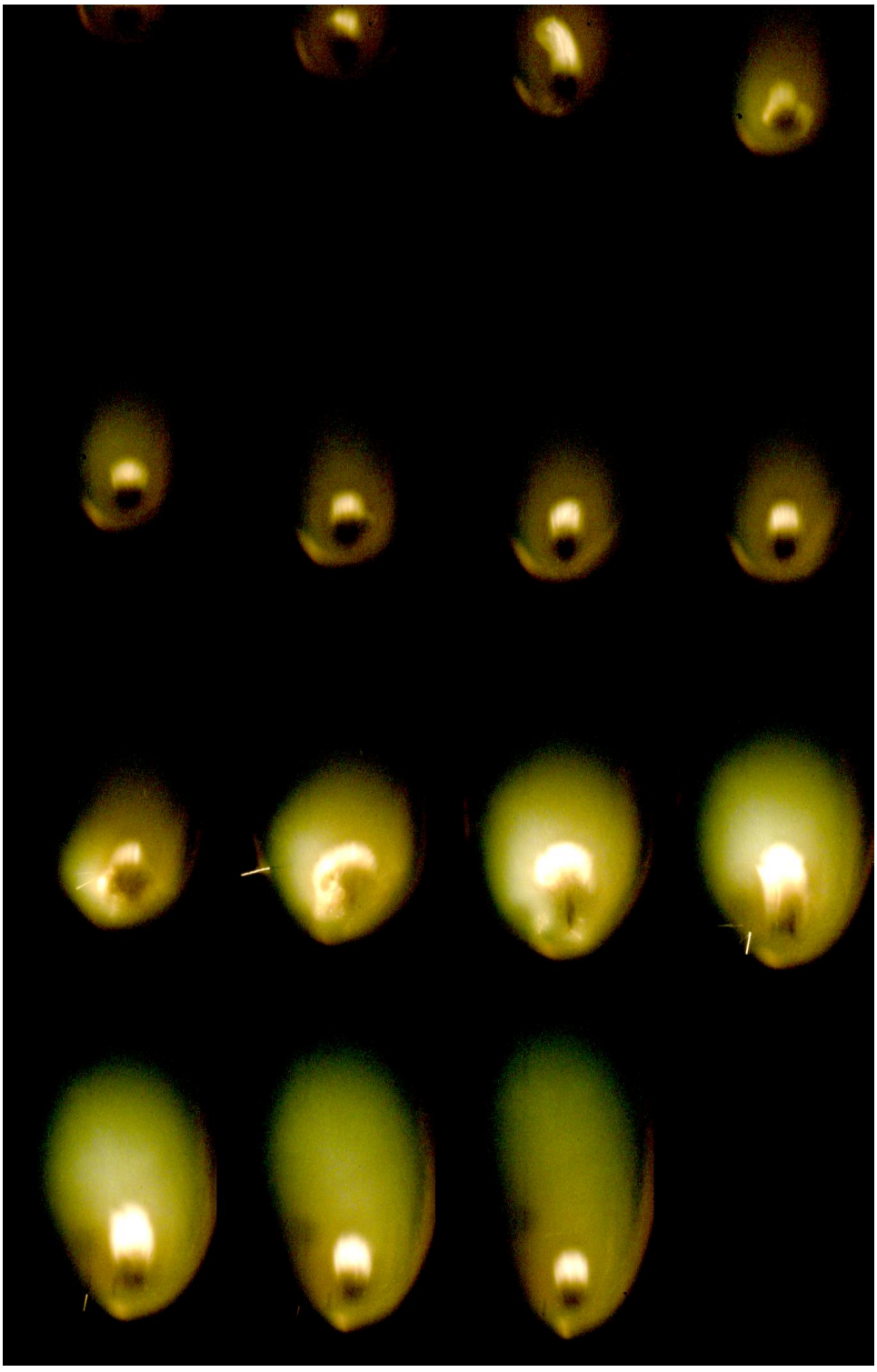

*Figure C.4: nAl/CuO/5%NC MPs in kerosene/TOPO (Droplet C). 61.1 to 69.9 ms burning time shown with 0.303 ms period. 3X brightness shown.*

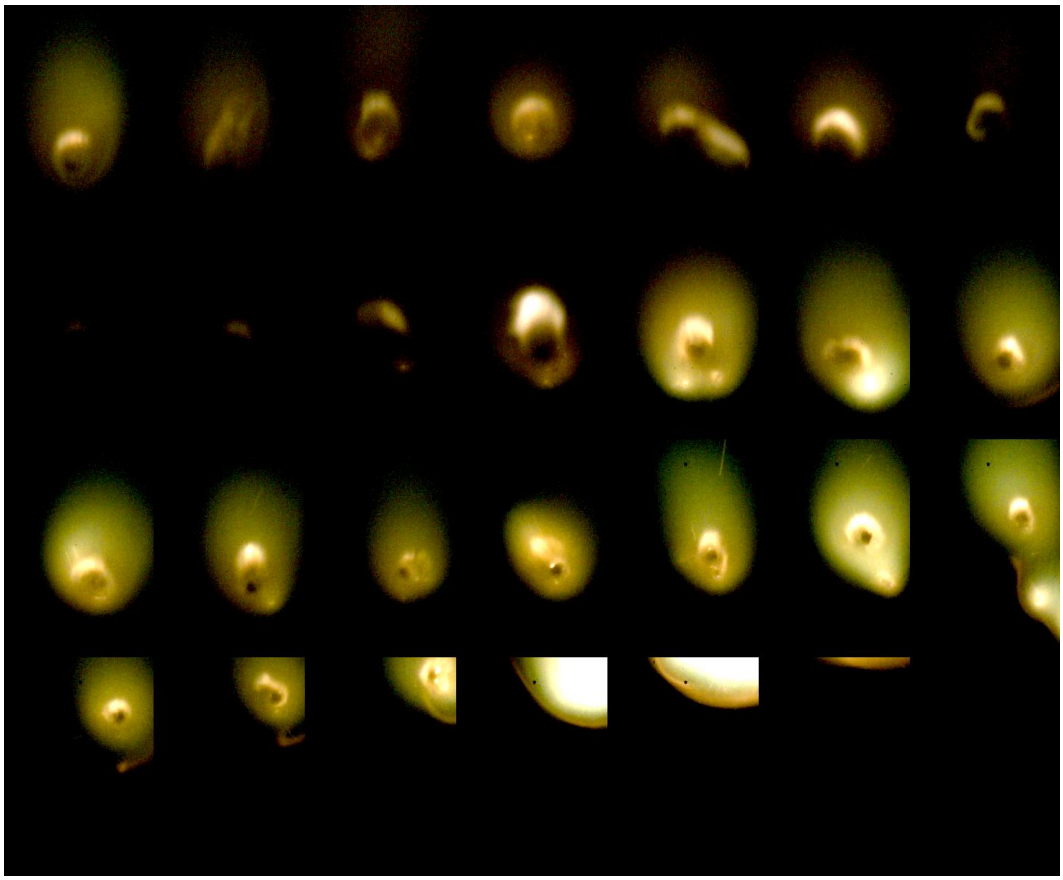

*Figure C.5: nAl/CuO/5%NC MPs in kerosene/TOPO (Droplet D). 114.0 to 137.6 ms burning time shown with 0.909 ms period. 3X brightness shown.*

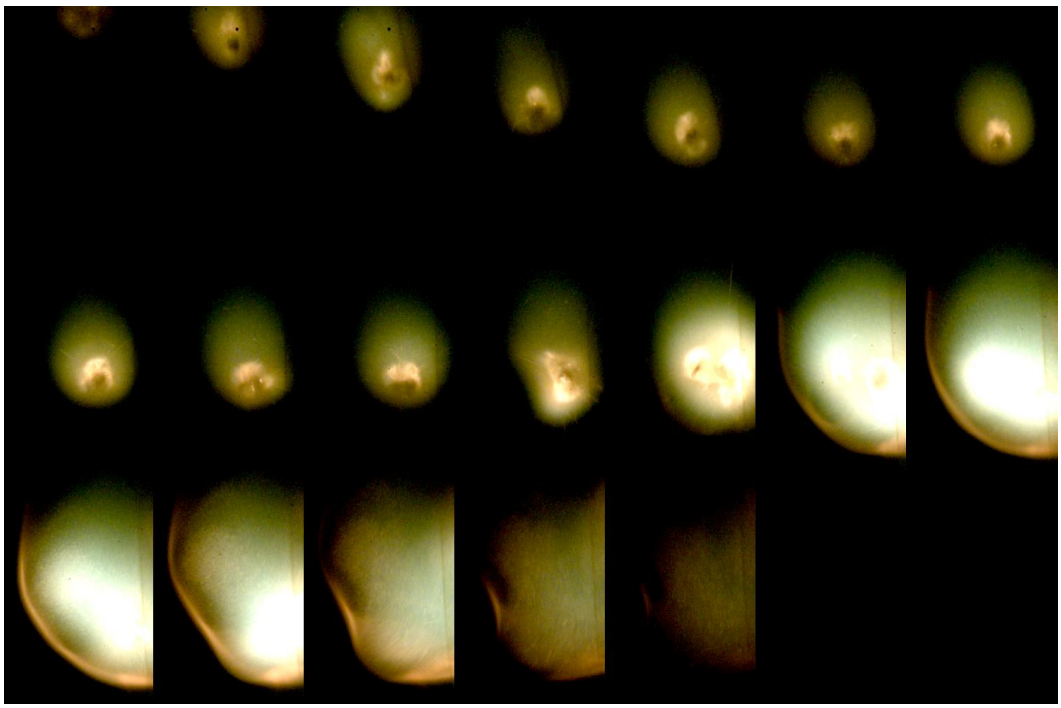

*Figure C.6: nAl/CuO/5%NC MPs in kerosene/TOPO (Droplet E). 132.5 to 143.4 ms burning time shown with 0.606 ms period. 2X brightness shown.*

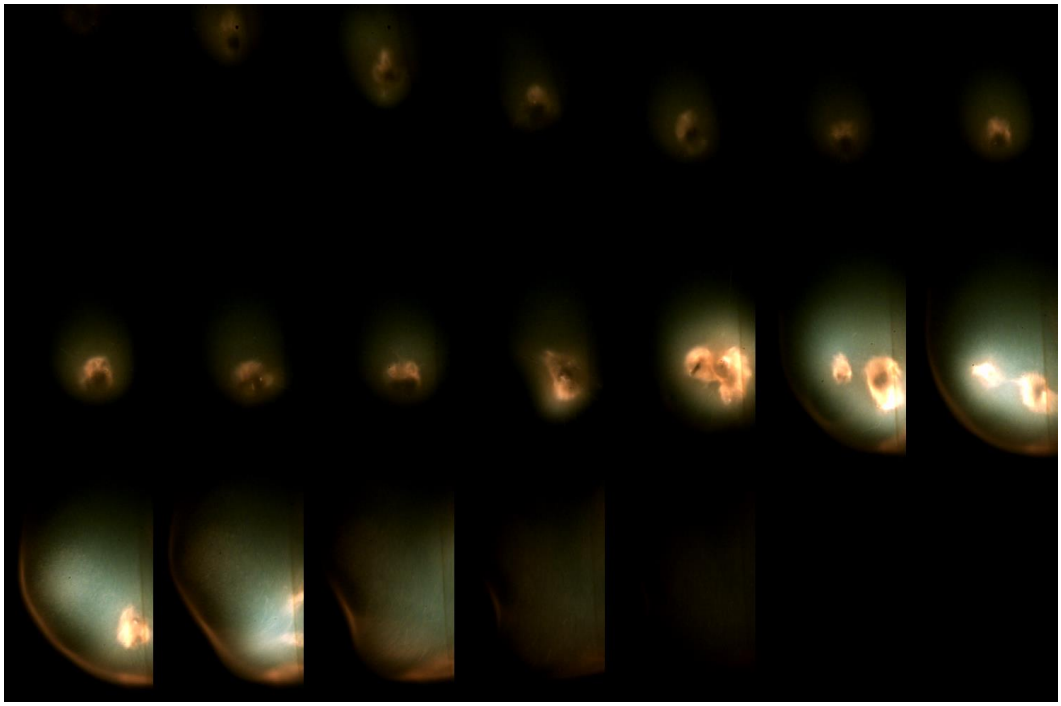

*Figure C.7: nAl/CuO/5%NC MPs in kerosene/TOPO (Droplet E). 132.5 to 143.4 ms burning time shown with 0.606 ms period. 1X brightness shown.*

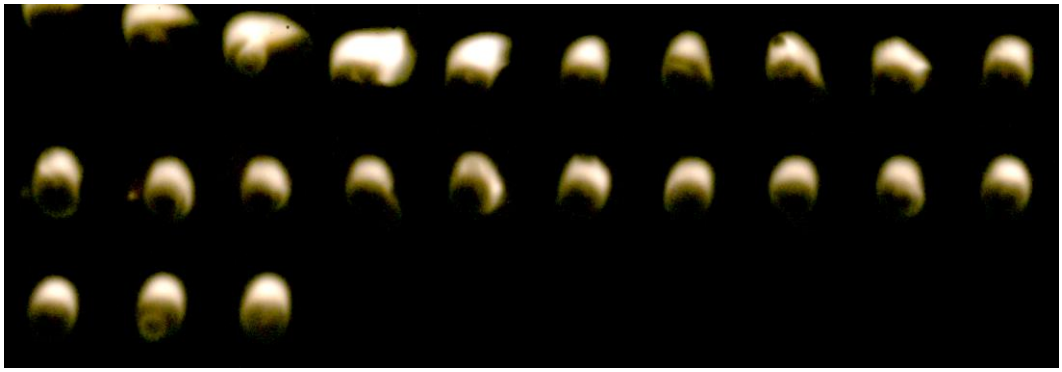

*Figure C.8: nAl/$KIO_4$/5%NC MPs in kerosene/TOPO (Droplet F). 61.0 to 67.7 ms burning time shown with 0.303 ms period. 3X brightness shown.*

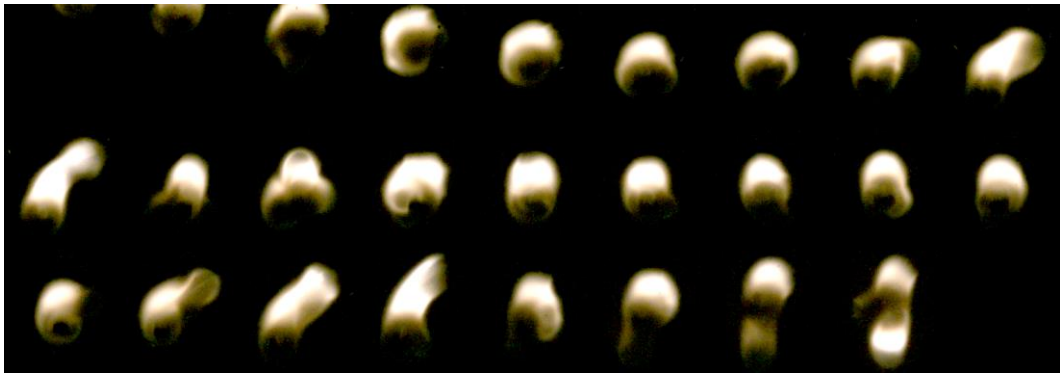

*Figure C.9: nAl/$KIO_4$/5%NC MPs in kerosene/TOPO (Droplet G). 86.7 to 94.3 ms burning time shown with 0.303 ms period. 3X brightness shown.*

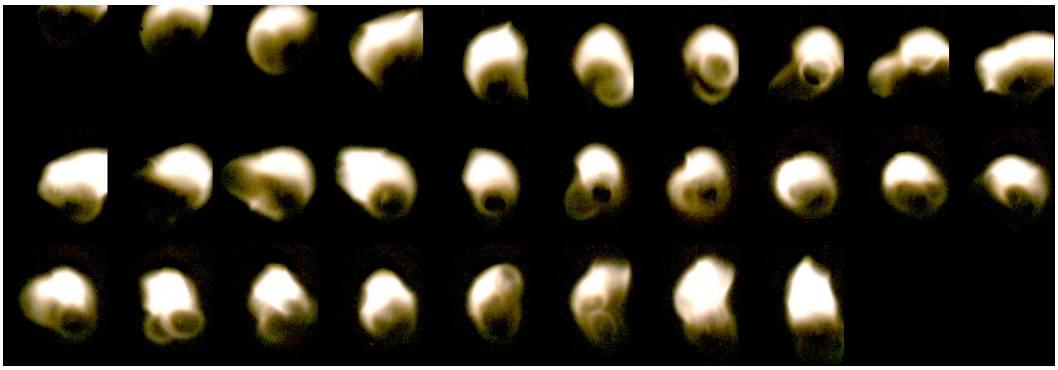

*Figure C.10: nAl/$KIO_4$/5%NC MPs in kerosene/TOPO (Droplet H). 104.4 to 112.6 ms burning time shown with 0.303 ms period. 3X brightness shown.*

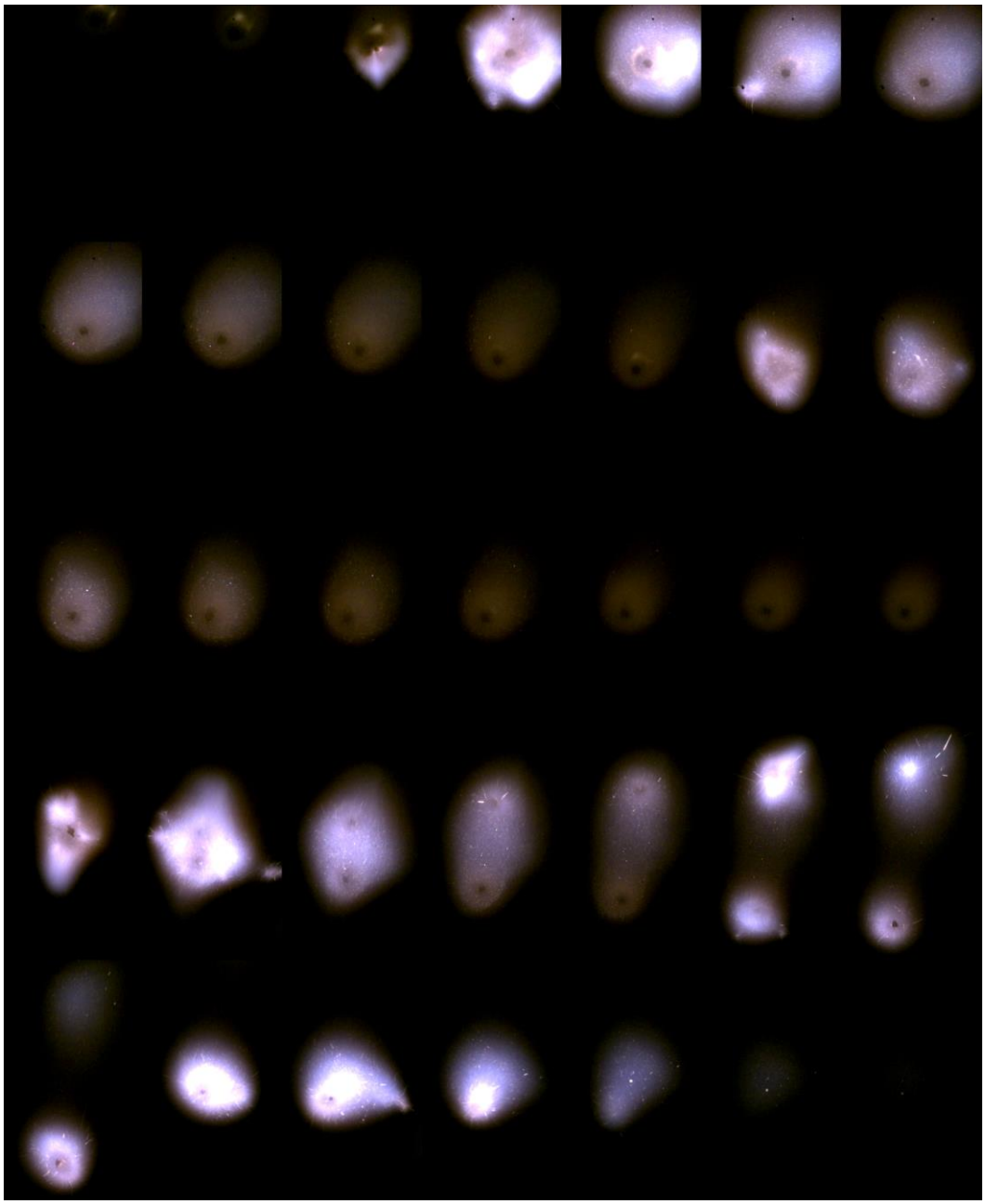

*Figure C.11: nAl/$KIO_4$/5%NC MPs in kerosene/TOPO (Droplet I). 118.6 to 139.2 ms burning time shown with 0.606 ms period. 1.5X brightness shown.*

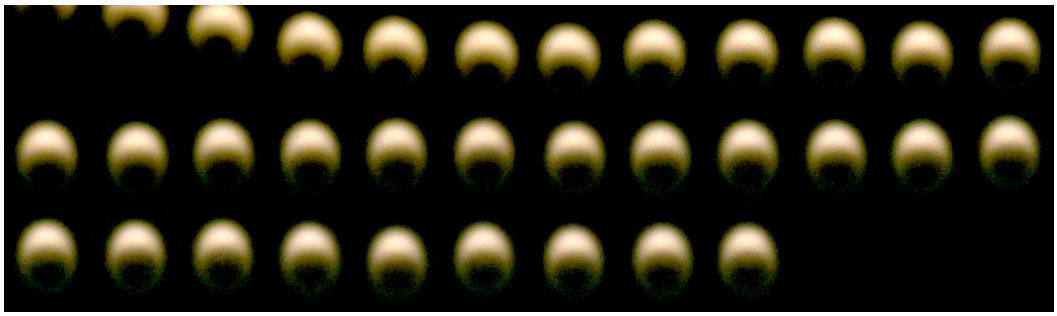

*Figure C.12: nAl/MgO/5%NC MPs in kerosene/TOPO (Droplet J). 3.4 to 13.1 ms burning time shown with 0.303 ms period. 3X brightness shown.*

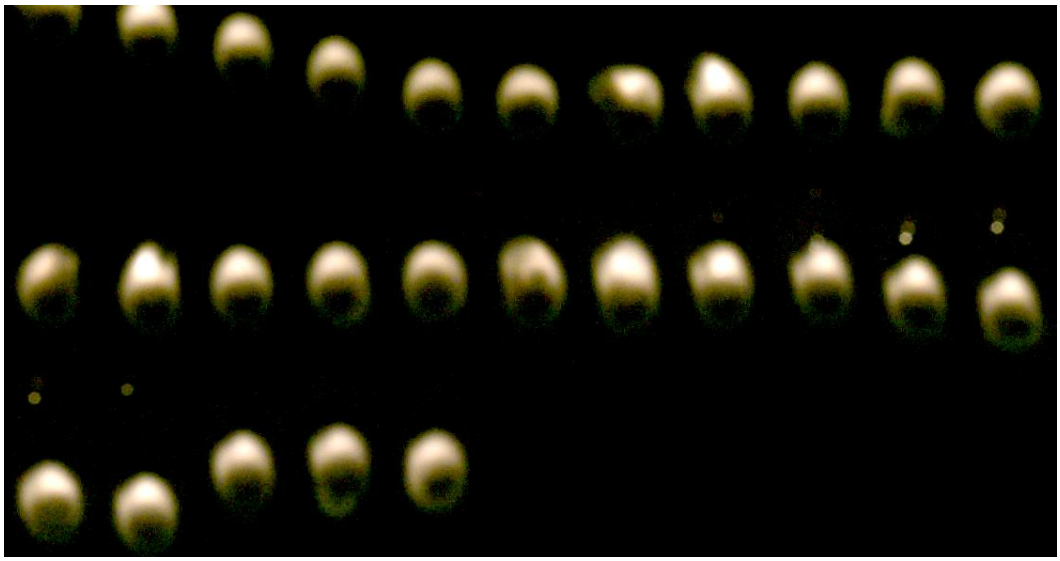

*Figure C.13: nAl/MgO/5%NC MPs in kerosene/TOPO (Droplet K). 46.1 to 53.9 ms burning time shown with 0.303 ms period. 3X brightness shown.*

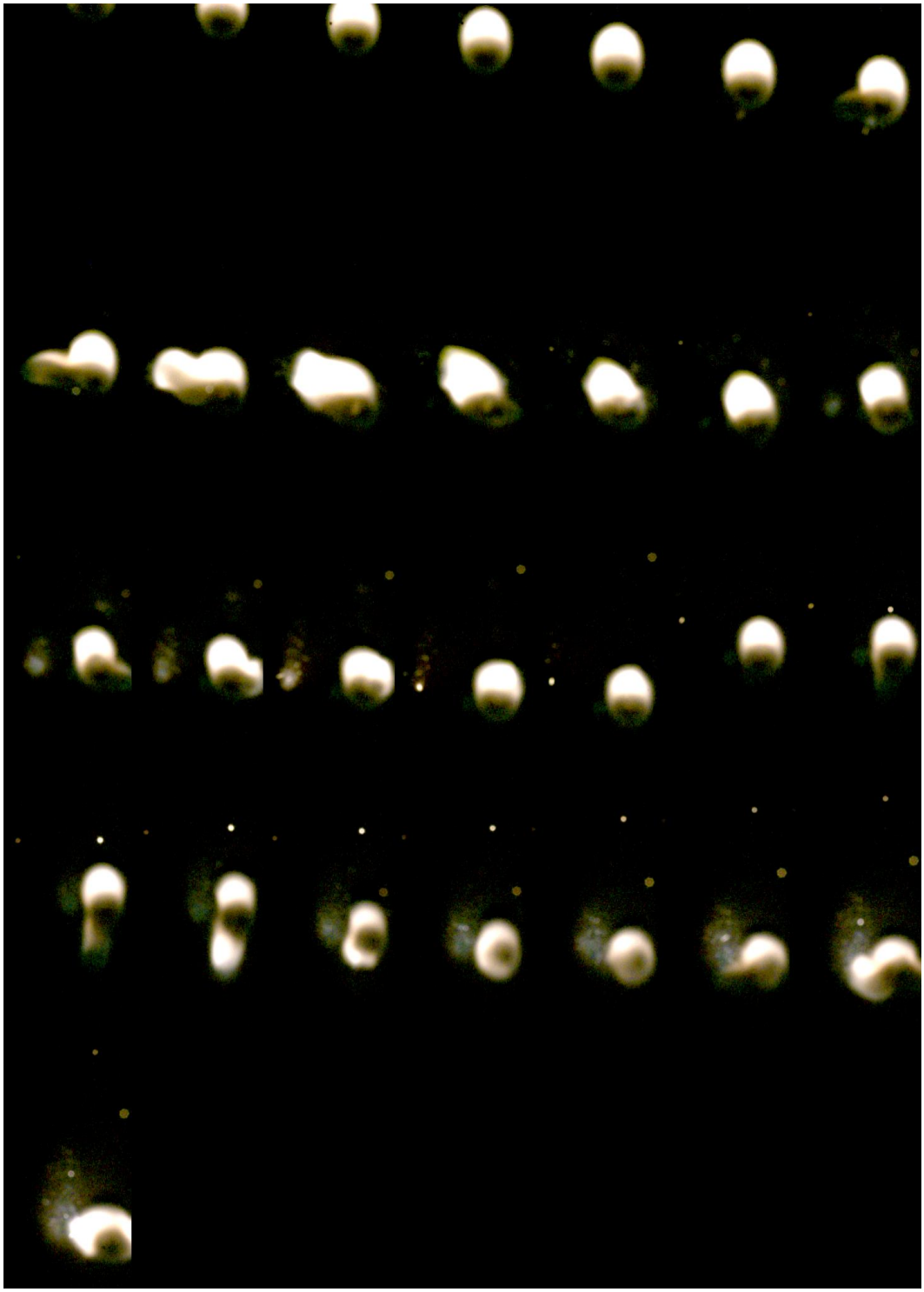

*Figure C.14: nAl/MgO/5%NC MPs in kerosene/TOPO (Droplet L). 98.8 to 107.3 ms burning time shown with 0.303 ms period. 3X brightness shown.*

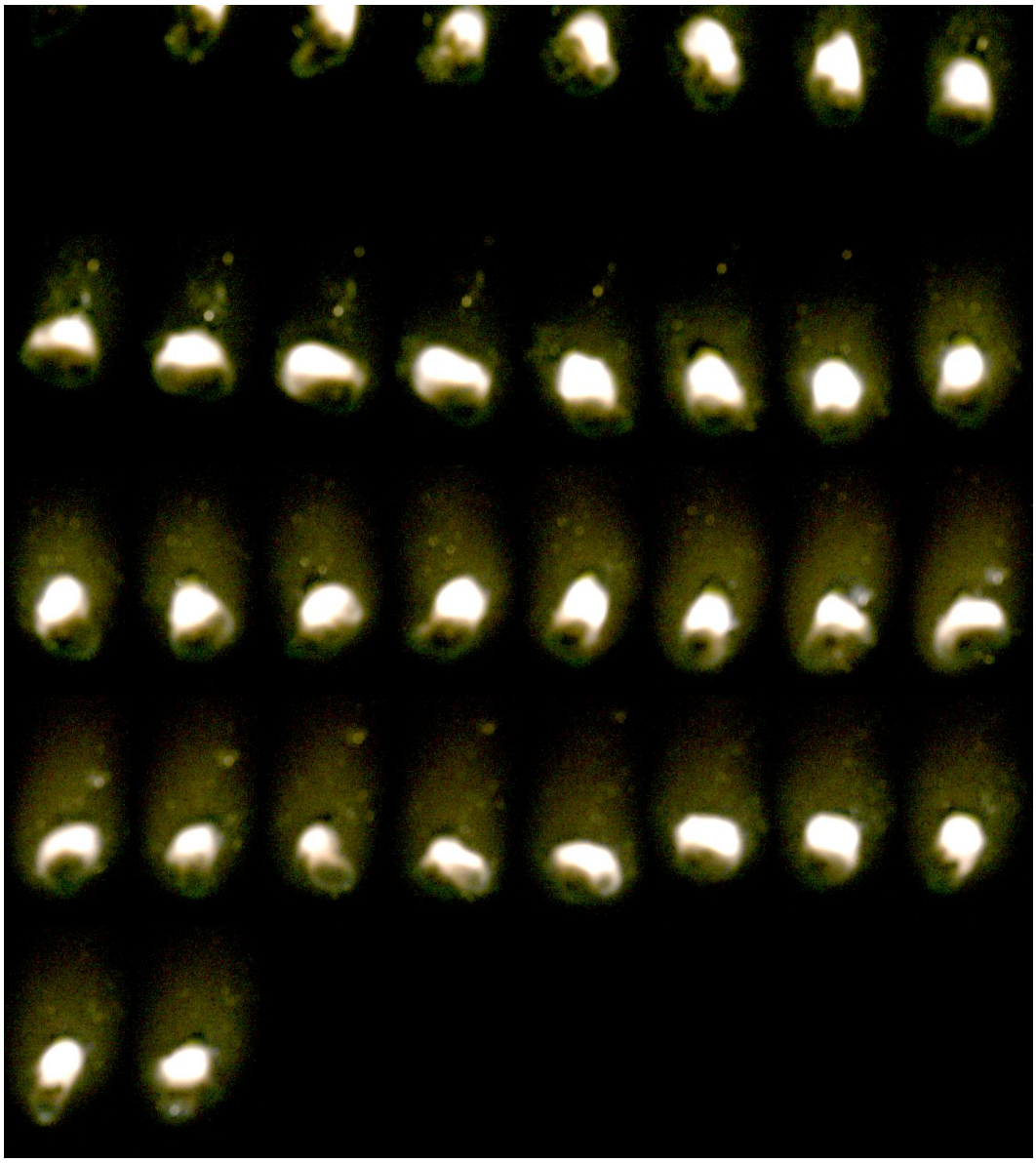

*Figure C.15: nAl/MgO/5%NC MPs in kerosene/TOPO (Droplet M). 115.5 to 125.5 ms burning time shown with 0.303 ms period. 3X brightness shown.*

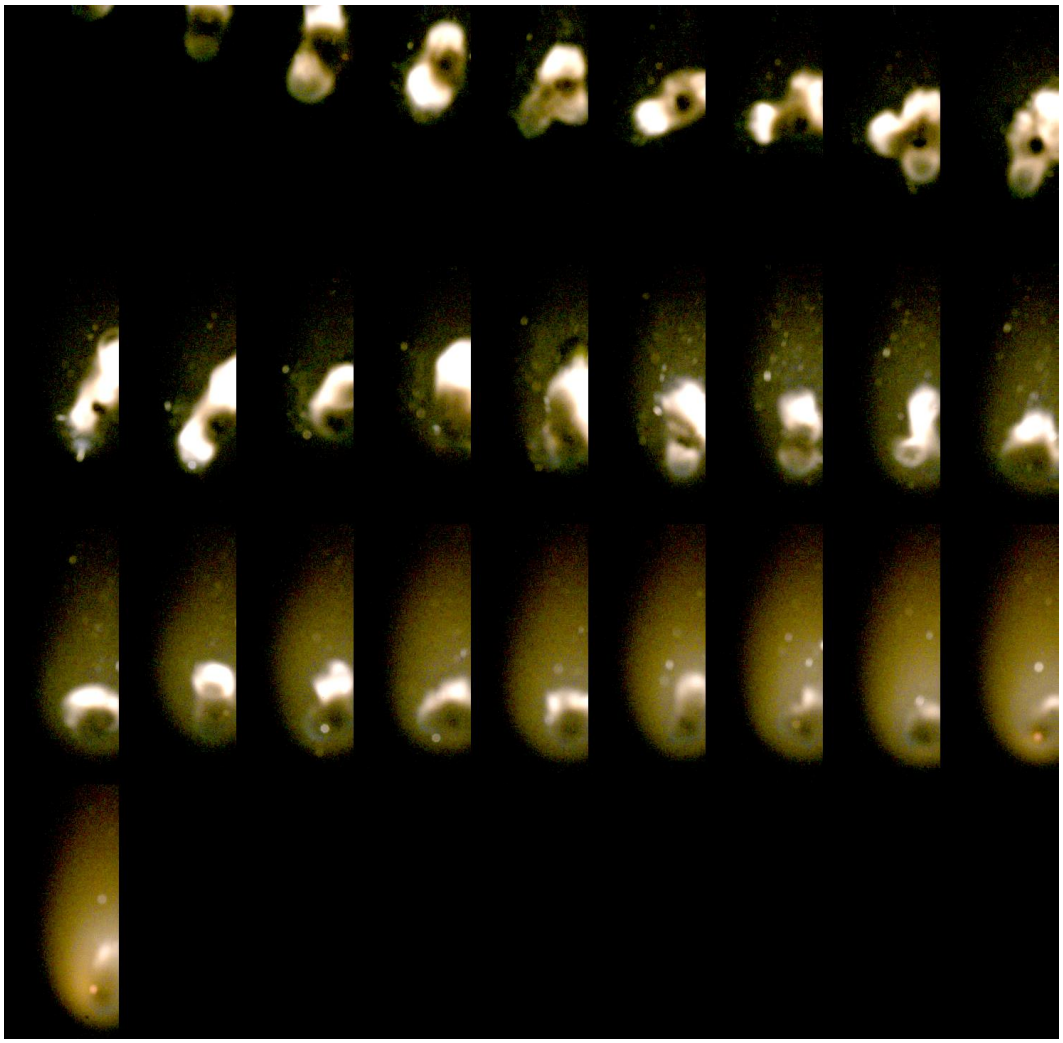

*Figure C.16: nAl/MgO/5%NC MPs in kerosene/TOPO (Droplet N). 121.9 to 138.2 ms burning time shown with 0.606 ms period. 3X brightness shown.*

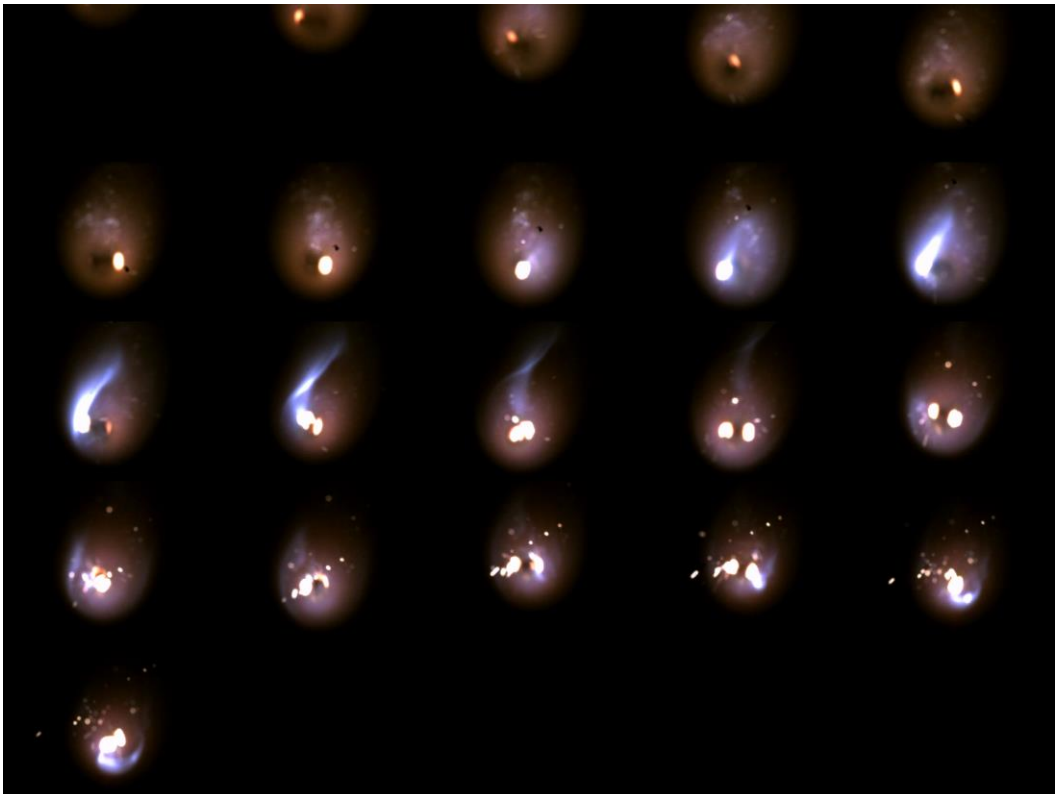

*Figure C.17: nAl/MgO/5%NC MPs in kerosene/TOPO (Droplet O). 138.9 to 151.0 ms burning time shown with 0.606 ms period. 1X brightness shown.*

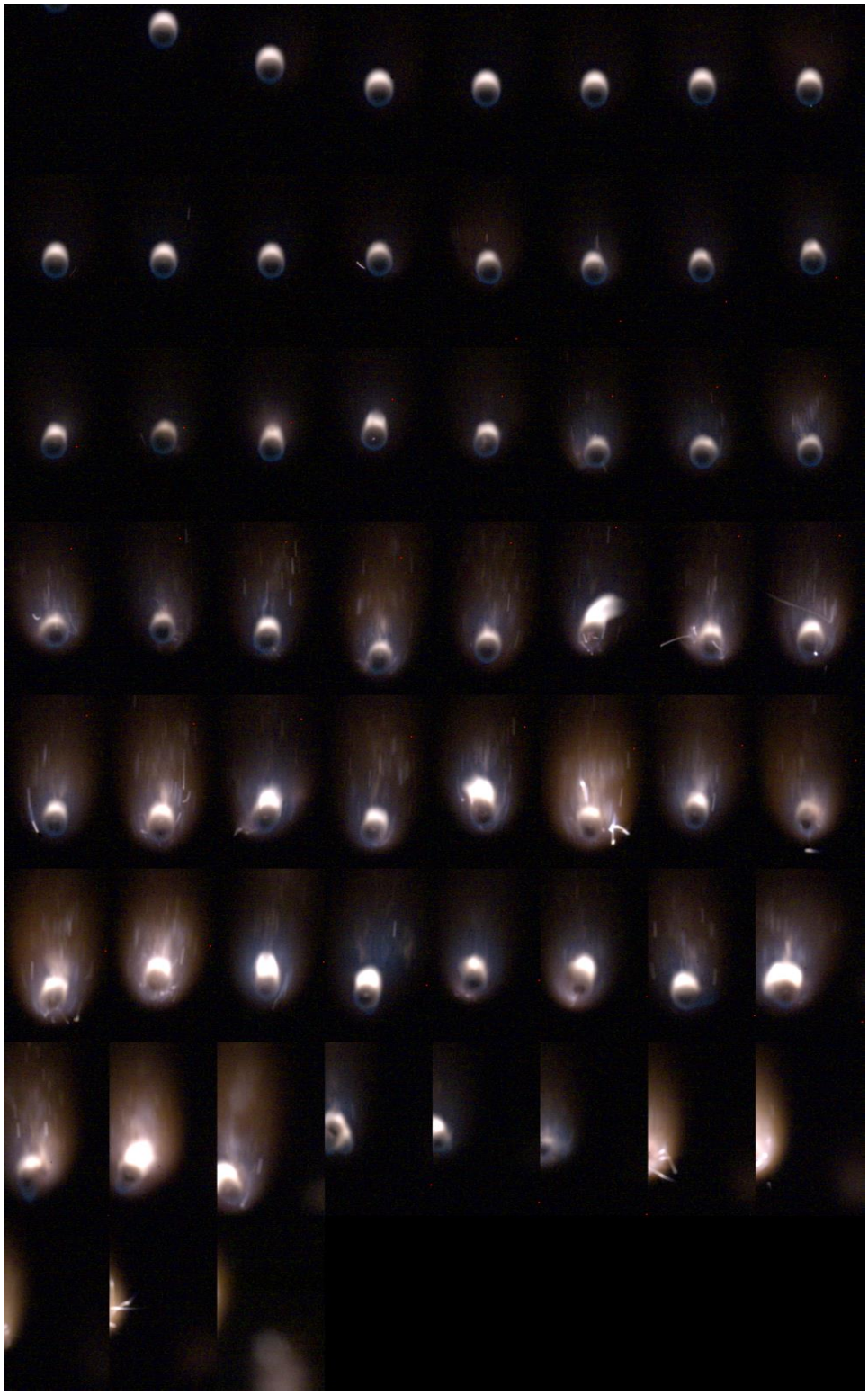

*Figure C.18: nAl/AP/5%NC MPs in kerosene/TOPO. 141.5 ms of burning time is shown with 2.424 ms period. 3X brightness shown.*

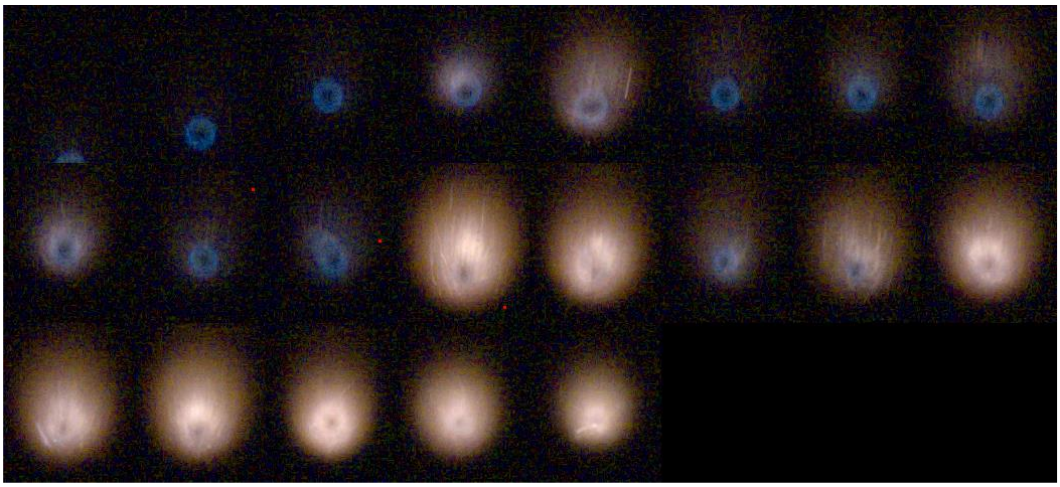

*Figure C.19: nAl/AP/5%NC MPs in kerosene/TOPO. 25.8 ms of burning time is shown with 1.212 ms period. 5X brightness shown.*

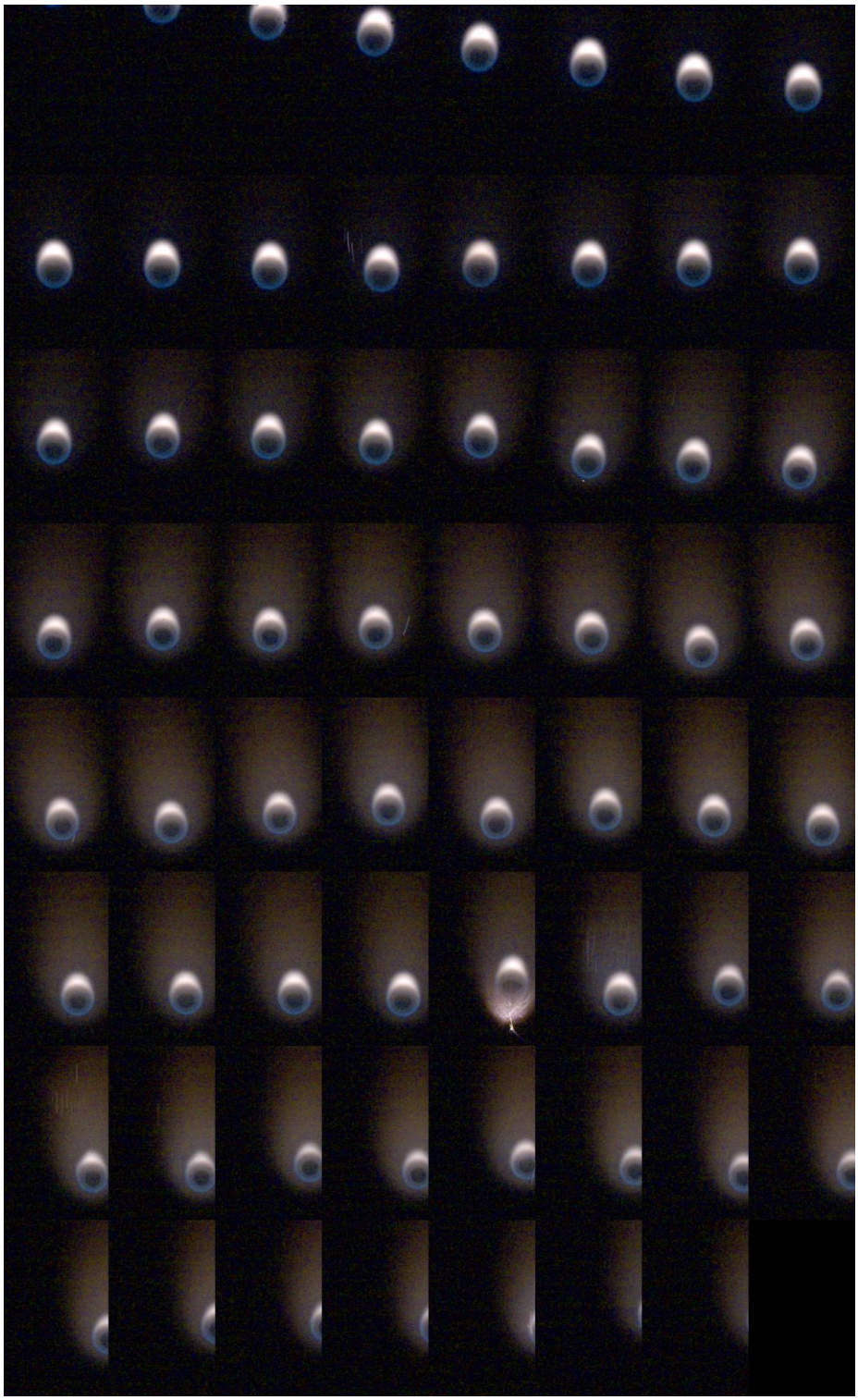

*Figure C.20: nAl/$Al_2O_3$/5%NC MPs in kerosene/TOPO. 107.3 ms of burning time is shown with 1.515 ms period. 4X brightness shown.*

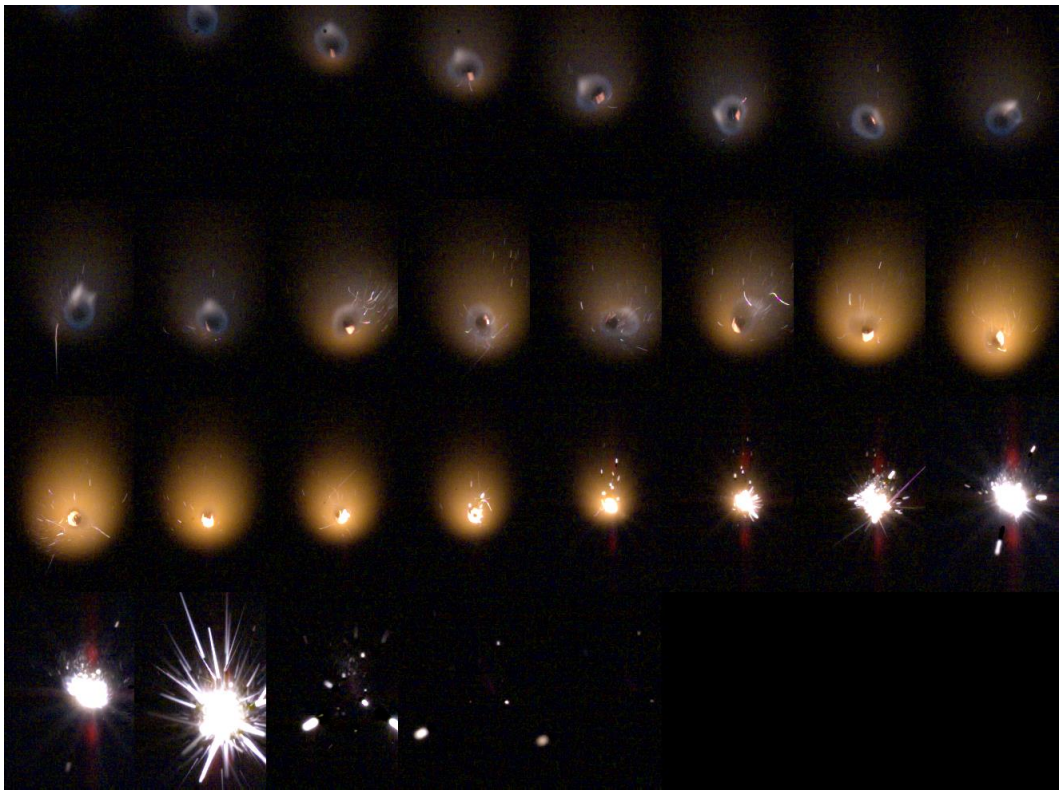

*Figure C.21: nAl/$Al_2O_3$/5%NC MPs in kerosene/TOPO. 30.6 ms of burning time is shown with 0.909 ms period. 3X brightness shown.*

*Table C.1: Results of NASA CEA calculation for the equilibrium of 8:3 Al(cr):AP(l) molar ratio at 298 K initial temperature with constant enthalpy and pressure (1 atm).*

| REACTANT | | WT FRACTION | ENERGY (KJ/KG-MOL) | TEMP (K) |
|---|---|---|---|---|
| FUEL | AL(cr) | 1 | 0 | 298.15 |
| OXIDANT | NH4CLO4(I) | 1 | -295767 | 298.15 |

| O/F= 1.63300 %FUEL= 37.979491 R,EQ.RATIO= 1.333284<br>PHI,EQ.RATIO= 1.599911 |
|---|

| THERMODYNAMIC PROPERTIES | |
|---|---|
| | |
| P, BAR | 1.0132 |
| T, K | 3541.8 |
| RHO, KG/CU M | 1.3935E-1 |
| H, KJ/KG | -1561.3 |
| U, KJ/KG | -2288.45 |
| G, KJ/KG | -31177.7 |

| | |
|---|---|
| S, KJ/(KG)(K) | 8.362 |
| | |
| M, (1/n) | 40.498 |
| MW, MOL WT | 33.912 |
| (dLV/dLP)t | -1.2383 |
| (dLV/dLT)p | 5.5888 |
| Cp, KJ/(KG)(K) | 20.2949 |
| GAMMAs | 1.0842 |
| SON VEL,M/SEC | 887.9 |

| MOLE FRACTIONS | |
|---|---|
| | |
| *H | 2.12E-01 |
| AL2O3(L) | 1.63E-01 |
| *H2 | 1.29E-01 |
| *N2 | 8.72E-02 |
| *CL | 6.58E-02 |
| HCL | 6.10E-02 |
| H2O | 5.13E-02 |
| ALCL | 4.72E-02 |
| *OH | 4.24E-02 |
| ALOH | 3.79E-02 |
| *O | 3.76E-02 |
| *ALO | 2.24E-02 |
| *AL | 1.51E-02 |
| AL2O | 9.00E-03 |
| *O2 | 5.73E-03 |
| *NO | 4.57E-03 |
| ALOCL | 3.55E-03 |
| AL2O2 | 2.95E-03 |
| ALOHCL | 5.15E-04 |
| ALH | 3.62E-04 |
| ALO2 | 3.53E-04 |
| ALCL2 | 3.52E-04 |
| AL(OH)2 | 1.52E-04 |
| HALO2 | 1.26E-04 |
| *N | 7.23E-05 |
| ALOHCL2 | 4.54E-05 |
| CLO | 4.22E-05 |
| HALO | 4.13E-05 |
| ALHCL | 2.18E-05 |

| | |
|---|---|
| AL(OH)2CL | 1.53E-05 |
| AL2O3 | 1.41E-05 |
| CL2 | 1.19E-05 |
| | |

* THERMODYNAMIC PROPERTIES FITTED TO 20000.K

NOTE. WEIGHT FRACTION OF FUEL IN TOTAL FUELS AND OF OXIDANT IN TOTAL OXIDANTS

# Appendix D: Detailed Operation, Maintenance, and Analysis of Free Droplet Combustion Apparatus

## *D.1 Standard Operating Procedures*

### D.1.1 Apparatus setup and maintenance: droplet combustion system

This procedure covers assembly of the droplet generation system including replacement of the sample delivery needle and droplet shedding nozzle and their alignment. For a typical procedure for daily operation of a set up apparatus, refer to Section D.1.6. The droplet generation system is assembled at the top of the tower and is shown below detached and steadied on a ring stand. Removal of the system in this manner for needle and/or nozzle replacement is useful the first time these procedures are undertaken, but final alignment must be performed attached to the tower.

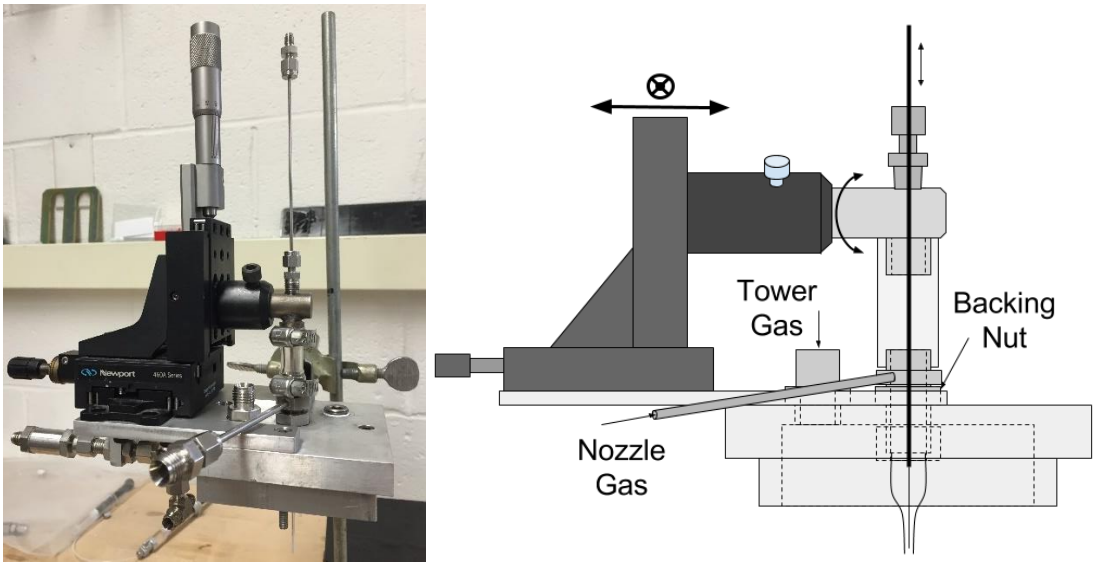


*Figure D.1: Droplet generation system on a ring stand and schematic*

The system consists of a static glass nozzle attached to the housing using a flange-mounted Swagelok union and a nested needle coaxial with the nozzle which is mounted using a bored-through Swagelok to NPT adapter on an X-Y stage to facilitate alignment (the Z function of the stage is not useful). The four primary needle position adjustments are X-Y stage post length (one axis of needle rotation relative to vertical and nominal Y zero position), axial position of the needle in its mounting compression fitting (Z position of the needle), and the X-Y movement of the translation stage (2-axis horizontal position of the needle). In most cases, the post on the X-Y stage will not need to be adjusted.

Typical procedure for needle/nozzle replacement begins with removal of an old needle. Loosen first the compression fitting on the needle, then the NPT end of this needle from the housing (as shown below) and remove the old needle.

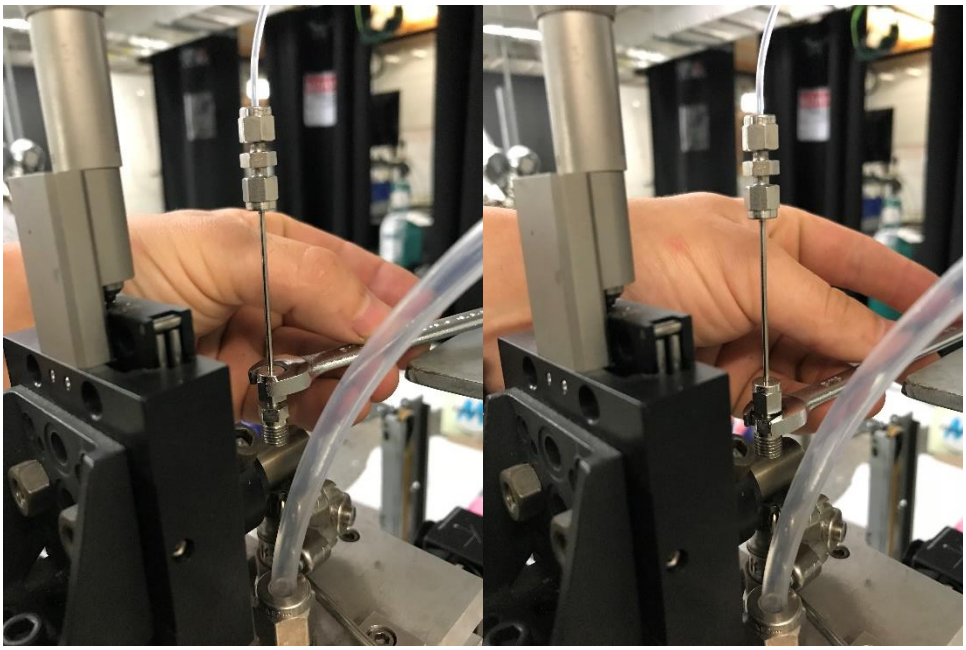

*Figure D.2: Needle mounting compression fitting removal*

To replace the nozzle, the droplet delivery assembly must be detached. If work is to be conducted with the droplet generation system removed as shown in the ring stand above, remove all tubing fittings from the assemble. Otherwise, fully loosen the 4 hex bolts attaching the top plate to the tower while holding the assembly in place (usually only the rear 3 are tightened for convenience).


*Figure D.3: Top plate hex bolts*

To work on the assembly attached to the tower, tuck the tower gas delivery line under the syringe pump platform as the assembly it rotated back and rested on the top of the tower, as shown below. The assembly should then remain in place. Loosen the ferrule nut with a 9/16” open-end wrench to remove the nozzle, compression ferrules, and ferrule nut.

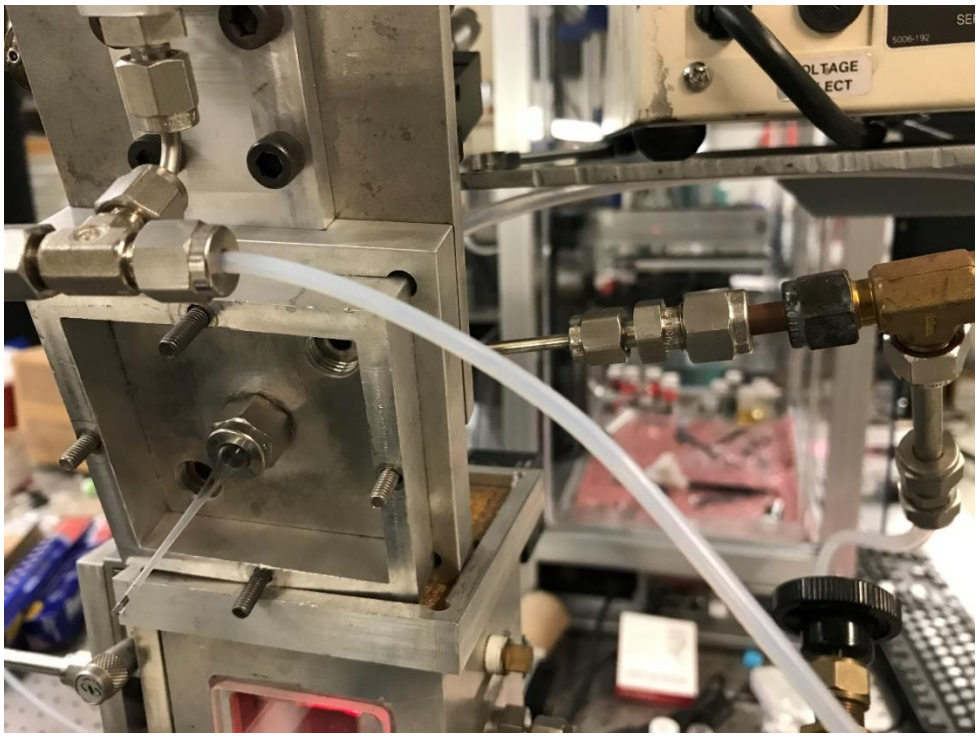

*Figure D.4: Droplet delivery system detached and rotated back for maintenance*

Replace the nozzle and maintain an extension of ~4.2 cm from the ferrule nut (this dimension can be adjusted to move the nozzle relative to the igniters for samples of varying volatility and thusly nozzle melt-down risk).

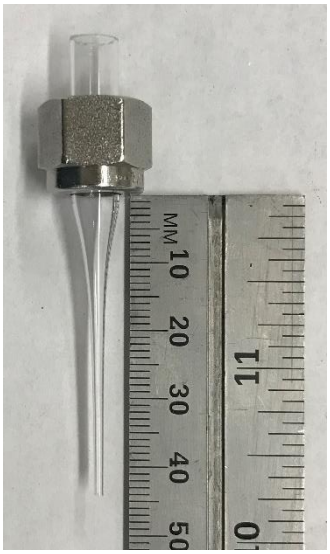


*Figure D.5: Replacement nozzle with ferrules and ferrule nuts*

The nozzle is mounted using a flange-mount style Swagelok union using compression ferrules to hold the nozzle and the ferrule nut to hold the union to the top plate against a backing nut (NOTE: the ferrules are plastic for removal as metal will not release compression and have been drilled out slightly to accept nozzles). Therefore, the torque on the ferrule nut creates both the compression of the flange mount on the top plate and the compression of the ferrules on the on the nozzle and balance must be achieved between these two for varying OD sizes of the pipet nozzles. The backing nut is visible in the view of the droplet generation system in the ring stand above, just underneath the nozzle delivery gas tube against the top plate. Larger nozzle diameters will require tightening of the backing nut and vice versa. An open-end wrench should be used on the nozzle ferrule nut and the torque required is only as much to prevent axial movement of the nozzle when pushed/pulled. If the ferrule nut cannot be tightened enough easily to hold the nozzle in this manner, then the backing nut is too tight. If the top end of the nozzle assembly is loose on the top plate when the ferrule nut is tightened, then the backing nut is too loose. As the ferrule nut is tightened, the nozzle gas delivery tube should be held up to avoid blocking the top plate hex bolt.

Carefully reattach the droplet delivery system to the tower by reversing the removal steps. Prepare a new needle as shown below with the mounting union at the bottom and only finger-tightened and carefully install this into the X-Y stage post, tightening only the lower NPT end of the adapter firmly with a wrench.

*Figure D.6: Replacement needle in its mounting adapter with NPT end to the right*

Loosen the upper Swagelok compression fitting on the needle mounting adapter and slight the needle down until it is within ~1-2 mm of the nozzle end as shown below. Compression/torque of the needle mounting will affect stability of its alignment so when the Z position of the needle is set, tighten the compression fitting firmly with a wrench so the alignment cannot be influenced by touching the top of the needle body (e.g. when attaching and removing the sample delivery line on the needle).

*Figure D.7: Needle nested in the nozzle showing misalignment, alignment, and successful droplet generation*

In most cases at this point the needle will not be aligned in the nozzle. If sample were pumped with the needle end in contact with the nozzle walls, sample would wet the nozzle, fine droplet generation would fail, and sample on the nozzle could burn melting down the nozzle. Alignment is difficult and patience is required. Tightening of the X adjustment on the left side of the X-Y stage will move the needle body to the right, while Y adjustment on the front will move the needle body forward towards the

operator. A needle position is desired in which these two adjustments result in the same direction of movement of the needle end, without the end contacting the nozzle walls. If misalignment is severe and the needle contacts a side of the nozzle above the end, this usually deflects the needle end back in the other direction. As such, X-Y adjustments will result in movement of the needle end in a direction opposite that of the adjustment indicating misalignment. In some cases, if better alignment cannot be achieved, this situation (with the needle end deflected off the nozzle wall back to center) is permissible if the needle end is centered in the nozzle, although this situation is not ideal.

To achieve needle/nozzle alignment as shown above, manually move the X-Y stage while using a flashlight to view the needle end in the nozzle. Seek a position in which the movement of the needle end follows the movement of the X-Y stage (i.e. no deflection of the needle off a nozzle wall). If this can be found by hand, use the X-Y stage adjustment screws to reach this position. If such a position cannot be found by hand and therefore is thought to not be within range of the X-Y stage, then higher level troubleshooting adjustments must be made (see Section D.1.8). The needle should be centered in the nozzle as well as possible.

Successful droplet generation without nozzle wetting should be insured by testing the system. With proper eye protection, the expanded HeNe laser backlight can be used to see generated droplets. With nozzle gas flowing (usually nitrogen), the system can be tested by flowing either carrier fuel from a syringe with the syringe pump, or using another volatile solvent (e.g. acetone) introduced with the plastic, hand

operated utility syringe. If a solvent is used instead of the carrier fuel, the nitrogen utility line should be used to blow out the needle before continuing.

Needle replacement will be necessary frequently as needles clog or samples are changed which risk cross-contamination. Nozzle replacement will be required less often, usually when nozzle melt-down has occurred or the nozzle is overly dirty.

D.1.2 Apparatus setup and maintenance: igniter tube replacement

Methane delivery tubes for ignition pilot flames slowly deteriorate over multiple days of experiments (or become broken during tower cleaning and maintenance) and require periodic replacement. Deterioration and occlusion typically occurs only at the tube ends and therefore can simply be broken and sanded flat to renew the tubes. Even in this case, the tubes need to be removed and reseated at the correct length. The procedure to do so is listed below:

1. Remove the PTFE tubing lines for methane delivery to the steel igniter manifold tube assemblies with two open end wrenches, as shown in the photographs below. Be careful not to translate any torque to the tower ends of these manifold assemblies where compression fittings hold the igniter tubes (single-hole 6 in ceramic thermocouple tubes; 0.02 in ID and 1/32 in OD; Omega ORA-020132-6) which are brittle and can break easily.

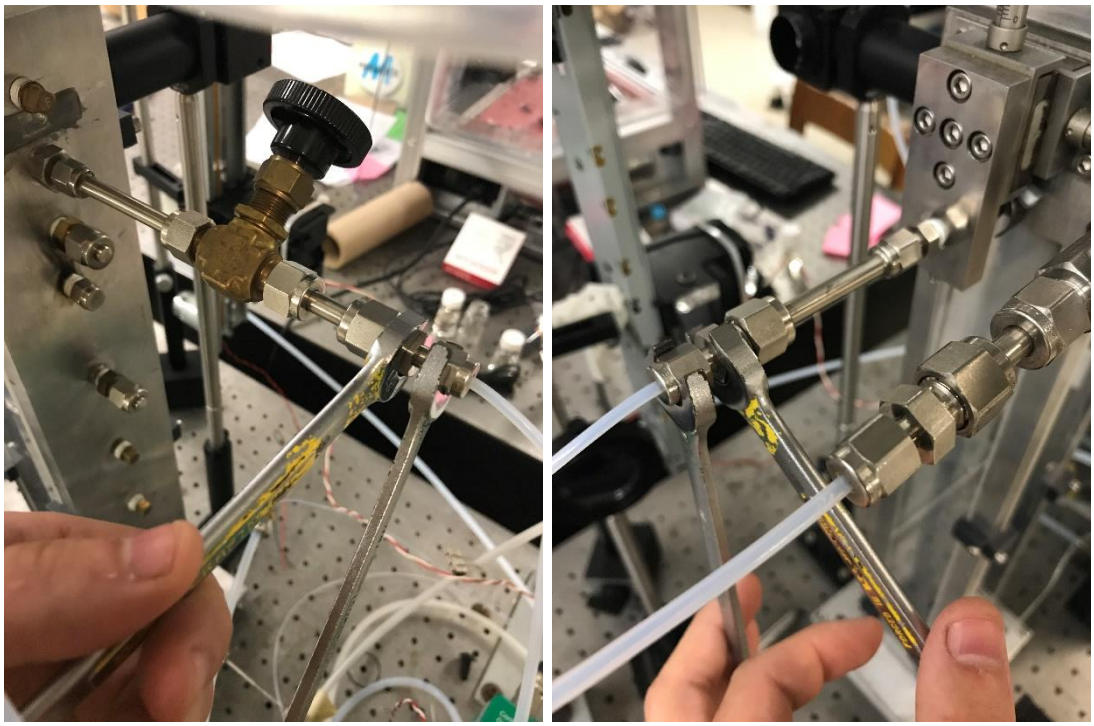

*Figure D.8: Removal of methane delivery tubes for igniter replacement*

2. Carefully unscrew the igniter manifolds (shown below) from the tower keeping them straight as they are removed so as to avoid breaking the ceramic igniter tubes.

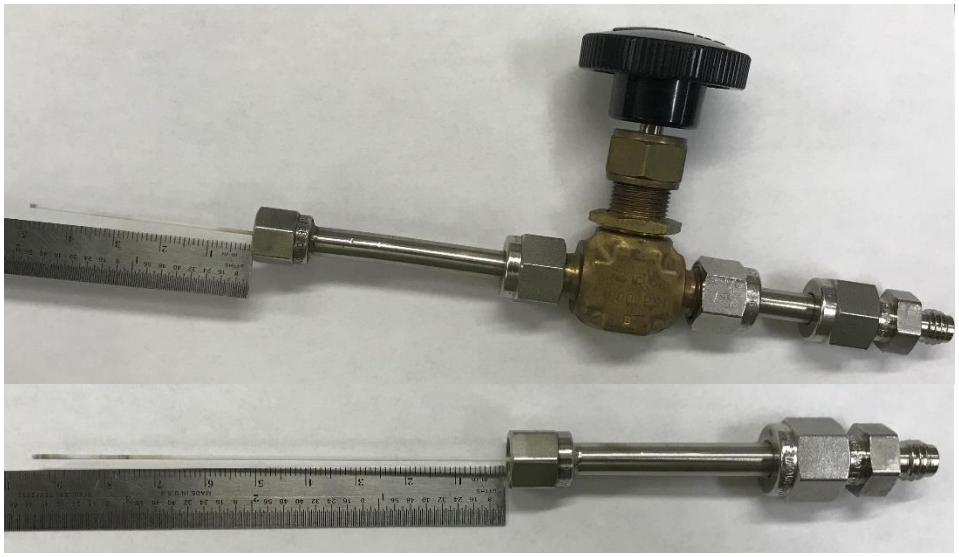

*Figure D.9: Igniter manifolds with compresison fittings*

3. Before removing the igniter tubes from the assemblies, measure their extension and note the distance as shown above. They should be 48.5 mm (right side) and 93.5 mm (left side). Igniter tubes can be pulled and removed from the PTFE ferrules to replace or break and refinish the ends.
4. Reinstall the igniter tubes by reversing the process. Specific care should be taken as they are reinstalled to avoid breakage. The compression fittings need only be finger tight to avoid methane leakage (which should be checked with soap solution) without overtightening and breaking the tubes.
5. Fine tuning of the igniter separation and positions under the nozzle can be accomplished either by manifold removal, adjustment, and reinstallation, or by removing the droplet generation assembly and loosening the compression fittings to finely adjust the needle positions.

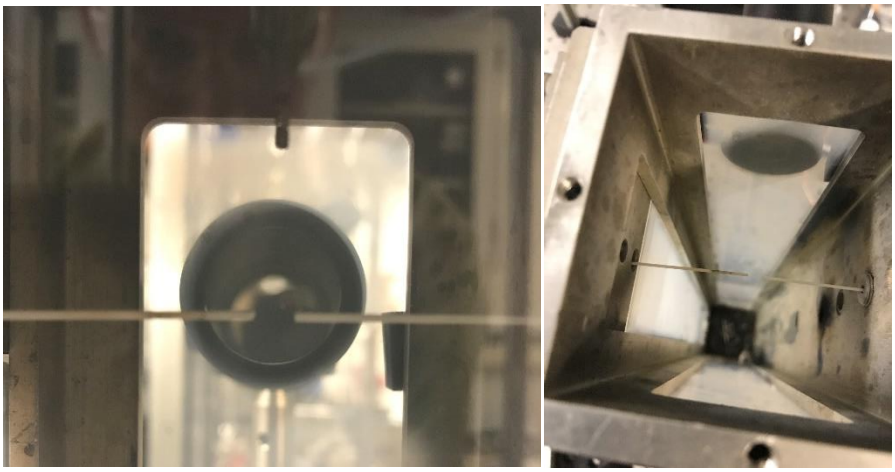

*Figure D.10: Fine-tuning igniter positions*

6. Reinstall the methane delivery tubes and leak check all connections.

D.1.3 Apparatus setup and maintenance: compressed gases

Three compressed gases are required (and a fourth recommended) for operation of the droplet experiment: methane (regulated to 20 psi), oxygen (regulated to 60 psi), nitrogen (regulated to 60 psi), and optionally air (building-supplied 45 psi) for purging the tower before and after experiments. Their connection to the system and the flow controls system design are shown in the schematic below.

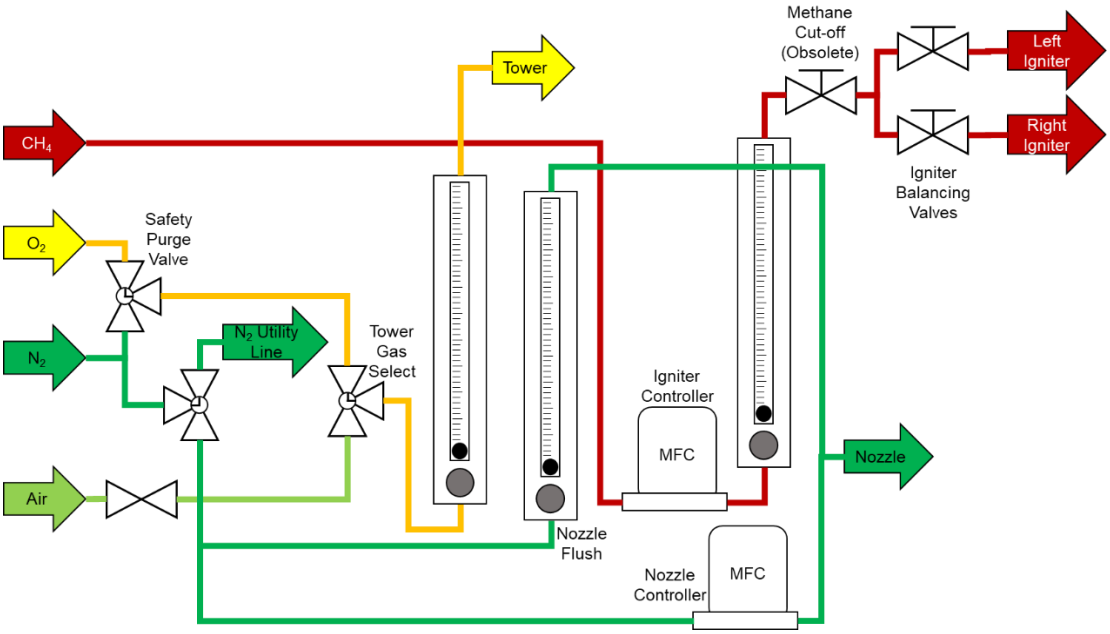


*Figure D.11: Gas connections and controls*

Methane flow is controlled with a mass flow controller set to 30 sccm nominally (varied between 15 and 40 sccm during experiments to be the lowest flow which reliably ignites droplets; last calibration point of MFC 70 = 68.9 sccm) then through an obsolete rate-only rotameter and screw-down valve before bifurcating for the two igniters each with screw-down valves for igniter balancing.

Oxygen is routed through a three-way safety valve at the tanks (for emergency purging of nitrogen), through a three-way valve for tower gas selection (oxygen or air), and through a rate-controlling rotameter calibrated to provide 15 LPM of flow. The only use of the air supplied is to replace oxygen in the tower with air at the conclusion of experiments or otherwise provide purge flow.

Nitrogen is bifurcated at the tank to enter the three-way safety valve (for emergency purging of the oxygen system) and a three-way valve for diverting flow to a utility line used most often with air-free samples (it is recommended that this be replaced with a trifurcation and a two-way valve so the utility line can be operated without interrupting nozzle flow). When the utility line is not in use, nitrogen exits the three way valve and bifurcates again entering a mass flow controller set to 220 sccm (MFC reading of 21) which normally provides flow to the droplet generation nozzle. The other route flows into a normally-closed flow controlling rotameter which can rapidly provide higher nozzle flow for flushing deposits or blowing off a flame which has attached to the nozzle from solvent vapor and threatens to cause nozzle meltdown.

### D.1.4 Camera setup for burning rate constant estimation

Configuration of the tandem high-speed cameras for estimating burning rate constants is shown in Figure 16 and in a schematic below. The two cameras are frame-synced for convenient 1-to-1 correspondence of each image frame which requires a hard-trigger provided by the rising or falling edge (rising usually used here) of a TTL pulse from either a SRS pulser box (which can optionally be driven by a photodiode to trigger by each droplet) or a custom-made camera trigger circuit activated by the red

momentary button on the apparatus control panel. The igniter camera is the black and white Phantom V12.1 camera oriented normally with the macro lens focused at infinity (i.e. any lens will work). The main camera in the color Phantom Miro M110 camera oriented at 90-degree rotation (using the right-angle mount to take advantage of the camera aspect ratio) with the wide-angle lens focused on the plane of the droplets and the CineFlash drive installed. Both cameras are set to a trigger position of 0 and one partition so the trigger causes the maximum recording time to be saved preceding the trigger. The video recording parameters typically used are tabulated below.

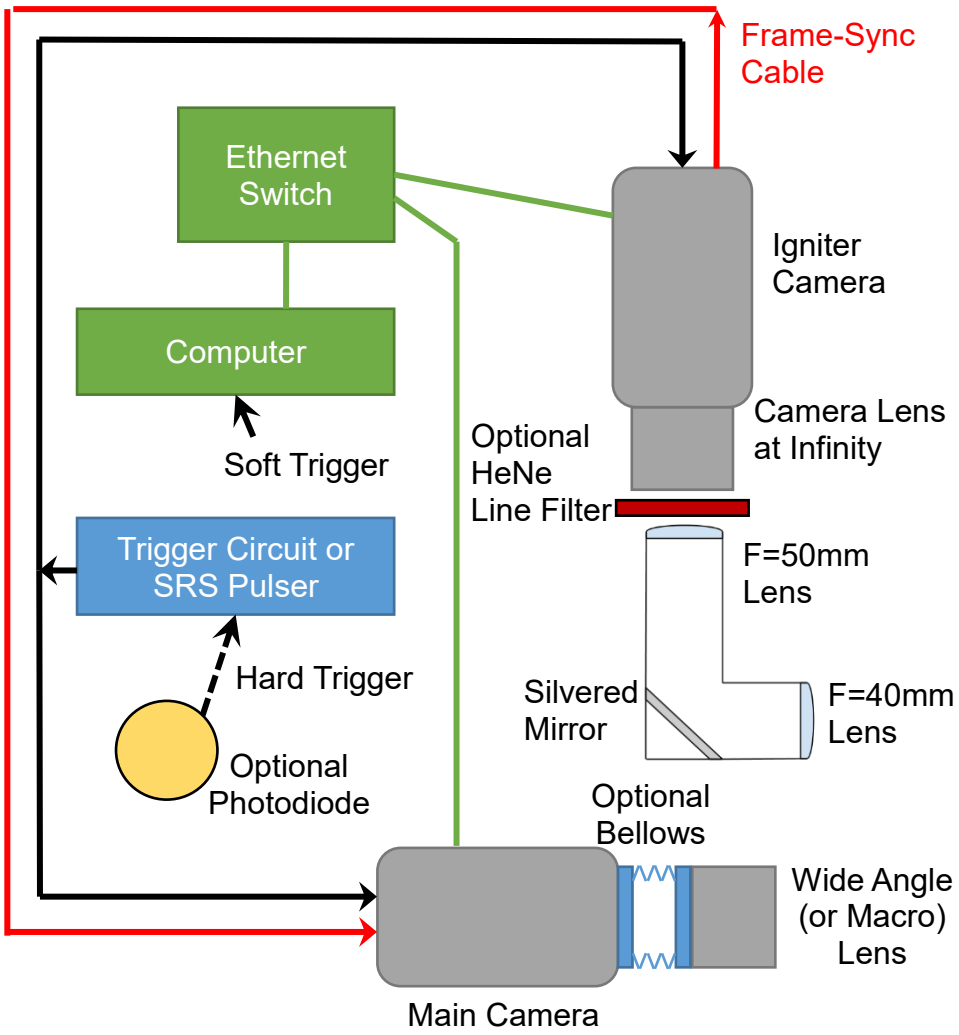


*Figure D.12: Setup and configuration schematic of high-speed cameras*

| Camera | Resolution | Frame Rate | Exposure | Frame Sync | F# |
|---|---|---|---|---|---|
| Miro M110 | 1024x200 | 6000 fps | 166 µs | Internal | 4 to 32 |
| V12.1 | 604x600 | 6000 fps | 10 µs | External | Minimum |

D.1.5 Camera setup for magnified videography

Configuration of the high-speed cameras to image magnified droplets as shown in Figure 19 is mostly the same as the above configuration for burning rate enhancement except for the position of the cameras and some recording parameters.

Unless otherwise noted here, other connections and parameters are the same as above. The black and white V12.1 camera is mounted on the right-angle mount with the wide-angle lens usually used for the color camera and oriented to view both the tower (to see the positions of droplet flames), and the color camera position as it moves in the vertical translation stage. The color MIRO M110 camera is fixed to the vertical translation stage with foam underneath to prevent camera damage. Usually, the macro lens is ample to achieve magnification of the droplets at its nearest focus setting, but bellows can be optionally used to increase this magnification. Camera settings are below. Color camera exposure and F# need to be adapted to specific samples for either visibility or desired saturation level (i.e. for pyrometry).

| Camera | Resolution | Frame Rate | Exposure | Frame Sync | F# |
|---|---|---|---|---|---|
| Miro M110 | 1280x400 | 3300 fps | 100-300 µs | Internal | 4 to 32 |
| V12.1 | 704x1024 | 3300 fps | 100 µs | External | 2.8 |

D.1.6 Experiment Operation Procedure

The usual procedure for operation of the droplet experiment in either camera configuration is listed below. Note that some variations necessary for air-sensitive samples are listed in the subsequent section. Prepare samples for experimentation by mixing suspensions the day prior (sonication then magnetic mixing overnight) and stir up to the point of experimentation if the as-mixed sample is to be tested (or allow to settle if the equilibrium decantant is to be tested).

1. Ensure the droplet generation system and cameras are set up according to the procedures above.

2. With appropriate eye protection, turn on the HeNe laser backlight. Align the laser through the plano-concave lens (F = -50 mm)) against the beam outlet, to the mirror/lens tube with a plano-convex lens against the tower window (F = 200 mm; ~52.1 cm separation between the lenses). The expanded beam should be generally aligned to illuminate the igniter tubes then the black and white camera view can be used to fine tune adjustments made at the laser mount for maximum brightness of the camera feed. If a high-volatility sample is igniting near the pilots enough that flame emission obscures the initial droplets imaged, situate the HeNe line filter between the camera lens and periscope tube.
3. Test the camera system triggers both cameras simultaneously using the red trigger button on the control panel.
4. Turn on all gases and engage tower air (~15 LPM on rotameter) and nozzle nitrogen (21 on MFC = 220 sccm) flows with the rotameter and mass flow controller respectively.
5. Fill a gastight syringe with blank solvent and connect a clean PTFE lead ~4-8 inches long to the needle with a 1/16” Swagelok union (this union is the only non-disposable part in contact with sample and should be cleaned frequently).
6. Test the droplet generation system is working correctly by flowing sample at 30 µL/min.

7. Switch the tower flow to oxygen and confirm its flowrate (15 LPM) on the rotameter.
8. Engage methane flow with the mass flow controller and check that its flow does not register on the silver ball of the fuel rotameter. Such a reading would indicate high flow from a malfunction and methane should be immediate cut off and the tower purged with $N_2$ (the black ball of the rotameter will rise slightly under normal opertation). The methane can be flowed up to 40 sccm on the mass flow controller (display is calibrated to sccm) while the delivery tubes fill but should be lowered to 30 for ignition. **Never flow methane without a tower flow of at least 12 LPM to avoid an explosive tower mixture.**
9. Use a spark igniter from a disassembled grill lighter through a tower port to provide sparks near the pilot tubes. Sometimes it can take up to 2 min for methane to fill the delivery tubes before ignition.
10. Check the pilot flames and lower their intensity to near minimum without extinguishing by changing the MFC set point. Balance their flows using the fine adjustment screw-down valves on their manifolds.
11. Begin sample flow at 20 µL/min to generate droplets of blank solvent.
12. Slowly increase the methane flow with the MFC set point until droplets consistently ignite. Allow 5-10 min of operation for the tower to heat up and record video of the blank control, checking that both videos trigger and capture correctly.

13. The system is now ready to test experimental samples. Control trials are recommended first and sample testing order should be carefully selected to minimize cross-contamination and risk of clogging. Usually, needles are changed if contamination of samples with different constituents is likely. Samples with varying concentrations of the same sample constituents are typically run through the same needle in the order of increasing concentration.
14. Stop the syringe pump, set the rate to 30 µL/min, then 20 µL/min but do not push enter to confirm 20 (this way pushing start will run at 30 until the enter button is pressed slowing it to 20). Ensure the cameras are in capture mode.
15. Prepare the first sample for testing by removing from the stir plate and placing in the sonicator bath starting a timer (no more than 60 s).
16. While sonicating (or before), remove the syringe lead from the Swagelok union and the syringe from the pump and clean the sample lead (physical agitation can be used to dislodge particles on the wall sometimes, otherwise contamination must be cut off). Draw in about ½ in of air into the lead for separation of the sample and blank solvent.
17. Remove the sample from the sonication bath (between this point and droplet generation, the sample is settling so move quickly and steadily; "fast is smooth, smooth is fast"), magnetically stir momentarily, and open the vial on the bench. Draw about 1.5 in of sample into the syringe

lead (more if a longer test window is required), then ½ in of air and wipe the lead clean. Close the sample vial.

18. Return the syringe to the pump and connect the lead to the Swagelok union on the needle. Immediately start the pump and confirm the cameras are in capture mode.
19. Droplets should soon begin falling from blank solvent left in the needle before the first air pocket arrives and the droplets pause. After this pause will be the experimental sample. When they begin flowing, push enter on the pump to decrease the flow to 20 µL/min and allow the camera recording time to elapse before triggering the cameras (or trigger them immediately if droplets cease from sample consumption or a clog).
20. If clogging risk is high, return the pump to 30-50 µL/min after the cameras are triggered to quickly pump out remaining sample and rinse with blank solvent behind it.
21. If a clog has not formed then the second air pocket will cause another pause before blank solvent resumes droplet generation. Allow blank solvent to flow at the higher flow rate for up to 30 s or until contamination is not noticed and decrease the flow to 10-20 µL/min (prolonged operation above 20 µL/min can risk nozzle melt-down).
22. Confirm that both cameras correctly captured droplet combustion and record notes on the trial. Use the color video to find the latest full droplet trace captured and the frame number of that droplet's ignition. Enter that

frame in the black and white video to find the $D_0$ frames for that first ignition of interest. Trim the black and white video immediately after these frames. Optionally trim the other end of this video and save the igniter CINE to the local PC disk, following the naming convention:

**YYYYMMDD_igniter_F*_S*_V##.cine**

where "Y" are year digits, "M" month, "D" day, "F*" any text for camera F-number, "S*" any text identifying the sample, and ## sequential numbering of the videos saved on that day, e.g.

20170923_igniter_F2-8_BzTol4_V06.cine

23. Trim the early end of the color video near the -15000 frame (the MIRO M110 has more memory and therefore records longer videos than the V12.1, the beginning of which are not useful). Save the CINE to FLASH (significantly faster than disk saving but no filename provided so saving time should be noted).
24. Once the videos have saved, the experiment is ready for the next sample. Return to step 13 and repeat. If needle clogging or nozzle fouling/melt-down occurs, replace parts and restart as needed. Refer to troubleshooting procedures below if problems arise.

### D.1.7 Procedure variations for air-sensitive samples

When experimenting with air and moisture sensitive samples, several procedure variations are necessary to ensure their stability until the moment that droplets enter the tower. Above all, the experimentalist needs to wear full PPE including the usual gloves,

long pants, and full coverage shoes, along with a lab coat and goggles with a face shield nearby at minimum. If a sample is especially unstable use a face shield. Be especially cognizant of the sample stability while it is in the syringe. Rapid sample decomposition from air or moisture exposure inside the syringe could cause catastrophic failure and be dangerous. Syringe plunger limits need to be removed so an accident would force the plunger out instead of exploding the syringe (these are usually already removed). Before these experiments, ready a beaker with acetone in the fume hood nearby. Whenever air is thought to have entered the syringe, immediate take it to the fume hood, pull down the sash to the lowest operational level, and inside the hood pull the syringe plunger out in the beaker of acetone to quickly give the sample room for safe expansion. When disposing normally, if no air is thought to be in the syringe, the plunger can be depressed to evacuate excess sample into an appropriate waste stream before removing the plunger. **In an emergency, place the syringe in the fume hood, close the sash, and back away. Brief all experimentalists on these safety measures.**

- Gas-tight syringes with quarter-turn valves built-in need to be used and should be well cleaned (acetone, dilute nitric acid, DI water, acetone) and rinsed last well with acetone or another volatile solvent. New sample lead tubing needs to be installed on the syringes (short leads preferred ~2-3 in). Plunger limits should be removed from the syringes, if they haven't already. These must be pumped into the glove-box where the samples are readied along with several sealable bags (the volatile

cleaning solvent will pump off under vacuum during the glove box evacuation chamber procedures).

- Only one sample can be tested per clean syringe pumped into the glovebox. ~0.5 mL is recommended per syringe and as little gas as possible should remain in the reservoir and care should be taken to avoid any sample remaining in the lead. Close the syringe valves and nest each syringe in at least two sealed bags before removing from the glove box.
- When a sample is to be tested (with the experiment fully set up and tested for correct operation):
    - Ready the nitrogen utility line and the 1/16 in Swagelok union.
    - Remove a loaded syringe from its bags and connect the nitrogen line with gas flowing.
    - Loosen the knurled nut at the syringe outlet to let nitrogen leak backwards through the sample lead purging it.
    - Meanwhile, the syringe can be loaded into the pump. Ready the pump for operation as usual.
    - Tighten the knurled nut to seal the syringe lead before switching the nitrogen flow back to the nozzle and quickly moving the sample lead from the utility line to the needle.
    - Open the syringe valve and begin pumping immediately.

- Many air-sensitive samples are prone to early ignition, flame propagation to the nozzle and nozzle meltdown. See troubleshooting procedures below.
- Between trials, stop the syringe pump to conserve sample if it tolerates this without clogging. Only a few trials will be possible with the 0.5 mL supply.
- If a clog does arise, there may be enough sample left to quickly change the needle:
    - Stop the syringe pump and pull back the plate to relieve pressure.
    - Close the syringe valve (be especially careful with the syringe closed like this and watch the sample for any reaction or gas evolution, following aforementioned safety measures).
    - Place a kim wipe around the knurled nut at the syringe outlet.
    - Transfer the sample lead to the nitrogen utility line with gas flowing.
    - Loosen the knurled nut with the kim wipe to let nitrogen flow purge the sample lead driving any excess sample into the kim wipe (dispose properly).
    - Leave the sample lead purging like this while the needle is replaced and tested with another syringe (acetone with the plastic test syringe recommended).
    - Take usual steps above in this section to restart the sample.

- As mentioned above, when finished with the sample, dispose of it properly in the fume hood by pushing out any excess into a clean beaker (to be directed into an appropriate waste stream after spontaneous reactions cease), then immediately remove the plunger to provide plenty of expansion volume for any residual sample. Rinse with acetone before using normal cleaning procedures.

D.1.8 Troubleshooting

- Droplet generation problems
    - Sample wetting the nozzle; misalignment
        - If normal alignment procedure with the X-Y stage is not successful, first remove the needle and recheck it for straightness. Retry alignment and operation.
        - The post on the X-Y stage can be loosened to change the rotation angle of the needle. This is rarely needed. Watch the needle with a flashlight in the nozzle while retightening, favoring the left side of the nozzle since the X-Y stage can adjust further right.
        - If all else fails, replace the needle and/or nozzle.
    - Clogging of the sample needle
        - Propensity to clog will increase as multiple samples are run through a needle (a cumulative effect). If this is suspected, replace the needle.

        - Specific samples prone to clogging have a greater chance of avoiding a clog if the sample pumping rate is not lowered from 30 µL/min for video capture.
        - See Chapter 9 for recommended redesign of the droplet delivery system for a shorter needle assembly.
    - Nozzle wetting
        - Usually caused by needle misalignment, see above.
        - Check nitrogen nozzle flow rate is appropriate.
- Ignition problems
    - Igniters imbalance/occlusion
        - As igniters deteriorate, balance can be maintained using the screw-down adjustment valves.
        - Some occlusions can be cleared by abruptly closing and opening the screw-down valves to blow out the tubes.
        - Replace or renew the igniter tubes.
    - Nozzle melt-down (flame propagation to the nozzle)
        - Usually caused by a higher than usual volatility sample, e.g. Toluene. Lower the igniter intensities with the MFC set point. This can be lowered below the point of reliable droplet ignitions until the droplets are the sample of interest at which point increase igniters to collect data before again reducing to avoid melt-down.

        - Check the separation of the nozzle end from the igniter. This can be adjusted for higher droplet generation (at the cost of some trajectory repeatability).
        - Any melt-down requires nozzle replacement.
        - Consider alternative nozzle sourcing material.

- Optical problems
    - Flames obscuring $D_0$ measurement
        - High volatility and sooting flames (e.g. toluene) may ignite closer to the igniter tubes, causing a flame in the view of the camera and obscuring the measurement. Use the HeNe filter between the camera lens and the periscope to filter out the flame (soot will likely still be visible). $D_0$ sizing error rates in MATLAB will be higher from soot presence but these are filtered out by the eccentricity check. Gain settings usually need to be higher for the intensity loss from the filter.
        - Optionally translate the $D_0$ camera up slightly to avoid flame development.
    - Poor $D_0$ focus
        - While the backlight is in a setup similar to a shadowgraph, the source is not well collimated and the optics still focus on the droplet. The result is resilient

droplet size as focus changes but sharp focus is still desired (and can change when a nozzle is changed).

- Fix with trial and error using a test sample i.e. blank solvent. The live feed can be watched to spot passing droplets sometimes, or a video can be taken to find a droplet and check focus. Move the camera/periscope stage towards/away from the tower (forward and back) with the translation stage adjustment knob to change focus. Small (1/4 turn) adjustments recommended.

## *D.2 Needle and Nozzle construction*

### D.2.1 Needle construction

Needles constructed for the droplet generation system are made from IDEX U-104 stainless steel tubing (1/16 in x 0.020 in x 30 cm) and Microgroup 31RW Hypodermic Tubing (316H31RW, 1-foot pieces). Both need to be cut to length by scoring and breaking to prevent collapse of the inner capillary diameter. Nozzles are constructed by selecting glass pipets (VWR 14672 5-¾ inch lime glass Pasteur pipets available in UMD Chemistry Store) for straightness and cutting to length by scoring with a diamond wheel and breaking. Procedures for construction of both components are below:

Needle Construction:

1. Trim yellow identification sleeves off as-received IDEX tubing.

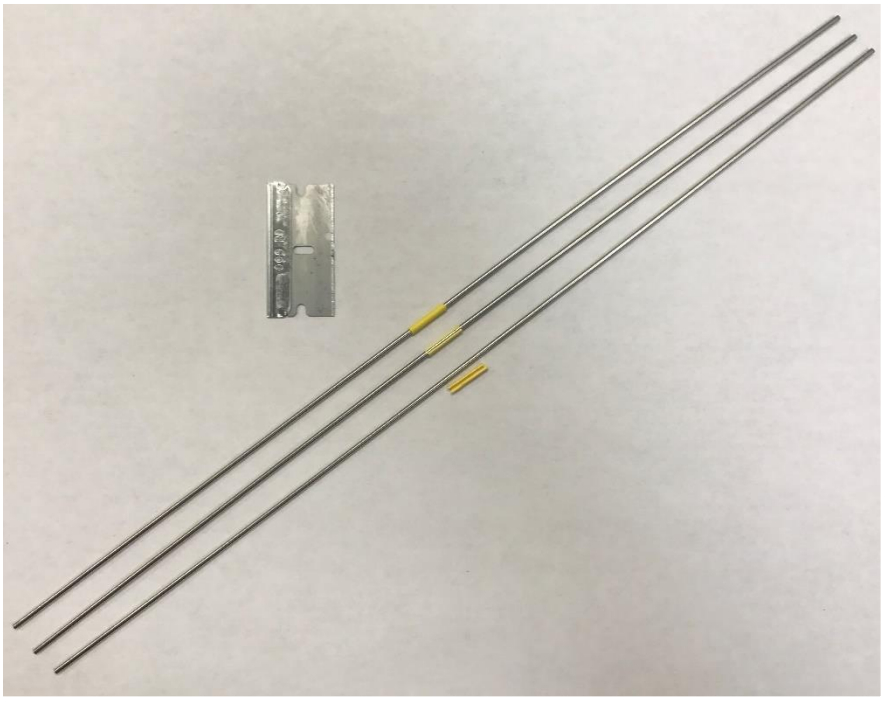

*Figure D.13: IDEX tubing for droplet needle bodies.*

2. Mark the bisection of the tubing (15 cm) and use the Dremel tool on the lowest speed setting with a metal cutting wheel (diamond wheels permissible) to score the tubing circumferentially without cutting into the inner diameter (enough to bend and break the tubing at this scoring without bending the surrounding tubing). Bend the tubing at the score back and forth until the tubing separates.

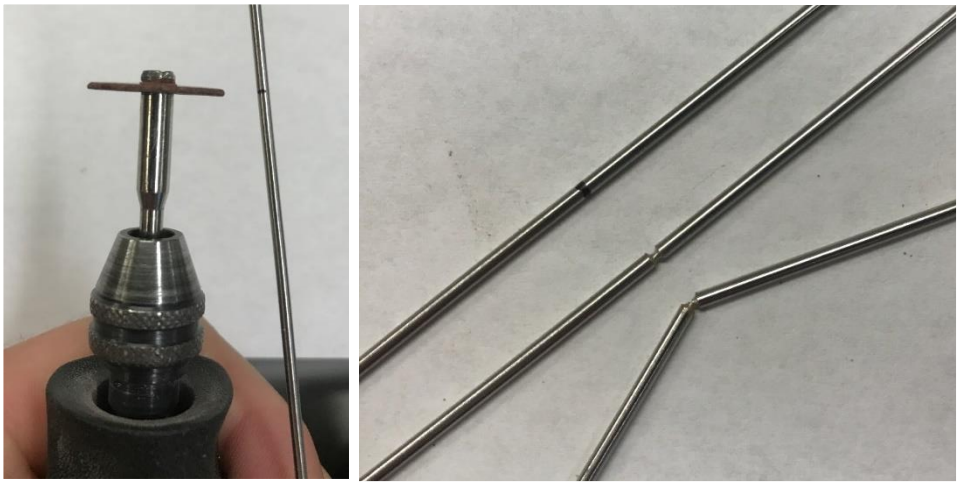

*Figure D.14: Cutting of IDEX tubing in half by scoring and breaking.*

3. Mark the hypodermic tubing approximately 2 mm from each end (which have usually been closed by factory cutting) and every 5.1 cm along the length between the end marks. Each mark needs to be cut. Use the Dremel tool on the lowest speed setting with a diamond wheel. Carefully spin the tubing between two fingers while making light intermittent contact with the cutting wheel to lightly score the tubing. The tubing needs to be scored enough to break without permanently bending the adjacent tubing (~50%). This step usually requires practice to complete consistently. The cut ends must be visually inspected (the stereo magnifier can be used for this) to ensure they have open inner diameters. If one has collapsed, it can be trimmed again as close as possible to the end to recut the end. Each tubing section can tolerate 1-2 recuts by 1-2 mm each and still be ample length for needles.

*Figure D.15: Cutting of hypodermic tubing by careful scoring and breaking.*

4. Repeat the tubing cuts until enough cut sections of IDEX and hypodermic tubes are available to construct the number of needles needed.

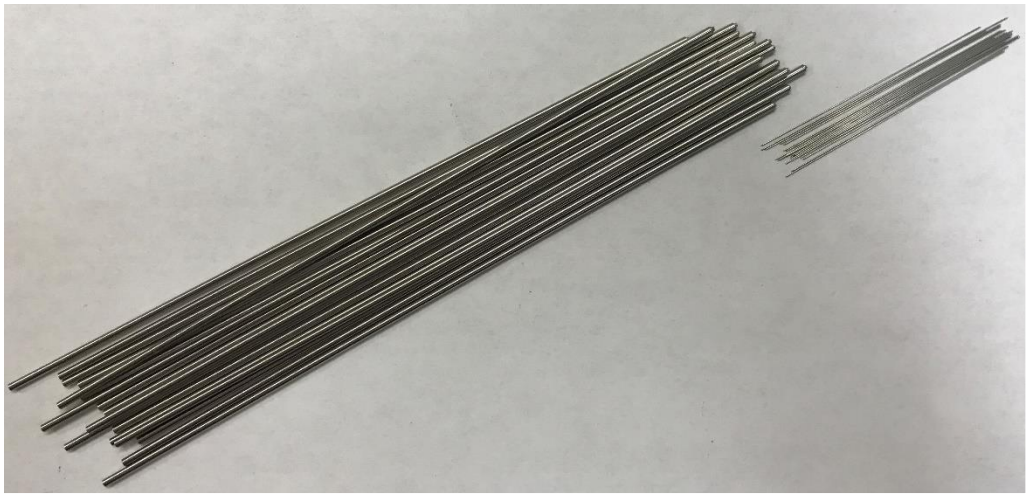

*Figure D.16: Sections of IDEX and hypodermic tubing cut to length.*

5. Mix well a small amount of 2-part JB-Weld steel reinforced epoxy. Use a pipet tip or other tool to pull a bead of epoxy leaving a string of epoxy extending off the bead.

*Figure D.17: JB Weld epoxy mixing and dispensing*

6. With the bead/string of epoxy in one hand and a piece of cut hypodermic tubing in the other, contact the tubing with the string of epoxy ~2mm from the end and spin the tubing to draw epoxy from the bead. Do not allow epoxy to cover the end of the tubing, blocking the opening.

7. Nest the hypodermic tubing with the epoxy into one end of the IDEX capillary tubing. Insert approximately 4 mm and draw the tubing in and out 5-10 times to draw some epoxy into the capillary tubing. The hypodermic tubing can also be spun during the step to keep the epoxy fairly even.

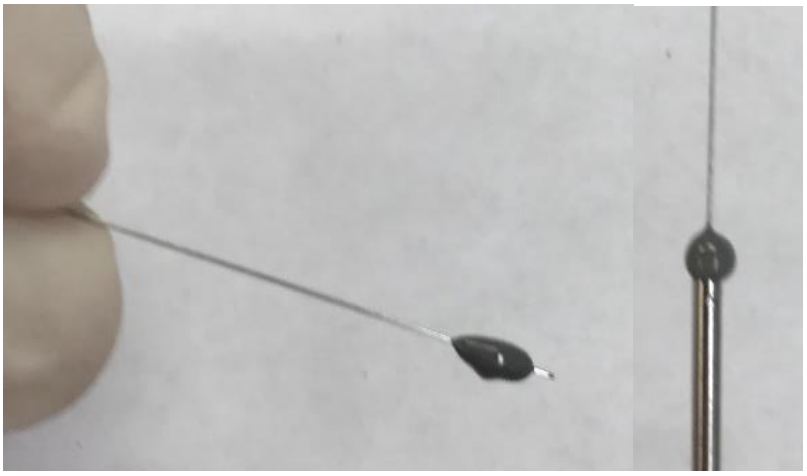

*Figure D.18: Epoxy deposited on the hypodermic tubing and nested in the capillary.*

8. Place the assembled needle epoxy-end-up in the drying rack. Try to keep the hypodermic tubing straight in the capillary. Misalignment will be fixed later. As seen in the sample image below, precise needle lengths can vary by about 5 mm depending on how far they are nested. Allow to dry at least 12 hours, preferably overnight.

*Figure D.19: Assembled needles in the drying rack*

9. Once dry, the needles need the excess epoxy sanded/broken off. Ensure the Dremel tool is at the lowest speed and place each needle in the chuck. Steady the needle with a kim whip before spinning it and then hold coarse sandpaper firmly against the epoxy. Usually, enough torsion on the excess epoxy will break it off at the end of the IDEX tubing, leaving hardened epoxy inside the capillary and around the hypodermic tubing to provide a seal. If it does not break, the epoxy can be sanded flush with the tubing outside diameter.

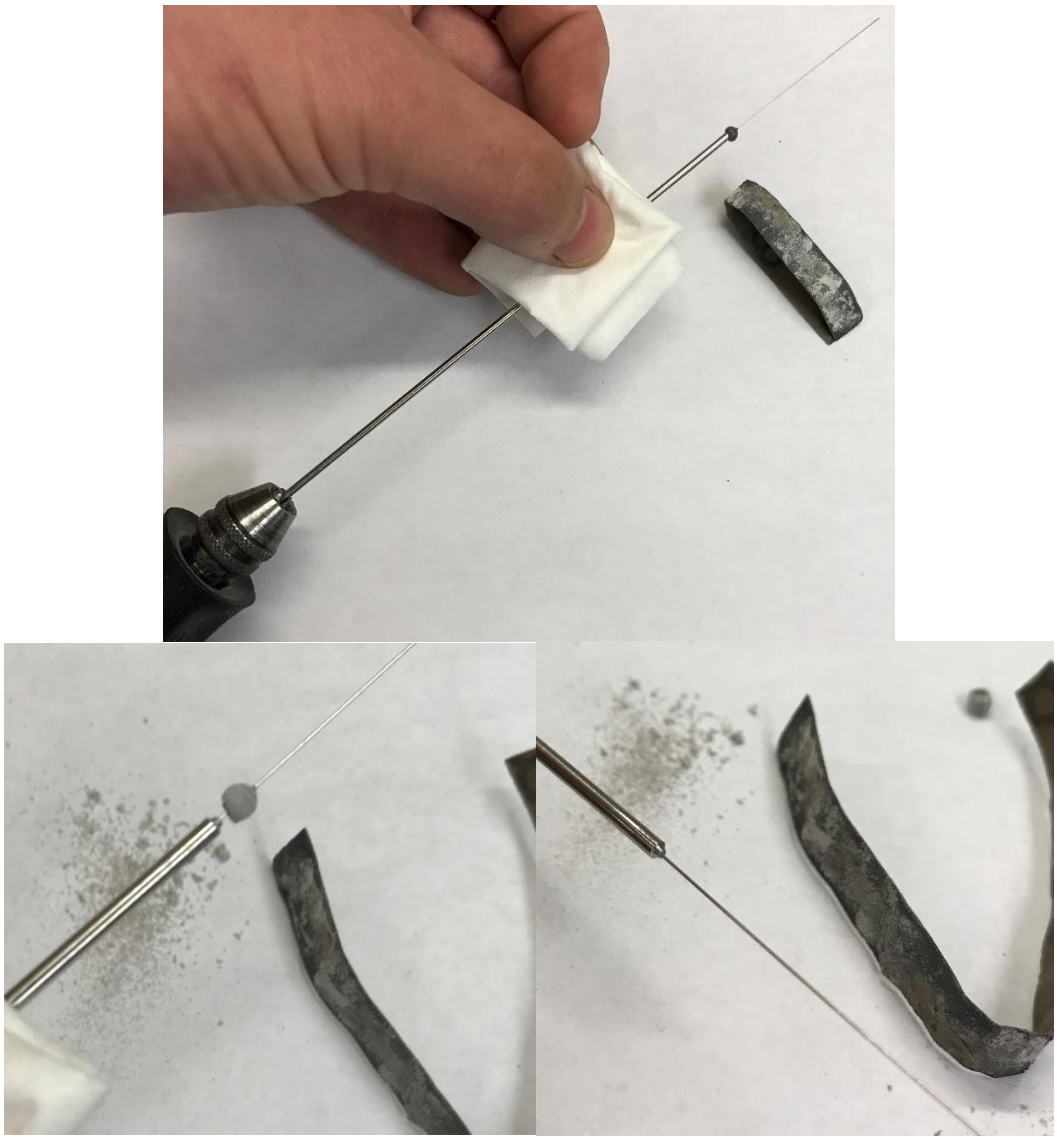

*Figure D.20: Sanding/breaking the excess epoxy from the needle assembly.*

10. The hypodermic tubing is usually misaligned relative to the capillary body. To straighten, hold under a work light and look down the length of the tubing while spinning the tubing between two fingers. A prevailing direction of the misalignment should become clear and can be held to one side as a gloved finger is used to careful bend the hypodermic tubing in the reverse direction to straighten.

*Figure D.21: Assembled needles being straightened and final product ~19 cm long.*

D.2.2 Nozzle selection and construction:

1. Each pipet is placed in the chuck of the hand drill and spun at the high speed with the screw-driving clutch set to 1. As the pipet spins, the straightness can be assessed by watching the lateral runout of the pipet end. Carefully remove from the chuck.


*Figure D.22: Pipet mounted in hand drill chuck for straightness sorting.*

2. Repeat the process sorting the pipets by straightness. Most of the pipets will have severe runout and should be disposed or repurposed. A smaller fraction will have a small amount of runout and can be kept and categorized “fair” while the lowest fraction will have minimal runout visible and should be categorized “good”. The latter should be used as available with “fair” nozzles used as needed.

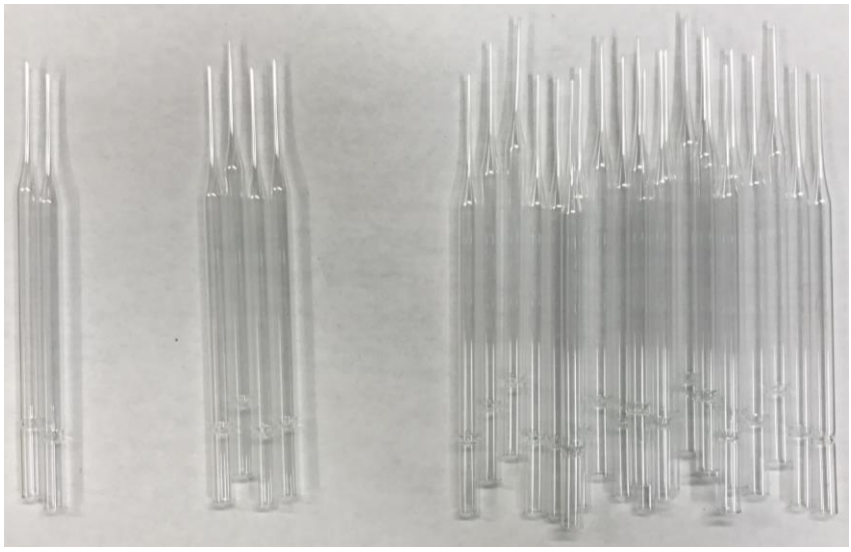


*Figure D.23: Example of pipets sorted by end runout (straightness).*

3. Mark the accepted pipets 6.5 cm from the convergent end. Spin the pipet next to a diamond wheel spinning on the Dremel tool at the lowest speed to score at the mark by ~50% the thickness of the glass.

*Figure D.24: Cutting glass pipets for droplet generation nozzles*

4. Carefully place bending force on the pipet at the scored cut. If it does not easily break, score the pipet slightly more and retry until it breaks.

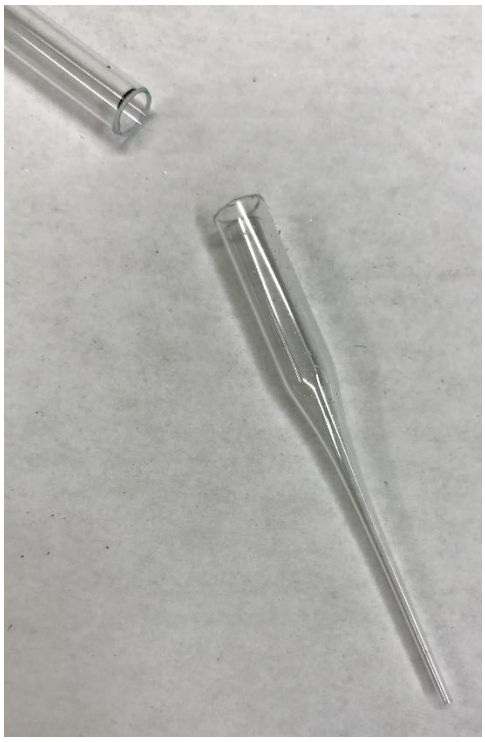

*Figure D.25: Pipet broken at the score mark to leave a nozzle cut to length*

## *D.3 MATLAB-assisted analyses*

### D.3.1 Data collection and analysis for burning rate measurements using MATLAB

1. CINE files recorded of initial droplets passing the igniters should be saved with the naming convention:

   **YYYYMMDD_igniter_F*_S*_V##.cine**

   where "Y" are year digits, "M" month, "D" day, "F*" any text for camera F-number, "S*" any text identifying the sample, and ## sequential numbering of the videos saved on that day, e.g.

   20170923_igniter_F2-8_BzTol4_V06.cine

2. CINE files recorded of full droplet flame trajectories corresponding to each igniter CINE should be saved with the naming convention:

   **YYYYMMDD_tower_F*_S*_V##.cine**

   The timeliest way to save these CINEs is using the CINEFLASH drive in the color camera and using "Save RAM Cine to FLASH" in PCC for each video. This will not save filenames and therefore the time and/or order these are saved should be noted. After transferring files to storage, sorting the igniter and tower CINEs by time in the same folder facilitates easy renaming of the tower CINEs with this naming convention.
3. Prepare all CINEs for MATLAB analysis by date and/or experimental set (multiple sample types allowed) by placing in one directory with read/write access in MATLAB (a NAS location is recommended for data backup and ample read/write speed during processing).
4. Analysis MATLAB scripts can be run from any working directory once the droplet analysis/SDK directory "PhMatlabSDK705-DropletAnalysis" has been added to the MATLAB path (all folders and subfolders).
5. Droplet analysis scripts for user interaction are stored in the top-level of "PhMatlabSDK705-DropletAnalysis" with the burning rate analysis scripts named with ascending alphabetical letter prefixes denoting the order of execution.

6. Split and resave a CINE video for each droplet passing in each video saved:
    a. Open **`A_d0splitting.m`**
    b. Check that `VPstart`, `VSstart`, and `VSstartD` are all set to 1. These are manual start positions for the video being processed, video being saved, and droplet in that video being saved first, respectively in their lists for use if the program crashes before completion and the user wants to pick up in the middle of a workflow.
    c. Change `vFolder` to the directory containing the CINE files.
    d. Execute the script, which performs the following:
        i. Finds igniter CINE files in the folder given over a threshold file size (to avoid previously saved individual droplet CINEs).
        ii. Uses the filenames and SDK to read properties of each CINE e.g. date, starting frame, etc.
        iii. Runs the d0splitter function on each CINE which scans the video for droplets and outputs an array of frame numbers corresponding to a droplet in-frame (one frame given per droplet). Important properties of each CINE including these droplet frame locations are saved to a MATLAB data file in the local directory with the

filename of the CINE appended with "_d0frames". Once this script is complete, these data files can be archived.

iv. Runs the `cineClipSaver` function for each droplet detected to save the frames around the droplet ensuring all frames with a full droplet have been included as a CINE file named the same as the input CINE file with "_D##" appended listing the droplet number. (NOTE: MATLAB sometimes crashes during this step. To continue, note the video and droplet number last saved on the screen printout, close and reopen MATLAB, temporarily comment out the processing loop near line 88, and set `VSstart`, and `VSstartD` to where you would like to resume.)

e. When completed, CINE files should be in the video directory of the experiment CINEs corresponding to each droplet in each original video. Original igniter videos can be archived or deleted as disk space is required.

7. Measure droplet diameters in each frame of a full droplet captured.

a. Open **`B_d0stack.m`**

b. Open an example droplet video and check the gain and gamma setting for good contrast of the droplet (usually 5 and 0.5 respectively or 8-10 and 0.5 if the HeNe line filter was used to

block flame emission of especially volatile and sooting samples). Set these gain and gamma values in the script.

c. Change `vFolder` to the directory containing the CINE files.

d. Execute the script which performs the following:

    i. Scans the folder provided for igniter CINES appended with "_D##" when saved by the previous script.

    ii. Uses filenames and the SDK to read properties of each droplet CINE and preallocate a structure array D for all the droplet information.

    iii. Runs d0thresh function for each droplet which processes each frame for the presence of a full droplet. This function shows an image of each droplet processed comparing the as-read image with the processed image with noise reduction and boundary location. Equivalent circular diameter and eccentricity are output by this function and saved by the script in the D structure if the eccentricity is less than 0.4 (higher indicated an error such as those caused on occasion by soot in especially high sooting fuels).

    iv. Saved the D structure with initial droplet data in a MATLAB data file with the filename date appended with "_D0" which is read by the next script.

8. Initialize the data table for droplet burning rate data aggregation.
    a. Open **`C_D0TrialTableConstruct.m`** (`C_D0TrialTableConstruct_SampleTracking` is old code which can be used to also manage data for sample constituent loadings so MATLAB can be used to plot various properties versus burning rate to look for correlations.)
    b. Set `Dfile` to the MATLAB data file output by the last script (usually the date appended with "_D0").
    c. Set the `experimentName` which is usually just the date and a note without spaces. If data is to be merged with another experimental set, use the same `experimentName` to append data.
    d. Set `useFileNameSampleStrings` to 1 to use the sample code strings in the filenames as the sample names. If sample codes are placeholders for longer names, you can set this to 0 to add detailed names for each sample.
    e. Execute the code which performs the following:
        i. Generates a key file with the sample codes and affiliated names and appends this to an existing key file for the `experimentName` if available or makes a new one.
        ii. Formats a data table ("TrialTable") for the droplet data and burning rates based on D0 data. If errors are found

in this data, they can be fixed with an algorithm in this script or manually fixed in the output data from this script.

iii. Either appends the initialized `D0TrialTable` to an existing one for the `experimentName` if available, or makes a new one and writes it to a MATLAB data file.

9. Estimate burning times and calculate burning rate constants.
    a. Open **`D_burntimeScript.m`**
    b. Check `D0Calib` is the correct magnification calibration (pixels per mm) for the igniter camera. Usually 262.921 is appropriate but if anything changed the usual magnification, a calibration image of an igniter tube should be used to check this value using PCC “Calibrate”.
    c. Set the `experimentName` to the appropriate string used in the last script.
    d. Set `Vstart` to 1 to being at the first CINE in the list, otherwise use this to resume a run in progress.
    e. Set gain and gamma usually to 10 and 2, unless the sample/video is especially bright and reflecting off the walls at these settings. Open a video in PCC to check.
    f. Set `igniterSub` to 1 in most cases. If the igniters cannot be seen with the gain/gamma you’ve used, you’ll need to set this to

0. Otherwise the igniters will be selected and removed from the images to ignore their emission.

g. Set `vFolder` to the folder with the CINE files.

h. Execute the code and follow on-screen instructions, which will perform the following, one CINE at a time:

    i. If applicable, the code shows a sample image from the CINE for the user to select the igniter emission. Multiple selection points can be given and screen instructions prompt the user if user mistakes are made.

    ii. Opens each CINE file automatically for the user to validate droplet ignitions and terminations (each time one opens while MATLAB is busy, the user can take the time to rotate the image and increase gain/gamma for visibility).

    iii. Code guesses how many droplet ignitions and terminations are expected, then searches for each with a coarse search then a fine search and displays the number found versus number expected. Frequently off by 1-2.

    iv. Table of droplets based on known droplets to exist from D0 data is displayed and the first value of the first row gives the CINE frame number of the first droplet ignition processed. User must enter this frame number into PCC

to find this droplet ignition and seek to the termination to identify the termination frame and enter it into MATLAB as prompted.

v. MATLAB will use the burning time of this first droplet to guess which terminations fit which ignitions and regenerate the table. The user needs to validate the ignition and termination frames correspond to correct droplets using PCC. MATLAB allows manual manipulation of the data table to adjust errors. Most errors happen when a sample is too bright or too faint for easy accurate MATLAB sensing. If recorded with good exposure and good gain/gamma are set, error rates are low.

vi. When the table is validated, the user confirms this and MATLAB continues to the next CINE. PCC for the last CINE can be closed and this process repeats for all CINEs in the list.

vii. Once complete, the results table is written to a MATLAB data file and an Excel file.

10. It is recommended that the user now takes the output Excel TrialTable and optionally moves it to a directory for manual data analysis. This file can be opened and the data formatted as a table in Excel to sort by

sample and retrieve burning rate constants (one for each droplet tested) in the last column. These can be copied to a data file for statistics calculation, comparisons, plotting, etc. as the user sees fit. An example Excel file for data post-processing is included in the "PhMatlabSDK705-DropletAnalysis" directory and can optionally be used as a template.

11. User should clean up the MATLAB data files output to the working directory and archive them.

### D.3.2 Emission spectroscopy and image creation

Within the "PhMatlabSDK705-DropletAnalysis" directory with the SDK and burning rate analysis scripts and dependencies is are folders with MATLAB scripts used for assisting with analysis of atomic emission specta as described in Chapters 7 and 8, for creating video image montages such as those shown in Appendix C, and for creating time-lapse images from CINE files. These are not meant to be automated workflows like the burning rate analysis codes but rather tools available for a proficient MATLAB user.

- "Atomic Emission Spectroscopy Tools" directory includes sample data files from the operator of the 32-channel spectrometer (Rohit Jacob herein) and MATLAB scripts used to measure various atomic emission peaks by baseline fitting and difference integration with the trapezoid method.

- “Falling Camera Scripts” directory includes two scripts for creating a montage of frame images and for rescaling pyrometry time data to burning time based on an ignition time found in the black and white wide field video.
    - The montage creator takes as an input a folder where frame images reside from a CINE clip of interest output as individual TIF files. To create this folder, open a CINE of magnified droplets, place frame limits for the region of interest, Save Cine…, make and/or navigate into an empty folder, set the filename (recommend the filename of the CINE) and append with “!5”. As described in the PCC manual, this placeholder inserts the frame number of each image into each filename with 5 digits. Save as type: “TIFF 16,48 images, *.tif” which saves the images as 16-bit TIFFs (or other format/bit depth as user sees fit).
    - The montage creator requires the user to put bounding boxes around each droplet and then crops each by a bounding box of the largest height and width of all the boxes around the center of each box for each frame. Providing the bounding boxes once will output a MATLAB data file which can be kept in the folder with TIF images (or added to a folder of TIF images of the same frames with different image settings e.g. gain) so avoid having to input the bounding boxes again. This process could be automated by thresholding the images and using `regionprops` function to find bounding boxes (code to do so not included).

- In the “Timelapse Creation” directory is a script which can be used to create time-lapse images directly from CINE files wherein multiple droplet flames are visible simultaneously. The script requires a CINE path and the frame limits for one droplet’s complete burning and prompts the user to select the droplet of interest in five frames over that range. This interpolates the droplet position roughly to crop each image and save the maximum pixel values to a summed time lapse image to make it without interference of other droplets.

### D.3.3 Installation of Vision Research Phantom SDK for MATLAB

A C compiler for MATLAB and the Vision Research Phantom SDK for MATLAB are required for droplet experiment analysis using a local installation of MATLAB on a Windows-based PC (these procedures and the analysis code as of October 2017 were tested with **MATLAB R2017a** and **Phantom SDK version 705**). The analysis scripts and functions use the Vision Research Phantom SDK for MATLAB written in C to read and save CINE files directly from MATLAB. For more information on compilers for MATLAB refer to the Mathworks website (https://www.mathworks.com/support/compilers.html). MinGW is an open source compiler suitable for this purpose available from mingw-w64.org. Once a compiler is installed on the local system and MATLAB is configured to use this compiler (see `mex` function), the SDK package available from phantomhighspeed.com and with the droplet analysis files (SDK version 705) need only be in the MATLAB path and the following commands run at the start of each MATLAB session to being using Phantom SDK functions in MATLAB:

```
LoadPhantomLibraries();
RegisterPhantom(true);
```

The following can be optionally run at the end of the session:

```
UnregisterPhantom();
UnloadPhantomLibraries();
```

# Bibliography

[1] V. Minkin, Glossary of terms used in theoretical organic chemistry (IUPAC recommendations 1999), Pure and Applied Chemistry 71 (1999) 1919-1981.
[2] R.D. Johnson, NIST Computational Chemistry Comparison and Benchmark Database: NIST Standard Reference Database Number 101, 2016, pp. http://cccbdb.nist.gov/.
[3] J. Akhavan, Royal Society of Chemistry (Great Britain), The chemistry of explosives, 2nd ed., Royal Society of Chemistry, Cambridge, UK, 2004.
[4] R. Yetter, G. Risha, S. Son, Metal particle combustion and nanotechnology, Proceedings of the Combustion Institute 32 (2009) 1819-1838.
[5] E. Dreizin, Metal-based reactive nanomaterials, Progress in Energy and Combustion Science 35 (2009) 141-167.
[6] R.L. Zurawski, J.M. Green, An evaluation of metallized propellants based on vehicle performance, (1987).
[7] D. Sundaram, V. Yang, R.A. Yetter, Metal-based nanoenergetic materials: Synthesis, properties, and applications, Progress in Energy and Combustion Science 61 (2017) 293-365.
[8] A.S. Rogachev, A.S. Mukasyan, Combustion of heterogeneous nanostructural systems (Review), Combustion Explosion and Shock Waves 46 (2010) 243-266.
[9] K.J. Blobaum, D. Van Heerden, A.J. Gavens, T.P. Weihs, Al/Ni formation reactions: characterization of the metastable Al9Ni2 phase and analysis of its formation, Acta Materialia 51 (2003) 3871-3884.
[10] K.T. Sullivan, N.W. Piekiel, C. Wu, S. Chowdhury, S.T. Kelly, T.C. Hufnagel, K. Fezzaa, M.R. Zachariah, Reactive sintering: An important component in the combustion of nanocomposite thermites, Combustion and Flame 159 (2012) 2-15.
[11] G.C. Egan, K.T. Sullivan, T. LaGrange, B.W. Reed, M.R. Zachariah, In situ imaging of ultra-fast loss of nanostructure in nanoparticle aggregates, Journal of Applied Physics 115 (2014) 6.
[12] G.C. Egan, T. LaGrange, M.R. Zachariah, Time-Resolved Nanosecond Imaging of Nanoscale Condensed Phase Reaction, Journal of Physical Chemistry C 119 (2015) 2792-2797.
[13] H.Y. Wang, G.Q. Jian, S. Yan, J.B. DeLisio, C. Huang, M.R. Zachariah, Electrospray Formation of Gelled Nano-Aluminum Microspheres with Superior Reactivity, Acs Applied Materials & Interfaces 5 (2013) 6797-6801.
[14] H. Wang, G. Jian, G. Egan, M. Zachariah, Assembly and reactive properties of Al/CuO based nanothermite microparticles, Combustion and Flame 161 (2014) 2203-2208.
[15] H.Y. Wang, J.B. DeLisio, G.Q. Jian, W.B. Zhou, M.R. Zachariah, Electrospray formation and combustion characteristics of iodine-containing Al/CuO nanothermite microparticles, Combustion and Flame 162 (2015) 2823-2829.

[16] G. Young, H.Y. Wang, M.R. Zachariah, Application of Nano-Aluminum/Nitrocellulose Mesoparticles in Composite Solid Rocket Propellants, Propellants Explosives Pyrotechnics 40 (2015) 413-418.
[17] R.J. Jacob, B.R. Wei, M.R. Zachariah, Quantifying the enhanced combustion characteristics of electrospray assembled aluminum mesoparticles, Combustion and Flame 167 (2016) 472-480.
[18] B.A. Palaszewski, Advanced launch vehicle upper stages using liquid propulsion and metallized propellants, (1990).
[19] S. Choi, J. Eastman, Enhancing Thermal Conductivity of Fluids with Nanoparticles, ASME International Mechanical Engineering Congress & Exposition, San Francisco, CA, 1995.
[20] P. CHOUDHURY, SLURRY FUELS, Progress in Energy and Combustion Science 18 (1992) 409-427.
[21] S. Cho, F. Takahashi, F. L DRYER, Some theoretical considerations on the combustion and disruption of free slurry droplets, Combustion science and technology 67 (1989) 37-57.
[22] M. Kao, C. Ting, B. Lin, T. Tsung, Aqueous aluminum nanofluid combustion in diesel fuel, Journal of Testing and Evaluation 36 (2008) 186-190.
[23] V. Sajith, C. Sobhan, G. Peterson, Experimental Investigations on the Effects of Cerium Oxide Nanoparticle Fuel Additives on Biodiesel, Advances in Mechanical Engineering (2010).
[24] N. Sarvestany, A. Farzad, E. Ebrahimnia-Bajestan, M. Mir, Effects of Magnetic Nanofluid Fuel Combustion on the Performance and Emission Characteristics, Journal of Dispersion Science and Technology 35 (2014) 1745-1750.
[25] N. Singh, R. Bharj, Effect of CNT-Emulsified Fuel on Performance Emission and Combustion Characteristics of Four Stroke Diesel Engine, Int. J. Curr. Eng. Technol 5 (2015) 477-485.
[26] R. Mehta, M. Chakraborty, P. Parikh, Nanofuels: Combustion, engine performance and emissions, Fuel 120 (2014) 91-97.
[27] H. Tyagi, P.E. Phelan, R. Prasher, R. Peck, T. Lee, J.R. Pacheco, P. Arentzen, Increased Hot-Plate Ignition Probability for Nanoparticle-Laden Diesel Fuel, Nano Letters (2008).
[28] T. Shaafi, K. Sairam, A. Gopinath, G. Kumaresan, R. Velraj, Effect of dispersion of various nanoadditives on the performance and emission characteristics of a CI engine fuelled with diesel, biodiesel and blends-A review, Renewable & Sustainable Energy Reviews 49 (2015) 563-573.
[29] B. Van Devener, S. Anderson, Breakdown and combustion of JP-10 fuel catalyzed by nanoparticulate CeO2 and Fe2O3, Energy & Fuels 20 (2006) 1886-1894.
[30] C. Allen, G. Mittal, C. Sung, E. Toulson, T. Lee, An aerosol rapid compression machine for studying energetic-nanoparticle-enhanced combustion of liquid fuels, Proceedings of the Combustion Institute 33 (2011) 3367-3374.

[31] J. Sabourin, D. Dabbs, R. Yetter, F. Dryer, I. Aksay, Functionalized Graphene Sheet Colloids for Enhanced Fuel/Propellant Combustion, Acs Nano 3 (2009) 3945-3954.
[32] J. Sabourin, R. Yetter, B. Asay, J. Lloyd, V. Sanders, G. Risha, S. Son, Effect of Nano-Aluminum and Fumed Silica Particles on Deflagration and Detonation of Nitromethane, Propellants Explosives Pyrotechnics 34 (2009) 385-393.
[33] J. Sabourin, R. Yetter, V. Parimi, Exploring the Effects of Nanostructured Particles on Liquid Nitromethane Combustion, Journal of Propulsion and Power 26 (2010) 1006-1015.
[34] K. McCown, E. Petersen, Effects of nano-scale additives on the linear burning rate of nitromethane, Combustion and Flame 161 (2014) 1935-1943.
[35] V.V. Bakulin, V.Y. Velikodny, Y.K. Levin, V.V. Popov, INVESTIGATION OF THE PROCESSES OF IGNITION AND COMBUSTION OF LIQUID HYDROCARBON FUELS WITH NANOADDITIVES, Nanoscience and Technology-an International Journal 7 (2016) 149-164.
[36] M. Ghamari, A. Ratner, Combustion characteristics of colloidal droplets of jet fuel and carbon based nanoparticles, Fuel 188 (2017) 182-189.
[37] B.H. Chen, J.Z. Liu, F. Yao, H.P. Li, J.H. Zhou, Effect of oleic acid on the stability and rheology of nanoaluminium/JP-10 bi-phase system, Micro & Nano Letters 12 (2017) 675-679.
[38] F.S. Shariatmadar, S.G. Pakdehi, Effect of various surfactants on the stability time of kerosene-boron nanofluids, Micro & Nano Letters 11 (2016) 498-502.
[39] M.J. Du, G. Li, Preparation of silane-capped boron nanoparticles with enhanced dispersibility in hydrocarbon fuels, Fuel 194 (2017) 75-82.
[40] K. Kannaiyan, R. Sadr, Asme, Influence of Nanoparticles on Spray Performance of Alternative Jet Fuels, Proceedings of the Asme Turbo Expo: Turbine Technical Conference and Exposition, 2016, Vol 3 (2016).
[41] K. Kannaiyan, K. Anoop, R. Sadr, Effect of Nanoparticles on the Fuel Properties and Spray Performance of Aviation Turbine Fuel, Journal of Energy Resources Technology-Transactions of the Asme 139 (2017).
[42] M. Mahrukh, A. Kumar, S. Gu, S. Kamnis, E. Gozali, Modeling the Effects of Concentration of Solid Nanoparticles in Liquid Feedstock Injection on High-Velocity Suspension Flame Spray Process, Industrial & Engineering Chemistry Research 55 (2016) 2556-2573.
[43] I. Javed, S. Baek, K. Waheed, Evaporation characteristics of heptane droplets with the addition of aluminum nanoparticles at elevated temperatures, Combustion and Flame 160 (2013) 170-183.
[44] I. Javed, S. Baek, K. Waheed, G. Ali, S. Cho, Evaporation characteristics of kerosene droplets with dilute concentrations of ligand-protected aluminum nanoparticles at elevated temperatures, Combustion and Flame 160 (2013) 2955-2963.
[45] I. Javed, S.W. Baek, K. Waheed, Effects of dense concentrations of aluminum nanoparticles on the evaporation behavior of kerosene droplet at elevated

temperatures: The phenomenon of microexplosion, Experimental Thermal and Fluid Science 56 (2014) 33-44.
[46] I. Javed, S. Baek, K. Waheed, Autoignition and combustion characteristics of heptane droplets with the addition of aluminium nanoparticles at elevated temperatures, Combustion and Flame 162 (2015) 191-206.
[47] H. Kim, S.W. Baek, Combustion of a single emulsion fuel droplet in a rapid compression machine, Energy 106 (2016) 422-430.
[48] D.M. Kim, S.W. Baek, J. Yoon, Ignition characteristics of kerosene droplets with the addition of aluminum nanoparticles at elevated temperature and pressure, Combustion and Flame 173 (2016) 106-113.
[49] K. Waheed, S.W. Baek, I. Javed, Y. Kristiyanto, INVESTIGATIONS ON THERMAL RADIATIVE CHARACTERISTICS OF LPG COMBUSTION: EFFECT OF ALUMINA NANOPARTICLES ADDITION, Combustion Science and Technology 187 (2015) 827-842.
[50] Y. Gan, L. Qiao, Evaporation characteristics of fuel droplets with the addition of nanoparticles under natural and forced convections, International Journal of Heat and Mass Transfer 54 (2011) 4913-4922.
[51] Y. Gan, L. Qiao, Combustion characteristics of fuel droplets with addition of nano and micron-sized aluminum particles, Combustion and Flame 158 (2011) 354-368.
[52] Y. Gan, Y. Lim, L. Qiao, Combustion of nanofluid fuels with the addition of boron and iron particles at dilute and dense concentrations, Combustion and Flame 159 (2012) 1732-1740.
[53] Y. Gan, L. Qiao, Optical Properties and Radiation-Enhanced Evaporation of Nanofluid Fuels Containing Carbon-Based Nanostructures, Energy & Fuels 26 (2012) 4224-4230.
[54] Y. Gan, L. Qiao, Radiation-enhanced evaporation of ethanol fuel containing suspended metal nanoparticles, International Journal of Heat and Mass Transfer 55 (2012) 5777-5782.
[55] S. Tanvir, L. Qiao, Effect of Addition of Energetic Nanoparticles on Droplet-Burning Rate of Liquid Fuels, Journal of Propulsion and Power 31 (2015) 408-415.
[56] S. Tanvir, S. Jain, L. Qiao, Latent heat of vaporization of nanofluids: Measurements and molecular dynamics simulations, Journal of Applied Physics 118 (2015) 8.
[57] S. Tanvir, L. Qiao, Droplet burning rate enhancement of ethanol with the addition of graphite nanoparticles: Influence of radiation absorption, Combustion and Flame 166 (2016) 34-44.
[58] S. Tanvir, S. Biswas, L. Qiao, Evaporation characteristics of ethanol droplets containing graphite nanoparticles under infrared radiation, International Journal of Heat and Mass Transfer 114 (2017) 541-549.
[59] A. Miglani, S. Basu, Coupled Mechanisms of Precipitation and Atomization in Burning Nanofluid Fuel Droplets, Scientific Reports 5 (2015).
[60] C. LAW, INTERNAL BOILING AND SUPERHEATING IN VAPORIZING MULTICOMPONENT DROPLETS, Aiche Journal 24 (1978) 626-632.

[61] C. LAW, RECENT ADVANCES IN DROPLET VAPORIZATION AND COMBUSTION, Progress in Energy and Combustion Science 8 (1982) 171-201.
[62] A. MAKINO, C. LAW, ON THE CONTROLLING PARAMETER IN THE GASIFICATION BEHAVIOR OF MULTICOMPONENT DROPLETS, Combustion and Flame 73 (1988) 331-336.
[63] C. WANG, X. LIU, C. LAW, COMBUSTION AND MICROEXPLOSION OF FREELY FALLING MULTICOMPONENT DROPLETS, Combustion and Flame 56 (1984) 175-197.
[64] M.E. Gluckstein, Hypergolic ignition method using organoaluminum compositions, Google Patents, 1970.
[65] C.J. MARSEL, E.O. KALIL, A. REIDLINGER, L. KRAMER, Preparation and Ignition Properties of Aluminum Alkyls, ACS Publications1959.
[66] H.M.T. Nguyen, H.Y. Tang, W.F. Huang, M.C. Lin, Mechanisms for reactions of trimethylaluminum with molecular oxygen and water, Computational and Theoretical Chemistry 1035 (2014) 39-43.
[67] M. Tacke, H. Schnöckel, Metastable aluminum chloride, AlCl, as a solid and in solution, Inorganic Chemistry 28 (1989) 2895-2896.
[68] P. TIMMS, CHEMISTRY OF BORON AND SILICON SUBHALIDES, Accounts of Chemical Research 6 (1973) 118-123.
[69] M. MOCKER, C. ROBL, H. SCHNOCKEL, DONOR-STABILIZED ALUMINUM(I) BROMIDE, Angewandte Chemie-International Edition in English 33 (1994) 1754-1755.
[70] G. Godsave. Studies of the combustion of drops in a fuel spray—the burning of single drops of fuel. Symposium (International) on Combustion; 1953: Elsevier. p. 818-830.
[71] D.B. Spalding. The combustion of liquid fuels. Symposium (international) on combustion; 1953: Elsevier. p. 847-864.
[72] M.Y. Choi, F.L. Dryer, Microgravity droplet combustion, Microgravity combustion: fire in free fall, combustion treatise (2001) 183-297.
[73] H. Hottel, G. Williams, H. Simpson. Combustion of droplets of heavy liquid fuels. Symposium (International) on Combustion; 1955: Elsevier. p. 101-129.
[74] H. Wise, J. Lorell, B.J. Wood. The effects of chemical and physical parameters on the burning rate of a liquid droplet. Symposium (International) on Combustion; 1955: Elsevier. p. 132-141.
[75] L.P. Yarin, G. Hetsroni, A. Mosyak, Combustion of two-phase reactive media, Springer Science & Business Media2013.
[76] A. Williams, Combustion of droplets of liquid fuels: a review, Combustion and flame 21 (1973) 1-31.
[77] A. Williams, Fundamentals of oil combustion, Progress in Energy and Combustion Science 2 (1976) 167-179.
[78] K. Annamalai, W. Ryan, Interactive processes in gasification and combustion. Part I: Liquid drop arrays and clouds, Progress in energy and combustion science 18 (1992) 221-295.

[79] J.C. Yang, Heterogeneous combustion, Environmental Implications of Combustion Processes (1993).
[80] S. Kumagai, H. Isoda. Combustion of fuel droplets in a falling chamber. Symposium (International) on Combustion; 1957: Elsevier. p. 726-731.
[81] S. Kumagai, T. Sakai, S. Okajima. Combustion of free fuel droplets in a freely falling chamber. Symposium (International) on Combustion; 1971: Elsevier. p. 779-785.
[82] C. Law, Unsteady droplet combustion with droplet heating, Combustion and Flame 26 (1976) 17-22.
[83] S.K. Aggarwal, A review of spray ignition phenomena: present status and future research, Progress in Energy and Combustion Science 24 (1998) 565-600.
[84] S.H. Chung, C.K. Law, An experimental study of droplet extinction in the absence of external convection, Combustion and flame 64 (1986) 237-241.
[85] C. Law, Asymptotic theory for ignition and extinction in droplet burning, Combustion and Flame 24 (1975) 89-98.
[86] C. Law, Multicomponent droplet combustion with rapid internal mixing, Combustion and Flame 26 (1976) 219-233.
[87] C. Law, S. Chung, N. Srinivasan, Gas-phase quasi-steadiness and fuel vapor accumulation effects in droplet burning, Combustion and flame 38 (1980) 173-198.
[88] A. Williams, Combustion of liquid fuel sprays, Butterworth-Heinemann2013.
[89] F.E. Fendell, M.L. Sprankle, D.S. Dodson, Thin-flame theory for a fuel droplet in slow viscous flow, Journal of Fluid Mechanics 26 (1966) 267-280.
[90] C. Law, F. Williams, Kinetics and convection in the combustion of alkane droplets, Combustion and Flame 19 (1972) 393-405.
[91] G. Williams, Combustion theory, (1985).
[92] X. E, X. Zhi, Y. Zhang, C. Li, J. Zou, X. Zhang, L. Wang, Jet fuel containing ligand-protecting energetic nanoparticles: A case study of boron in JP-10, Chemical Engineering Science 129 (2015) 9-13.
[93] A. Singh, G. Van den Mooter, Spray drying formulation of amorphous solid dispersions, Advanced Drug Delivery Reviews 100 (2016) 27-50.
[94] I.G. Loscertales, A. Barrero, I. Guerrero, R. Cortijo, M. Marquez, A. Ganan-Calvo, Micro/nano encapsulation via electrified coaxial liquid jets, Science 295 (2002) 1695-1698.
[95] A. Jaworek, A. Sobczyk, Electrospraying route to nanotechnology: an overview, Journal of electrostatics 66 (2008) 197-219.
[96] A. Jaworek, Micro-and nanoparticle production by electrospraying, Powder technology 176 (2007) 18-35.
[97] N. Bock, M.A. Woodruff, D.W. Hutmacher, T.R. Dargaville, Electrospraying, a reproducible method for production of polymeric microspheres for biomedical applications, Polymers 3 (2011) 131-149.
[98] S. Yan, G. Jian, M.R. Zachariah, Electrospun nanofiber-based thermite textiles and their reactive properties, ACS applied materials & interfaces 4 (2012) 6432-6435.

[99] B.J. McBride, S. Gordon, Computer Program for Calculation of Complex Chemical Equilibrium Compositions and Applications II. Users Manual and Program Description. 2; Users Manual and Program Description, (1996).
[100] J.M. Densmore, M.M. Biss, K.L. McNesby, B.E. Homan, High-speed digital color imaging pyrometry, Applied Optics 50 (2011) 2659-2665.
[101] J. Kalman, T. Hedman, On the Origin and Use of the Emissivity Approximations for Alumina Particles, Propellants, Explosives, Pyrotechnics 41 (2016) 793-797.
[102] S. Basu, A. Miglani, Combustion and heat transfer characteristics of nanofluid fuel droplets: A short review, International Journal of Heat and Mass Transfer 96 (2016) 482-503.
[103] G. Jian, L. Zhou, N. Piekiel, M. Zachariah, Low Effective Activation Energies for Oxygen Release from Metal Oxides: Evidence for Mass-Transfer Limits at High Heating Rates, Chemphyschem 15 (2014) 1666-1672.
[104] W. Zhou, J. DeLisio, X. Wang, M. Zachariah, Reaction mechanisms of potassium oxysalts based energetic composites, Combustion and Flame 177 (2017) 1-9.
[105] K. Okuyama, I. Lenggoro, Preparation of nanoparticles via spray route, Chemical Engineering Science 58 (2003) 537-547.
[106] J. Xie, J. Jiang, P. Davoodi, M. Srinivasan, C. Wang, Electrohydrodynamic atomization: A two-decade effort to produce and process micro-/nanoparticulate materials, Chemical Engineering Science 125 (2015) 32-57.
[107] H.Y. Wang, R.J. Jacob, J.B. DeLisio, M.R. Zachariah, Assembly and encapsulation of aluminum NP's within AP/NC matrix and their reactive properties, Combustion and Flame 180 (2017) 175-183.
[108] G. Jian, J. Feng, R. Jacob, G. Egan, M. Zachariah, Super-reactive Nanoenergetic Gas Generators Based on Periodate Salts, Angewandte Chemie-International Edition 52 (2013) 9743-9746.
[109] R.W.B. Pearse, A.G. Gaydon, Identification of molecular spectra, Chapman and Hall1976.
[110] P. Linstrom, W. Mallard, The NIST Chemistry WebBook: A chemical data resource on the internet, Journal of Chemical and Engineering Data 46 (2001) 1059-1063.
[111] S.R. Turns, D. Mueller, Ignition and combustion characteristics of metallized propellants, (1993).
[112] C. Parigger, J. Hornkohl, Computation of AlO B-2 Sigma(+) -> X-2 Sigma(+) emission spectra, Spectrochimica Acta Part a-Molecular and Biomolecular Spectroscopy 81 (2011) 404-411.
[113] C. Parigger, D.M. Surmick, A.C. Woods, A. Donaldson, J.L. Height, Measurement and Analysis of Aluminum Monoxide Flame Emission Spectra, Measurement (2013).
[114] B. BENT, R. NUZZO, L. DUBOIS, SURFACE ORGANOMETALLIC CHEMISTRY IN THE CHEMICAL VAPOR-DEPOSITION OF ALUMINUM FILMS USING TRIISOBUTYLALUMINUM - BETA-HYDRIDE AND BETA-

ALKYL ELIMINATION-REACTIONS OF SURFACE ALKYL INTERMEDIATES, Journal of the American Chemical Society 111 (1989) 1634-1644.